Vapour shielding of liquid metal walls in nuclear fusion devices

Document status and date:
Published: 15/05/2018

Document Version:
Publisher's PDF, also known as Version of Record (includes final page, issue and volume numbers)

Please check the document version of this publication:

• A submitted manuscript is the version of the article upon submission and before peer-review. There can be important differences between the submitted version and the official published version of record. People interested in the research are advised to contact the author for the final version of the publication, or visit the DOI to the publisher's website.
• The final author version and the galley proof are versions of the publication after peer review.
• The final published version features the final layout of the paper including the volume, issue and page numbers.

Link to publication

Vapour Shielding of Liquid Metal Walls in Nuclear Fusion Devices

G.G. van Eden

Vapour Shielding of Liquid Metal Walls in Nuclear Fusion Devices

PROEFSCHRIFT

ter verkrijging van de graad van doctor aan de Technische Universiteit Eindhoven, op gezag van de rector magnificus prof.dr.ir. F.P.T. Baaijens, voor een commissie aangewezen door het College voor Promoties, in het openbaar te verdedigen op dinsdag 15 mei 2018 om 13:30 uur

door

Gustaaf Galein van Eden

geboren te De Bilt

Dit proefschrift is goedgekeurd door de promotoren en de samenstelling van de promotiecommissie is als volgt:

voorzitter:	prof.dr.ir. G.M.W. Kroesen
1^e promotor:	prof.dr.ir. M.C.M. van de Sanden
2^e promotor:	prof.dr. N.J. Lopes Cardozo
copromotor:	dr. T.W. Morgan (DIFFER)
leden:	prof.dr.ir. G.J.F. van Heijst
	dr.ir. G.C. De Temmerman (The ITER Organization)
	dr. M.A. Jaworski (Princeton Plasma Physics Laboratory, USA)
adviseur:	prof.dr.ir. Jan Leen Kloosterman (TU Delft)

Vapour Shielding of Liquid Metal Walls in Nuclear Fusion Devices

G.G. (Stein) van Eden
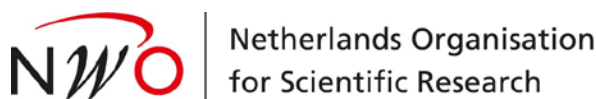
Eindhoven University of Technology
March 2018

"It would be possible to describe everything scientifically, but it would make no sense. It would be a description without meaning - as if you described a Beethoven symphony as a variation of wave pressure"

Albert Einstein

Table of contents

List of figures

Part A

Framework and Overview of the Research

1   Introduction

The background and motivation of this thesis work is described first, for which purpose a general explanation of nuclear fusion in magnetic confinement devices and the wall challenge is provided. The specialised reader may readily proceed to section 2, where the objectives and outline of this thesis are presented.

1.1   The global energy challenge

It is becoming widely recognized that our planet is being pushed into a trajectory of irreversible climate change caused by human activity. This may result in a crisis of unprecedented magnitude since parts of our world are likely to become inhabitable by either drought or rising sea levels [1]. Consequential migration may further push limited resources which can potentially increase the risk of conflicts [2]. Mitigating the effects of human activity on global warming should be of the highest urgency today in order to ward off the most severe possible scenarios. The first counteracting steps are being taken by the majority of countries through signing the Paris Agreement which aims to limit the global temperature rise to maximally $2\,°C$ compared to pre-industrial levels [3]. This is only feasible if the levels of CO_2 emission during the second half of the 21st will be much reduced compared to levels today despite the projected growth of the world population from the current 7.6 billion to 11.2 billion by the end of this century, most notably taking place on the African continent [4]. It is expected that more people will migrate towards the urban landscape, resulting in the growth of megacities (>10 million inhabitants) in size and number due to expected rising prosperity. The global energy demand by the year 2050 could consequently be three times higher than levels at the beginning of the century, assuming that emerging economies follow traditional development paths [5]. In addition, further electrification of our world, most notably that of transportation and heating/cooling, is expected to cause an increase in electricity usage of 36-39 % by 2050 with respect to current levels [6]. With more people becoming increasingly reliant on permanent energy availability while no additional CO_2 production can be accepted, finding a solution for a sustainable energy system is of paramount importance for a prosperous and habitable planet.

Energy production from renewable sources such as wind and solar is becoming increasingly important but suffers from the problem of intermittency, is generally of low energy density and is dependent on geography. An analysis of the German power system in recent years pointed out that only 40 % of the baseload power can be carried by renewables due to the intermittency limitation [7]. The development of technologies dealing

with storing and transportation of these sources, for instance by converting renewable energy into artificial fuels and exploiting high-capacity energy storage, are progressing and are expected to help ameliorate this problem. Providing continuous baseload power for megacities is however unlikely to be feasible via this scheme since it requires long distance transmission in addition to the inherent low-energy density and intermittency of renewable sources.

In nuclear fusion, energy is harvested from the highest energy-density fuel known in the universe, namely the energy stored inside atomic nuclei. This process can theoretically yield immense fuel-to-electricity efficiencies, while at the same time being an intrinsically safe process [8] with no possibility of nuclear meltdown. The impact on land use could be dramatically reduced compared to renewable energy sources. While this is likewise the case for nuclear fission, the problem of storing nuclear waste for thousands of years disappears. However, given the level of technological maturity of fusion, it is too early to judge whether nuclear fusion will solve the energy crisis we are facing. It certainly holds promise in alleviating this complex objective as it may allow for large-scale, continuous electricity production in a low-carbon economy. Rapidly advancing fusion technology to maturity is hence imperative in order to make a significant impact on the energy mix of the second half of this century.

Given the desirability of fusion, its development as a viable future CO_2 neutral energy source is now included in the Integrated Strategic Energy Technology Plan written by the European Commission, herein describing Europe's technology long-term vision of 2050 [9]. Maintaining Europe's competitive position in energy technology is a key priority for the EU. The development of magnetic confinement fusion is part of these efforts with its ultimate goal having fusion electricity in the grid by the second half of the century [10]. Crucial in these plans is the successful realization of ITER [11], a large-scale global scientific experiment that aims to demonstrate the technological and scientific feasibility of fusion. Its goal is to demonstrate significant fusion power generation, self-sustained tritium production and allowing for fusion power plant technologies (e.g. remote handling, steady-state heating) to mature. The roadmap further aims at achieving sufficient know-how to start constructing a demonstration power plant (DEMO) by 2030-2035. This facility is envisaged as the only stepping stone between ITER and a commercial fusion power plant.

Other partners in ITER are also pursuing their own fusion agendas. For example, the goal for China is to have fusion energy in the grid by 2050 via intermediate nuclear fission solutions such as Pressurized Water Reactors and Fast Breeder Reactors [12]. The advantage of this route is that the development of tritium breeding technology and materials

testing can greatly benefit from the high-energy neutron spectrum present in such reactors, hereby exploring uncharted territory highly relevant to fusion. By constructing the China Fusion Engineering Test Reactor (CFETR) [13], China furthermore aims to bridge the gap between the ITER and DEMO devices, hereby rapidly advancing the development of commercial fusion.

1.2 Fusion on earth

The basic process of nuclear fusion entails the coalescence of two light atomic nuclei into a single heavier one, hereby releasing large quantities of thermal energy, following from Einstein's famous formula $E = mc^2$ where m represent the mass difference between the fusion product and the combined masses of the particles prior to the fusion process. Extremely high kinetic energies are required in order to overcome the Coulomb repulsion between the positively charged particles. At small enough interatomic distance, the strong force comes into play and the nuclei can fuse. Net energy can be produced if enough fusion reactions can be produced for a given input energy rate used to heat the nuclei. The conditions for fusion to reach ignition, i.e. for the fusion reaction to be self-sustaining, can be reached once the product of ion density (n_i), ion temperature (T_i) and energy confinement time (τ_e) are greater than a certain number, as expressed by the Lawson criterion: $n_i T_i \tau_e \geq 3 \times 10^{21}\ \mathrm{m}^{-3}\,\mathrm{keV}$ [14]. These conditions are naturally reached
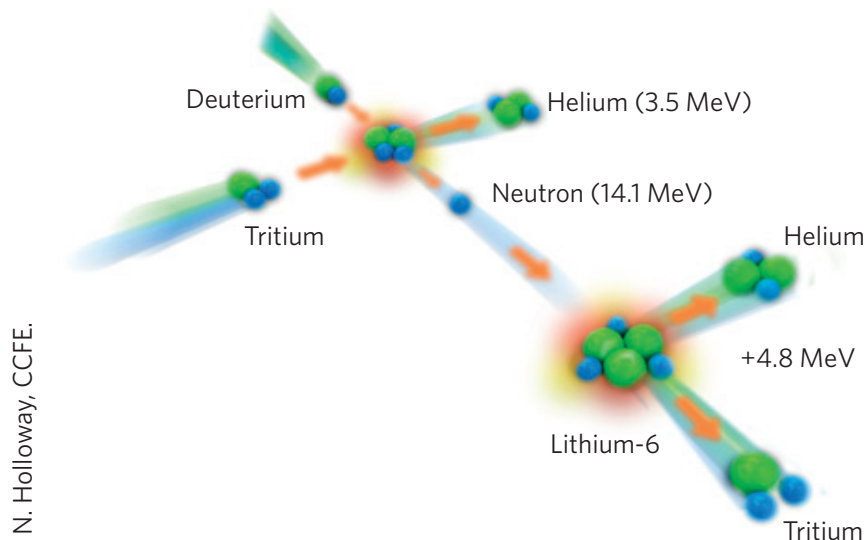
Fig. 1.1 The Deuterium-Tritium fusion reaction path. *Image courtesy of EUROfusion. The fusion reaction between deuterium and tritium atoms results in the formation of a helium atom while releasing an energetic neutron which is exploited for electricity generation. The produced neutron also breeds tritium via a reaction with lithium-6.*

in stars, where fusion reactions occur over a range of atomic masses with respective probabilities due to extremely high pressures and temperatures prevailing in their cores. The temperature inside the sun's core is 15 million K while the pressure is about 10^{11} times larger than that on the surface of the earth due to the much larger mass of the sun [15]. In terrestrial fusion devices, where the pressure is much lower and limited by technological constraints, the Lawson criterion can still be accomplished by applying both a ten times higher temperature and relying on a fuel mixture exhibiting the highest reaction probability known: the fusion of deuterium (D) and tritium (T) ions, both isotopes of hydrogen, into a 3.5 MeV helium (He) atom while releasing a 14.1 MeV neutron. This reaction path is visually summarized in Fig. 1.1.

The fusion fuel is abundant on our planet since D can be extracted from our oceans found at a fraction of 1/6420 in water while T can be made available from a nuclear reaction between lithium-6 and a neutron. The latter neutron results from a multiplication process of the 14.1 MeV fusion neutron released in the DT fusion reaction. Lithium can be extracted from oceans and rocks of which 7.6 % is the isotope lithium-6. Fuel resources are calculated to be sufficient for millions of years to come, only surpassed by solar energy [16]. Thanks to the high energy yield of this process, 15 g of DT is in principle sufficient to generate all the electric energy needed by an EU citizen for a lifetime [15].

The challenge for man-made fusion lies in sustaining an extremely hot substance while its container should be relatively cold to preserve its integrity. The substance and container are far away from thermal equilibrium with each other, a situation which can only be sustained if these sub-systems are mutually decoupled. Heating a gas towards fusion-relevant conditions means that the plasma phase of matter is entered, which is characterized by fully or partially ionized states of atoms due to the removal of electrons orbiting the nuclei. The plasma is sensitive to electric and magnetic fields due to the electric charge of its constituents. Exploiting this feature allows a plasma to be confined by magnetic fields, hereby increasing the pressure of the fuel without the help of gravitation such as in stars, as well as to reach a temperature of 150 million K and minimizing energy loss to the machine walls. The class of fusion technologies based on this principle is called Magnetic Confinement Fusion (MCF).

1.3 Magnetic confinement fusion

Essential to MCF devices is the exploitation of plasma anisotropy: the plasma flow parallel to magnetic field lines is about ten orders of magnitude larger than particle transport perpendicular to this due to the extreme difference in mean free paths for these directions. Clever shaping of the magnetic fields hence allows for confinement of the plasma so

that it can be heated to fusion-relevant temperatures. The neutrons produced by the DT fusion reaction (see Fig. 1.1) escape the plasma volume since they are not sensitive to the magnetic field. The neutrons are slowed down outside of the plasma volume so that the released thermal energy can be used in a conventional steam turbine cycle to generate electricity.

The two most successful designs based on this principle are the stellarator and the tokamak, of which the latter is most extensively studied and briefly discussed now. The tokamak, invented by Russian scientists in the 1950s, is a Russian acronym which translates as *toroidal chamber with magnetic coils*, to describe a device that uses magnetic fields to confine a torus-shaped plasma. The generic shape of a tokamak plasma and the direction of the magnetic fields are shown in Fig. 1.2.
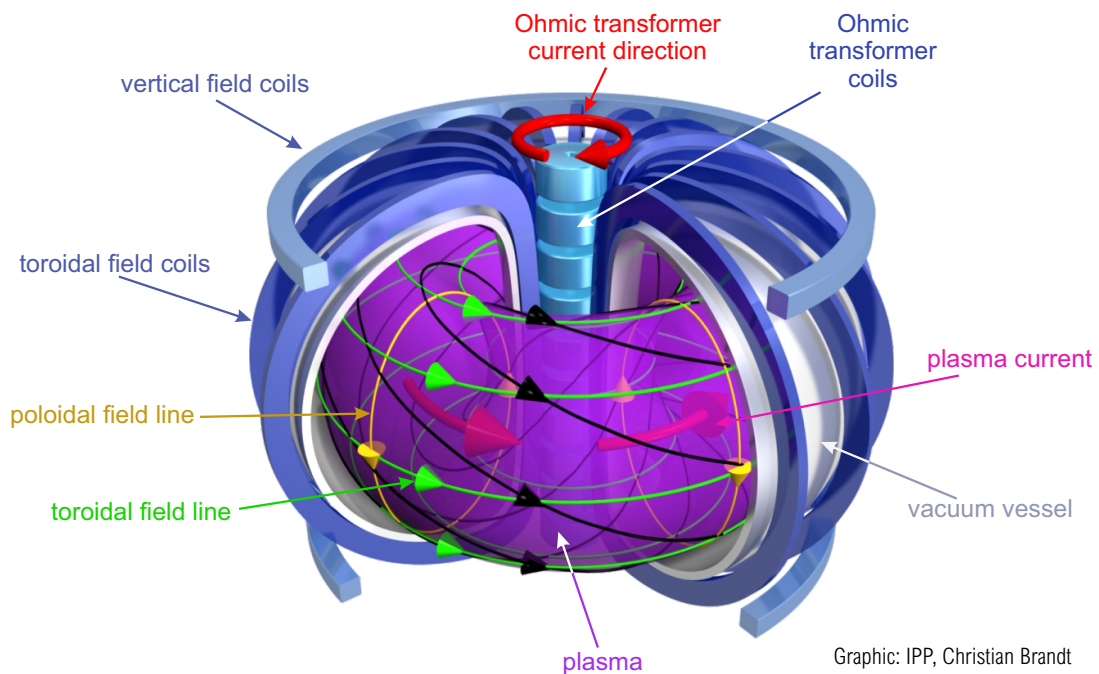
Fig. 1.2 The tokamak principle. Courtesy of C. Brandt, IPP Greifswald. An externally applied toroidal magnetic field creates a torus-shaped plasma in a vacuum vessel. Following from the transformer principle, a toroidal electric current is subsequently induced in the plasma which causes a plasma-generated poloidal magnetic field. The resulting total magnetic field contains a rotational transform which is found to greatly improve plasma confinement. The plasma current additionally provides heating of the plasma.

A toroidal magnetic field is generated and used to bend particles to travel along toroidal magnetic field lines which close on themselves. However, given that the toroidal magnetic field strength is inversely proportional to the radius of the torus, a vertical drift of the particles occurs, which can lead to charge separation and plasma loss [15]. A solution to

this problem is found by 'winding' the field lines around the surface of the torus. The drift in the inner part of the torus is now compensated by a drift in the outer part. The number of windings around the torus per full trajectory parallel to the torus is called the rotational transform, or field line pitch, and results from a combination of the toroidal field and the poloidal field. The tokamak and stellarator differ in the way such a helical magnetic field is generated.

The tokamak design commonly uses a transformer coil positioned at the vertical symmetry axis of the machine, which induces a plasma current in the torus-shaped plasma volume (acting as the secondary winding of the transformer) resulting in a magnetic field perpendicular to the toroidal field. The combination of these two provide the desired twisted toroidal field (indicated in green in Fig. 1.2). Since the plasma-induced current must maintain the same direction, the operation of a tokamak is normally pulsed since it is driven by the discharge of the transformer.

The full rotational transform in a stellarator on the other hand is solely achieved via external magnetic fields, without the need for a plasma current and plasma-generated magnetic fields. This results in a plasma less prone to Magneto-Hydrodynamic (MHD) instabilities and allows for steady-state operation. The research described in this thesis is in principle fully applicable to both the tokamak and stellarator design. We will however concentrate on its potential use in a tokamak environment, which is more advanced along its development path than the stellarator line.

Reaching fusion conditions in a MCF device occurs by heating the plasma in several steps. Firstly, the induced plasma current heats the plasma by electron-ion collisional energy transfer, the so-called Ohmic heating phase. This process becomes less efficient as the plasma temperature rises because the plasma resistivity decreases with temperature [14]. Other methods which are functional at higher temperatures are Ion Cyclotron Heating [17] and Electron Cyclotron Heating [18], both relying on the absorbance of microwaves and subsequent thermalization of the plasma. Additional heating of the plasma is realized by the injection of fast neutral particles, which drives energy into the plasma through collisional energy transfer [19].

Plasma confinement in a MCF device is limited due to continuous loss of energy and/or particles through conduction, convection and radiation from the confined region of the plasma, potentially aggravated by turbulent processes driving energy and particles towards the edge [20]. The ratio of stored energy and input power sets the typical energy confinement time (τ_e) of the device. It is predicted that a tokamak plasma can reach a regime of self-sustained 'fusion burn' once the energy losses are counterbalanced by alpha particle heating, thus taking away the need for external heating. Reaching the

necessary conditions can be approximated by $p\,\tau_{\mathrm{e}} > 20\,\mathrm{atm\,s}$ with p the plasma pressure [16]. Demonstrating this regime in a controlled way is a major scientific milestone yet to be achieved. This goal may come closer in ITER, currently under construction in Cadarache, France, where sustaining a fusion plasma in which a significant fraction of the heating power is provided by alpha particles is a key priority [16].

1.4   The divertor

Sustaining a plasma inevitably means a transfer of energy and particles from the confined plasma region towards the periphery. Although in principle it is desirable to minimize such losses, removal of impurities residing in the plasma is needed since an excess of such particles may cause too much energy loss through radiation. In addition, the fusion reaction product, He, needs to be extracted to prevent fuel dilution. In order to avoid damage of sensitive wall elements and diagnostics, interaction of the edge plasma with the wall can be controlled by intentionally creating an intersection of the magnetic field lines with a heat-resistant material structure, a so-called 'limiter'. The last closed magnetic flux surface of the confined plasma touches the limiter surface, as is drawn in Fig. 1.3a. Excessive erosion of the limiter surface may however result in plasma performance degradation.

Over the last few decades MCF devices have commonly made use of a 'divertor' instead of a limiter to control the plasma exhaust. This concept relies on the presence of an additional poloidal magnetic field, creating a poloidal magnetic null point near the plasma edge (the X-point). As can be seen in Fig. 1.3b, a separation between the closed magnetic field lines and open magnetic field lines now comes into existence (the boundary is called the separatrix). The section of the edge plasma with open field lines is called the Scrape-Off-Layer (SOL) and has a relatively high impurity density. This thin layer of plasma is guided by the magnetic field towards the divertor material surfaces [21]. The key advantage of the divertor design is that the region of plasma-wall interaction (PWI) is now better isolated from the core plasma. This allows PWI to take place in a controlled zone allowing for the removal of heat and He ash at reduced risk of releasing additional impurities into the core plasma. Modes of increased confinement in the core can also be reached in this way. Additionally, particles in the SOL travel over longer distances before hitting the divertor strike-point compared to the situation of a limiter, which means that a greater fraction of energy may be lost along the way due to collisions and radiation, resulting in a lower temperature at the divertor plates.
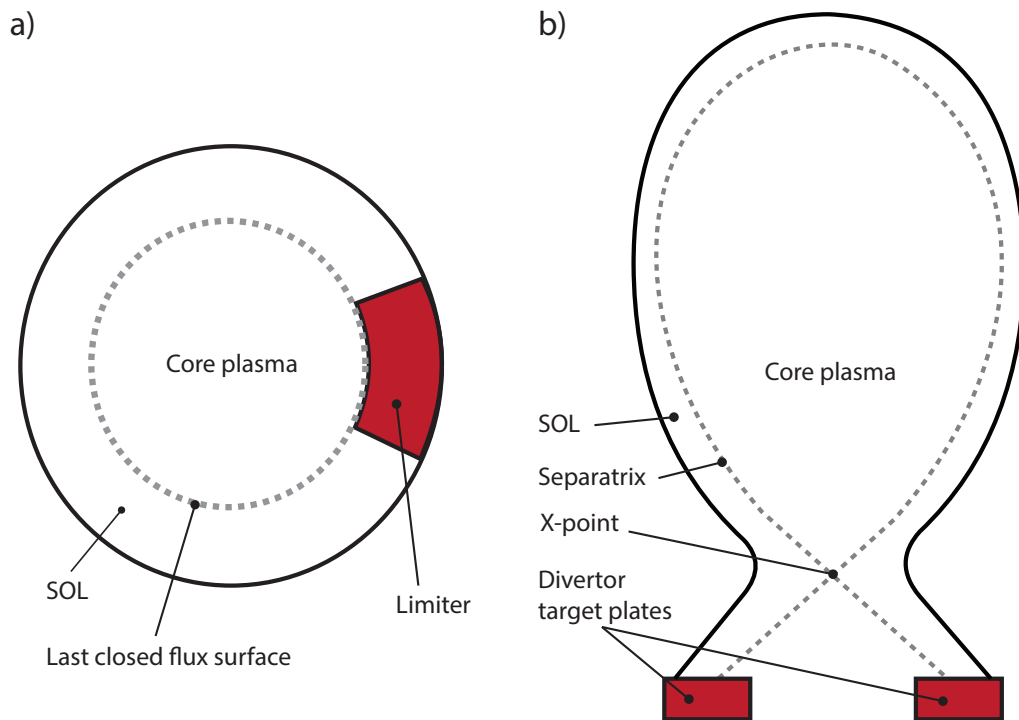
Fig. 1.3 The limiter and divertor principle. The limiter is a material component which intersects the last closed magnetic flux surface aiming to protect sensitive components embedded in the wall (a). The divertor principle relies on an additional magnetic field which provides a plasma-material interaction zone away from the confined plasma, greatly reducing the impurity content of the plasma (b).

1.5   The plasma exhaust challenge

The baseline design of the European DEMO reactor as of 2015 is shown in Fig. 1.4. The highlighted first wall encompasses the plasma and is subject to high neutron fluxes, and, incidentally, in direct contact to the plasma during off normal events such as disruptions and vertical displacement events. These events happen when the plasma current quickly quenches and the entire plasma volume displaces. The divertor area is highlighted in the bottom of Fig. 1.4. It is this area where the plasma which travels on open field lines hits material surfaces, creating a harsh environment for any material.

The development path of MCF experiments [15], both historically and when extrapolating towards the future, is characterized by increasing device dimensions alongside increasing stored energies. The resulting exhaust powers (i.e. power entering the SOL) are seen to increase in parallel to that, hence increasing heat fluxes towards the machine walls, predominantly that of the divertor. Understanding the rich physics of plasmas interacting with materials is a challenging research field in itself [23], greatly stimulated by the fusion
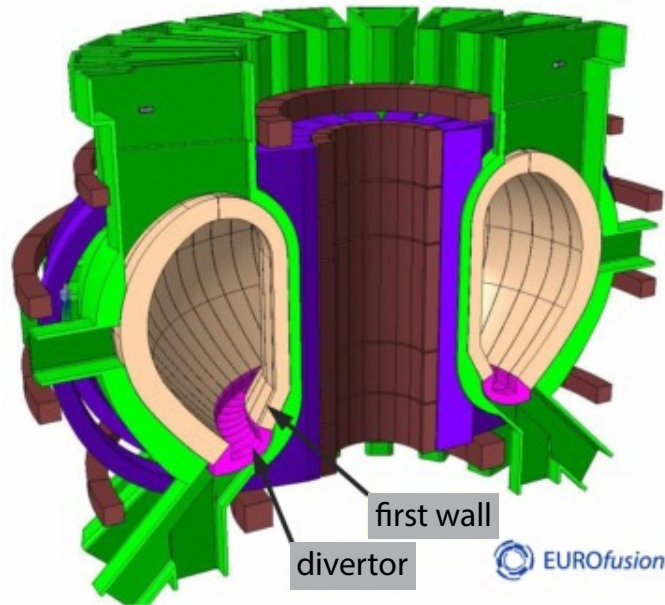
Fig. 1.4 Baseline design of DEMO in 2015. *Image from [22] (EUROfusion). Impression of the 2015 baseline design of the European DEMO reactor. Designing plasma facing components of the highlighted first wall and divertor are an extreme challenge.*

endeavour posing engineering problems of unprecedented difficulty. Demonstrating a robust solution to the issue of heat and particle exhaust beyond ITER is now identified as a key objective to be accomplished in order for nuclear fusion power plants to ever become a reality [10].

It has now been decided that the Plasma Facing Components (PFCs) of the ITER divertor will be entirely engineered from tungsten (W) [24]. An illustration of an ITER divertor cassette is shown in Fig. 1.5. Engineering constraints dictate that the maximum tolerable stationary heat load for the vertical targets (withstanding the largest power fluxes), should remain below 5-10 $\mathrm{MW\,m^{-2}}$ in order to preserve structural integrity during long-term operation [11]. Improving conventional divertor designs is not expected to push this limit much further. The power entering the SOL in DEMO is however expected to increase by a factor 4-7 compared to the ITER level [25]. Additionally, the heat flux finally transferred to the divertor region is strongly dependent on the heat flux channel width λ_q (the characteristic deposition scale-length in the divertor) and power spreading factor, which are both highly debated for the case of ITER [26–28] and DEMO [29]. The heat flux width may turn out to scale unfavourably with machine size, indicating a very small (<1 mm) λ_q for these devices which would lead to a plasma wetted area of comparable size for DEMO with ITER despite the much larger heat flux entering the SOL of the former relative to the latter.
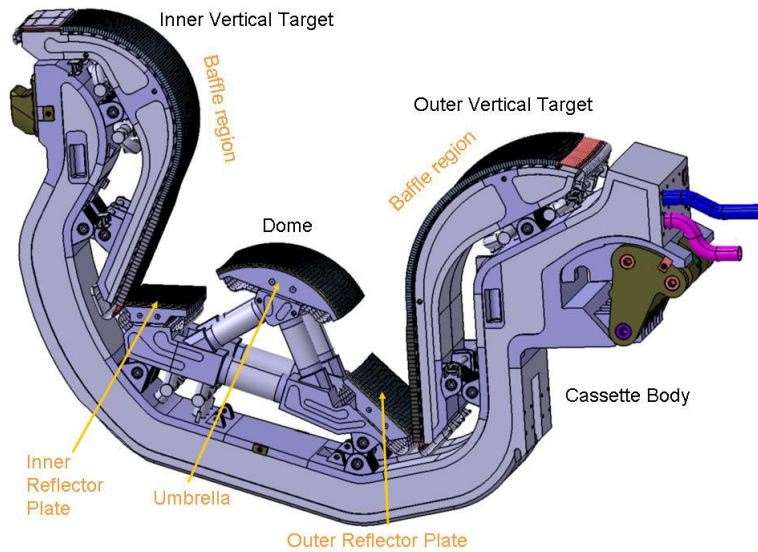
Fig. 1.5 Full-W ITER divertor cassette body. *Picture from ITER.org. Overview of a single full-W ITER divertor module as of 2008. The inner and outer vertical targets are exposed to the largest heat fluxes within the entire fusion device.*

Reducing the divertor heat loads to tolerable levels in DEMO is foreseen through radiating a significant amount of power in the SOL [30] and operating in detached divertor conditions [31]. The steady-state peak power load encountered by the PFCs is estimated to be $15\,\mathrm{MW\,m^{-2}}$ in attached conditions, while still relying on 90 % total radiated power loss and a plasma temperature of 4 eV close to the material surfaces [29]. This already exceeds tolerable levels. Also, the question remains whether the high radiated power fraction of DEMO is compatible with operating in high confinement regimes in the core [32] and if stable detached divertor operation is feasible under high heat fluxes [30]. On top of that, a potential loss of control over radiative power dissipation in the SOL and core could result in irreversible damage to the divertor. The latter point, in addition to the unknown heat flux channel width, motivates the search for alternative divertor solutions such as super-X [33], snowflake [34] and the use of liquid metal (LM) PFCs [35]. Such efforts are essential as risk mitigation for DEMO [30] and for overall progression towards the ultimate goal of building a machine capable of net energy production through fusion power.

1.6   Materials for heat exhaust

A list of material requirements has to be met for successful divertor PFC operation: a high heat handling capacity, a high resilience to neutron impact, low erosion levels and a high sputtering threshold. Preserving its structural integrity and maintaining good

thermal contact with the cooling structure is further imperative. Tungsten serves as a very good solid PFC due to its high melting point, excellent thermophysical properties, low sputtering rate and low neutron damage [36]. However, uncontrolled erosion and penetration of W into the core plasma may hamper plasma operation and could trigger hazardous disruptions. Modelling efforts pointed out that the fractional concentration of W in the core plasma should remain below a few 10^{-5} at all times [37], which means that only very limited erosion can be tolerated. Also, neutron enhanced embrittlement, swelling and transmutation [38], resilience to transients, He bubble/fuzz formation [39] and H blistering [40] may cause reduced heat handling capacity [41] and consequently damage accumulation of W over time. In addition to existing concerns, moving from ITER to DEMO requires even more extreme demands due to higher operating temperatures, increased neutron levels (1-9 displacements per atom per full power year in the divertor [42]) and longer duty cycles [36]. It may be clear that further research is necessary in solving this major challenge.

1.7 Liquid metals

Solid materials with low atomic number (Z), for instance Be and C, are attractive by plasma compatibility considerations since a larger fraction of such elements can be tolerated in the core plasma, but, as a PFC, they are normally not attractive due to higher erosion levels [43]. Despite having excellent heat handling properties, C may form dust which can retain significant amounts of tritium (co-deposition [44]) which is a safety concern as it hinders efficient tritium handling [23]. Liquid metals (LM) may ease some of the requirements mentioned above and in the previous section since plasma compatibility constraints can be disconnected from structural and heat handling requirements. Also, the necessity of having an excellent heat handling performance at all times to avoid the accumulation of damage such as in the case of W, is not an issue for a liquid since a sacrificial surface exists which can be replenished by liquid flow. Overall, LMs are self-healing which means that a pristine surface can be repeatedly presented to the harsh plasma environment. The issue of impurity release through erosion, sputtering and predominantly evaporation is obviously magnified compared to solids but may be controlled by making modifications to the existing general divertor geometry [45] or potentially relying on high surface re-deposition [46]. Taking this up from a different angle, particle release from the wall may be exploited since it allows for additional power dissipation channels which can aid in reducing the power flux reaching the divertor strike-points. The latter phenomenon will be extensively discussed later on.

An early comprehensive overview of the merits and challenges of the LM concept for fusion applications can be found within the US APEX program initiated in 1998 [47], investigating free-flowing LM (Li, Sn-Li eutectic) surfaces on solid walls facing the plasma. The following potential advantages of such materials were stated [47]: high power density capability, improved plasma stability and confinement, increased disruption survivability, reduced volume of radioactive waste, reduced radiation damage in structural materials and, lastly, higher availability.

The effects sorted by LM use in MCF devices can be distinguished in two classes, those with consequences for plasma operation (LMs on first wall) and those for heat exhaust (LMs in divertor). In terms of plasma operations, beneficial effects of liquid Li wall coatings have been frequently confirmed [48–50]. An important effect is the feature of reduced recycling compared to most other materials, which means that edge plasma particles hitting the surface are absorbed by the Li, hence greatly reducing the fraction of cold reflected neutrals. It is believed that zero-recycling causes the edge plasma to stabilize resulting in the suppression of Edge-Localized-Modes (ELMs) and reduced temperature gradients (flat temperature profiles) [51]. In addition, an increase in the energy confinement time in NSTX is reported using Li wall-coatings [52]. This scheme is believed to be feasible for an ITER-like tokamak as well [53, 54].

In terms of benefits for heat exhaust regions, a metal in liquid state does not have a permanent crystal lattice which makes it inherently resilient to neutron damage and cracking. Removal of T, He ash and dust in the LM can be facilitated by flowing the contaminated liquid to areas away from the plasma-wall interaction zone. The problem of erosion is aggravated compared to solids, especially for Li, since evaporation can play a major role in addition to sputtering at elevated temperatures. However, the release of LM impurities in the near-surface plasma may aid in power handling since volumetric energy dissipation pathways become available. The formation of a vapour cloud in front of the strike-point consumes energy by the latent heat of vaporization and subsequent excitation and/or ionization of the eroded impurities in the plasma. This energy is released via neutral particles and radiation isotropically, hence leading to a reduced areal power density at the strike-point. When eroded LM atoms and ions exhibit short lifetimes due to a fast evaporation/condensation cycle, coronal equilibrium may never be reached for such species. It is known that the radiative capability of particles out of coronal equilibrium can increase by several orders of magnitude, as is frequently proposed for the case of Li atoms at low temperatures [55–57] which is normally a poor radiator in this regime. Maximizing this effect is beneficial since it would allow for even more power to be converted into radiation and spread over a larger area. Higher heat flux limits for LMs compared to

solids may thus be achieved in addition to better damage tolerances. Dispersing power in front of the PFC through volumetric processes caused by wall-eroded impurities is called vapour shielding, which is the central topic of this thesis. A discussion of its history and current status is provided in section 1.9.

The key challenges identified by the APEX study included understanding the physics of plasma-liquid and liquid surface-bulk interactions, the control of hydrodynamic flows in magnetic fields and temperature control of the free surface [47]. Strongly related to substrate geometry, thickness of the liquid layer and flow dynamics, instabilities are generally a significant challenge for liquid surfaces [58]. Kelvin-Helmholtz instabilities in a free surface may lead to droplet formation, causing anomalous erosion. A Capillary-Porous-Structure (CPS) alternatively holds the LM in a quasi-static arrangement [59], greatly reducing this issue but losing the benefits of flow for dust removal and the facilitation of tritium extraction.

Open issues to date are ensuring stability of LM surfaces and flows and understanding the consequences of surface chemistry (especially for Li) in a complex plasma environment [58]. In addition, depending on the specific element, geometry and arrangement (flowing or static), the acceptable operational temperature window in integrated scenarios is unclear. Limits on impurity release into the main plasma set the maximum evaporation flux, hence determining the maximum allowable liquid surface temperature [60, 61]. The magnitude of screening effects by the incoming plasma flow, as well as entrainment and prompt re-deposition [46] of ionized impurities in the magnetic field near the divertor surfaces are however not included in this simplified picture. The VS effect, self-limiting on the surface temperature rise and strongly affected by the re-deposition fraction in a realistic divertor environment, may push the operational space further, hence favouring the use of LMs despite added complexity.

1.8   Lithium and tin as candidate liquid metals

The LMs most extensively studied up to now are Sn, Li, Ga and the Sn-Li eutectic [58], sharing a low melting point but widely different in their evaporation rate, liquid-state temperature range and atomic number. Important intrinsic properties to consider are furthermore their boiling points, heat conductivity and chemical reactivity with the plasma, substrate materials and in-vessel surfaces. Our studies have been focused on the power handling characteristics of liquid Sn and Li for their reported benefits as a liquid PFC material. The Sn-Li eutectic has not been considered yet due to the added complexity of assessing the physics of power handling for a mixed material. Gallium is also neglected since it shows strong reactivity with metals suitable as substrate materials [30].

Lithium is attractive for being an excellent impurity getter and high retention levels which suppresses edge recycling. Also, good chemical compatibility with common substrate materials such as stainless steel (SS), W and Mo has been reported. By being low-Z (Z=3), large erosion levels can in principle be accepted which opens possibilities for heat exhaust through evaporative cooling and vapour shielding (see next section). Negatives for Li as a PFC material are the limited temperature window due to the very high vapour pressure, high T retention [62], strong reactivity leading to hydride formation [63] and the requirement of active cooling by means other than water for safety reasons.

For Sn, despite its high atomic number (Z=50) and strict limits on the acceptable core concentration in a reactor [61], this element is now gaining interest as a potential PFC alternative for the absence of complex surface chemistry, wide liquid-state temperature range, low T uptake and compatibility with expected higher operating wall temperatures in e.g. DEMO.

The intrinsic material Properties of Sn and Li are summarized in table 1. Parameters at elevated temperature are found from extrapolating datasets valid at a lower temperature range. The higher temperature level is chosen from the consideration of establishing an evaporation flux equal to the typical plasma particle flux in a divertor of 1×10^{24} m^{-2} s^{-1}.

Table 1 Thermophysical properties of tin and lithium. *Properties of the LMs Sn and Li at their respective melting points and at typical elevated temperatures where the evaporation flux is similar to the divertor plasma particle flux.*

	Sn		**Li**	
melting point (K)[1]	505		452.2	
boiling point (K)[1]	2548.2		1590.2	
	T_m	1850 K	T_m	1020 K
density (kg m^{-3})[1,6]	6980.1	6096.6	514.8	464.8
th. conductivity (W m^{-1} K^{-1})[2,6]	29.6	6.7	42.4	60.3
spec. heat (J kg^{-1} K^{-1})[1,3]	253.1	141.1	30.8	28.9
viscosity (kg m^{-1} s^{-1})[1,4]	2.1×10^{-3}	8.0×10^{-4}	6.4×10^{-4}	2.8×10^{-4}
surface tension (N m^{-1})[1,5]	0.54	0.44	0.4	0.32

[1] ref. [64]
[2] at melting point obtained from [65], elevated temp. obtained from extrapolating empirical dataset valid up to 1473 K obtained from [66]
[3] extrapolated from temp. range valid up to 810 K [64]
[4] ref. [65]
[5] ref. [67]
[6] ref. [68]

The contrasting properties of Li and Sn give rise to individual pros and cons when it comes to application as a divertor PFC. A critical parameter for any wall-eroded species in MCF devices is the maximum impurity concentration which can be tolerated in the core plasma without compromising its performance. For Li (low-Z) this is caused by fuel dilution whereas Sn (high-Z) may cause the ratio of Bremsstrahlung losses versus alpha heating to become critically high [61]. The latter phenomenon may trigger hazardous disruptions [69] which are to be avoided at all times since they carry the risk of damaging plasma-facing components.

The tolerable LM impurity concentration in the core is linked to the acceptable erosion flux which sets on its turn the operational temperature window of LM PFCs. However, the surface re-deposition rate strongly affects the net erosion and hence affects the operational temperature window again. Reaching a high vapour pressure in its turn may control the surface temperature due to the possibility of heat flux mitigation by vapour shielding, hereby possibly self-limiting the net evaporation rate [58]. Re-deposition and vapour shielding are identified as key processes influencing the practical temperature window of LM PFCs. Given its importance to the work here, the vapour shielding concept as it appears in several forms in the literature are reviewed below, followed by our definition adhered throughout this study.

1.9   Vapour shielding

The first appearance of vapour shielding (VS) in the literature stems from 1977, where a dense high-Z plasma blanket, a so-called 'virtual limiter', is theoretically described [70]. Plasma particles in the SOL near a Mo limiter are intercepted by incompletely stripped high-Z ions and their energies converted into X-rays produced via Bremsstrahlung, re-combination radiation and collisional de-excitation. The distance of the emission plume with respect to the wall is treated in this scheme as a critical parameter as it determines the fraction of the radiation flux absorbed by the wall.

Early works, both modelling and experimental, focus on disruption-type transients and ablated high-Z materials at very high densities ($>10^{25}\,\mathrm{m}^{-3}$), producing primarily black-body radiation [71, 72]. Transient plasma loading of Li CPS targets up to $25\,\mathrm{GW\,m}^{-2}$ (pulse duration of $200\,\mu\mathrm{s}$) were performed in the QSPA plasma gun facility [73], reporting the formation of a thick Li cloud extending $50\,\mathrm{mm}$ from the surface and finding the capillary structure to remain intact [59]. Steady-state testing of Li CPS targets up to $25\,\mathrm{MW\,m}^{-2}$ was performed using an e-beam facility where a reduction of $70\,\%$ in the absorbed power was obtained [59]. It must be noted that only evaporative power loss occurred here since no plasma and magnetic fields were present. Exposing a Li limiter in the Russian T-11M

tokamak to heat fluxes estimated around $30\,\mathrm{MW\,m^{-2}}$ revealed strongly enhanced radiative flux to the wall, up to 80 % of the Ohmic heating power while direct plasma heat flux to the limiter decreased to 5 % of the Ohmic heating power [74]. A 'radiative mantle' concept is based on this, strongly relying on emission by Li atoms out of coronal equilibrium [55]. Lastly, self-shielding of a surface due to volumetric energy loss in front of the target, similar to VS but caused by H neutrals out-gassed from the wall rather than due to erosion, has been observed for the case of W during transient plasma pulses in Pilot-PSI [75].

Current efforts to address the question of the potential of VS in increasing the power handling limits of LMs are pursued by limiter tests in tokamaks and e.g. the 'vapour box' concept developed in Princeton, USA [76, 45]. For instance, a liquid Sn limiter is currently being tested on the Frascati Tokamak Upgrade (FTU) in Italy in order to assess its power handling characteristics [77] and operational temperature limits, as well as to allow for a performance comparison to a Li limiter in the same device and to look for evidence of VS at high temperatures [78, 79]. Steady-state VS and its consequences for the operational temperature window can however not easily be addressed given the limited discharge duration (<5 s) and the fact that the Sn CPS is positioned in the SOL (limiter) where it encounters different plasma conditions compared to those in the divertor region where the particle flux is higher and the average electron temperature lower. Also, given the difficulty of confining released particles close to the limiter surface, the proposed mechanism may be closer to the 'radiative mantle' concept [55] rather than to VS. As for Li, a heat handling concept based on volumetric power dissipation in a geometrically closed divertor leg (vapour box) is proposed [76, 45]. This design exploits a series of differently pumped chambers allowing for an increased neutral pressure with increasing distance from the box entrance. Lithium enters the plasma in this vapour box via evaporation/condensation cycles from the wall, allowing for power spreading by ionization and radiation. Experimental testing needs to be performed in order to confirm otherwise promising modelling results [45]. The concept further assumes enhanced radiation loss due to non-coronal radiation from Li [55] which should be experimentally confirmed in divertor conditions, which also holds true for other LM concepts relying on strong radiative dissipation by Li.

Reactor relevant conditions, where re-deposition rates can be naturally high, need to be achieved in order to determine the real temperature window which is influenced by the potential of vapour shielding and hence the maximum heat handling capability of a LM PFC. Tackling this question requires experimental testing in devices where DEMO-relevant divertor conditions can be achieved which is currently challenging. Also, progressing towards a solution may benefit from the experimental comparison to results from integrated modelling (connecting the divertor and core) using e.g. Sn PFCs [80].
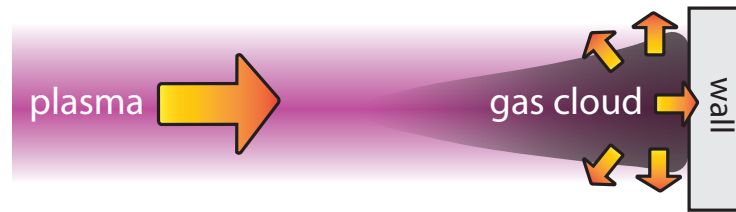
Fig. 1.6 The vapour shielding principle. Plasma heat flux impinging a liquid metal surface gives rise to strong evaporation, leading to a dense cloud of neutrals (gas) in the vicinity of the surface which protects the surface. The incoming plasma heat flux (left arrow) is partially converted into radiation and neutral particles leaving the plasma beam (arrows on the right), hereby spreading the heat flux over a larger area than in the case without a vapour cloud.

As may be clear by the variety of examples given above, a variety of physical mechanisms, sometimes even different in their nature, appear under the name 'vapour shielding' in the literature. We are stating now our definition of VS adhered throughout this thesis work for clarity: *vapour shielding entails the physical process where particles released from the wall create a region localized close to the wall which aids in reducing the impinging plasma heat flux by means of volumetric power dissipation.* The very case of VS by liquid metals - the topic here - can thus be interpreted as a subclass within the broader definition of VS. A visual impression of the principle can be found in Fig. 1.6.

2 Objective and outline

The previous sections aimed to sketch the background in which this thesis work was carried out. The fundamental research questions and plan of approach are stated hereafter. An overview of the most important results obtained in our studies, not necessarily chronologically, can be found in the following chapters.

2.1 Problem statement

Liquid metals are behind on a technology readiness level compared to their solid counterpart due to limited experimental testing, especially in fully-integrated tokamak scenarios. It is thus, as of yet, unclear if LM PFCs will ultimately outperform solid PFCs. Even if they do not perform better than solid materials in terms of power handling, a superior lifetime and damage resilience may still be concluded which makes it a better solution to the wall challenge. Liquid metals are surely a promising alternative and it is therefore necessary to do further research in order to reach a level where a comparison with solids based on experimental performance can be made. Moving towards a solution integrating all PFC requirements asks for separate fundamental research tasks, of which the topic of heat handling is central to this thesis work.

It may be clear by now that VS is a complex process following from multiple interlinked processes such as moving surfaces, plasma transport, evaporation-condensation, ionization and complex atomic physics producing radiation. A clear understanding of the potential of VS in protecting the liquid surface to high heat fluxes and its effect on the operational temperature window in a MCF device is missing, as stated in the previous section. At the outset of this work, the feasibility of steady-state VS (and continuous heat flux reduction) for LMs was generally an open question. The results obtained in this work shed light on this matter, were we have most extensively studied liquid Sn as a case study. It is worth comparing our results with Sn to the case of Li whilst researching the nature of produced Li radiation in conditions similar to those in a future fusion reactor divertor.

Plasma exposures were carried out using the linear plasma generators Pilot-PSI and Magnum-PSI at DIFFER [81–83], both capable of replicating an ITER relevant (density $>10^{20}\,\mathrm{m}^{-3}$ and temperature of 1-5 eV) divertor plasma of significant duration ($>10\,\mathrm{s}$ for Pilot-PSI, ~hours for Magnum-PSI). A bolometry system for Magnum-PSI, intended to study radiated power loss in the near-surface target region during vapour shielding, is developed as part of this thesis project.

Summarizing, the main goal in this thesis is:

The investigation of the physics of vapour shielding and its potential application as a power exhaust mechanism for nuclear fusion devices, eventually bringing forth a solution for protection of fusion reactor walls.

This goal is approached by finding answers to the fundamental research questions:

- Can vapour shielding be clearly demonstrated using liquid metals in linear devices?

- Can the underlying physical mechanisms behind continuous vapour shielding be identified?

- What is the potential of liquid metal vapour shielding in mitigating the plasma heat flux in a divertor?

- Can the radiated power fraction directly be measured in Magnum-PSI using bolometry?

- What is the radiated power fraction in the power balance during vapour shielding and what is the nature of this emission?

2.2   Approach to the problem

We have addressed the question of heat handling by mapping the different power dissipation channels present during steady-state VS. The experimental work is executed using linear plasma generators which aim to simulate the divertor environment of fusion reactors. A large part of the work is devoted to the development of bolometry diagnostics capable of measuring radiation from LM impurities as well as quantifying the radiation fraction in the power balance during VS.

   The first two research questions stated in section 2.1 were investigated by exposing liquid Sn CPS samples to plasma heat fluxes ranging 1-22 $\mathrm{MW\,m^{-2}}$ in Pilot-PSI. Tin was initially chosen as a proxy material for Li, since the necessary equipment for handling Li in a protected atmosphere was not available at the start of the project. DIFFER moved to Eindhoven in 2015, causing experimental downtime. The project was continued at the Princeton Plasma Physics Laboratory (PPPL) in the US (starting April 2015) by being a collaborator in an international team to develop an Infrared Video Bolometry (IRVB) system for the National Spherical Torus Experiment Upgrade (NSTX-U). Lab testing of the previously used NSTX resistive bolometry system served as a benchmark to the newly

developed IRVB system. The flagship machine Magnum-PSI resumed operations at DIFFER in December 2016, now equipped with a superconducting magnet allowing for continuous operation at a magnetic field strength of 2.5 T. Once back at DIFFER in Eindhoven, the development of a resistive bolometry system for Magnum-PSI was initiated. Experimental testing of Li CPS targets to divertor-relevant heat fluxes with simultaneous bolometry measurements was carried out. Characterization and testing of the bolometry system occurred in parallel to Li CPS experimental work.

2.3   How to read this thesis

The main findings obtained during the investigation of liquid metal vapour shielding can be found in chapter A.2.2. chapter A.4 describes the development of bolometry diagnostics for both NSTX-U and Magnum-PSI and provides first results obtained using these new diagnostics. The possible implementation and relevance of VS by LMs in a future fusion reactor environment is described in chapter A.5. Conclusion are drawn in chapter A.6.

Part B contains the works which are published in the literature. Steady-state power handling of liquid Sn CPS targets and the observation of 'self-regulated' plasma heat flux mitigation due to the VS effect is described in chapter B.1. This process is found to be oscillatory by nature: a dynamic equilibrium exists between the evaporation flux (vapour formation) and heat flux mitigation by impurity-driven plasma detachment (plasma cooldown). Details of this work can be found in chapter B.2. The development of an IRVB system, designed to study plasma radiation in the divertor of NSTX-U is described in chapter B.3. The time resolution and noise equivalent power density are determined during tabletop testing. This characterization study is compared to the performance of a conventional resistive bolometry system. Chapter B.4 is devoted to the design and implementation of a resistive bolometry system for Magnum-PSI. The level of radiated power loss from the plasma in a range of operational settings is described for the first time, as well as first attempts to measure enhancement of the radiated power fraction by Li impurities.

3 Overview of results

The physical process of evaporation, exponentially dependent on temperature, is a double-edged sword: it potentially allows for additional power dissipation channels but its use ought to be limited and/or the vapour formation should be confined near the surface. Encouraging results of power reduction through Li vapour shielding had previously been obtained in simulations of plasma transients [59]. The re-deposition fraction in these experiments was however negligible since no means of confining the expanding vapour were applied, causing power to be solely dissipated by the liquid-gas phase change. Inspired by these results, this work started with the aim of finding conditions in which the vapour pressure would be counterbalanced by the plasma pressure, in order to mitigate exacerbated impurity loss. Our hypothesis was that steady-state VS would be efficient in this regime. Figure 3.7 shows the evaporation flux as function of temperature for both Sn and Li [84]. The highlighted region in the inset of Fig. 3.7 shows the temperature range
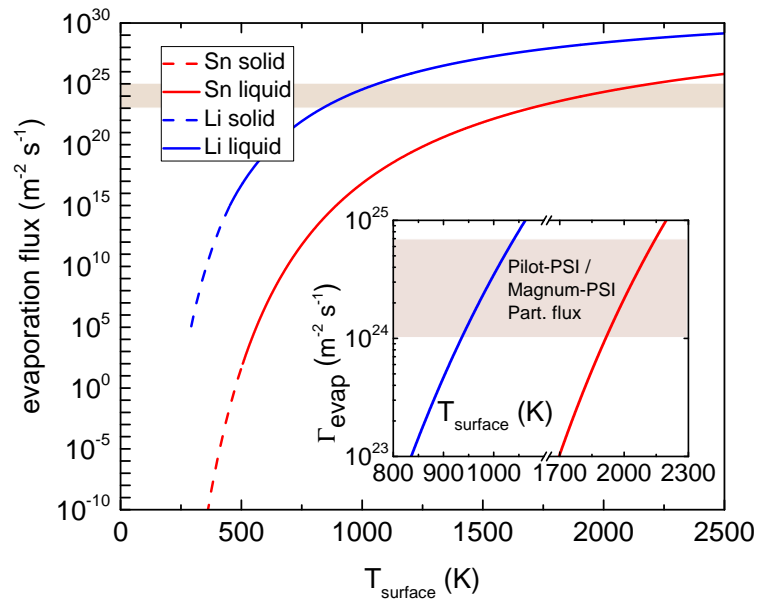
Fig. 3.7 The evaporation rates as function of temperature for Sn and Li. *The typical particle flux at the target surface in Pilot-PSI and Magnum-PSI is shown by the highlighted area. The inset shows this regime in detail.*

where the evaporation flux is of similar magnitude as the typical plasma particle flux (Γ_{part}) produced in Pilot-PSI and Magnum-PSI. Entering the regime where the Sn vapour flux is of the same order as the plasma flux thus requires a surface temperature >1850 K for Sn and >940 K for Li. Our hypothesis was tested by exposing LM CPS samples to plasmas which raised the surface temperature above these limits. The vapour pressure of Li is higher

than that of Sn which makes it the obvious element of choice among these LM candidates. For reasons previously stated, we however initially set out testing our hypothesis for the case of liquid Sn. A brief description of the experimental setup is provided now before presenting the main findings. Specific details on the experimental exposure conditions can be found in chapters B.1 and B.2.

3.1 The linear plasma generators Pilot-PSI and Magnum-PSI

The Magnum-PSI (MAgnetized plasma Generator and NUMerical modeling for Plasma-Surface Interactions) linear plasma device is designed for testing and fundamental studies of PFC materials under ITER-relevant divertor conditions while allowing for easy diagnostic access and replicative conditions [85]. A schematic impression of the device is shown in Fig. 3.8. Divertor simulation in such devices is important since current tokamaks cannot
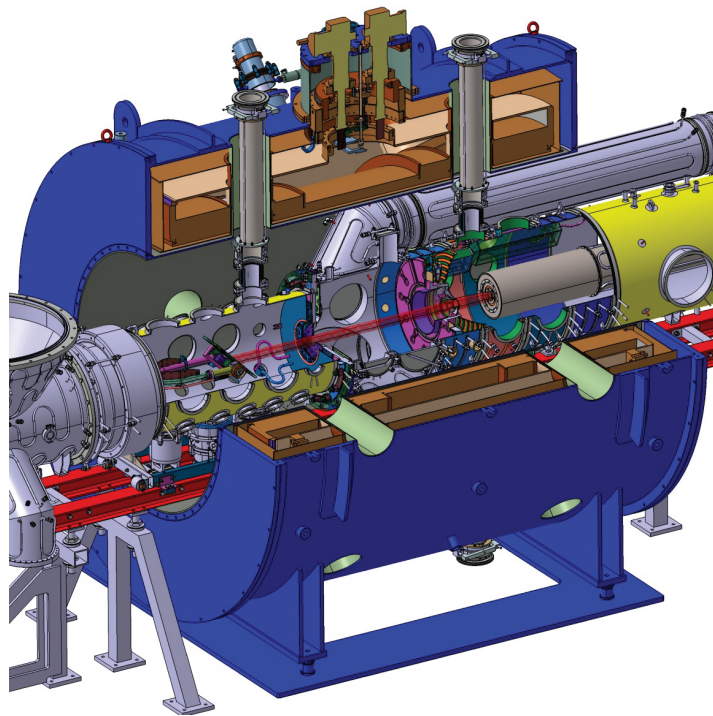
Fig. 3.8 The Magnum-PSI linear plasma device. *Illustration of the superconducting Magnum-PSI capable of producing ITER divertor conditions at realistic fluences. The postion of the source (r.h.s.) and target (l.h.s.) can be freely adjusted along the central axis of the machine.*

reach ITER divertor-like conditions of high density $n_e > 10^{20}$ m^{-3}, low plasma temperature $T_e = 1\text{-}5$ eV, particle flux $\Gamma_p > 10^{24}$ m^{-2} s^{-1} and heat flux q>10 MWm^{-2}. The difficulty lies in obtaining a low neutral particle flux near the target while the plasma source produces a

relatively cold plasma [82]. Magnum-PSI is unprecedented in this capability thanks to a differential pumping scheme between subsequent chambers of the machine [86], causing the neutral particle fraction at the target to be dominated by target recycling rather than originating from the background gas [85]. The device is designed to study plasma-material interaction physics in the 'strongly-coupled regime' which means that the mean free path of eroded particles is smaller than the plasma beam size and hence become trapped in the near-surface plasma. Magnum-PSI is equipped with a vacuum analysis chamber for post-processing target investigation, a holder for realistic divertor target testing and the capability of exposing targets at grazing incidence. The position of both the target and source can also be adjusted linearly. A superconducting magnet up to 2.5 T has been operational since December 2016, allowing for exposures up to several hours, in practise limited only by operational planning rather than physical limits. Many questions related to LMs, such as power handling, can be well-investigated in linear plasma devices, though topics relating to the specific geometry of tokamaks, such as core-edge coupling, are better suited to study in toroidal confinement devices.

Pilot-PSI [87] is the predecessor of Magnum-PSI and served for many years as a test facility providing valuable experience to aid the development of the latter, next to being an excellent experimental setup by itself to study PMI physics. A schematic overview containing the positions of its main diagnostics is shown in Fig. 3.9. The key differences of Pilot-PSI with respect to Magnum-PSI is that it is a smaller device with fixed distance between source and target (0.56 m), has a maximum B-field strength of 1.6 T with a maximum pulse length at this field of 9.5 s and features no differential pumping, causing the neutral fraction at the target to be higher than in the case of Magnum-PSI. Also, the position of the target and source can be adjusted linearly in the latter device. A divertor-relevant ion flux and heat transfer to the target are however reached in both machines, of which the operation is now discussed in a general sense.

The plasma in both devices is produced in a high-pressure wall-stabilized cascaded arc source [88]. A drawing of the source which its key elements is shown in Fig. 3.10. The gas flow (H, D, He, Ne, Ar) and source current are set while the voltage drop between a lanthanum oxide-doped W cathode tip and a grounded anode plate adjusts dependent on the resistivity of the plasma discharge. The source channel consists of electrically insulated copper plates of increasing potential difference with respect to the cathode which guide the electric field. The inner diameter of the source channel increases in steps from 9 mm (upstream) to maximally 16.5 mm (downstream). The ionized gas is ejected from the source nozzle (~100 Pa) supersonically due to the pressure difference with respect to the source chamber ($<10^{-2}$-10^{-3} Pa). A magnetic field confines the plasma
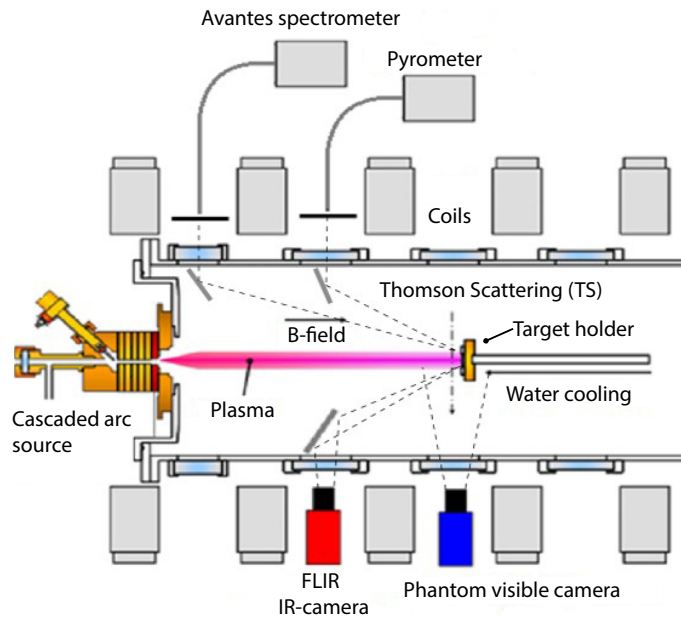
Fig. 3.9 Schematic overview of Pilot-PSI and positions of its diagnostics. *The plasma is produced in a cascaded arc plasma source and guided to the target surface via a magnetic field generated by conventional copper coils. In contrast to Magnum-PSI the position of source and target are fixed.*
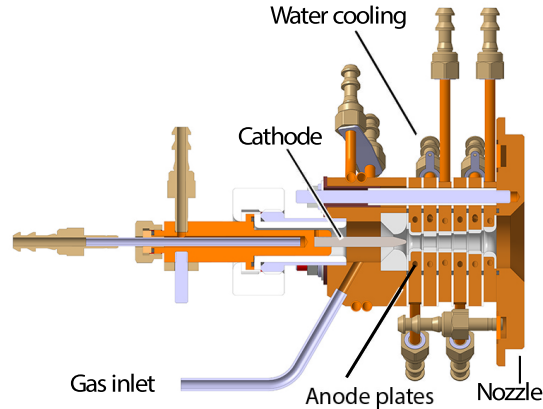
Fig. 3.10 The cascaded arc source used in Pilot-PSI and Magnum-PSI. *The potential drop between the cathode tip and the anode plates increases in steps, alongside an increase of the inner diameter of each subsequent plate. A high-density, low temperature plasma is generated which is ejected from the nozzle due to the pressure difference between the source channel and the vacuum vessel.*

into a beam hitting a water-cooled target. Electron densities and temperatures ranging $3\text{-}7\times10^{20}\,\mathrm{m}^{-3}$ and 1.5-3 eV respectively were reached during He experiments which are described in this thesis. A current path due to the voltage difference between anode and cathode in the source causes an electric current path to form through the plasma

[89]. When an electrically conducting target is part of the circuit, a radial current may be induced. This can affect LM flow which is described in section 3.7.

A key diagnostic on both machines is a Thomson Scattering (TS) system, capable of measuring radial profiles of the electron density (n_e) and electron temperature (T_e) [90]. The axial measurement position in Pilot-PSI is 17 mm in front of the target surface whereas the system in Magnum-PSI has the flexibility of measuring close to the source or close to the target surface (of which the position can be adjusted). The particle flux reaching the surface is routinely determined from the plasma parameters by assuming that the ions reach sound speed upon entering the sheath potential drop present near the target. The sheath heat transmission factor $\gamma_{sh} \approx 7$ has been experimentally determined for the operational conditions in Pilot-PSI [91] and thermal relaxation of the plasma species ($T_e \approx T_i$) has been previously concluded [92]. Using this, the surface heat flux (q) can be calculated from the particle flux at the sheath entrance Γ_{part} [21]:

$$q = \gamma_{sh} k_B T_e \Gamma_{part} = \frac{1}{2} \gamma_{sh} k_B T_e n_e \sqrt{\frac{k(T_e + \gamma T_i)}{m_i}} \tag{1}$$

where $\gamma = 5/3$ (adiabatic flow with isotropic pressure) and m_i the ion mass. For the case of LM exposures, determining the exact heat flux arriving at the surface is more difficult since γ_{sh} is dependent on some parameters with significant uncertainty such as recycling coefficients for electrons and ions at elevated temperatures as well as secondary electron emission yields [93] in our conditions. Also, due to technical limitations, TS measurements cannot be performed close to a liquid surface due to a risk of damaging the optical parts of the diagnostic system by LM droplets. We have therefore executed reference exposures on solid metal targets at identical operational settings. The heat flux received in such a way, called q, is equated to the heat flux that a LM surface would have received: $q \equiv q_{ref}$.

The temperature of the target cooling water is continuously monitored allowing the performance of calorimetric measurements of the total net heat flux arriving at the target. The voltage and current characteristics of the source are logged, providing information about the upstream plasma behaviour over time. Additionally, the following diagnostics installed on Pilot-PSI and Magnum-PSI were used throughout the experiments: spectroscopy of the near-surface plasma and tangentially of the plasma beam at a specified position, pyrometry for an emissivity-independent measurement of the target temperature, IR camera for fast surface temperature monitoring, fast camera analysis monitoring of emission by (Li, Sn) impurities, and, for Magnum-PSI, a resistive bolometry system for radiated power measurements (chapter B.4). In combination with power input at the source and target calorimetry, the latter diagnostic provides the possibility of assessing the

full power balance in Magnum-PSI. Further details on dedicated diagnostic usage during specific experiments are addressed in the subsequent chapters.

3.2   Target design

Among a multitude of proposed LM target concepts, only designs based on the CPS principle [94] for LM containment have been applied in our studies. The risk of splashing and ejection of the liquid has been found reduced most effectively for this type of design [58] and has been tested on a number of tokamaks [55, 74, 77]. The presence of capillary pressure in micrometer-sized pores provides flow for surface re-generation and self-sustainment necessary to balance the pressure exerted by the plasma and gravity [95]. A simple equation relates the pore size to the effective pressure through capillary action: $\Delta P = 2\sigma \cos(\theta)/r$, with σ and θ the temperature dependent surface tension force and wetting angle respectively [59]. The necessary minimum pore diameter, r, can be found from this. When choosing a substrate material, resilience to high temperatures and temperature gradients, resilience to neutron impact, low mixing, excellent wetting and absence of corrosion by the LM substance are necessary. High-Z metals such as W and Mo are usually compatible with these demands although difficulty of machining may impact the range of options [61]. A simple yet effective solution is using a stack of meshes to provide a highly porous medium to confine the LM. This strategy is adhered to in our sample manufacturing process.

Different sizes of substrate geometries have been applied for experiments involving Sn in Pilot-PSI and Li in Magnum-PSI. Both are briefly described now.

- **Sn CPS | Pilot-PSI.** The substrate is shaped as a 3 mm deep cup of 22 mm in diameter, made of Mo, and contains the liquid as shown in Fig. 3.11. Filling the holder with Sn involves of a number of steps. Securing optimal wetting of liquefied Sn on the high-Z mesh and avoiding the entrapment of impurities during the filling procedure are most important. The first step entails melting ~0.5 g into the cup in a vacuum oven. The oven operates at 800°C at which excellent wetting of Sn on the Mo substrate is seen due to removal of oxides while impurities are out-gassed from the liquid at the same time. Typically 1.5 g of Sn is melted which yields a layer of 1 mm thickness. Next, 4 circular W meshes of ~22 mm diameter are inserted in the hot liquid Sn and are secured by a lip extending from the Mo cup. Each mesh has a plain weaving pattern with pore opening width of 0.2 mm and 0.05 mm wire diameter. Typically 2.7 g of Sn is added to obtain a wetted Sn surface. The final step is the resolidification of the Sn as the sample cools down to room temperature in the oven. Tin quickly

enters the liquid phase once exposed to the plasma and the oxide layer is removed by the plasma.
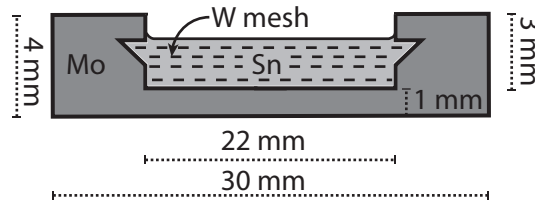
Fig. 3.11 Design of Sn CPS target. Used in Pilot-PSI for vapour shielding studies.

- **Li CPS | Magnum-PSI.** The substrate design for the Li exposures in Magnum-PSI is a 3 mm deep cup of 30 mm in diameter, made out of Titanium-Zirconium-Molybdenum (TZM) as shown in Fig. 3.12. This Mo alloy exhibits a higher recrystallization temperature, higher tensile strength and is easier to machine than pure Mo. Since Li is extremely reactive with oxygen and nitrogen, adding Li to the substrate is performed in a purge box under Ar atmosphere. The Mo and W meshes are cleaned in order to chemically remove oxides which prevents wetting. The Mo cup is heated up to approximately 600 °C with presence of the meshes. The liquid Li has a very high surface tension which requires temperatures well above its melting temperature of 180 °C to reach sufficient penetration through the porous medium. It has been found challenging to reach proper wetting of the meshes which suffer from possible oxide contamination and poor thermal connection to the heated cup. Once fully wetted to the surface, the samples are covered with a stainless steel foil and transported in inert atmosphere to the Magnum-PSI target chamber. The samples are exposed to air up to a minute in the period between removing the stainless steel foil and pumping down the target chamber, hereby only contaminating a thin surface layer of Li which can be removed by plasma cleaning.
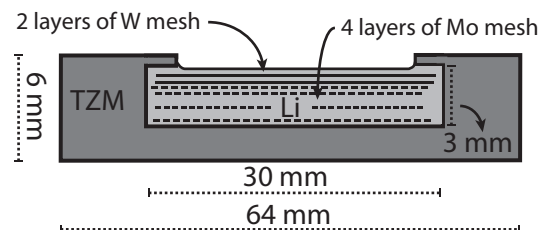
Fig. 3.12 Design of Li CPS target. Used during plasma exposures in Magnum-PSI.

3.3 Liquid Sn high heat-flux power handling

The total plasma pressure along a flux tube is given by $p_{tot} = mnv^2 + p_i + p_e$, where p_i and p_e represent the static pressure contribution from ions and electrons, and v the plasma flow speed [21]. Considering now only the static pressure and the constraint $T_i = T_e$, we obtain the static pressure at the target plate: $p_s = 2n_e k_B T_e$. The evaporation flux is found using the Langmuir evaporation law in conjunction with an empirically derived function of the vapour pressure as function of surface temperature (T_{surf}) [84]:

$$\Gamma_{evap}(T_{surf}) = \frac{10^{(a-b/T_{surf})}}{\sqrt{2\pi m_{Sn} k_B T}}. \tag{2}$$

With a=10.268 and b=15332 for the case of Sn valid from $T_m < T < 1850$ K and a=10.061 and b=8023 valid from $T_m < T < 1000$ K for the case of Li [84]. The previously presented Fig. 3.7 shows the curves of the empirical evaporation flux as function of temperature for both Sn and Li.

Figure 3.13, discussed in-depth in chapter B.1, shows both the surface temperature in the centre of the liquid Sn CPS and a solid reference sample during exposures by a He plasma at heat fluxes (q_{ref}) varying 2.5-22 MW m^{-2}. The Sn CPS in this experiment is
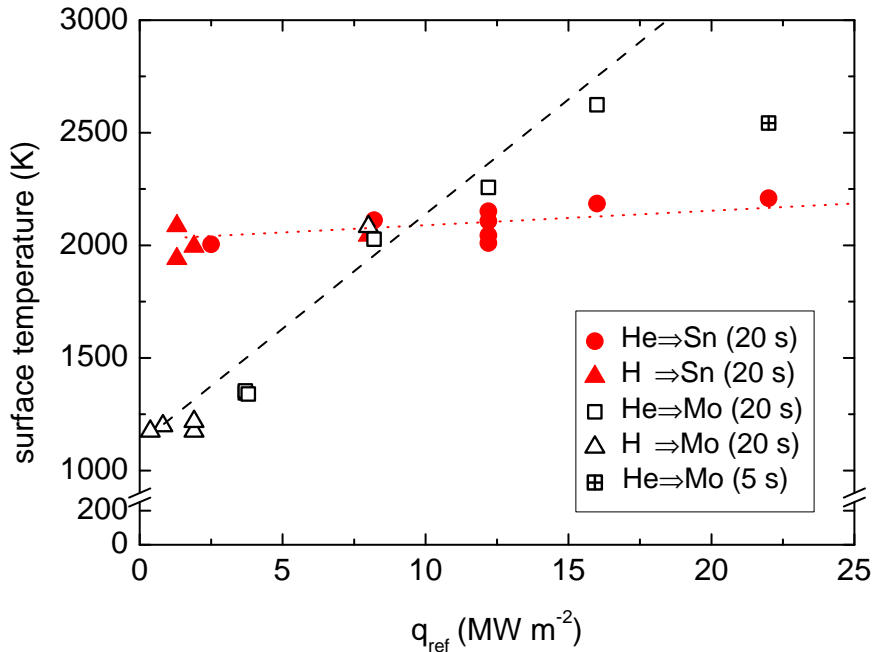
Fig. 3.13 Surface temperature of Sn CPS and solid Mo as function of plasma heat flux. *Appears in chapter B.1. The liquid Sn surface temperature is approximately constant over the heat flux range whereas the solid Mo sample increases with heat flux as expected based on conductive power dissipation.*

intentionally poorly cooled to reach high temperatures, causing the surface temperature to be >1850 K where $\Gamma_{ev} > \Gamma_p$, even at lowest q_{ref}. Additional power dissipation by means other than conduction is concluded when examining the temperature evolution of the liquid CPS (Fig. 1.40 in chapter B.1). This temperature is roughly 650 K lower than what would be expected based on pure conductive heat dissipation of Sn with q_{ref}= 16 MW m^{-2}. The latter estimation is based on finite element modelling using ANSYS. Strikingly, the surface temperature shown in Fig. 3.13 stays approximately constant for the entire range of q_{ref}. A ten-fold increase in q_{ref} is observed to lead to a maximum surface temperature change of 200 K. The increase of surface temperature from 1850 K to 2050 K over the entire heat flux range causes the Sn evaporation rate, however, to increase by a factor 6.1 due to its exponential dependency on temperature.

The vapour pressure for these temperature points, calculated using Eg. (2), is now plotted against the static plasma pressure near the target surface in Fig. 3.14. The plasma parameters are obtained during TS reference exposures on a solid Mo target. Both the
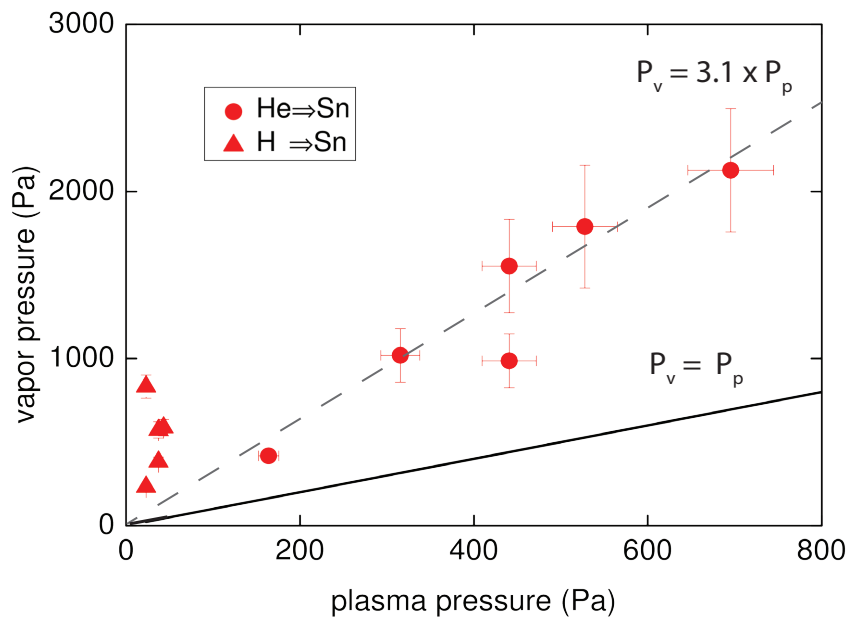
Fig. 3.14 Balance between plasma pressure and vapour pressure. *Exposures where the surface temperature appears decoupled from q_{ref} as in Fig. 3.13 are characterized by a fixed equilibrium between plasma pressure and vapour pressure.*

maximum surface temperature and maximum plasma pressure, which coincide with the centre of the plasma beam, are mutually compared in this pressure balance calculation. The discharges performed in He yield the largest range in plasma pressure and can be well fitted by a linear function, giving $P_v = 3.1 \times P_p$. It is interesting to see that all discharges which showed a decoupling between q_{ref} and surface temperature (Fig. 3.13) align well on

this fitted line. The fraction P_v/P_p can be expected to decrease when taking additionally the dynamic pressure into account. Given the unknown ion temperature and plasma flow velocity away from the sheath edge, the situation of pressure balance is assessed in Fig. 1.42 in chapter B.1 by comparing the evaporation flux to the plasma particle flux, resulting in $\Gamma_v \approx \Gamma_p$.

The first important result is that we have clearly entered the VS regime here. A significant fraction of the plasma heat flux is dissipated volumetrically before reaching the target surface, of which the fraction of the power dissipated in the vapour cloud increases with q_{ref}. The latter observation leads to the conclusion of a 'self-regulatory' behaviour at play: higher q_{ref} leads to more evaporation hence more shielding, resulting in a quasi-equilibrium situation in which the particle fluxes (or pressure) from evaporation and plasma particles are nearly the same.

A natural question to ask is where did the power go? A comparison of calorimetric measurements of both a solid Mo reference target and Sn CPS show that, at least for the case of $q_{ref} > 5\,\mathrm{MW\,m^{-2}}$, 1/3 of the power is dissipated through means other than conduction. In other words, through heat dissipation channels solely available by the LM target. The relative fraction of q_{ref} which is conducted by the substrate furthermore decreases with increasing q_{ref} which is in line with the conclusions of the previous paragraph.

The liquid-gas phase change is often mentioned as a power dissipation channel [59]. This is however only a net energy sink if evaporated particles condense somewhere other than their origin which means we have to take into account the fraction of Sn particles re-deposited at the CPS target. Very conservative estimations based on the depletion time of the Sn CPS (assuming an empty CPS) still yields a re-deposition rate of 87 %. This number is surely a lower bound, since macroscopic loss mechanisms such as droplet ejection could not be distinguished from atomic diffusion losses. Calculating now the latent heat of vaporization for 13 % lost particles, maximally 10 % of the power loss through VS can be attributed to the phase change (see chapter B.1). Dedicated measurements of the re-deposition rate of Sn around 1200 °C in Pilot-PSI using Cavity-Ring-Down-Spectroscopy (CRDS) revealed, however, a re-deposition fraction of 98-99.8 % [96]. This high fraction of returned particles is explained by swift ionization and entrainment of the Sn particles in the plasma, upon which they are confined by the B-field and transported back to the surface. Such high re-deposition fractions lead to the inclination of neglecting power loss through the liquid-gas phase change pathway altogether in high-flux plasma conditions such as present in Pilot-PSI and likely in the ITER-divertor.

If evaporation does not play a significant role, two other power dissipation channels remain: radiative power loss from the vapour cloud, and, secondly, recombination of the

plasma followed by mass loss since the neutral gas is no longer confined by the B-field. The question remains how large each individual contribution is to the overall power balance. The electron temperature in the vapour cloud has been determined via spectroscopic means following the Boltzmann line ratio method, resulting in values ranging 0.5-1 eV for q_{ref}>5 MWm^{-2}. Details on the procedure are given in chapter B.1. These results were indirectly confirmed by measuring the target floating potential during VS which is proportional to T_{e} as described in chapter B.2. This potential was found to be less negative than during solid target exposure by a factor ~3, depending on q_{ref}.

Figure 3.15 shows the ionization and recombination rates of H and He as function of T_{e} as well as rates for Molecular Assisted Recombination (MAR) present for H, for the case of $n_{\text{e}} = 10^{20}$ m^{-3}. As can be inferred from these rates, the atomic processes taking place in the vapour cloud are dominated by recombination rather than ionization due to the strongly reduced T_{e}. The electron density in the vapour cloud is found to be increased as will be discussed in the next section, which does not have a strong effect on the dominant atomic processes in this range (10^{20}-10^{21} m^{-3}). Neutrals resulting from the recombination process are no longer confined by the magnetic field and diffusive out of the system while carrying energy away from the near-surface plasma. The average upstream penetration depth of the Sn neutrals, as will be discussed later, is ~6.5 mm. If we assume isotropic movement of neutralized H or He at this position away from the beam volume, a crude calculation learns that 33 % hits the target surface. The majority of the power dissipated via mass loss is thus transferred to the machine walls, or, in a divertor, to areas away from the main strike-point region where strongest evaporation occurs.

So far we have discussed the observation of reduced heat flux reaching the LM surface and a stabilization phenomenon in which the ratio of volumetric to surface energy dissipation grows in accordance with increased q_{ref}. The intricate coupling between the near-surface plasma, itself interacting with a high fraction of Sn neutrals and ions, and the flowing LM surface yields complex yet exciting physics. A key to elucidate the physical mechanism underlying the observed self-regulatory behaviour has been found in investigating this coupling on a sub-second timescale.

3.4 Dynamical vapour shielding

High-speed IR images of the liquid Sn surface, once in the VS regime, revealed a fast oscillating temperature around a stable base level. It is this 'base level' which is seen to remain approximately constant across a heat flux scan as shown in Fig. 3.13 and which is lower than expected based on conduction only. An example of the temperature evolution
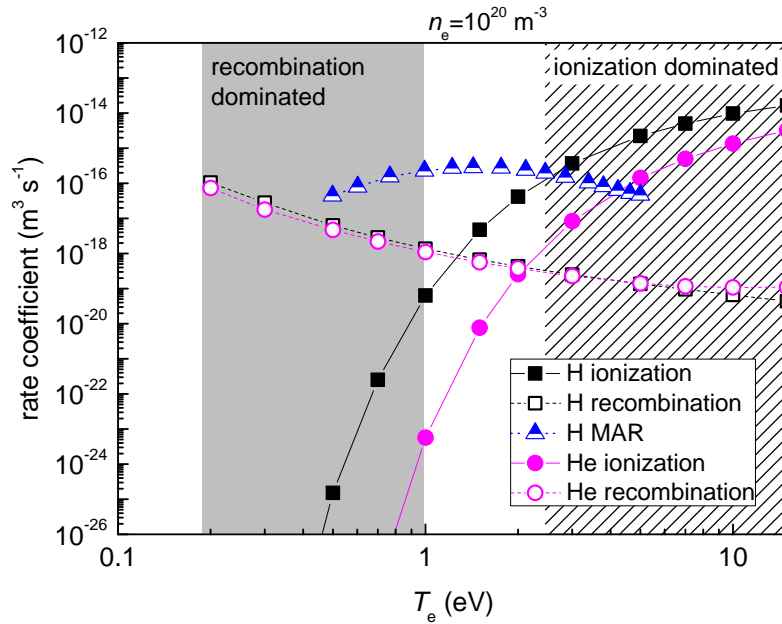
Fig. 3.15 Atomic rate coefficients of H and He. *Appears in chapter B.2. Rate coefficients are obtained from ADAS [97]. Under conditions present during vapour shielding (<0.8 eV), the plasma is characterized by being predominantly recombining rather than ionizing. This effect is aggravated for H due to the presence of MAR processes.*

of both the centre and edge of the Sn CPS in response to q_{ref}=12.2 and 22 MW m^{-2} is shown in Fig. 3.16, which appears again in chapter B.2.

Since both the centre and edge temperature evolution are individually shown, it can be inferred that the centre surface temperature quickly stabilizes (~1 s) while thermal equilibrium is only reached after 10 s or more at the edge of the Sn CPS. The thermal gradient between edge and centre, as well as the magnitude of q_{ref}, are proposed to affect the frequency of the temperature oscillations, which is a subject of discussion later.

Interestingly, when examining a few temperature oscillation cycles in detail, we immediately see wave-like behaviour of similar period and frequency in many other measurable parameters. An important one is emission produced by Sn neutrals, more specifically the line-transition *5s^{2}5p6s-5s^{2}5p^2* producing photons at $\lambda = 452.5$ nm. The total number of photons at this transition summed in the near-surface plasma volume during three consecutive cycles are shown in Fig. 3.17c alongside the centre and edge temperature traces in 3.17a-b. Deeper analysis (details in chapter B.2) performed on the neutral Sn emission yields information of the typical (upstream) axial extend d_{ax} and typical width d_{width} of the vapour cloud. These numbers are obtained from fitting an exponential function to the axial and radial emission profiles and extracting the characteristic $1/e$ length. The axial penetration depth and radial width of the neutral cloud are plotted in 3.17d-e respectively
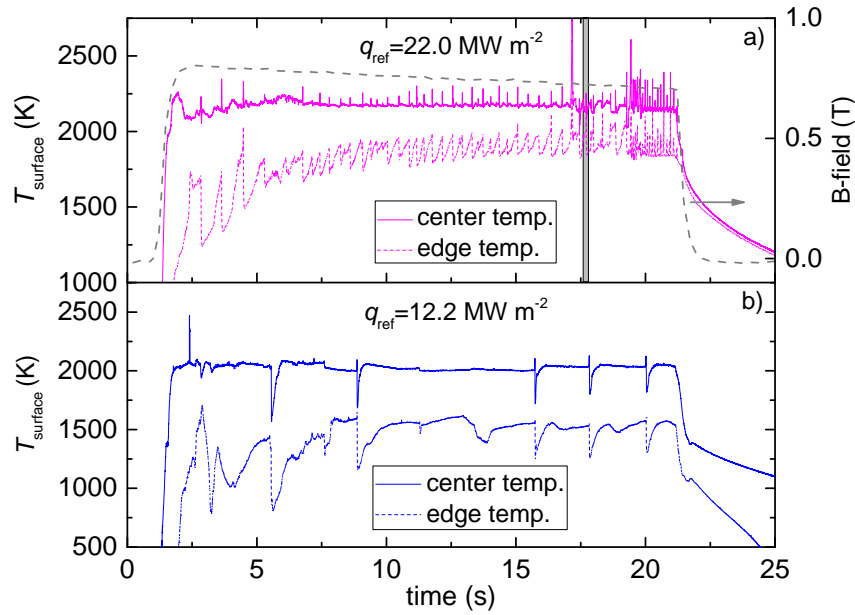
Fig. 3.16 Temperature evolution of the Sn CPS surface during vapour shielding. *Appears in chapter B.2. Fast oscillatory features on a sub-second timescale indicate the presence of a dynamical vapour shielding phenomenon at play. The area indicated by the grey vertical box is investigated in detail hereafter.*

and are both seen to oscillate in phase with the total emission ΣI_{Sn0} plotted in panel *c*. In simpler words, the vapour cloud is seen to grow and shrink during a single oscillation cycle.

The surface temperature in the centre of the CPS shows an intriguing evolution when examining this in parallel to the simultaneous neutral Sn emission as provided by Fig. 3.17. It is seen to rise during the first half of the cycle, in parallel to increased edge temperature and increased ΣI_{Sn0} as well as cloud size expansion. This period within the cycle is named 'phase I'. The following section of the cycle, 'phase II', is characterized by a declining surface temperature in the centre of the CPS while the edge temperature and total emission still rise together with a still increasing overall vapour cloud size. It is during this phase that the surface becomes effectively shielded as evidenced by the temperature reduction in the centre. The flux of Sn neutrals to the near-surface plasma is, however, still fuelled through evaporation from the edge region at a lower but still rising temperature and which comprises of a larger surface area. We postulate that, at a given q_{ref}, a critical amount of Sn atoms need to be released in the near-surface plasma (through evaporation and/or sputtering) to trigger the decline of surface temperature which marks the start of phase II. The last section of the cycle marks the disappearance of the vapour cloud, phase III. The surface temperature has been critically reduced due to shielding in phase II, such that
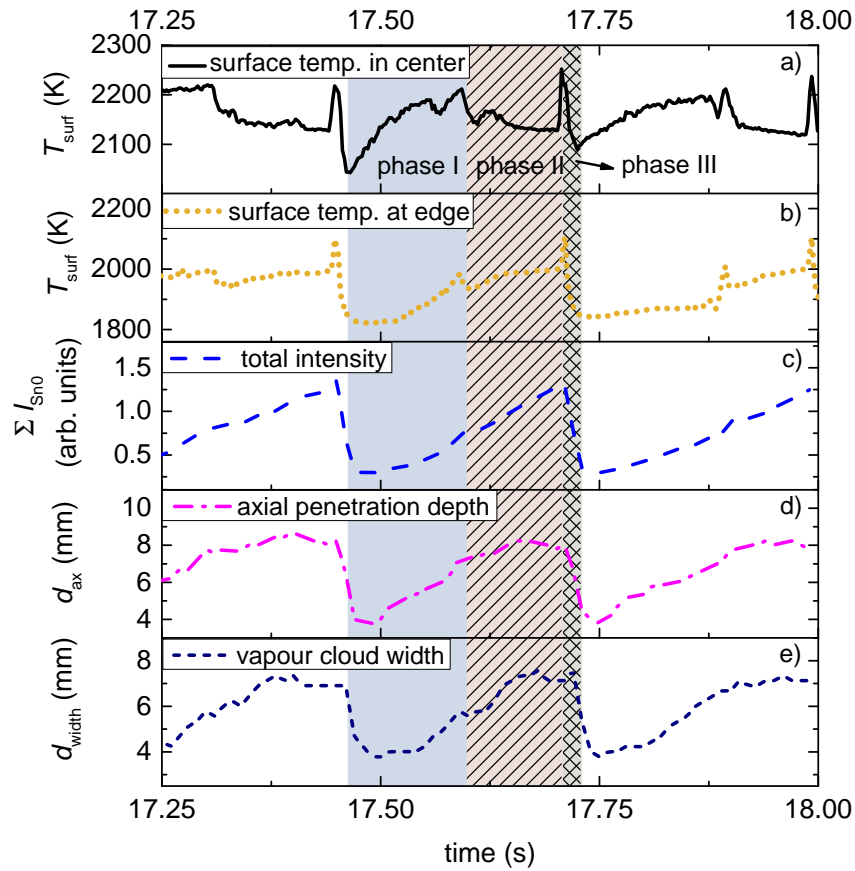
Fig. 3.17 Oscillations in surface temperature and neutral Sn emission. *Surface temperature in the centre (a) and edge (b) of the Sn CPS is found correlated to the total emission by neutral Sn atoms in the near-surface plasma (c) and axial (d) and radial (e) extent of the vapour cloud.*

high surface evaporation ceases and the vapour cloud cannot be longer sustained. The remaining Sn atoms condense at the surface and a new cycle starts since the surface is no longer shielded. The rapid temperature increase which is seen during phase III is believed to be unphysical and a consequence of surface flow, as discussed in section 3.7.

Measurements of the target floating potential (V_{fl}) showed that the magnitude of the sheath potential drop in floating conditions using a liquid Sn CPS during VS is smaller than in the case of the solid Mo reference for equal upstream plasma conditions (see Fig. 2.49a in chapter B.2). The difference is roughly a factor 3 and increases with increased q_{ref}. Given that $V_{fl} \propto T_e$ under the assumption of a fixed plasma potential, we can use measurements of V_{fl} as a function of time to qualitatively asses the time-evolution of T_e. The floating potential drop is found strongly reduced (i.e. less negative) during the VS cycle while it returns to a value similar to a non-liquid surface at the end of a shielding cycle (shown in Fig. 2.49b in chapter B.2). We thus conclude that T_e is periodically reduced

in the vapour cloud to maximally 0.5-0.8 eV (obtained from Boltzmann method) during the shielding cycle.

The qualitative behaviour of the plasma density (n_e) as a function of time is obtained by examining the continuum radiation (ϵ_{cont}) in the wavelength range of 360-580 nm. This emission emerges from free-bound radiative recombination, and, to a lesser extent, free-free Bremsstrahlung [98] and is proportional to the plasma parameters in the following way: $\epsilon_{cont} \propto n_e^2/\sqrt{T_e}$. We first consider the exposure of the Sn CPS at q_{ref}=12.2 MW m^{-2} as shown in 3.16b. The temperature in the centre and edge of the CPS surface is found to suddenly drop at certain stages during the exposure, which is believed to be triggered by reaching a critical concentration of Sn in the near-surface plasma. A surface temperature of 1600-1700 K is reached in the centre of the CPS during such cycles which means Γ_{evap} = $10^{22} - 10^{23}$ m^{-2} s^{-1} which is lower than the plasma particle flux by a factor 50-500. When assuming that the presence of Sn during such stages of the exposure is negligible in this case (q_{ref}=12.2 MW m^{-2}), we can calculate n_e during the period of stationary VS where the temperature is relatively constant. Recall that the floating potential during the temperature minima is similar to the case of solid Mo exposure, which indicates that T_e is at least not strongly affected by Sn during such phases (the temperature minima).

Figure 3.18b (appears also in chapter B.2) shows the continuum emission at q_{ref}=12.2 MW m^{-2} where phase I indicates the start of a shielding cycle (equal to a temperature minimum) and 'phase II' the phase of stationary VS (appears as T_{surf} =constant, for instance during a period t=10-15 s). Taking now the ratio of the spectral radiance during stationary (subscript 'VS') and the spectral radiance during the temperature minima (subscript '0') where we assume negligible VS to occur, we can derive the following expression for n_e during the VS phase:

$$n_{e,VS} = \left(\frac{\epsilon_{cont,VS}}{\epsilon_{cont,0}} \sqrt{\frac{T_{e,VS}}{T_{e,0}}} \right)^{\frac{1}{2}} n_{e,0} \tag{3}$$

The electron temperature during exposure of solid Mo at 12.2 MW m^{-2} is 2.5 eV while this is reduced in the vapour cloud to 0.5 eV (see table of exposure conditions in chapter B.2). The spectral radiance is found to increase by a factor 20 when comparing the stage of VS to the temperature minima (see again Fig. 3.18). Substituting these numbers in Eq. 3 yields $n_{e,VS} = 16.4 \times 10^{20}$ m^{-3}. Given that the plasma pressure is proportional to $n_e T_e$, we find the relative change of pressure in the centre of the plasma beam due to VS: $p_{VS}/p_0 = n_{e,VS} T_{e,VS}/n_{e,0} T_{e,0} = (0.5 \times 16.4)/(2.5 \times 5.5) = 0.6$ (at q_{ref}=12.2 MW m^{-2}).

From previous calculations we have arrived at the conclusion that the plasma pressure, due to VS, is reduced by 40 % compared to the case without Sn during exposure at q_{ref}=12.2 MW m^{-2}. Recall that mass loss due to recombination of the plasma is proposed
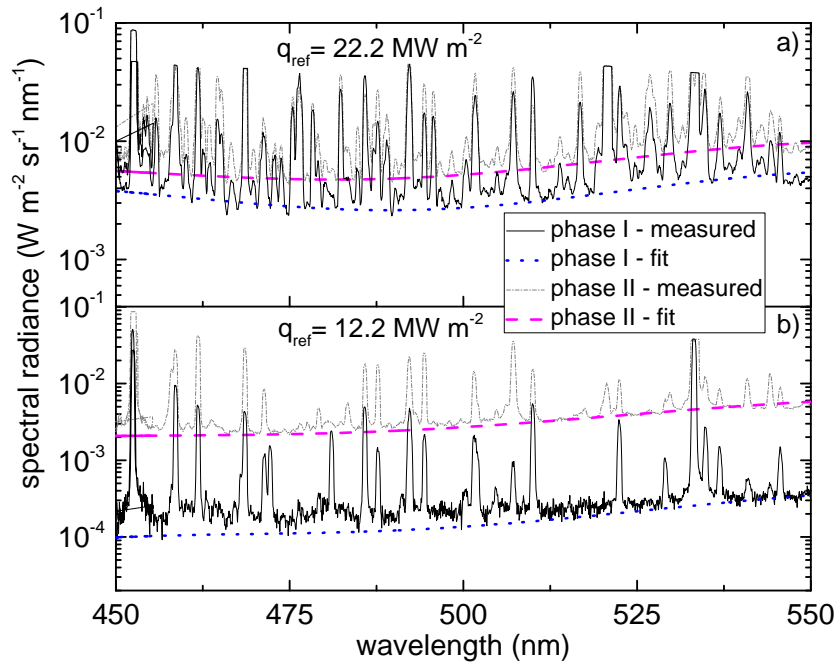
Fig. 3.18 Continuum emission from near-surface plasma region. *Appears in chapter B.2. Shown for the cases of q_{ref}=12.2 MW m^{-2} and q_{ref}=22.2 MW m^{-2} at both the start of a VS cycle (phase I) and the period of most effective shielding (phase II)*

as a significant power loss mechanism during VS. Based on this observation, the scenario which occurs during a VS cycle appears quite similar to that of divertor detachment, characterized similarly by large pressure gradients along the magnetic field lines resulting in reduced heat fluxes to the material surfaces [99]. In the case of VS, it is 'impurity-driven', induced by impurities released from the wall and localized within a few cm from the surface rather than due to a raised neutral pressure fraction in the plasma and occurring over larger distances. It is this detachment-like state which is periodically reached which causes the heat flux reaching the surface, hence the surface temperature, to oscillate in time.

3.5 Plasma cooling mechanism

The electron temperature during steady-state VS ranges 0.5-0.8 eV as described extensively in chapter B.1. The plasma temperature in absence of any vapour is ~5 times higher, ranging 2.4-3.1 eV (see table 5 in chapter B.2). The question is how the reduction in T_e is effectuated. Detailed understanding into the evolution of T_e in connection to increasing vapour density is a rather complex question since it is strongly dependent on the vapour

density in front of the surface, which on its turn depends on the phase within the shielding cycle. For instance, the direct electron impact ionization rate coefficient of neutral Sn (C_{ion}) differs by 4 orders of magnitude over the range 0.4-2 eV, as shown in Fig. 3.19. These
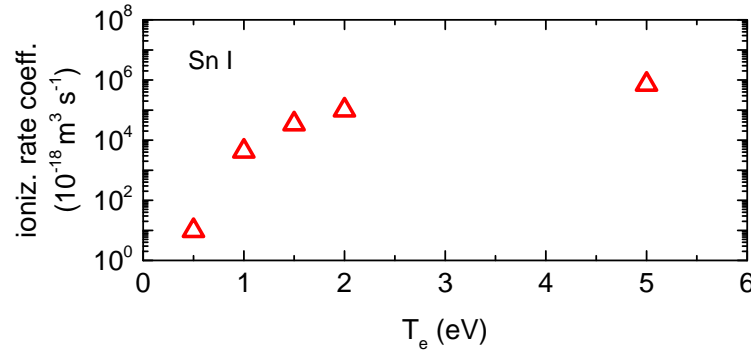
Fig. 3.19 Direct impact ionization rate coefficients for Sn. *Atomic rate coefficients obtained from [100]. The ionization rate is a steep function of T_e in our range of interest.*

rate coefficients are retrieved from the FLYCHK atomic database [100] which employs a so-called 'schematic atomic level' approach where the energy levels are computed from ionization potentials. It is explicitly mentioned that rates near the ground state and at low temperatures are highly uncertain given the method of calculation. We assume a level of accuracy within a factor 5 which is believed to be enough for a qualitative understanding of the phenomena. Given the rates in Fig. 3.19, ionization of Sn is expected to be dominant during the first stage of surface heating where no significant vapour density is present but reduces drastically once the near-surface plasma cools and stabilizes into a quasi-stationary (oscillatory) state.

The same computing engine has been used to run a collisional radiative model (CRM) to obtain the charge state distribution for Sn as function of T_e. The results for steady-state local thermal equilibrium (LTE) at $n_e=10^{20}$ m^{-3} are shown in Fig. 3.20.

Relaxation of the excited state $5s^2 5p6s$ into the ground state is accompanied by photon emission at λ=452.5 nm. We have used the intensity of photon emission at this specific wavelength to monitor the dynamics of the neutral Sn atoms in the vapour cloud at high speed using a tangentially positioned camera recording at 10 kHz. The excitation rate of ground state Sn ($5s^2 5p^2$) into the excited level $5s^2 5p6s$ is calculated using [101]. A similar procedure is followed to obtain the recombination rate from the ion level (Sn II) leading to population of the same excited state of SnI. The ratio of these processes as function of T_e is presented in Fig. 3.21 while correcting for the temperature dependency of the charge state population by multiplying the ratio by $\alpha = (N_{Sn^0} / \sum_j N_{Sn^{+j}}) / (N_{Sn^+} / \sum_j N_{Sn^{+j}})$ plotted in Fig. 3.20. It is clear from Fig. 3.21 that populating the excited level $5s^2 5p6s$ occurs
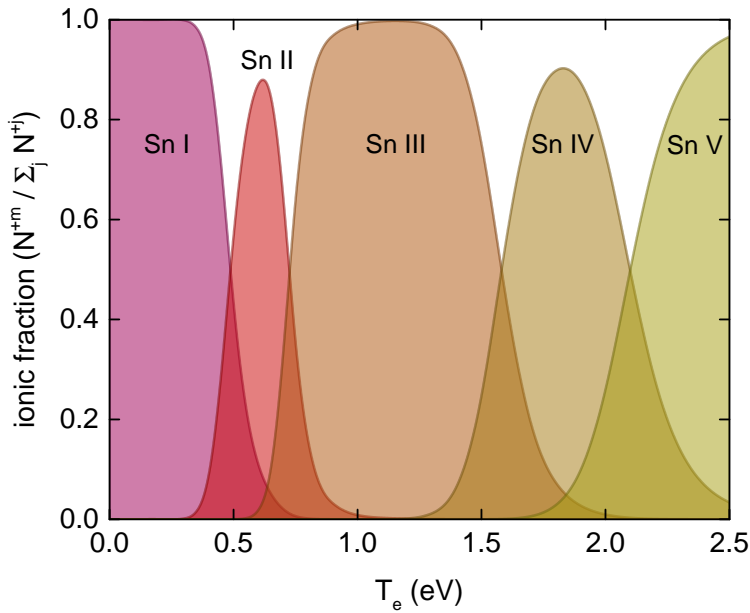
Fig. 3.20 Charge state distribution of Sn as function of temperature. *The relative abundance of Sn charge states as function of T_e determined at $n_e = 10^{20}\ m^{-3}$.*

predominantly via excitation from the ground level rather than via ion recombination in our temperature range of study which proves that measuring the emission intensity at 425.5 nm provides a good representation of the neutral Sn distribution over time.
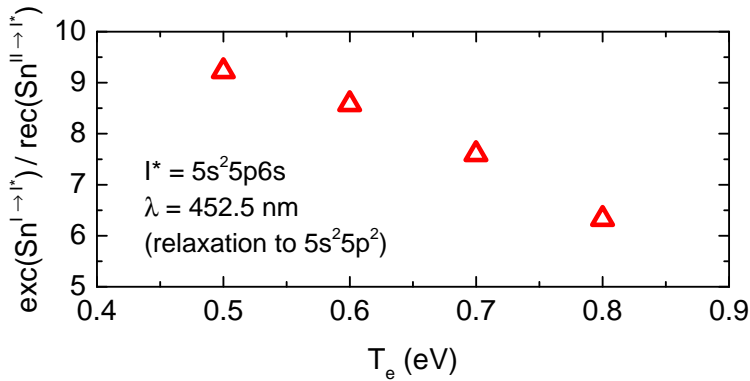
Fig. 3.21 The ratio of excitation versus recombination in populating the state $5s^2 5p6s$ **of neutral Sn.** *Ionization and recombination rates are corrected for the charge state distribution as function of T_e obtained from FLYCHK [100].*

We will now explore the apparent physics mechanism underlying cooling and pressure loss due to the presence of Sn vapour, leading to the observed plasma conditions during steady-state VS. The upstream plasma obviously comprises ions and electrons, for which we limit ourselves to the case of singly charged He ions and electrons. The source of Sn

particles is located at the target position and is dominated by evaporation (Eq. 2), for which we further assume that all Sn particles enter as neutrals. Sputtering as a particle source is neglected; the sputtering threshold of Sn by He and Sn itself are 35.54 eV and 18.32 eV respectively which is much higher than the maximum energy of the ions in the sheath where $T_i \approx T_e \lesssim 3.5$ eV.

The dominant collisional processes during He exposures at 12.2 and 22.0 MW m^{-2}, widely varying in VS oscillation frequency, are investigated now. The axial diffusion of evaporated Sn neutrals can be described using Fick's first law:

$$\Gamma_{\text{evap}}(T_{\text{surf}}) = -D\frac{\partial n_{\text{Sn0}}}{\partial z} \approx -D\frac{\Delta n_{\text{Sn0}}}{\Delta \lambda_{\text{ion}}} \tag{4}$$

with a diffusion coefficient $D = kT_{\text{Sn}}/m_{\text{Sn}}C_{\text{ion}}n_e$ where T_{Sn} represents the vapour temperature, m_{Sn} the atomic mass of Sn and C_{ion} the direct impact ionization coefficient (Fig. 3.19). The average thermal velocity of the Sn atoms is simply calculated as $v_{\text{Sn}} = \sqrt{3kT_{\text{Sn}}/m_{\text{Sn}}}$ by inserting $T_{\text{Sn}} = T_{\text{surf}}$. Using this, the ionization mean free path can be calculated as $\lambda_{\text{ion}} = v_{\text{Sn}}/C_{\text{ion}}n_e$. Rewriting Eq. (4) yields a simple expression for the atomic Sn density in front of the CPS surface:

$$n_{\text{Sn}} = \Gamma_{\text{evap}}\sqrt{\frac{3m_{\text{Sn}}}{kT_{\text{Sn}}}}. \tag{5}$$

The Sn neutral density and temperature, the ionization mean free path and the ionization rate are shown in table 2 for two cases of q_{ref} in the vapour shielding regime. Since the temperature of the plasma reduces in the axial direction towards the CPS surface, ionization becomes increasingly less important closer to the surface. The aim is however to describe a mere general case rather than a spatially resolved one so we compare two values of the electron impact ionization rate, namely at 0.5 eV and at 1.5 eV (see Fig. 3.19). The typical elastic collision times between the different charged particle species are calculated using [14] and are shown in table 2 as well. Since the neutral Sn density is high compared to the plasma ion density in both cases, it is important to calculate the neutral-ion elastic collision rate:

$$\nu_i = n_0\sigma_0{}^{i,0}\sqrt{\frac{kT_i}{m_i}} \tag{6}$$

with $\sigma_0{}^{i,0} = 8.9 \times 10^{-18}$ m^{-2} and $\sigma_0{}^{i,0} = 1 \times 10^{-17}$ m^{-2} the neutral-ion momentum transfer cross section [102] for the cases of q_{ref}=22 MW m^{-2} and q_{ref}=12.2 MW m^{-2} respectively. Again, we focus on these two cases since the oscillation dynamics were found to be most different. The atomic polarizability of Sn equal to 6×10^{-30} m^{-3} [103] appears in the expression for this cross section as well as the relative kinetic energies of the colliding

particles. We assumed the relative motion of the Sn atoms to be opposite to the He ions for simplicity (the He plasma flow is directed towards the target). The ion-neutral collision time, $\tau_{\mathrm{He+,Sn0}} = 1/\nu_i$, as well as the mean free path of the evaporated Sn neutrals λ_{Sn0} are shown in the outermost right columns of the table.

q_{ref} MWm^{-2}	T_e (eV)	n_e ($\times 10^{20}$ m^{-3})	T_{SnI} (eV)	n_{SnI} ($\times 10^{20}$ m^{-3})	Γ_{evap} ($\times 10^{24}$ m^{-2}s^{-1})	
22.0	3.1	7.0	0.19	520	11.8	
C_{ion} (m^3 s^{-1})	λ_{ion} (m)	τ_{ion} (s)	$\tau_{\mathrm{e,He+}}$ (s)	$\tau_{\mathrm{e,Sn+}}$ (s)	$\tau_{\mathrm{He+,Sn+}}$ (s)	$\tau_{\mathrm{He+,Sn0}}$ (s)	λ_{Sn0} (m)
9.7×10^{-18}	1.0×10^{-1}	1.5×10^{-4}	1.2×10^{-6}	3.4×10^{-5}	5.4×10^{-9}	2.5×10^{-10}	1.7×10^{-7}
3.4×10^{-14}	2.9×10^{-5}	4.2×10^{-8}	1.2×10^{-6}	3.4×10^{-5}	5.4×10^{-9}	2.5×10^{-10}	1.7×10^{-7}

q_{ref} MWm^{-2}	T_e (eV)	n_e ($\times 10^{20}$ m^{-3})	T_{SnI} (eV)	n_{SnI} ($\times 10^{20}$ m^{-3})	Γ_{evap} ($\times 10^{24}$ m^{-2}s^{-1})	
12.2	2.5	5.5	0.18	149	3.3	
C_{ion} (m^3 s^{-1})	λ_{ion} (m)	τ_{ion} (s)	$\tau_{\mathrm{e,He+}}$ (s)	$\tau_{\mathrm{e,Sn+}}$ (s)	$\tau_{\mathrm{He+,Sn+}}$ (s)	$\tau_{\mathrm{He+,Sn0}}$ (s)	λ_{Sn0} (m)
9.7×10^{-18}	1.2×10^{-1}	1.9×10^{-4}	1.1×10^{-6}	3.2×10^{-5}	1.4×10^{-8}	8.6×10^{-10}	5.7×10^{-7}
3.4×10^{-14}	3.5×10^{-5}	5.4×10^{-8}	1.1×10^{-6}	3.2×10^{-5}	1.4×10^{-8}	8.6×10^{-10}	5.7×10^{-7}

Table 2 Typical atomic collision times in Sn/He near-surface plasma. *Properties of the plasma near the CPS surface are compared between exposure conditions at 22.0 MW m^{-2} (top section) and at 12.2 MW m^{-2} (lower section). These two cases displayed the greatest difference in oscillation dynamics. Furthermore, cases using different values of the direct impact ionization rate coefficient (C_{ion}), namely at T_e= 0.5 eV and 1.5 eV, are shown for both.*

The dominant pathways of plasma cooling by the presence of neutral Sn can be elucidated by examining the results presented in table 2. What immediately becomes clear is that, due to a high neutral density, the elastic ion-neutral interaction time is extremely short compared to the electron-ion collision times. Depending on the fraction of Sn ions in the overall charge state distribution, thermal relaxation by interaction between He and Sn ions is the second dominant pathway for cooling of the plasma ions. Thirdly, the electrons lose their energy predominantly through Coulomb scattering and inelastic collisions with the He ions rather than with Sn ions due to the larger mass of the latter. In short, cooling of the plasma by neutral-ion elastic energy transfer, sometimes being referred to as ion-neutral friction, followed by ion-electron thermalization is concluded

to be the dominant energy loss route in our regime of study here. This statement is in agreement with the behaviour of the floating potential as reported in the previous section: the increase in emission from Sn neutrals (Fig. 3.17c) means increased neutral Sn density causing increased neutral-ion friction and hence stronger cooling.

The experimentally determined characteristic axial penetration depth of Sn neutrals during the exposure at $22.2\,\mathrm{MW\,m^{-2}}$ ranges 4-8 mm (Fig. 3.17). The table shows an ionization mean free path λ_{ion} (hence loss of neutrals) ranging between 8.2×10^{-2} m (at 0.5 eV) and 2.3×10^{-5} m (at 1.5 eV) for the case of q_{ref}=22.0 $\mathrm{MW\,m^{-2}}$. The measured penetration depth thus lies within these limits which further indicates that T_{e} lies within the range 0.5-1.5 eV, which is in agreement with the results from Boltzmann analysis which yielded 0.5-0.8 eV.

The effect of plasma cooling through plasma-vapour interaction, leading to a state resembling that of detachment, is illustrated in Fig. 3.22. The energies of the particle
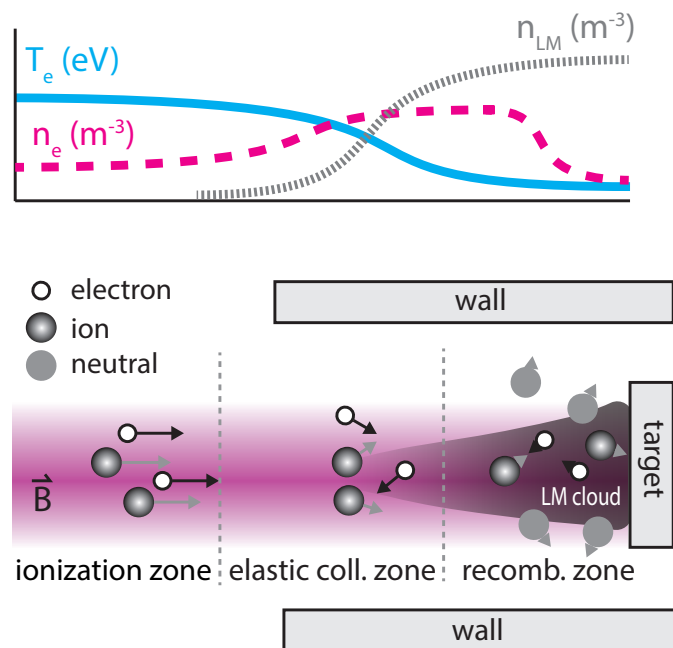
Fig. 3.22 Representation of impurity-induced detachment. *Plasma ions and electrons lose energy in a two-step interaction process with the Sn vapour cloud, eventually leading to a recombination dominated plasma where neutral particles escape the near-surface plasma region transferring energy to the machine walls.*

species are represented by the length of the arrows. The qualitative behaviour of T_{e}, n_{e} and n_{Sn} (SnI density) as function of distance from the LM surface are drawn in the top panel. The plasma processes upstream (left in picture) are dominated by ionization (>3 eV). The neutral Sn cloud extents maximally 8 mm from the CPS surface (see Fig. 3.17)

which causes the plasma ions to lose their energies via elastic collisions in interaction with the Sn atoms (elastic collision zone). Electron-ion thermal relaxation prevails in this region where T_e=1-3 eV, of which the typical collision time scales as $\tau_{ei} \propto n_e^{-1} T_e^{3/2}$ [104]. The increase in n_e during the VS cycle thus enhances electron-ion relaxation, hereby reaching temperatures and densities which are characteristic for a recombining plasma (<1 eV). The three-body recombination time scales as $\tau_{EIR} \propto n_e^{-1} T_e^{9/2}$ [104]. Recombination thus rapidly increases with reduced T_e. Neutral products from recombination further cool-down the ions and electrons hereby causing a negative feed-back leading to more recombination (recombination zone). The recombined particles are partly lost to the machine walls transferring energy away from the near-surface region.

3.6   Oscillatory behaviour

The question why the cooling mechanism as previously described gives rise to oscillatory behaviour is addressed now. We will still discuss the case of Sn, but the mechanism is believed to be applicable to other LM candidates too, as will be discussed in the next section. Table 2 summarizes the collision times for two cases of dynamical VS which exhibit very different behaviour in temperature variation, frequency and duration of the oscillations, see Fig. 3.16. The exposure at 12.2 MWm^{-2} (panel b) shows large variations and it takes a significant amount of time for the plasma to recover after a single oscillation cycle. The cycles during the exposure at 22.0 MWm^{-2} are however faster paced and exhibit smaller temperature excursions.

   We believe that the ultimate cause of the observed oscillatory behaviour can be found in the large difference between the characteristic timescales of the coupled processes. The fastest timescale in the system is cool-down of the plasma through momentum exchange between neutrals and ions ($\tau_{He+,Sn0} \sim 10^{-9} s$), leading to plasma recombination/detachment, once a critical LM atom density is reached in the vapour cloud. The slowest phenomena are however conductive/convective heating of the liquid surface which occurs over a millisecond timescale. The reduction of surface temperature during shielding is faster since heat can be extracted by active cooling, typically τ_c=250 μs. This is however still vastly different from the plasma timescale.

   Stationary heating and evaporation characterizes phase I. An increasing amount of Sn atoms reside in front of the surface. As long as n_{Sn} is subcritical, normal conduction type heating of the liquid prevails. The Sn atoms released from the surface are quickly ionized as a result of the low ionization potential (7.34 eV) and still high T_e. The latter gradually decreases over the course of phase I. A critical density of Sn is defined as the density where ion-neutral collisions become dominant over Coulomb collisions, leading

to such cool-down of the plasma that the plasma becomes recombining. The produced neutrals aid in the plasma cool-down process culminating in a runaway process where the plasma temperature quickly drops, causing the recombination process to be extremely rapid. Cool-down of the surface, on the other hand, is determined by the specific heat handling capability of the material, as well as thermal gradients across the materials set by specific cooling conditions.

The proposed mechanism can be modelled by starting from the general heat equation, describing the evolution of the surface temperature (T_s) while subject to power input from the plasma q_{ref} and a volumetric loss term due to VS:

$$\rho(T)C_p(T)\frac{\partial T_s}{\partial t} = -k(T)\frac{\partial^2 T_s}{\partial z^2} - k(T)\frac{\partial^2 T_s}{\partial r^2} + \frac{\partial}{\partial z}q_{ref} - \frac{n_i E_{VS}}{\tau_i}. \tag{7}$$

The parameters ρ, C_p and k are the density, heat capacity and thermal conductivity respectively. Both radial (r) and axial (z) conduction are considered. E_{VS} represents the cooling action performed by a single impurity particle while n_i is the impurity density and τ_i the typical residence time in the plasma. In steady-state where $\frac{\partial T_s}{\partial t} = 0$, the incident power from the plasma is balanced by conductive heat transfer and volumetric losses:

$$q_{ref} = k_z\frac{\Delta T_s}{\Delta z} + k_r\frac{\Delta T_s}{\Delta r} + E_{VS}\Gamma_{evap}(T_s). \tag{8}$$

Equation 8 is simplified from Eq. 7 by assuming linear temperature gradients. The thermal conductivities in radial and axial direction are explicitly stated since these can be different in a mixed (and anisotropic) material such as a CPS. It is immediately clear that heat dissipation is dominated by conduction at low temperatures where $\Gamma_{evap}(T_s)$ is negligible. Heat dissipation in the vapour cloud is directly proportional to $\Gamma_{evap}(T_s)$ which is itself an exponential function of temperature (Eq. 2). When n_{Sn0} becomes large enough, volumetric heat dissipation becomes important and the surface temperature starts to decrease where its rate is dependent on the radial and axial temperature gradients as well the respective thermal conductivities. The reduction in temperature on its turn readily affects $\Gamma_{evap}(T_s)$ and hence the volumetric energy loss term.

We now subject the experimental data shown in Fig. 3.16 and table 2 to these considerations. The surface temperature during the exposure at 12.2 MW m^{-2} is roughly 200 K lower than the exposure at 22.0 MW m^{-2}. The evaporation flux is hence approximately 4 times lower. The combination of a lower release rate in addition to lower plasma pressure ($\propto n_e T_e$, for $n_e = n_i$ and $T_e = T_i$) exerted on the evaporated particles (entrainment) in the latter case, results in a longer duration to reach a critical impurity density in the near-surface

plasma. As a result, the ratio of neutral-ion collisions versus Coulomb interactions is lower in the case of low q_{ref} compared to high q_{ref}. Once the plasma is detached and the surface temperature drops, it obviously requires longer to recover due to a lower heating power from the plasma.

The characteristic oscillations frequency is thus believed to be ultimately dependent on q_{ref}, total plasma pressure p_{tot}, evaporation rate of the LM, conductive/convective heat removal rate of the liquid surface (depending on mechanical design and specific thermal properties) and mass of the LM species. The difference in atomic characteristics between species such as ionization, excitation and radiation once the LM is released in the plasma is furthermore expected to be influential, but not believed to be dominant in setting the oscillation frequency.

Our hypothesis of reaching efficient VS by equilibrating the plasma pressure to the vapour pressure has also been tested using liquid Li. Our CPS Li target design turned out to be unsuccessful in achieving a relevant surface temperature so we have resorted to study exposures of a different sample design, containing a large amount of Li in a reservoir and a Mo surface mesh to present the liquid to the plasma in a capillary structure. This type of target is envisaged as a divertor test module for NSTX-U [105]. Exactly as predicted, an approximately flat base temperature level accompanied by oscillations was achieved once the liquid Li surface was heated to temperatures >960 K where the evaporation flux is greater than 1×10^{24} m^{-2}s^{-1} (Fig. 3.7). The resulting temperature evolutions in the centre of the liquid Li surface in response to He plasma heat fluxes ranging 7-8 MWm^{-2} are shown in Fig. 3.23. Similarly to observations of liquid Sn, the average surface temperature of the liquid surface is drastically lowered compared to the solid reference target made of TZM exposed to the same q_{ref}, indicative of strong VS. The exposure at q_{ref}=8 MWm^{-2} oscillates around a base temperature level of 1050 K ($\Gamma_{evap} = 8.1 \times 10^{24}$ m^{-2}s^{-1}). The drop in surface temperature during each cycle is very steep, which may be attributed to the higher ($\times \sim 10$) thermal conductivity of liquid Li compared to liquid Sn at elevated temperatures as shown in table 1. Unfortunately, radiated power measurements (using bolometry) could not yet be conducted, hence the question of potentially increased near-surface emission due to Li could not be addressed for the exposures shown in Fig. 3.23.

3.7 Surface flow

An important aspect regarding the application of LM PFCs is the question of stability. Although greatly reduced by a quasi-static arrangement such as a CPS, surface flow and instabilities were encountered during high heat-flux power handling experiments. The specific volume of Sn increases by 14.6 % from the melting point up to 1970 K [106] due
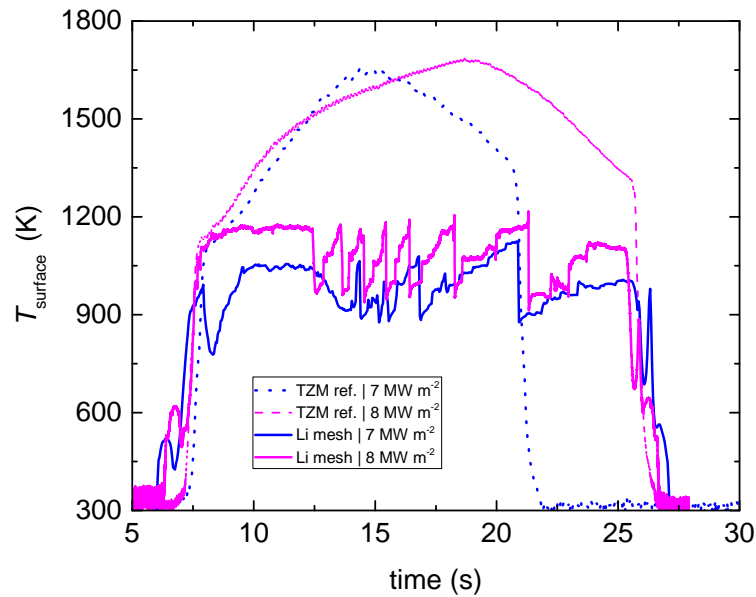
Fig. 3.23 Vapour shielding oscillations of a liquid Li surface. *Observation of liquid Li surface temperature oscillations (solid lines) due to steady-state vapour shielding. The surface temperature is overall drastically reduced compared to exposures on a solid TZM reference target (dashed lines). This observation is similar to the results obtained using a Sn CPS during VS.*

to addition of thermal energy from the plasma. A 2.7% expansion resulting from the solid-liquid phase change should be accounted on top of that. The expansion causes the liquid Sn to flow beyond the available space bounded by the capillary structure, forming a liquid film on top of the CPS. Having to deal with a free liquid surface despite using a CPS, particularly when operating at high temperatures to allow for VS, needs to be taken into account when designing a LM divertor component.

The specifics of LM flow are dependent on the presence of thermal gradients, electric currents and magnetic fields which may in turn affect convective heat transfer. Conditions in Magnum-PSI and Pilot-PSI give rise to interesting phenomena due to the nature of the cascaded-arc source which generates a current path through the plasma column from cathode to anode. A metallic surface can be part of the electrical circuit as it provides a low-resistance component in the radial direction [89]. The LM located at the edge of the surface is seen to spin around the central axis in clockwise direction during phases I and II of the shielding cycle which is compatible with $\mathbf{J} \times \mathbf{B}$ driven motion in floating target conditions, i.e. rotational flow driven by Lorentz-forces emerging from the orthogonality between the magnetic field and radial currents induced by the plasma.

As described in detail in chapter B.2, the liquid flow is furthermore seen to alternate between such azimuthal rotation during the onset of VS and radial inward flow during the detachment-like phase. Also, the rotation speed is seen to decrease over the duration of

the shielding cycle for intermediate q_{ref} which confirms that the particle flux to the target is reduced during VS. Finding an explanation for the inward transport is however challenging. Thermo-capillary convection may give rise to radial transport when differences in surface tension between hot and a cold areas exist. This should be directed from the centre of the target to the edge in our case, which is in contradiction to the observation of an inward movement.

It must also be considered that the plasma pressure is highest in the centre of the beam and lowest at the edges which forces the liquid to flow to the edge region, exactly where rotational flow is most clearly observed. Since the plasma pressure in the detachment-like phase is maximally reduced, it is hypothesized that a surface wave driven by surface tension forces transports the LM from the edge towards the centre of the target, hereby minimizing the free surface energy. This surface instability gives rise to an emissivity change which explains the apparent rapid temperature rise (spike) as observed in the temperature measurement during phase III (see Fig. 3.17a). This temperature excursion was deemed unphysical given the large heat flux variation required and is therefore attributed to a change in emissivity.

The free surface flow on top of a CPS is expected to be different in a tokamak geometry where the direction of the magnetic field with respect to the strike-point is different, alongside possible differences in thermal gradients. Such differences are however not expected to implicate our findings about dynamical VS where changes in the liquid flow direction and speed are to be a consequence rather than a cause of the oscillatory behaviour. The relevance of our findings to the situation of a divertor is discussed in section 5.

3.8 A general description of steady-state vapour shielding

This section provides an explanation of the physics mechanism of steady-state vapour shielding in a general sense. An attempt to illustrate the multitude of processes underlying the vapour shielding phenomenon, some of which are mutually synergistic, can be found in Fig. 3.24. The sizes of drawn particles qualitatively represent their kinetic energies. The plasma heat flux arriving on the LM surface initiates the release of LM impurities into the near-surface plasma region once the liquid surface temperature is high enough. Impurity release from the surface is perpetuated over time, albeit in a oscillatory fashion when the upstream heat flux is high. Sputtering can be assumed negligible in our experimental conditions but may aid LM release into the plasma in real divertor conditions where T_{i} may potentially be higher. A large fraction of evaporated/sputtered atoms return to the surface due to a combination of plasma entrainment and prompt ionization. The high
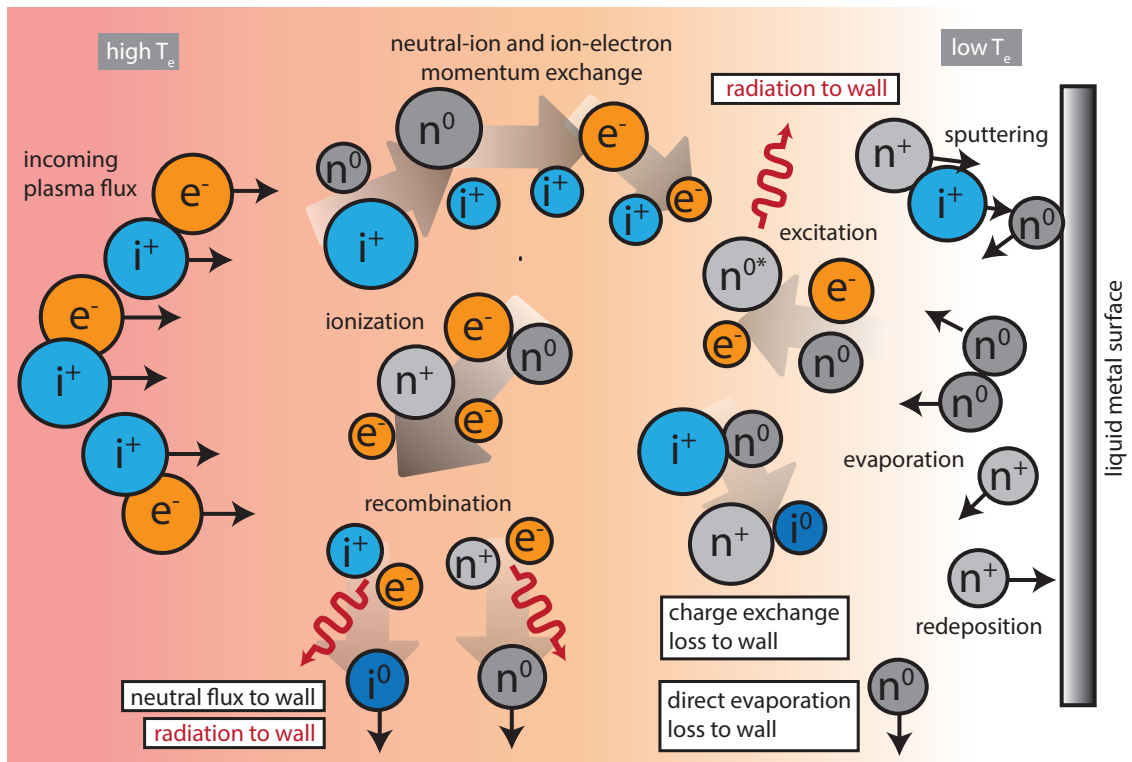
Fig. 3.24 Illustration of the general vapour shielding phenomenon. *Relative sizes of the particles indicate their kinetic energy. A multitude of interlinked processes contribute to the conversion of the incoming plasma power into particle loss and radiation, eventually reducing the surface heat flux.*

density of neutral atoms just in front of the surface provides a 'gaseous wall' in which the plasma loses part of its energy in a two-step process. Firstly, the plasma ions lose their energy via momentum exchange with cold LM neutrals. Secondly, the electrons are cooled-down by interaction with plasma ions and LM ions (the latter is less likely for Sn, see table 2). Electron impact ionization is another power dissipation mechanism but this may be regarded as small in the centre of the vapour cloud where T_e is drastically reduced due to the two-step cooling process. Power is furthermore dissipated via inelastic collisions between electrons and plasma ions as well as between electrons and LM neutrals, both leading to radiative losses transporting energy to remote regions. This process is enhanced by the increase of n_e during VS as evidenced from the increased continuum emission (Fig. 3.18). The plasma enters a regime dominated by recombination in the vapour cloud due to the strong cooling, producing even more neutrals which further induce cooling through ion-neutral interaction. This class of particles is not confined by the magnetic field and transported to regions outside the plasma beam, carrying energy away. The final

process appearing in Fig. 3.24 which we have not discussed is charge exchange between LM neutrals and plasma ions. The resulting LM ion may be promptly redeposited on the surface due to confinement by the magnetic field and entrainment in the plasma flow directed towards the surface while the neutralized plasma ion may escape the magnetic field.
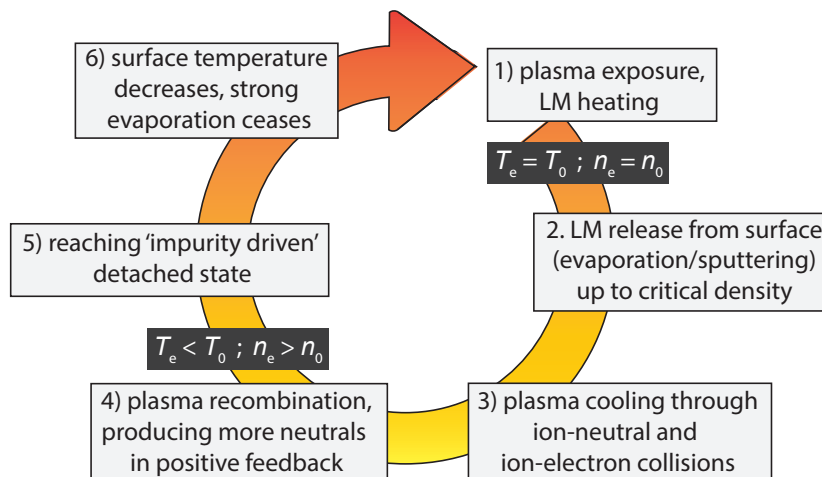
Fig. 3.25 Time-cycle of dynamical vapour shielding. *The boxes indicate the different phases during a single vapour shielding cycle.*

It became clear in our studies that the phenomenon as previously described naturally gives rise to a quasi-static situation, where the efficiency of VS, i.e. the capability to mitigate the surface heat flux, oscillates in time for stationary heat fluxes $>10\,\mathrm{MW\,m^{-2}}$. The chain of events is drawn in Fig. 3.25. The start of the cycle is marked by heating of the liquid surface by the plasma (1) in absence of significant vapour presence. Evaporation and sputtering increase the LM vapour density up to a level (2) where the occurrence of ion-neutral elastic collisions (friction) dominate over Coulomb scattering (3). Plasma recombination sets in, producing more neutrals that promote further energy loss of the plasma (4) leading eventually to an impurity-induced detached state of the plasma with pressure loss (5). As a result of reduced heating power by the plasma, the evaporation rate quickly drops and the vapour cloud is no longer sustained (6). The vapour atoms diffuse out of the centre of the plasma beam and vapour ions predominantly return to the surface guided by the magnetic field. Without significant vapour presence, the plasma re-attaches and a new heating cycle commences.

4　Diagnostic development

The development of radiated power diagnostics, a subject which became a goal in itself during the progress of this thesis project, is discussed now. The Design and characterization of an Infrared Video Bolometer (IRVB) for NTSX-U along with a brief introduction to performed research on NSTX/NSTX-U is described first, followed by a discussion of the novel Resistive Bolometry (RB) system developed for Magnum-PSI.

Power loss through radiative processes is foreseen to play a key role in controlling the heat exhaust in future fusion devices [32]. The DEMO divertor should be operated in full detachment in order to mitigate heat fluxes to the divertor materials through radiative dissipation [107]. Liquid metal PFCs can further aid in protecting the wall in case of loss of control over radiative dissipation, and, during VS, by converting the power into photon emission which is spread isotropically. Increased physics understanding of combined radiative phenomena in the SOL, edge and divertor regions is necessary to make meaningful extrapolations from current devices to future power plants. Also, increased diagnostic capability can improve the effectiveness of active control schemes [108, 109], hereby increasing the operational efficiency of future reactors.

In the framework of VS, significant power reduction through volumetric heat dissipation (transport of neutral particles and radiation) is concluded in the previous section. High levels of power loss carried by neutral impurity particles which are subsequently transported to the core region can however be undesirable due to fuel dilution in the case of Li, and, in the case of Sn, due to the risk of excessive Bremsstrahlung losses [61]. The question is what fraction of the target heat flux is converted into radiation during VS and what fraction is lost by neutral particles diffusing to areas away from the strike-point. The latter pathway potentially carries the risk of releasing too many wall-eroded neutrals into the core plasma and may thus limit the effectiveness of VS.

Measuring the amount of radiative power dissipation during VS provides a way to distinguish the neutral particle loss contribution from the radiative loss contribution in the overall power balance. Furthermore, maximizing and potentially controlling the radiated power fraction, possibly by exploiting the frequently proposed non-coronal emission [55–57], can be a key step in using VS to protect the LM surface since it ameliorates the risk of excessive impurity loss from the divertor region. Particularly quantifying the radiation loss term during VS motivated the development of radiation diagnostics within the scope of this thesis work, both for the application on NSTX-U and on Magnum-PSI. The investigation of non-coronal emission for Li was a secondary motivation.

4.1 The NSTX-U device

The National Spherical Torus Experiment Upgrade (NSTX-U) is soon to be resuming operations after an extensive upgrade campaign of its predecessor NSTX [110]. NSTX-U is a medium-sized spherical torus with a major radius of 0.85 m, plasma current of 2 MA and a magnetic field strength of 1 T with a maximum discharge duration of 6.5 s. A key objective of this upgrade is the installation of a second Neutral Beam Injection (NBI) system which should allow for 100 % non-inductive operation at high β levels [111].

NSTX experiments provided many important insights into the application of Li inside MCF devices. Several Li wall coating techniques have been explored since 2006. Coating of its C tiles occurred through the injection of solid Li pellets in Ohmically heated He discharges. The Li released from the pellets is transported along the magnetic field lines and deposited on the divertor targets in this scheme. A porous Mo substrate containing Li positioned at the outer divertor leg, the so-called Liquid Lithium Divertor (LLD) module, was first installed in 2010. The LLD was extended in 2011 with an additional row of lithiated Mo tiles at the inner strike point to perform dedicated studies of Li PFC issues under NSTX divertor conditions [112].

Some of the major accomplishments as a result of Li wall application were the observation of reduced ELM activity, both in number and amplitude, and reduction in the H-mode power threshold [113]. The edge neutral density was found reduced accompanied by increased pedestal electron and ion temperatures and improved energy confinement time [112]. The effective ion charge and radiated power fraction was found increased inside NSTX, notably by increased emission from carbon and medium-Z impurities rather than Li, which fraction remained <0.1 % in the core [50].

In terms of heat flux handling, the peak heat load on the divertor strike-point surface of the LLD was found reduced from 5.5 to 2 $\mathrm{MW\,m}^{-2}$, as a consequence of evaporating a total of 300 g Li prior to the discharges [114]. Bolometry revealed increased localized radiation above the inner and outer strike-points in parallel to a measured reduction of the surface heat flux. When changing from 150 g to 300 g evaporated Li, the bolometric signals in the inner and outer strike point regions were found increased by a factor 4 while the bolometric signal in the private flux region decreased by the same factor [114]. An explanation based on a reduction of MARFE (Multifaceted Asymmetric Radiation From the Edge) activity near the X-point is proposed but could not be confirmed due to limited bolometric coverage of this region. The need for expanding the capability of measuring the movement of the emissive region through the divertor region, with and without the presence of Li, motivated new bolometry tools for NSTX-U.

Further diagnostic possibilities on NSTX-U were explored by developing a prototype IRVB [115] in 2015. Due to its benefit of producing 2D images representing radiated power levels, particularly this type of diagnostic was expected to be useful in plasma studies where non-axisymmetric fields, such as near the X-point region, yield 3D radiation structures. Once NSTX-U commences operations, the IRVB system is foreseen to complement a completely new Resistive Bolometry (RB) system currently under development to study core and edge radiation. Only a brief overview of the IRVB diagnostic is provided below, details of the hardware design and its bench-top characterization are provided in chapter B.3.

4.2   The IRVB system for NSTX-U

The IRVB concept relies on a 2.5 µm thin Pt absorber foil of whose temperature evolution, due to impinging plasma radiation, is measured by an IR-camera (see Fig. 4.26). The temperature distribution along the monitored foil is fed to the time-dependent 2D heat conduction equation from which the absorbed incoming power term can be calculated once the spatially localized thermal properties and emissivity of the foil are known [116]. The concept was first developed for the Large Helical Device in 1997. Such a system has the advantage that several thousand effective lines of sight (LOS) through the plasma volume are achieved while no wiring or feedthroughs across the vacuum interface are required [117]. The latter feature solves the generally encountered issue of electromagnetic (EM) noise of which RB systems, otherwise mechanically robust, are prone. Additional, the IRVB exhibits a lower cost per bolometer channel than conventional systems next to being less sensitive to the nuclear environment [118]. The main drawbacks with respect to a RB system are reduced mechanical robustness due to the large unsupported foil, a higher Noise-Equivalent-Power-Density (NEPD) and the complexity of running an IR-camera in strong magnetics fields [116].

The NSTX-U IRVB is designed to fit on an upper port of NSTX-U, providing a poloidal view of the divertor and part of the centre stack [119]. The time response and sensitivity of the IRVB system was investigated on the benchtop using modulated laser irradiation in order to compare its performance to that of an RB system. The raw IR signal increase divided by the standard deviation of the signal without heat applied (i.e. the Signal-To-Noise-Ratio (SNR)) as function of laser power density is shown in Fig. 4.27a for several different IR camera types used to monitor the foil. The SNR of the RB system, both measured on the tabletop using the laser and previous experimental data from the Alcator C-Mod tokamak [120] (hence influenced by the EM tokamak environment) are shown similarly in the plot.
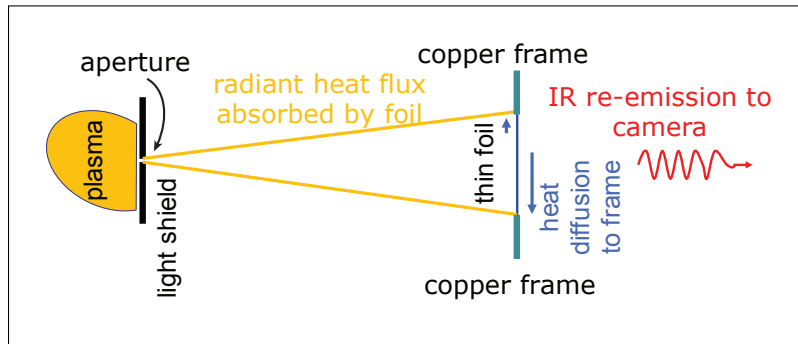
Fig. 4.26 The Infrared-Video-Bolometer principle. *Plasma radiation exposes a thin absorber foil which is monitored by an IR-camera. The incoming power can be calculated from the spatial and temporal temperature distribution.*
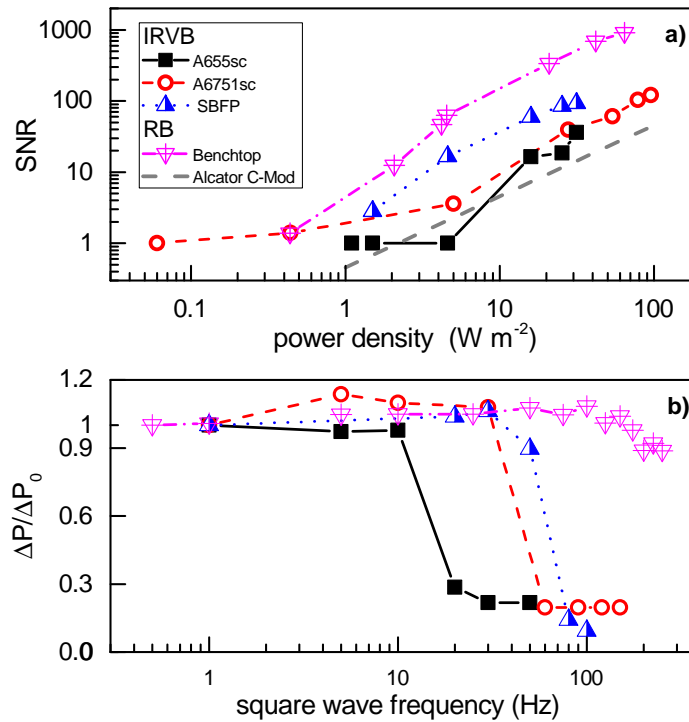
Fig. 4.27 Performance characterisation of the IRVB compared to a resistive bolometer. *Figure appears in chapter B.3. The signal to noise ratio of the IRVB as function of incident power density (a) and time-response characterisation (b) while equipped with IR-camera types as indicated.*

Although a proper calculation of the radiation evolution impinging the IRVB foil requires solving the full heat diffusion equation, its time evolution can be approximated by neglecting spatial heat diffusion. The radiated power absorbed by an area of the foil is then directly proportional to the IR-camera signal (S) or temperature (T) via the relation: $P_{rad} \propto P = S + \tau \partial S / \partial t$, with τ the typical ($1/e$) time constant of the system. This is similar

to the equation for an RB which is always treated as an individual sensor (hence no heat transfer between adjacent channels). The equation of the RB reads $P_{rad} \propto P = V + \tau \partial V / \partial t$, where V represents the bridge voltage. The signal increase (ΔP) is normalized to signal increase at slowest pulse rate (ΔP_0) and plotted against laser frequency in Fig. 4.27b. This ratio should be equal to 1 for constant laser power, if temporally resolved. The frequency at which it falls below 1 is the maximum resolvable frequency by the system. As can be inferred from Fig. 4.27b, IRVB signals up to 50 Hz can be resolved if equipped with the SBF-161 and A6751sc cameras. This is much lower than the tabletop performance of the RB system which is roughly around 200 Hz but high enough to discern between type-I ELM and inter-ELM phases in NSTX-U.

The potential of Li as a radiator in the plasma edge and divertor is of general interest to the NSTX-U team at PPPL. One of the aims set at the start of this thesis work was to use the edge plasma parameter space of NSTX-U as an extension to the Magnum-PSI divertor-like operational space in mapping the radiating potential of Li impurities. Due to technical difficulties of considerable severity, NSTX-U has not been able to realize its planned experimental campaigns in time. It has therefore not been possible to utilize the IRVB system for this tokamak and no plasma data has been taken.
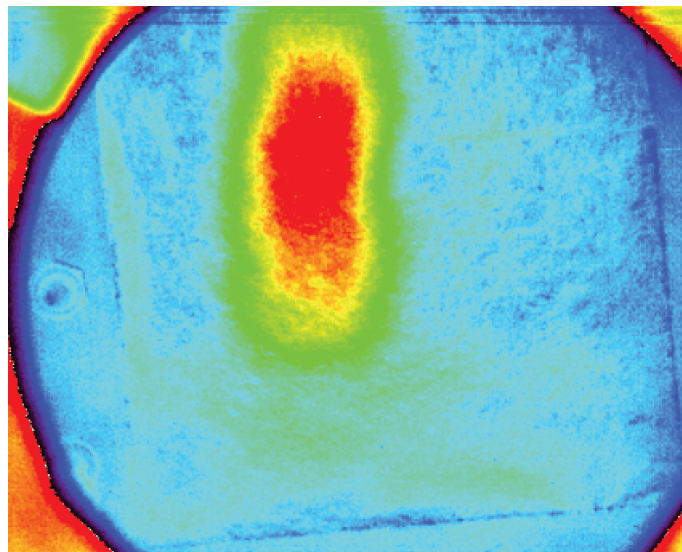
Fig. 4.28 The IRVB foil during plasma radiation exposure in Alcator C-mod. *Courtesy of M.L. Reinke [121]. Picture of the IRVB foil taken by an IR-camera during plasma radiation exposure in the Alcator C-mod tokamak. The colour qualitatively shows the temperature distribution (hot regions in red).*

The prototype IRVB has however been temporarily deployed on the Alcator C-Mod tokamak [122], where, despite not being optimized for, the diagnostic was successful in

qualitatively assessing the radiated power distribution during radiative H-mode operation [121]. The temperature distribution of the foil during plasma exposure is shown in Fig. 4.28 which serves only as a preliminary demonstration of the IRVB's capabilities. The red area in the centre is indicative of increased foil temperature as a result of plasma radiation coming from the core. The foil was not calibrated during this prototype test which prevented it from quantitatively deriving the incident radiated power.

4.3   Radiated power measurements in linear devices

Pursuing dedicated studies of exhaust physics in present MCF devices is difficult given the complexity of controlling plasma conditions and often limited diagnostic coverage due to spatial constraints [123]. Investigations using linear plasma devices can be of importance in finding solutions to this end since conditions are easier to control and plasma-surface interactions can be studied with good diagnostic access [23]. The possibility of doing relevant detachment studies in linear devices has been previously highlighted [124] and is among the key priorities on the experimental campaign of Magnum-PSI.

Understanding the power balance during detachment and possibly linking the reduction of target heat flux to increased plasma emission require a direct measurement of plasma radiation loss $(\mathrm{W\,m^{-3}})$. Similarly, understanding the relative contributions of power dissipation channels during VS motivate measurements of plasma radiation loss in close vicinity of the target (within a few mm from the target surface), which has been lacking so far. Bolometry can also be used to help estimate the efficiency of heating systems. The installation of a bolometry system for the proto-MPEX linear plasma device [125] at ORNL in the US is planned for this purpose, aiming to assess the efficiency of radio frequency heating in this machine. Lastly, measurements of radiation loss in a controlled plasma environment such as potentially available in linear devices is invaluable for benchmarking theoretical models.

4.4   A resistive bolometer for Magnum-PSI

Previous considerations motivated the development of a diagnostic capability of measuring radiated power loss from the plasma in Magnum-PSI. A resistive bolometry system was identified as a suitable candidate for this aim given its approximately constant sensitivity over the plasma photon energy range and due to its superior long-term sensitivity stability as compared to AXUV diodes [126]. The Signal-To-Noise Ratio (SNR) of an IRVB system during benchtop testing was found worse by a factor ~5 compared to resistive bolometry (Fig. 4.27) which makes it, despite improved spatial coverage, unsuitable as a

potential diagnostic on Magnum-PSI where the expected line-integrated brightness was expected to be low due to a combination of a small plasma volume and overall low plasma temperature. The magnitude of emission levels in the Magnum-PSI plasma was modelled using the ADAS [97] Collisional-Radiative-Model (CRM) while taking Thomson Scattering measurements of the plasma parameters as input. Modelling results indicated a capability of measuring plasma emission with SNR>5 which gave confidence in the feasibility of measuring plasma radiation loss in Magnum-PSI using resistive bolometry.

The bolometer for Magnum-PSI has been developed and installed as part of this thesis work and marks the first application of this diagnostic on a linear device. Essential to this diagnostic is a 4-channel resistive foil [127] manufactured by IPT Albrecht, capable of measuring plasma radiated power over a wide energy range with almost unity absorption. This type of sensor is currently planned for use in ITER [128]. Each of the four channels of the Magnum-PSI bolometer detector consist of a 5 μm gold (Au) foil covered with a 150 nm thick aluminium (Al) heat conducting layer. The Au foil is mounted on a SiN membrane (an electrical isolator) which transfers the heat efficiently to a meander-like electrical circuit. The energy carried by radiation incident on the foil is calculated from the temperature-dependent change in the electrical resistance of the meander which is accurately detected using a Wheatstone bridge circuit [127]. Each sensor unit is in principle immune to thermal drifts of the entire detector by design. However, since a temperature change of the foil is detected, the technique is also sensitive to the influence of background neutrals. Especially the effect of possibly high-energetic charge-exchange (CX) neutrals should be considered [129]. This issue is however expected to be reduced in Magnum-PSI where the energies of such neutrals are small ($T_i \approx T_e \lesssim 5$ eV). Active pumping of the background gas [86], including inside the bolometer housing, further mitigates heating of the RB foil due to neutral impact.

Figure 4.29 shows a schematic overview of the resistive bolometer unit mounted the Magnum-PSI. The bolometer channels are viewing the plasma column orthogonally each with a unique view of the plasma beam in the axial direction. The detector is connected to a linear manipulator stage capable of adjusting the radial distance between the detector and the plasma column by 100 mm, hereby creating the possibility of viewing only a radial section of the beam (at reduced signal level due to a narrower solid angle). The schematic drawing (not to scale) in Fig. 4.30 shows the Field Of View (FOV) of the diagnostic in radial (*a*) and axial (*b*) direction. All measurements described here were performed at a distance between aperture and sensor of 72.8 mm. Additional technical details of the resistive bolometer system can be found in the appendix of chapter B.4.
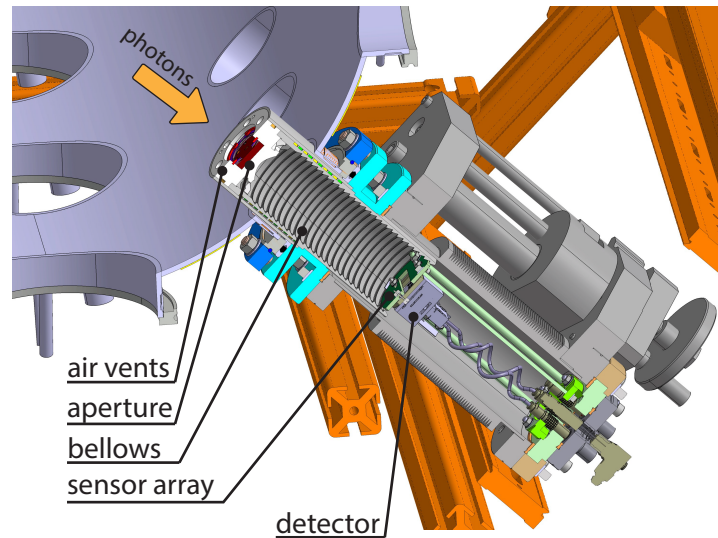
Fig. 4.29 Overview of the resistive bolometry system for Magnum-PSI. *The 4-channel bolometer views the plasma tangentially and is mounted on a linear translation stage by which the distance between plasma and detector can be varied by 100 mm, hereby changing the radial resolution.*

Figure 4.31 shows the absorption efficiency of Pt bolometer sensors as function of wavelength/photon energy experimentally performed by Meister [130], together with the expected absorption based on theory [131]. This characteristic spectral absorbance plot is expected to be similar for the case of a Au foil. Although the absorption is found to be close to unity for a wide range of photon energies, it decreases by >50 % in the visual wavelength range (350-700 nm). It has been pointed out that a significant fraction of the plasma radiation in divertor conditions is emitted at wavelengths >100 nm due to line radiation from incompletely stripped ions [132]. This situation was expected to be even more applicable to the case of Magnum-PSI which overall exhibits a low average plasma temperature containing low-ionized states of atoms [133].

To increase absorption towards lower photon energies of the Pt foils, a thin layer of C (maximally 150 nm) has been deposited on two of the four sensor surfaces by magnetron sputter deposition, while two were left uncoated for comparison purposes. The spectral absorbance of both the coated and uncoated Au sensors are shown in Fig. 4.58. Further details can be found in A.3. A signal increase of 13-15 % in the TCV divertor has been evidenced as result of coating the sensors which demonstrates the effectiveness in divertor conditions [132].

The radiated power incident on a bolometer sensor P_s can be calculated using the measured change of the bridge imbalance voltage ΔU_b using a sensitivity constant (S) and
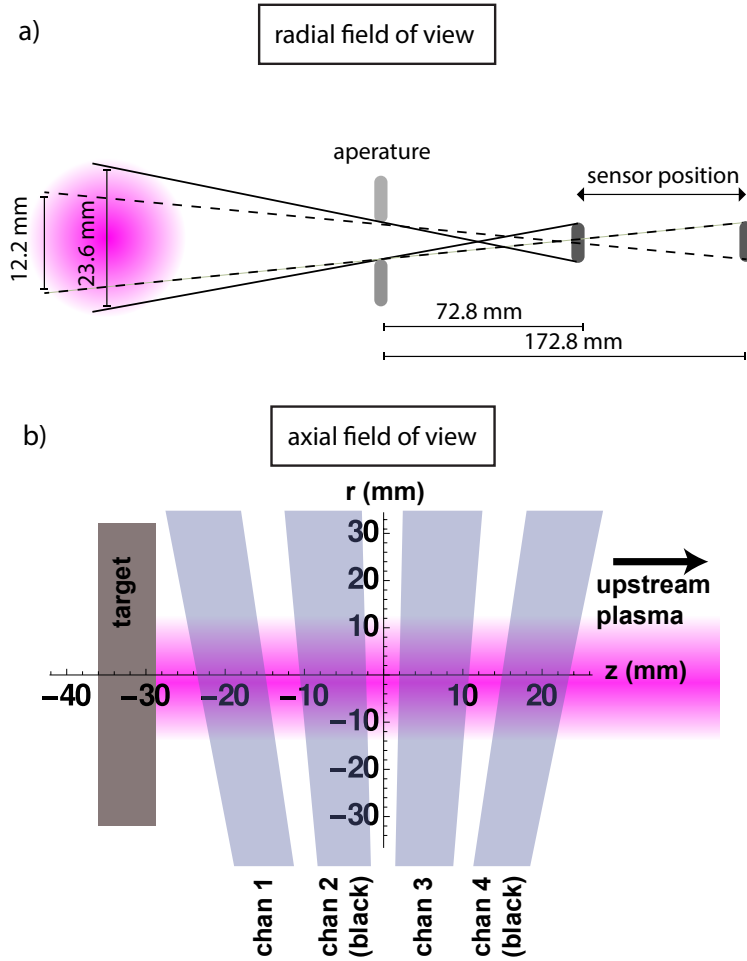
Fig. 4.30 Field of view of the Magnum-PSI bolometer. *Panel a shows the radial field of view of the bolometer channels at closest and farthest position from the plasma. The axial field of view for each of the individual sensors is shown in panel b.*

the typical heat diffusion time τ [134]:

$$P_s = \frac{1}{S}\left(\Delta U_{\mathrm{b}} + \tau \frac{d\Delta U_{\mathrm{b}}}{dt}\right). \tag{9}$$

This expression is a commonly encountered simplification of the complete expression which takes e.g. the cable resistances into account [135]. The line-integrated brightness of the plasma $\int \varepsilon \, dl$ can be calculated from the measured P_s using the aperture size (A_{ap}), sensor size (A_{s}) and the typical distance between the sensor and aperture ($l_{\mathrm{s,ap}}$):

$$\int \varepsilon \, dl = 4\pi \frac{1}{\cos^2(\theta)} \frac{l_{\mathrm{s,ap}}^2}{A_{\mathrm{s}} A_{\mathrm{ap}}} P_{\mathrm{s}} \tag{10}$$
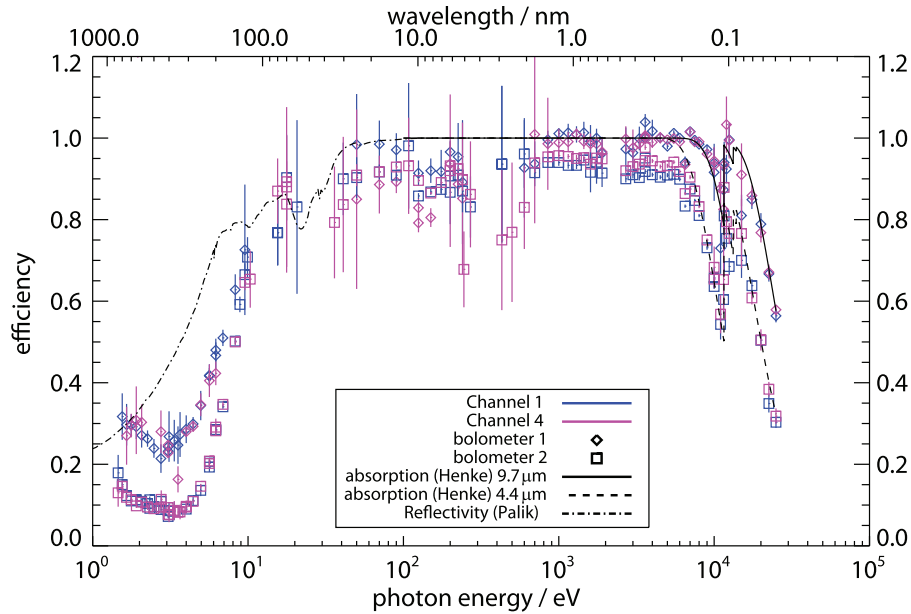
Fig. 4.31 Spectral absorption of Pt bolometer sensors. *Figure from [130] with permission of H. Meister. The bolometer spectral sensitivity is shown in comparison to theoretical absorption data from [131]*

where the calibration constants S and τ have been experimentally obtained as described in chapter B.4. The angle θ represents the deviation of the line-of-sight with respect to perpendicular incidence. Since θ is close to 0 across the detector surface, this factor leads to a variation of <1 % in the current configuration of Magnum-PSI. We have omitted this factor during analysis for simplicity.

The difference in absorption between coated and uncoated sensors is clearly observable in the time-trace of line-integrated emissivity shown in Fig. 4.32 by comparing the levels during steady-state Ar exposure (t=20-150 s). Next, the radiated power from the plasma is seen to change from $10\,\mathrm{kW\,m^{-2}}$ to typically $55\,\mathrm{kW\,m^{-2}}$ resulting from the change from an Ar plasma to a He plasma at higher gas flow rate in the source. If the solid W target is brought close to the bolometer viewing position this influences the emissivity levels due to changing plasma surface conditions in the pre-sheath region alongside an increased density of target-reflected neutrals. This is further discussed in chapter B.4.

4.5 Radiated power measurements during Li CPS exposure

Figure 4.33 shows the line-integrated emissivity ($\int \varepsilon \, dl$) measured by channels 1 and 2 as a function of time during plasma exposure of a Li CPS and a solid TZM reference target.
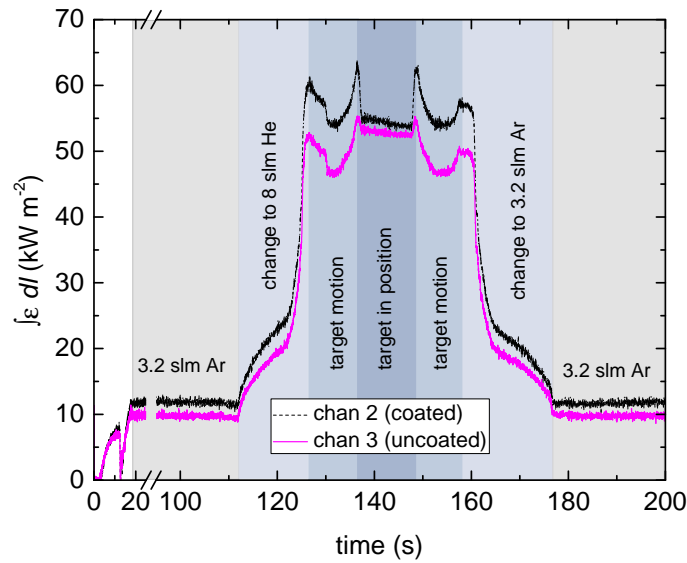
Fig. 4.32 Typical time evolution of plasma radiation in Magnum-PSI. *The change in plasma conditions and gas flow result in changing plasma radiation received by the bolometer. The coated bolometer shows the highest signal level due to increased absorption.*

The target surface in both cases is positioned at z=-20 mm which means that channel 1 is aligned with the plasma-exposed surface while channel 2 provides a measurement of the plasma volume ~12 mm in front of this (see Fig. 4.30b). Similar to the situation
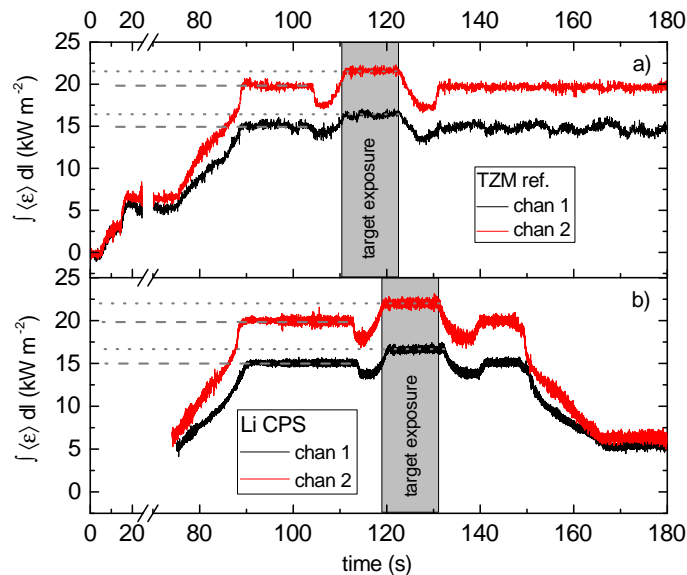
Fig. 4.33 Radiated power measurements during Li CPS exposure. *No enhanced radiated power loss from the near-surface plasma due to presence of Li is evidenced for these exposure conditions.*

shown in Fig. 4.33, the gas is changed from Ar to He during t=75-90 s. The target moves

into position at t=110 s. The radiation levels in the time range of 90-100 s are assumed equal since the operational settings are the same while the target is far away from the bolometer measurement position. As can be readily inferred by comparing panels a and b in Fig. 4.33, no difference in the radiated power loss is measured by either channel 1 (at the target) or channel 2 when comparing the Li CPS to the TZM reference. Hence, for the plasma conditions applied here, no enhanced radiation by Li impurities in the plasma has been detected.

The influence of q_{ref} on potential near-surface emission by Li is assessed now. The bolometric signal received from the near-surface plasma region with presence of a target is subtracted from the case without a target, yielding the parameter $\Delta \int \varepsilon \, dl$ as plotted in Fig. 4.34a. The heat flux in this case is obtained from n_e and T_e (similar to the calculation of q_{ref}) measured close to the source exit, rather than localized near the target. The near-surface emission characteristics of the solid TZM reference target are compared to both a Li CPS and an NSTX-U prototype test module containing Li in a reservoir [105] which penetrates to the surface via capillary action.
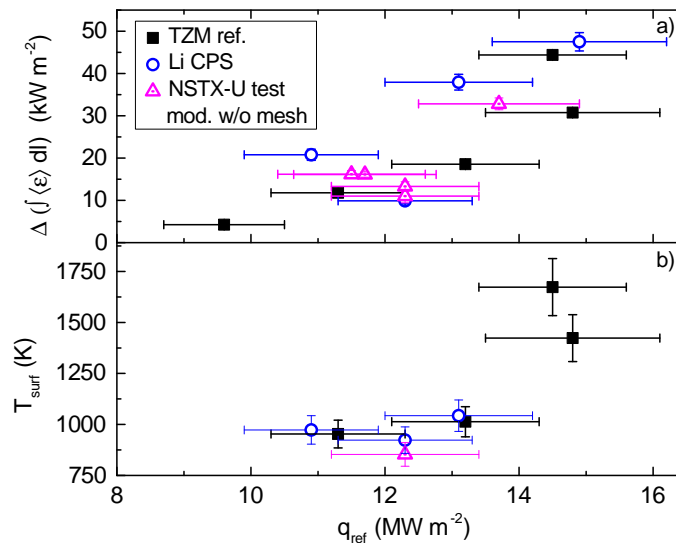
Fig. 4.34 Relative increase in radiated power loss from the near-target region for solid TZM and liquid Li samples. *Panel a shows the increase in plasma emission from the near-surface region as function of q_{ref}. Panel b shows the corresponding surface temperatures for most of the exposures.*

The radiation loss produced in the near-surface plasma is seen to increase linearly with upstream power in the investigated parameter range of 8-15 MW m^{-2}. No clear sign of enhanced near-surface radiation due to the release of Li is found. This result seems unexpected given that clear signs of oscillatory VS due to the presence of Li was

observed using a similar NSTX-U divertor test module exposed to a downstream heat flux of 7-8 $\mathrm{MW\,m^{-2}}$ as shown in Fig. 3.23.

Two points should be taken into account regarding this apparent discrepancy. Firstly, the emission characteristics shown in Fig. 4.34a are plotted as function of upstream heat flux, while it is known that a significant drop of T_e occurs in the plasma beam when comparing target conditions to those at the source. Hence, the calculated q_{ref} drops accordingly which decrease the actual target heat flux. Secondly, the NSTX-U prototype target used during the bolometry measurements comprised of a combination of a textured TZM surface combined with a surface mesh made of Mo. The Li vapour shielding cycles were however observed on a target which contained a mesh without a textured subsurface. It is likely that the surface temperature of the mesh could quickly rise due to a poor thermal connection to its substrate, hence allowing the temperature to increase >1050 K and entering the VS regime.

Panel b of Fig. 4.34 shows the surface temperature of both the Li-containing samples as well as that of the reference, obtained from pyrometry measurements which are emissivity independent. Some of the measurements were below the instrument threshold temperature of approximately 850 K or saturated (when the Li CPS was overheated due to a thermally isolated mesh) and are thus missing. Interestingly, a surface temperature of 1040 K was reached on the Li CPS sample during exposure at q_{ref}= 13.1 $\mathrm{MW\,m^{-2}}$and Γ_{part}=3×10^{24} $\mathrm{m^{-2}\,s^{-1}}$. As can be inferred from Fig. 3.7, this is equal within error to Γ_{evap} and is thus expected to lead to VS which was not observed. The clear sign of oscillatory VS using the Li test module was however preceded by a phase characterized by a much higher surface temperature, which may be necessary to reach a critical Li density in front of the target to initiate the oscillatory behaviour. A phase such as this has not been observed during exposures of the Li CPS. Increasing q_{ref} to elevate its surface temperature proved unsuccessful because the mesh became thermally disconnected, resulting in overheating and subsequent damage of the mesh. No stable thermal equilibrium >~800 K could be achieved. It is hypothesized that voids between the lower mesh layers and the substrate prevented proper conductive cooling to the substrate.

The upstream heat flux distributions during exposures of the reference, Li CPS and NSTX-U test module targets, are calculated from the plasma parameters and consequently approximated by Gaussian functions. Next, the total power in the beam is obtained by performing an areal integration of these analytical functions. Figure 4.35 shows a comparison between the total power in the plasma beam upstream and the target calorimetric power. In agreement with the bolometric measurements shown in Fig. 4.34 and discussed above, the presence of Li in the target is not seen to decrease the calorimetric energy yield.
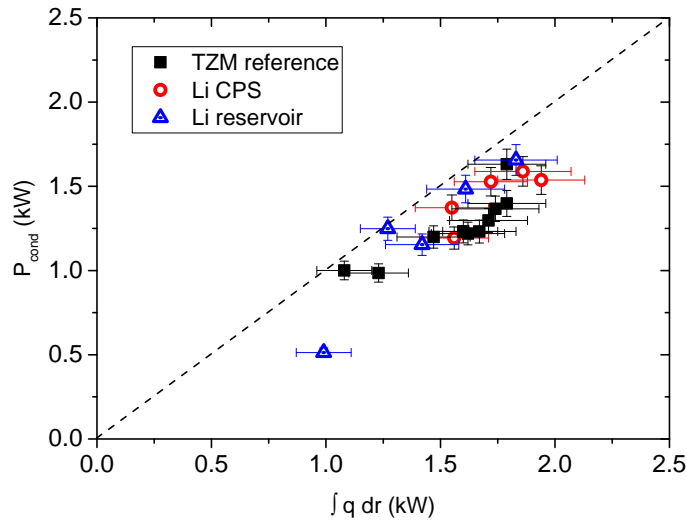
Fig. 4.35 Comparison of upstream power and calorimetry. *The upstream power in the plasma beam is found from a 2D-integration of the Gaussian heat flux profile as function of radius. The conducted power at the target is obtained from calorimetric analysis.*

This is in stark contrast to the reduction of calorimetric power during Sn VS up to levels of 30 %. It is believed that the VS regime for Li is not reached under the conditions as tested here, concluded on both the absence of enhancement radiation by Li and no reduction on the calorimetric energy yield. The question regarding the nature of Li emission (a possible increase in radiated power due to non-coronal processes) could hence not be addressed. Future studies of Li VS in Magnum-PSI using the bolometer setup are expected to shed light on this matter.

4.6 Plasma emission and power balance

Next to radiated power measurements of the near-surface plasma, the characteristic volumetric plasma emission in absence of a surface during steady-state plasma operation was investigated for the purpose of performing simple power balance calculations. The power input efficiency in the cascaded arc plasma source is difficult to quantify and is only performed previously for the case of H [88]. In addition, Ohmic heating of the plasma beam may occur outside of the source, further complicating assessment of the total input power [81].

A simplified picture of power balance in Magnum-PSI is now considered, where energy loss only occurs via radiation along the plasma beam P_{rad} and via transfer to the target P_{tar}. Power loss carried by neutral particles transferring their energies to the machine walls are neglected in this picture. The radial distribution of the surface heat flux $q(r)$ is

calculated using radially resolved values of n_e and T_e [21], measured at the same position as the bolometer FOV. This distribution can be well approximated by a Gaussian function. By using the rotational symmetry of the plasma beam along the centre axis, the total power in the plasma beam transferred to the target is obtained by performing a 2D areal integration of this analytical function, yielding P_{tar} in units of Watts. The total power lost in the form of radiation from the plasma beam can be found from the line-integrated plasma emissivity measured by the bolometer, assuming homogeneous emission over the length of the plasma beam (z_{tot}):

$$P_{rad} = \frac{1}{4}\pi d_p z_{tot} \int \varepsilon \, dl. \tag{11}$$

The typical width of the plasma beam, d_p, is assumed equal to the plasma FWHM. Figure 4.36 shows P_{rad} as function of $P_{tot} = P_{rad} + P_{tar}$ for the gas species Ar, Ne, He and H. The radiated power loss is generally seen to increase with increasing total power in the beam. Radiative loss, at similar input power, is larger for Ar than Ne which is in agreement with increased expected emissivity of the former based on theory.
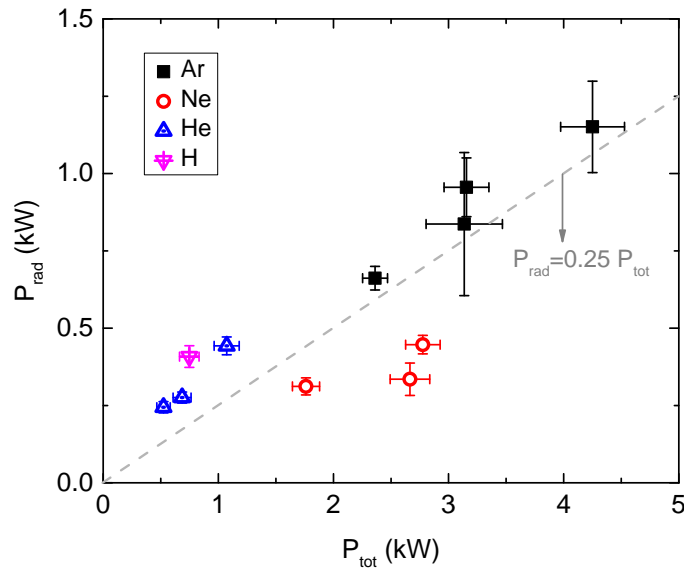
Fig. 4.36 Total radiated power loss from the Magnum-PSI plasma beam. *P_{tot} is defined as the sum of P_{tar}, power transferred to the target, and P_{rad}, the radiation loss term. The emission from the plasma is assumed to be homogeneous along the entire length of the plasma beam for simplicity.*

The measured levels of P_{rad} for the cases of Ar and Ne fall within bounds by a factor 2 and 5 respectively of predicted radiation levels obtained from synthetic diagnostic analysis based using the ADAS CRM [136] (see details in chapter 5). However, the measured levels for He are a factor ~10 higher than expected based on theory. Comparing the H results to

the modelling results is not possible since MAR effects are expected to greatly affect the measured radiation levels which are not accounted for in the model.

The fraction of radiative power loss in the total power balance for the case of He, ~50 %, is also in disagreement with the results shown in Fig. 4.35, where maximally ~20 % of the power is lost when comparing the upstream plasma power to the calorimetric energy yield. It must however be noted that the obtained values for the radiative fraction in the power balance are an overestimation for the following reasons: the relative contribution of P_{rad} decreases once power loss through particle diffusion from the confined region to remote areas are taken into account (which increases P_{tot}) and the measured emissivity value are assumed to be constant as function of z while it is well-known experimentally that the plasma conditions change along z from source to target. Lastly, the FWHM of the plasma beam becomes larger with increased z due to radial diffusion of the plasma particles, which leads to an overestimation of the total radiated power when making the assumption of homogeneous emissivity as function of z.

Improved accuracy of the power balance furthermore requires better knowledge of both the input power at the source and Ohmic heating outside of this, which is beyond the scope of this study. The results presented in Fig. 4.36 should hence be regarded as a rough initial assessment of the power balance which became possible by quantifying the radiated power loss in Magnum-PSI for the first time using bolometry.

4.7 Outlook: an FPGA-based bolometry system for Magnum-PSI

The Magnum-PSI bolometer setup is currently equipped with a conventional analogue electronic processing system from IPT Albrecht [137]. The Wheatstone bridge circuit in each sensor is driven by an excitation voltage (20 kHz, 20 V_{pp}) provided by an amplifier. The bridge imbalance voltage resulting from the resistance change is extracted via AC synchronous detection and subsequent low-pass filtering [127] in the same unit. This technique greatly reduces signal noise commonly present in a tokamak environment. Analogue electronics are however limited in flexibility of use, prone to changes in the electromagnetic environment and commonly seen to produce a drift in the imbalance voltage over time in absence of plasma irradiation. The latter issue is commonly encountered but can often be mitigated by performing a voltage drift correction. It becomes however problematic in the case of Magnum-PSI where radiation measurements need to be executed over very long exposure durations (>>100 s). Radiated power measurements over extended periods of time will also be needed for ITER (discharge duration of 400 s). Hence, the investigation of some of the bolometer system limitations in Magnum-PSI may prove valuable for the diagnostic development applied in future reactors.

A new FPGA-based (Field Programmable Gate Array) system for bolometry analysis has recently been developed [138] by CCFE in partnership with D-tAcq solutions Ltd. [139]. This system is originally developed for MAST-U to perform back-end analysis of bolometry radiated power measurements of the super-X divertor [140]. The attractiveness of this system is that it combines both analogue-to-digital (ADC) and digital-to-analogue (DAC) convertors integrated in a single compact FPGA chip. Signal processing is hence performed fully digital which increases speed and sensitivity at a lower cost per bolometer channel. Given that the hardware is configurable, the sensor excitation frequency can be adjusted in case of environmental interference. Also, the calibration procedure can be performed in-situ lasting only several seconds which is a great improvement to the existing situation where calibration is performed on the bench.

The feasibility of measuring radiated power loss in Magnum-PSI using resistive bolometry has been successfully shown. The current system is now being upgraded, both from the electronic analysis side and its hardware. The installation of a D-tAcq FPGA-based test module, allowing signal processing at 1 MSPS using 16 bits ADCs is planned. The bolometer hardware is being improved by installing a shutter in front of the aperture. Closing the exposure to radiation is needed to re-balance the bridge voltage while background neutrals can still diffuse towards the sensor. The net voltage increase due to radiation only can hence be detected once the shutter is opened. The possibility of frequently re-balancing the sensor in addition to the possibility of executing a 'remote reset' using the FPGA electronics will greatly improve the measurement precision, flexibility and availability of the RB. The sensitivity of the calibration parameters to environmental variation such as a changing background gas pressure can be accounted for in this way. Long timescale radiation measurements will become possible by applying an automated calibration/reset procedure at fixed intervals during the plasma exposure while the shutter is closed, hereby greatly improving the overall diagnostic capability of the Magnum-PSI bolometer.

5 Implications of the work for tokamaks

In this section we attempt to extrapolate our findings concerning VS to conditions expected in a future tokamak divertor. We will also discuss the applicability of this work for a potential LM divertor design.

5.1 Operational temperature window for Sn and Li in DEMO

We concluded that attaining a situation of approximate pressure balance between the plasma and the vapour cloud is necessary in order to reach a state where the incident heat flux is efficiently mitigated by VS, resulting in a situation where the incident heat flux is partially decoupled from the surface temperature. We now consider the feasibility of reaching such a regime for the cases of Li and Sn in a DEMO divertor. The expected divertor strike-point particle flux in the DEMO divertor is similar to the plasma conditions in Magnum-PSI and Pilot-PSI (10^{23}-10^{25} m^{-2}s^{-1}) which means that operating at a very high surface temperature, namely >1850 K, should be considered for the case of Sn (see Fig. 3.7).

The core impurity density is determined by combined transport processes from divertor to SOL and from SOL to core. The impurity rate moving upstream from the divertor surfaces ($\Gamma_{\mathrm{div,loss}}$) is the sum of the sputtering rate and the evaporation rate taking into account the re-deposition fraction R: $\Gamma_{\mathrm{div,loss}} = (1 - R)(\Gamma_{\mathrm{sputt}} + \Gamma_{\mathrm{evap}})$. The magnitude of this term depends on the energy of the incident ions and the local re-deposition rate which is sensitive to the local plasma pressure distribution. The fraction of particles lost from the divertor region as a whole is again heavily dependent on the geometry and plasma transport dynamics.

Full transport modelling of impurities released at the divertor penetrating upstream needs to be performed in order to find realistic numbers on the tolerable impurity release from the LM surface. Work from Poradziǹski *et. al.* using COREDIV simulations [80], where the core and SOL transport equations for plasma and impurities are self-consistently solved, indicate that a total Sn evaporation rate of 0.4-6.2×10^{21} s^{-1} (depending on the coolant temperature), can be sustained without reaching a critical core impurity density. These calculations are based on the DEMO 2015 configuration where the maximum Sn core concentration should remain <0.06 % [80]. The erosion rate can be converted into a rate per unit area using the expected total plasma wetted divertor area in DEMO. The predicted outer target strike-point width in DEMO is roughly 20 cm (conservative) [141], based on an extrapolation of attached regimes in current devices [26] with a peak power flux of ~20 MW m^{-2}. Assuming now an equal strike-point width for the inner- and outer

target, located at r=7 m and r=8.3 m respectively (Fig. 6 in [141]), the total estimated strike-point area in DEMO is 1.9 m^2. The total acceptable Sn erosion flux calculated by Poradziǹski *et. al.* is hence 0.2-3.3×10^{21} m^{-2} s^{-1}.
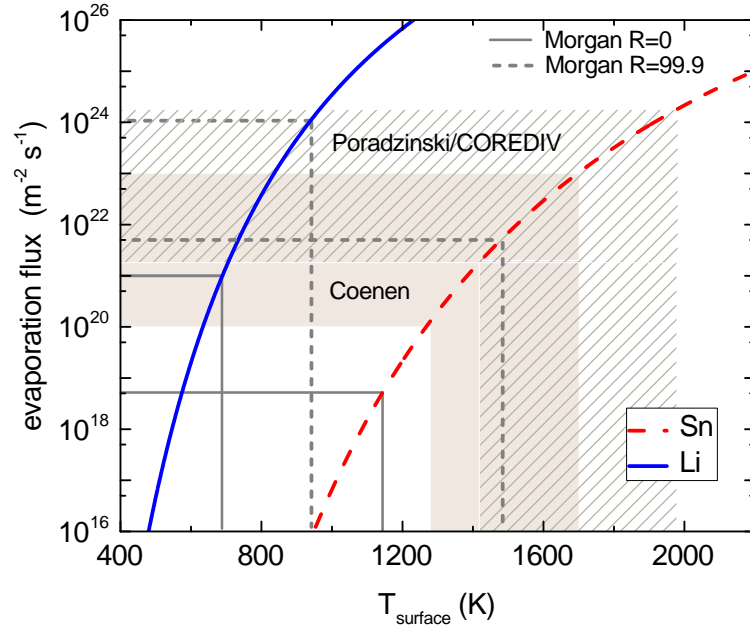
Fig. 5.37 The operational temperature window based on acceptable evaporation limits. *The tolerable limits on evaporation are drawn on the evaporation curves as function of temperature for Sn and Li. Results from DEMO 2015 modelling from Poradziǹski et. al. [80] is shown by the marked area while the pink area indicates the acceptable evaporation range based on impurity radiation losses by Coenen et. al., ranging from R=0 (the lower bound) to R=99.9 (upper bound) [61]. Dashed lines indicate the limits based on impurity influx for the case of R=99.9 (solid line indicates R=0) calculated by Morgan et. al. [142].*

The allowable Γ_{evap} from COREDIV modelling is highlighted by the marked area in Fig. 5.37, showing the temperature/evaporation curves of both Sn and Li. Given the fact that no re-deposition is taken into account (only prompt re-deposition), the erosion limits obtained by Poradziǹski *et. al.* are plotted for the cases of both R=0 (lower bound) and R=99.9 (upper bound), which means 100 % and 0.1 % lost particles. It is clear from Fig. 5.37 that operating at 1420 K is feasible in case of R=0. Interestingly, in the event of a strong re-deposition level of R=99.9, even a maximum surface temperature of ∼1950 K may still be possible.

These modelling results greatly exceed the simple estimation based on the ratio of Bremsstrahlung losses versus the alpha heating power performed by Coenen *et. al.* [61], giving an erosion flux ranging $10^{20} – 10^{23}$ m^{-2} s^{-1} ($R = 0 – 99.9$), depending on the re-deposition rate. Morgan *et. al.* approximates the tolerable erosion rate by relating the

core concentration to the impurity influx under typical DEMO conditions, finding ~ 5×10^{18} m^{-2} s^{-1} for Sn and ~ 1×10^{21} m^{-2} s^{-1} for Li assuming no re-deposition to occur. The results by Coenen *et. al.* and Morgan *et. al.* for R=0 and R=99.9 are indicated in Fig. 5.37 by the shaded area and lines respectively. The temperature range from the simpler models do not account for (temperature-enhanced [143]) sputtering.

5.2 Steady-state vapour shielding in a DEMO divertor using tin

We conclude from the previous considerations that, based on COREDIV simulations, a state where the plasma pressure is balanced by the vapour pressure could potentially be achieved for liquid Sn in a conventional divertor geometry. The re-deposition fraction is found to be a key parameter in this: a liquid surface temperature >1850 K can potentially be sustained by virtue of an extremely high re-deposition fraction >99 %. Although appearing to be high, this number may be reached in the high flux region of the divertor where plasma entrainment can be strong. A re-deposition fraction larger than 99 % of Sn, Mo and Cu elements, in cases of the highest plasma particles fluxes, has recently been concluded from experiments performed in Magnum-PSI [46]. The re-deposition fraction in this study was found to scale upwards with plasma particle flux and density which is promising for Sn in a divertor. Another way to extend the operational temperature window can be found in considering a different divertor geometry where better confinement of the impurity content can be realized. An example of this is the vapour-box concept proposed for Li which uses a series of baffled chambers at different pressures and temperatures [45].

Although potentially feasible in view of plasma compatibility constraints, engineering limits are likely to prohibit a liquid Sn surface temperature >1850 K. This temperature is likely to be too high to apply in connection to a steady-state cooling scheme. Finding adequate porous substrate materials that are resistant to corrosion at such temperatures for a significant duration is very challenging [144]. Particularly W turns out to be the best substrate material because of its low-corrosion properties and low solubility in Sn (0.001 at% at 2273 K [61]), but the question of how this evolves at extended periods of time would need to be addressed.

Despite considerable engineering constraints, protecting divertor PFCs by Sn VS in a conventional divertor design can be found in mitigating 'slow transients' [145], which are excursion of the exhaust power far beyond the nominal stationary heat flux of ~10 MWm^{-2} lasting several seconds. Such events may be hazardous for solid PFCs where this can be a starting point for the accumulation of damage [146]. Uncontrolled erosion of the LM may be acceptable in the case of slow transients since the overall divertor sub-surface can be protected. If the lost LM material can be replenished on fast timescales

and if the VS phenomenon as described is similarly effective on fast timescales (ms), the divertor may be protected similarly to disruptions, Vertical Displacement Events (VDEs) or unmitigated ELMs.

5.3   Steady-state vapour shielding in a DEMO divertor using lithium

In contrast to the case of Sn, Li is a material where the vapour pressure of the LM PFC can be of the same magnitude as the divertor plasma pressure in stationary conditions. Lithium exhibits a much larger vapour pressure (Fig. 3.7) than Sn and is more benign to the plasma which makes that a much larger impurity content can be accepted in the plasma without impeding performance. As can be inferred from Fig. 5.37, the approximate estimations by Coenen *et. al.* and Morgan *et. al.* reveal a possible temperature window of 600 K (R=0) to 850-950 K (R=99.9) for Li, again based on evaporation only.

The heat flux reaching the DEMO divertor PFCs should remain below 5-10 MWm^{-2} by engineering limits, similar to the case of ITER [147]. Also, the plasma temperature in the divertor should be <5 eV in order to limit excessive erosion [147]. Considering now a Li-based CPS surface facing the plasma, reaching a relatively high surface temperature of ~900 K should be possible, which means that entering the regime of continuous (oscillatory) VS is likely to be feasible for the case of Li. The physics of Sn VS as described in this thesis may hence be viewed as a proxy for the case of Li, which is believed to be highly similar as described earlier.

Since the VS oscillations are ultimately caused by the interaction of systems characterized by widely different timescales (atomic physics versus the thermal diffusion time of the PFC), this phenomenon may also be expected in a Li-CPS based divertor during steady-state VS. The near-surface plasma can be cooled by ionization of the evaporated Li atoms followed by ion-neutral energy loss. It is pointed out by Goldston *et. al.* [45] that reaching a detached plasma state by means of impurities from the wall may aid and/or replace the need for conventional divertor detachment. Our work shows that this detached state is oscillatory by nature once the plasma-vapour equilibrium point is reached.

5.4   Comparison of the geometry between a linear device and divertor

A number of differences between plasma exposures in the Pilot-PSI and Magnum-PSI linear devices and a conventional tokamak divertor should be kept in mind in order to extrapolate our findings. A schematic overview of both geometries and the direction of important parameters are shown in Fig. 5.38.
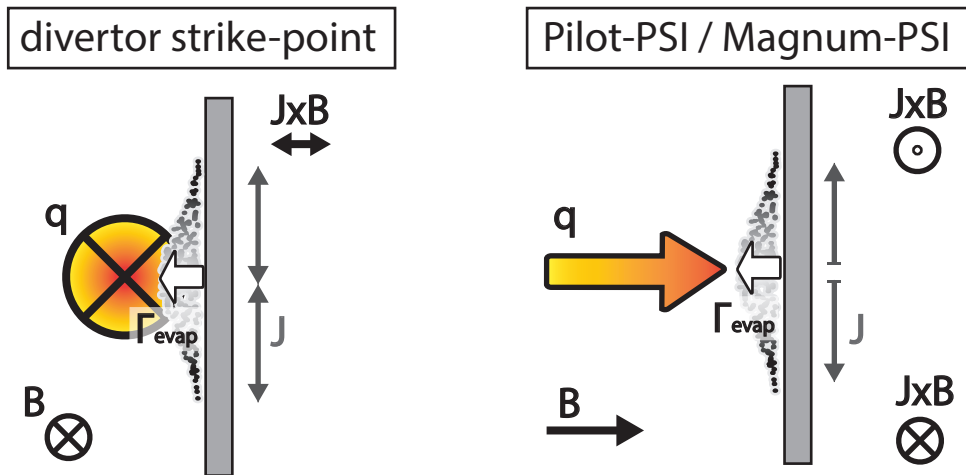
Fig. 5.38 Geometry of plasma exposure in a divertor versus Pilot-PSI/Magnum-PSI. *The orientation of the plasma heat flux (q) with respect to the divertor strike-point, alongside the direction of the magnetic field (B) and plasma-induced currents (J) leading to **J** × **B** driven flow (l.h.s.). The target orientation with respect to the plasma heat flux and other parameters in Pilot-PSI and Magnum-PSI (r.h.s.).*

As can be seen, the inclination angle of the magnetic field with respect to the target surface is extremely small in a divertor (just above 1-2 degrees for DEMO [147]) while it is orthogonal to the target surface in our linear devices. The direction of the plasma flow in a divertor is consequently at grazing incidence to the strike-point surface which is expected to affect the physics of VS. Particles which are thermally released from the surface are predominantly ejected perpendicularly to the liquid surface, hence orthogonal to the divertor plasma flow. In a linear device, evaporated impurities are entrained in the plasma flow directed towards the target surface by ion-neutral collisions, opposite to their thermal motion.

A toroidally symmetric heat flux reaching the divertor strike-point is however still expected to result in sufficient local vapour pressure to balance the plasma pressure. The entrainment effect disperses the impurities along the toroidal direction of the strike-point surface in such a way that the local heat flux is mitigated by particles which are eroded some distance upstream. Cases of a toroidally asymmetric heat flux may result in a somewhat reduced effectiveness of VS in the divertor. The evaporated impurities still provide cooling of the plasma as described by an 'ion energy cost' approach [74, 45] but the regime where plasma cooling is dominated by ion-neutral relaxation may be slightly more difficult to reach given the locally reduced neutral pressure. More research into

VS with CPS surfaces at grazing incidence should be performed to shed light on these concerns.

Secondly, the direction and magnitude of electric currents in the plasma are likely to be different in a tokamak divertor, hereby affecting LM flow differently. Local differences in the ion- and electron fluxes reaching the surface can give rise to electric currents in the LM PFC [148]. This is particularly expected during detached plasma conditions where T_e at the divertor strike-point may be lower than outside of this region [31]. Resulting currents in the LM are oriented parallel to the divertor surface (poloidal) and may induce $\mathbf{J} \times \mathbf{B}$ driven flow perpendicularly to the CPS surface (i.e. pushing the liquid deeper in the CPS or opposite), due to the presence of a strong toroidal magnetic field. This effect should be taken into account when calculating the minimum pore size to stabilize the liquid in a CPS [95].

Lastly, the cooling capability of the liquid surface, particularly set by thermal gradients along interfaces such as between the liquid and the container may be very different in a LM divertor design compared to our samples. As is described in section 3.6, the surface cooling rate affects the size and frequency of the temperature oscillations during steady-state VS which are thus ultimately set by the engineering design.

Concluding, the application of the VS effect in order to mitigate the plasma heat flux in a LM divertor region requires substantial changes to conventional designs, most importantly due to restrictions on the allowable impurity influx from the wall and the direction of the plasma flow with respect the strike-point surfaces. The latter issue can be resolved by increasing the angle of incidence but this increases the areal power density. It has been shown that the current engineering limits on the tolerable surface heat flux of 5-10 MWm^{-2} in DEMO can however be increased to ~20 MWm^{-2} using a monoblock design equipped with a Sn CPS surface [149], in agreement with our experiments in linear devices up to 22 MWm^{-2}. Increasing the temperature window while ensuring plasma compatibility is likely to be possible in an alternative (closed) divertor geometry where a larger density of impurities can be accumulated close to the strike-point. A state of impurity-induced detachment which aids in mitigating the plasma heat flux by power dispersion may be attainable in this case.

6 General conclusions

A summary of the main conclusions in conjunction with the fundamental research questions stated in section 2.1 is provided below.

- **Can vapour shielding be clearly demonstrated using liquid metals in linear devices?**

  – A liquid tin surface embedded in a capillary porous structure, exposed in the linear plasma device Pilot-PSI to heat fluxes ranging 1-22 $\mathrm{MW\,m^{-2}}$, has been found self-regulatory in mitigating the plasma heat flux through vapour shielding, if conditions are such that the vapour pressure is approximately equal to the plasma pressure. Once in equilibrium, any increase in heat flux reaching the surface induces additional evaporation which cools the near-surface plasma. As such, a quasi-static equilibrium can be achieved where the surface temperature of the liquid metal appears to be decoupled from the plasma heat flux. A reduction in the conducted power fraction by 1/3 was found for the case of liquid tin compared to a solid reference, explained by an increased fraction of volumetric power dissipation in the overall power balance.

- **Can the underlying physical mechanisms behind continuous vapour shielding be identified?**

  – In the case of liquid tin, the plasma temperature in the vapour cloud is found reduced to 0.5-0.8 eV independent of the plasma heat flux. The cool-down is effectuated by, initially, ionization of evaporated tin atoms followed by elastic collisions between cold tin neutrals and plasma ions when the vapour density becomes high enough. The electrons are cooled by energy exchange with the plasma ions rather than with tin ions, in addition to inelastic collisions with tin neutrals producing line radiation. The plasma becomes recombining upon interaction with the vapour cloud, hereby releasing more neutrals which further promote cool-down and recombination. An impurity-induced detachment state leading to pressure loss of the plasma is hence reached, greatly reducing the heat flux reaching the liquid metal surface.

  – Vapour shielding is found to be oscillatory by nature, if the vapour pressure/plasma pressure point is surpassed. The vapour cloud size, near-surface plasma parameters (n_{LM}, n_{e}, T_{e}) and temperature of the liquid metal surface

are found to oscillate in correlation to each other. This phenomenon is experimentally observed for both liquid tin and liquid lithium surfaces and is believed to be in essence applicable to other metals and understood to be independent of target geometry.

– Oscillations are triggered once a critical amount of liquid metal impurities are accumulated in the near-surface plasma and are a consequence of mutually interacting systems operating at widely different characteristic timescales: plasma physics effects ($\sim\mu$s) in correlation with the the thermal diffusion timescale of the plasma facing component ($\sim$ms).

- **What is the potential of liquid metal vapour shielding in mitigating the plasma heat flux in a divertor?**

  – Exploiting vapour shielding leads to increased control over the liquid metal surface temperature in addition to larger damage tolerances, hereby self-limiting impurity release through evaporation. This is promising for use in a divertor. At high re-deposition conditions (>99 %), plasma operation with liquid tin divertor surfaces at temperatures >1850 K, where steady-state vapour shielding is found effective, is concluded to be compatible with core plasma operation. However, the very high surface temperature required is likely to be unpractical or even impossible at extended durations due to engineering constraints. The application of tin vapour shielding is deemed promising in protecting the divertor during slow transient events, or potentially during disruptions, Vertical Displacement Events or large Edge-Localised-Modes which would damage solid components, if it can be shown that this phenomenon is also present on fast timescales.

  – By virtue of extremely high re-deposition rates (99.9 %) and/or a closed divertor design, excessive ingress of impurities to the edge and core plasma can be limited, hereby increasing the operational temperature window of liquid tin in a divertor. Research in magnetic confinement fusion devices is required to assess the real liquid metal erosion flux which can be sustained, as it is greatly influenced by the local re-deposition rate which is difficult to model. This ultimately sets the effectiveness of vapour shielding in protecting liquid metal plasma facing components.

  – Steady-state vapour shielding is expected to be a promising mechanism in protecting a lithium capillary porous structure plasma facing component which

is found to be compatible with divertor operation. The lithium surface temperature is greatly reduced during steady-state plasma exposure compared to a solid reference surface, similar to the case of Sn. This is likely to reduce the cooling requirements for a divertor design.

- **Can the radiated power fraction directly be measured in a Magnum-PSI using bolometry?**

  – The radiated power loss in Magnum-PSI could be successfully quantified using a resistive bolometry system, confirming previous emission calculations using a collisional radiative model. The bolometer is designed, characterized and integrated in the diagnostic suite of Magnum-PSI over the course of this thesis project and marks the first application of this sort on a linear plasma device.

  – The location of the target is found to affect the radiated power loss significantly which is explained by emission from recycled neutrals. The volumetric emissivity of the plasma in Magnum-PSI is furthermore found to be a linear function of the plasma particle flux.

  – Approximate power balance measurements revealed 15-27 % total radiated power loss from the Magnum-PSI plasma beam for inert plasma species (He, Ne, Ar). Further use of the bolometer is found in measuring increased emission levels during e.g. detachment studies and vapour shielding.

- **What is the radiated power fraction in the power balance during vapour shielding and what is the nature of this emission?**

  – The Magnum-PSI bolometer has been successful in measuring radiation loss in front of a liquid metal surface. However, no enhancement of the near-surface radiation due to the presence of lithium is evidenced for the lithium exposures conducted as part of this thesis work. This result is explained by the absence of vapour shielding for these cases, due to the limited surface temperature reached. The absence of increased radiation loss from the near-surface plasma is in agreement with calorimetry measurements. It must be noted that bolometry was not available during the exposures indicative of strong lithium vapour shielding using the NSTX-U prototype lithium module. The magnitude of radiation loss in the vapour shielding power balance (to distinguish mass loss from radiation) could hence not yet be addressed.

  – Following from the previous point, the potential benefit of exploiting non-coronal emission from lithium impurities during vapour shielding could not

be investigated up to this point. This question should be addressed in the future.

Summarizing, the problem of coping with the tremendous heat exhaust hitting material walls in nuclear fusion reactors is a major obstacle on the development path of fusion as a viable energy source. The interaction of such plasma conditions with a material wall is an unprecedented engineering challenge which involves physics of considerable complexity. This is particularly the case when considering liquid wall materials which otherwise feature beneficial properties which may aid in progressing towards the ultimate solution. The creation of a dense layer of neutrals in front of a liquid metal surface brings forth a situation where all possible states of matter are aligned, naturally evoked through energy dissipation by self-regulation. The plasma carries a high energy density which is gradually reduced by conveying this energy to particles carrying kinetic energy and converting the energy into photons, both dispersing the power over a much larger volume. The resulting energy transferred to the liquid and solid materials are consequently much reduced compared to the case where the gas and liquid phases are insignificant players in the chain of energy transfer. The increase in power handling and damage tolerances of liquid plasma facing components compared to their solid counterpart are found promising. It is therefore of great importance for this solution to be further researched, in order to make comparisons based on their respective performances while operational in fusion reactors.

Part B

Publications

1   Self-regulated plasma heat flux mitigation due to liquid Sn vapour shielding

G.G. van Eden, T.W. Morgan, D.U.B. Aussems, M.A. van den Berg, K. Bystrov, and M.C.M. van de Sanden

Abstract - A steady-state high-flux H or He plasma beam was balanced against the pressure of a Sn vapour cloud for the first time, resulting in a self-regulated heat flux intensity near the liquid surface. A temperature response of the liquid surface characterized by a decoupling from the received heating power and significant cooling of the plasma in the neutral Sn cloud were observed. The plasma heat flux impinging on the target was found to be mitigated as heat was partially dissipated by volumetric processes in the vapour cloud rather than wholly by surface effects. These results motivate further exploration of liquid metal solutions to the critical challenge of heat- and particle flux handling in fusion power plants.

1.1   Introduction

Designing an efficacious interface between an intense plasma flux and a solid material has been a challenge for many decades and is among the top issues in realizing fusion energy as a viable energy source on Earth. Plasma-solid interactions under fusion divertor conditions cause continuous material erosion and may result in performance degradation of the plasma facing components [150, 145, 41]. An alternative path is opened by exploiting liquid metals as an interface between the plasma and solid material world [47], which can potentially alleviate many of the problems of heat exhaust in the divertor. Understanding the unique power loss channels of liquid metals in contact with a plasma is also highly relevant for other applications such as metal-arc welding [151].

Additional power handling capabilities such as evaporative cooling [152, 59] and the vapour shielding effect [71, 153] are inherently available for a liquid surface. The meaning of vapour shielding encompasses several physical processes. Firstly, the presence of a neutral cloud in front of the target is foreseen to absorb power by excitation and ionization of its species. Subsequent radiation occurs isotropically which reduces the areal power

density. Secondly, the cloud of neutrals leads directly to mass transport losses but also to friction and recombination of impinging plasma particles, ultimately reducing the energy flux to the surface.

In this letter, for the first time, we provide experimental evidence of steady-state vapour shielding at fusion divertor relevant plasma heat- (0.5-22 $\mathrm{MW\,m^{-2}}$) and particle fluxes ($>10^{24}\,\mathrm{m^{-2}\,s^{-1}}$). In addition, the experimental validation of using Sn for high heat flux applications as previously predicted by modeling [61] is now provided. The work was motivated by the question of what the potential of vapour shielding is in protecting a surface. To ensure a vapour pressure of similar magnitude as the plasma pressure, the Sn targets were intentionally badly cooled. The power handling characteristics of liquid Sn were compared to those of solid Mo (high heat handling capability and substrate material for Sn) while exposed to similar plasma conditions and target cooling in the linear plasma generator Pilot-PSI [87].

The thermal response of the liquid upon receiving an intense plasma heat flux up to 22 $\mathrm{MW\,m^{-2}}$ lasting 5-20 s is described. A self-regulated plasma heat flux mitigation by the liquid/vapour system and cooling of the electrons in the vapour cloud is observed, leading to an approximately 30 % reduction in heat flux measured by calorimetry, compared to a solid Mo target. Up to 20 % of this missing power could be associated with evaporative cooling whereas >80 % is dissipated via other processes, including radiation from the plasma and cooling and recombination of the plasma due to the vapour cloud.

1.2 Methods

The linear plasma device Pilot-PSI [87] employs a wall-stabilized thermal arc source [88] to produce a high-flux plasma which is subsequently confined into a beam by an axial B-field (0.4-1.2 T). A power scan of the source resulted in H or He particle- (Γ_{part}) and heat fluxes (q) of 0.9-6.4$\times 10^{24}\,\mathrm{m^{-2}\,s^{-1}}$ and 0.5-22 $\mathrm{MW\,m^{-2}}$ respectively impinging on the target centre. The particle- and heat fluxes as function of the plasma beam radius can be well represented by a 2D Gaussian function (FWHM$\approx$10.4 mm). The values were calculated based on the plasma parameters 11 mm in front of the solid Mo target obtained from Thomson Scattering (TS) measurements [154]. Heat fluxes were calculated as in [21] assuming $T_{\mathrm{i}} \approx T_{\mathrm{e}}$ (the source produces a thermal plasma), that flow was adiabatic with an isotropic pressure and that the sheath heat transmission coefficient was set equal to 7.

As TS was not available, the upstream plasma conditions during Sn exposures have been assessed from reference shots on Mo, where we assume that the upstream plasma power should be highly similar for both targets. This is justified as the I-V characteristics of the plasma source were similar for discharges on Mo and Sn targets and no traces of

Sn were found in the vicinity of the source after operation. Also, the mean free path of the Sn neutrals (6 mm) is much shorter than the distance to the plasma source (560 mm). The incoming heat flux which must be balanced by heat removal processes in equilibrium conditions is therefore the reference heat flux (q_{ref}) which is the measured heat flux received by a Mo target for identical Pilot-PSI operational settings.

A 2-channel spectrometer (Avantes ULS2048) was used to measure the radiation intensity in the 299-579 nm range. The detector was focused at the target centre (~15 degrees normal to surface) with a spot size of 1 mm. The surface temperature was measured using both an IR camera (FLIR SC7500MB, 4.5 kHz) and a multi-wavelength spectropyrometer (FAR associates FMPI). A temperature-dependent emissivity was applied, previously obtained by comparing the IR and pyrometer data. We assume that any IR emission from the vapour cloud itself is negligible as its density is 8 orders of magnitude lower than that of the liquid. Finally, Sn neutral emission was recorded by a fast visible camera (Phantom V12, 10 kHz) equipped with a 452.5 nm SnI filter positioned tangentially to the target. The targets consist of a 3 mm deep Mo cup where the Sn content is held secured by a stack of W meshes, see Fig. 1.39. This design is based on the capillary-porous-system (CPS) principle [94].
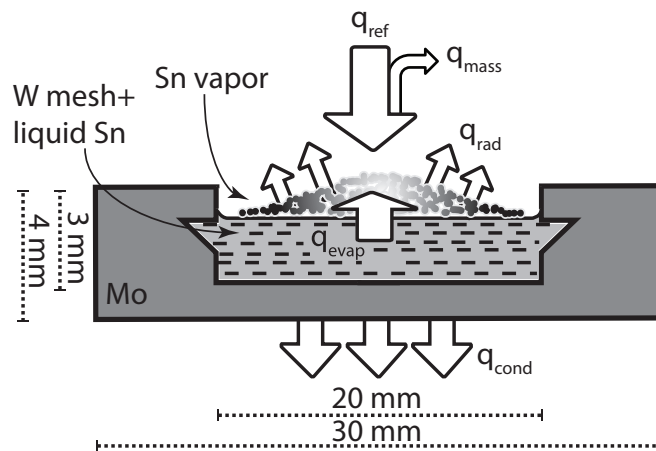
Fig. 1.39 Cross-section drawing of the Mo CPS target filled with Sn. *Sn is held in place by a W mesh structure. The Sn surface receives a plasma heat flux (q_{ref}) which leads to evaporation and subsequent vapour formation in front of the target. The power is dissipated via evaporation and direct mass transport (q_{evap}), radiation by the Sn vapour cloud (q_{rad}) and mass transport resulting from CX and recombination processes (q_{mass}). The remaining heat is conducted to the cooling water (q_{cond}).*

The plasma heat flux (q_{ref}) is dissipated via a number of processes. Firstly, power is dissipated by vaporization if evaporated neutrals do not return to the surface (q_{evap}). Secondly, power is lost by radiation of Sn neutrals and ions in the vapour cloud (q_{rad}) and

mass transport (q_{mass}) from the plasma as a result of Charge Exchange (CX) and recombination processes. The remaining heat is transferred to the Mo cup (and subsequently cooling water) via conduction and convection of the liquid Sn (q_{cond}). Only low ionization stages of Sn are reached due to the low temperature in the plasma beam. Ionization to much higher states is expected in a tokamak, which may affect Sn transport and the heat handling scheme for that geometry.

1.3 Results and discussion

Figure 1.40 shows the temperature evolution at the centre of the liquid Sn and solid Mo surfaces while exposed to $q_{ref} = 16\,\mathrm{MW\,m^{-2}}$. Notable differences in thermal response are observed. Firstly, an approximately steady-state surface temperature is reached after ~0.5 s on the liquid surface while the Mo temperature still rises. Secondly, the temperature ramp in the Sn case does not follow a conduction-based cooling curve, where the temperature increases following Newton's law of cooling until the conducted heat equals the received plasma heating as for the Mo case. Results from 3D finite element modeling using ANSYS [155] for the same q_{ref} and target materials are shown as well. The mesh has been accounted for in the model for Sn by assuming a 6.25 weight percent of W and applying thermal properties of the mixed material. Only conduction-based cooling has been taken into account and the absorbed heat by the cooling structure has been modeled to match the experimental results for Mo. Comparing the model with the experimental data for Sn, a reduction of ~700 K compared to expectations at the end of the discharge is observed which indicates the presence of additional heat dissipation channels for the liquid. It should be noted that the conduction based model predicts a higher surface temperature for Sn than Mo due to the lower thermal conductivity of the former. The experiment shows however a lower final surface temperature for Sn compared to Mo which gives a clear demonstration that other power loss processes are important.

Figure 1.41 shows the central surface temperature at the end of 20 s plasma discharges for both sample types as a function of q_{ref}. It is striking to see that the surface temperature of the liquid Sn is almost independent of the applied heat flux. The final temperature at the solid Mo target increases with rising plasma power as expected. The data point for Mo at $22\,\mathrm{MW\,m^{-2}}$ represents the temperature after a 5 s discharge (to avoid melting the target) and did not reach an equilibrium temperature.

The magnitude of Γ_{part} versus the evaporation flux is assessed now. The vapour pressure (p_v) as function of surface temperature (T (K)) is calculated as in [84]: $\lg(p_v) = 10.268 - 15332/T$. The flux of particles leaving the surface by evaporation (Γ_{evap}) at a temperature T (K) is assumed to follow from the Langmuir evaporation law [156],
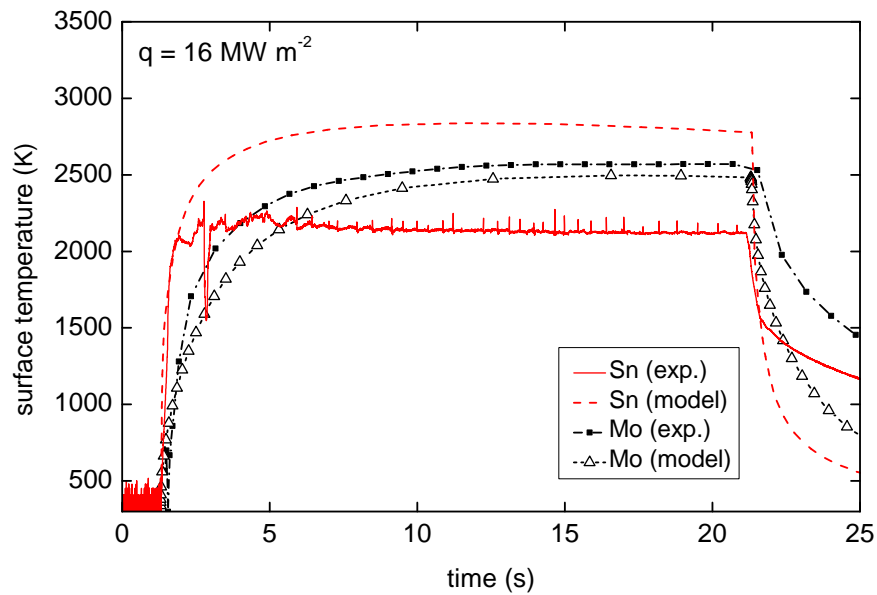
Fig. 1.40 Temperature evolution of liquid Sn surface temperature. *A comparison of the central surface temperature of liquid Sn and solid Mo during experiment and ANSYS simulations for q_{ref}=16 MW m^{-2}. The steady-state temperature of Sn reduces significantly due to vapour shielding compared to the conduction-based model without vapour shielding.*
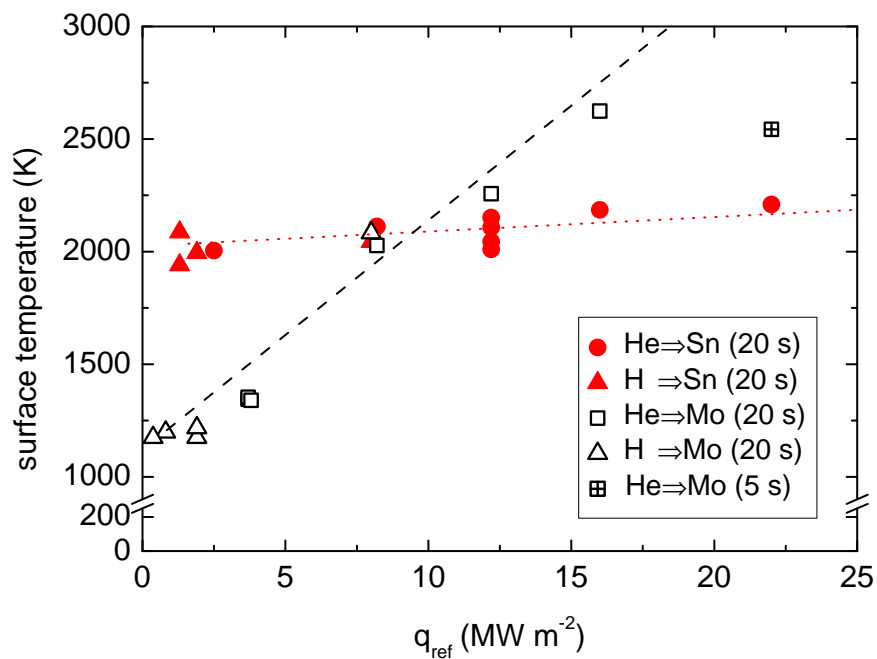
Fig. 1.41 Liquid Sn surface temperature as function of heat flux. *Temperature of the target surface centre after 20 s of plasma exposure for liquid Sn and solid Mo. The lines are drawn to guide the eye. The surface temperature of liquid Sn is almost independent of q_{ref} for the given parameter space. The data point for Mo at 22 MWm^{-2} had a 5 s shot duration to prevent melting the target.*

$\Gamma_{\text{evap}}(T) = p_{\text{v}}/\sqrt{2\pi m k_{\text{B}} T}$, where k_{B} represents the Boltzmann constant and m the mass of Sn (kg). Fig. 1.42 shows Γ_{evap} (calculated using the temperatures as shown in Fig. 1.41) versus Γ_{part} in the beam centre. It is clear from this Fig. that Γ_{evap} increases linearly
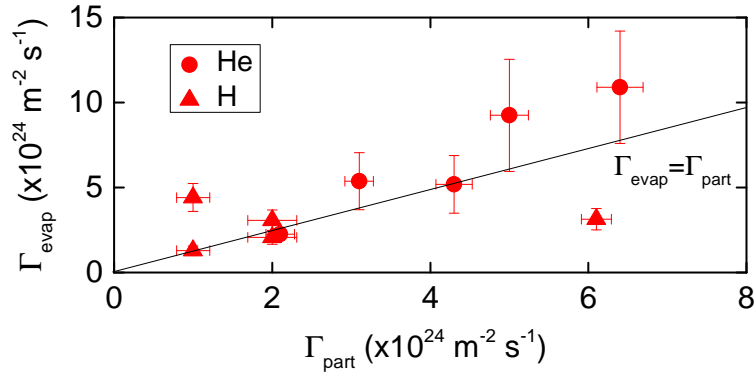
Fig. 1.42 Balance between evaporation flux and plasma particle flux. *Evaporation flux (Γ_{evap}) versus the plasma particle flux (Γ_{part}) in the centre of the beam for He and H discharges. The solid line represents a perfect equilibrium between plasma- and evaporation flux.*

in proportion to Γ_{part} for all He discharges and roughly follows $\Gamma_{\text{evap}}=1.6\times\Gamma_{\text{part}}$. The Sn evaporation flux during H discharges is seen to remain approximately at the same level. It is proposed that because of the lower mass of H compared to He, the former is affected more strongly by momentum loss via collisions with Sn, therefore resulting in a lower surface temperature and thus evaporation rate.

The temperature rise of the cooling water was used to determine the average deposited power during each discharge. The average conducted power per unit area, q_{cond}, is $\langle P_{\text{cond}}\rangle/\pi a^2$ where a is the target radius. Results of $\langle P_{\text{cond}}\rangle$ are shown in Fig. 1.43a. The non-linearity of $\langle P_{\text{cond}}\rangle$ at small q_{ref} (and offset) is attributed to a systematic error in the value of the cooling water speed. Further analysis is not affected as ΔP_{cond} is calculated. The total transferred heat is lower for all exposures on Sn compared to exposures on Mo for $q_{\text{ref}}>2.5\,q_{\text{ref}}$ and indistinguishable within or below this. The difference in conducted power between the Mo and Sn target increases with increasing q_{ref}. The question is therefore by what other dissipation mechanisms this power is removed.

Figure 1.43b shows the difference in conducted power between Sn and Mo at equal q_{ref}: $\langle\Delta P_{\text{cond}}\rangle = \langle P_{\text{cond,Mo}}\rangle - \langle P_{\text{cond,Sn}}\rangle$. As a result of the Gaussian profile of the plasma parameters in the beam, the surface temperature is a circularly symmetric profile and can be well represented by a Gaussian function: $T(r) = T_{\max}\exp(-r^2/2\sigma^2)$. The total power dissipated due to evaporation can now be calculated by multiplying this by the latent heat
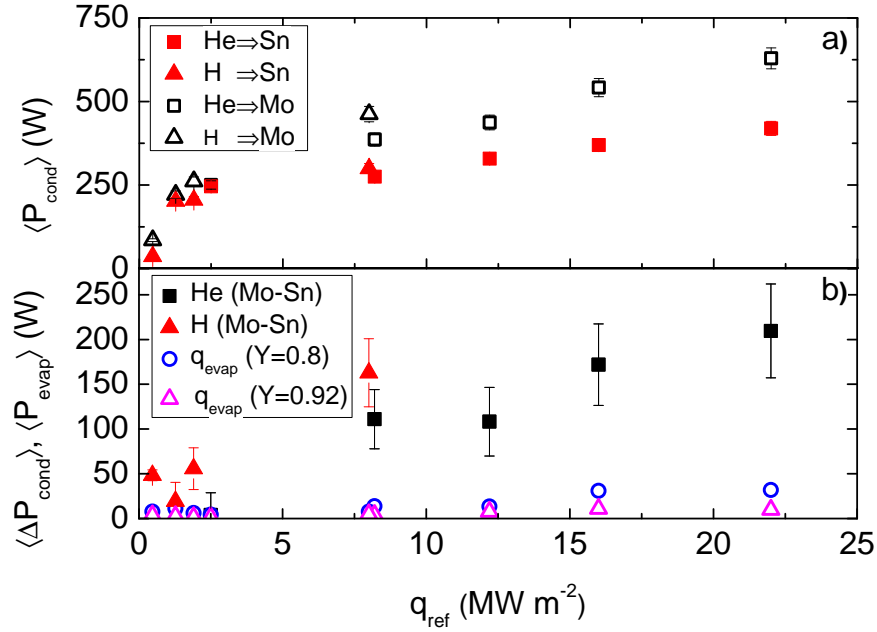
Fig. 1.43 Calorimetry and the role of evaporation. *Power transferred to cooling water as function of q_{ref} for both target types (a) and the difference in conducted power between Mo and Sn (b). The open circles in b indicate the power dissipated via evaporation assuming $Y = 0.8$. The inverted triangles represent the lost evaporative power in case of $Y = 0.92$ [157].*

of vaporization and integrating over the target area:

$$\langle P_{\text{evap}} \rangle = (1 - Y) \frac{\Delta H_{\text{evap}}}{N_{\text{A}}} \int_0^{2\pi} \int_0^a \Gamma_{\text{evap}}(T(r)) r \, dr \, d\theta, \tag{12}$$

where N_{A} represents the Avogadro constant and Y the particle redeposition fraction.

The peak surface temperature (T_{max}) during the Sn exposures is presented in Fig. 1.41. By measuring the FWHM of each Gaussian temperature profile, $T(r)$ is obtained and $\langle P_{\text{evap}} \rangle$ is calculated using equation 12. Consequently, $q_{\text{evap}} = \langle P_{\text{evap}} \rangle / \pi a^2$.

As the ionization energy of Sn is only 7.34 eV, a large fraction of Sn atoms are ionized and consequently entrained in the plasma and redeposited onto the surface. The removed power for these particles is redeposited onto the surface and is thus not a power loss channel. Redeposition rates of Sn in Pilot-PSI at similar conditions have been previously reported and revealed fractions $Y \geq 0.92$ [157]. Also, a depletion of Sn in the top layer of mesh in the target was observed after 100 s of plasma exposure, resulting in a loss of 0.45 g Sn. When assuming evaporation without redeposition, 3.4 g is lost for the same duration, yielding a redeposition rate of 87 %. The lost power by evaporation for $Y = 0.92$ and $Y = 0.8$ (i.e. 8 and 20 % lost particles) are shown in Fig. 1.43*b*. The latter represents a lower bound, accounting for uncertainties in assessing the depletion of Sn in the sample.

The effect of the vapour cloud on the electron temperature (T_e) was studied using spectroscopic analysis. Fig. 1.44 shows a spectrum obtained during a H discharge [158]. The requirement of Partial Local Thermal Equilibrium (PLTE) for our H plasma (typically $n_e = 10^{20}\,\mathrm{m}^{-3}$ and $T_e = 1\,\mathrm{eV}$) is fulfilled for energy levels $n>4$ [98]. The density of the upper state (n_j) is proportional to its line intensity (I_j): $n_j \propto (4\pi/A_{ji})I_j$ where A_{ji} represents the Einstein coefficient for this particular transition.

The emission intensities of the following H lines were used: 9-2 (383 nm), 8-2 (388.9 nm), 7-2 (397 nm), 6-2 (410.2 nm) and 5-2 (434 nm) (Balmer series with $n>4$) followed by a background subtraction. For He discharges, unobscured lines for analysis where selected for each discharge separately from the following set: $1s9s - 1s2p$ (360 nm), $1s8d - 1s2p$ (363.5 nm), $1s8s - 1s2p$ (365.3 nm), $1s7d - 1s2p$ (370.6 nm), $1s6d - 1s2p$ (382.1 nm), $1s6s - 1s2p$ (386.9 nm), $1s4d - 1s2p$ (447.3 nm).

The ratio of densities of such lines gives T_e, as expressed by the Boltzmann relation [98]:

$$\frac{n_j}{n_i} = \frac{g_j}{g_i} e^{-(E_j - E_i)/k_B T_e}.$$

(13)

The inset in Fig. 1.44 shows n_j/g_j versus the upper state energy level (E_j) for a series of high-n H transitions. The PLTE requirement is regarded to be fulfilled when this fit yields a straight line [159]. The inverse slope of the fit then yields T_e [160]. For a given plasma discharge, T_e was determined from averaging multiple spectra during the phase of constant B-field in the discharge.

The applicability of this method was verified by cross-checking T_e with values obtained from TS during H exposures on Mo. The methods were seen to yield similar values for T_e as shown in Fig. 1.45a which gives confidence in the procedure. T_e in the Sn/H and Sn/He near-surface plasma are shown in Fig. 1.45b. It is striking to see that T_e in front of the liquid surface is roughly 80 % lower than in case of the solid target and that it is approximately constant at ~0.5 eV for $q_{ref}>5\,\mathrm{MW\,m}^{-2}$. As the region of highest radiation levels lies just above the surface, the emission we observe comes predominantly from there. Therefore, T_e obtained by the Boltzmann method gives the conditions in the Sn/He and Sn/H near-surface plasma.

The reduction in T_e by interaction with the vapour cloud is interpreted to be a two-step process. Firstly, as the ion-neutral cross-section is much larger than the electron-neutral cross-section due to the mass difference between electrons and ions, predominantly it is the ions that lose their energy by elastic collisions with Sn neutrals. Secondly, the electrons are cooled by energy exchange with ions which increases as T_e decreases [161]. The ionization and recombination rates for He at 2 eV and $n_e=10^{20}\,\mathrm{m}^{-3}$ are almost equal
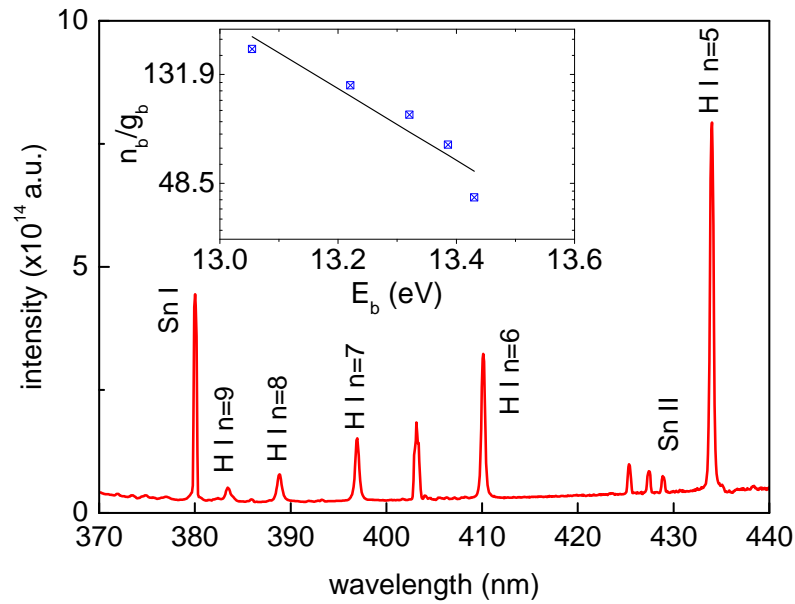
Fig. 1.44 Spectrum of H/Sn near-surface plasma. *Typical spectrum showing high-n states of H. The inset gives an example of the Boltzmann method: n_j/g_j is plotted versus the upper state energy level E_b. The inverse slope of the fitted line gives T_e.*
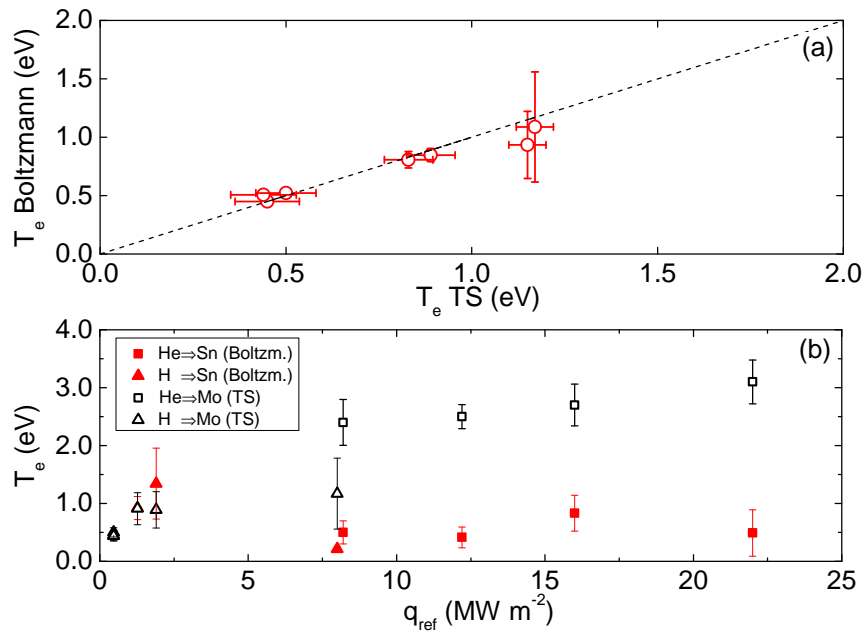
Fig. 1.45 Electron temperature in the near-surface plasma. *T_e as function of q_{ref} for the Boltzmann and TS method compared for exposures on Mo (a). Comparison of T_e near a liquid Sn and solid Mo surface for H and He exposures (b). T_e is found to be significantly lower in front of the liquid surface compared to the solid reference (especially in the case of He).*

whereas the recombination rate dominates the ionization rate by a factor $>10^6$ for $T_e{<}1\,\text{eV}$ at this density [97]. Given the measured T_e as shown in Fig. 1.45, the plasma transitions from an ionizing to a recombining regime upon entering the vapour cloud.

It may be noted that Fig. 1.45 shows that the decrease in T_e at a given q_{ref} is larger for H than for He. This observation could be explained by the additional presence of Molecular Assisted Recombination (MAR) processes leading to increased H recombination by a factor of 8-10 at low values of T_e [162]. For both plasma species we may also consider that CX processes with the neutral Sn play a direct role to neutralize the hot ions which are then no longer confined by the B-field. Overall these processes are proposed to account for a significant power loss since neutralized particles leave the plasma beam carrying energy away (q_{mass}). This loss channel is in addition to evaporated Sn particles that do not return to the surface (q_{evap}).

1.4 Conclusion

In summary, balancing the steady-state plasma pressure with the vapour pressure in front of a liquid surface led to a range of interlinked phenomena resulting in a reduced target heat flux. Power is dissipated via evaporation (up to 20 %), radiation and mass loss, which reduces the surface heat load by ~1/3 compared to the solid case. T_e in front of the Sn target is measured to decrease by ~80 % compared to the solid reference, indicating that mass transport processes are playing an important or even dominant role. The overall effect appears self-regulatory, where an increase of heat- and particle flux is balanced by an increased evaporation flux leading to an approximately constant heat load received by the liquid PFC. While the issue of Sn exceeding the tolerable impurity fraction in a magnetic fusion plasma could not be addressed due to differences in magnetic geometry and vapour cloud production, this work takes a critical step towards the design of a liquid metal solution for a fusion power plant, namely, the demonstration of the effectiveness of vapour shielding.

1.4.1 Acknowledgments

2   Oscillatory vapour shielding of liquid metal walls in nuclear fusion devices

G.G. van Eden, V. Kvon, M.C.M. van de Sanden and T.W. Morgan
published as Nat. Comm. 8, 192 (2017)

Abstract - Providing an efficacious plasma facing surface (PFC) between the extreme plasma heat exhaust and the structural materials of nuclear fusion devices is a major challenge on the road to electricity production by fusion power plants. The performance of solid PFCs may become critically reduced over time due to progressing damage accumulation. Liquid metals, however, are now gaining interest in solving the challenge of extreme heat flux hitting the reactor walls. A key advantage of liquid metals is the use of vapour shielding to reduce the plasma exhaust. Here we demonstrate that this phenomenon is oscillatory by nature. The dynamics of a Sn vapour cloud are investigated by exposing liquid Sn targets to H and He plasmas at heat fluxes $>5\ \mathrm{MW\,m^{-2}}$. The observations indicate the presence of a dynamic equilibrium between the plasma and liquid target ruled by recombinatory processes in the plasma, leading to an approximately stable surface temperature.

2.1   Introduction

Nuclear fusion power plants may turn out to be the sole candidate for centralized large-scale electricity production in a future carbon-free energy system. However, the largest obstacle on the development path of this technology is the tremendous power flux that hits the interior walls of such reactors. The largest fusion device to date, ITER ('The Way' in Latin), is currently being built and expected to have a combined exhaust power from external heating and alpha particles of $\approx 150\,\mathrm{MW}$ [107] while future electricity producing plants such as DEMO (DEMOnstration power plant) will have exhaust powers in the range ~580 to ~980 MW [25]. The latter device may possess an even narrower scrape-off layer width due to its larger size or increased magnetic fields [26] hereby delivering a critical heat load to its exhaust area. The maximum heat load removal capability for conventionally designed divertors beyond ITER is not expected to increase much above the ITER limits of 5-10 $\mathrm{MW\,m^{-2}}$ [38] and the surface area receiving the power exhaust

will remain similar to the case of ITER, which makes it essential to dissipate high power fractions via radiation in the scrape-off layer and main chamber. As the tolerable heat load onto the divertor has a small error margin due to heat handling degradation for temperatures above recrystallization such as observed for W [145, 41], any accidental reduction of radiative cooling in DEMO and beyond causes increased divertor heat loads which may be fatal to its armour integrity. At the same time, good divertor performance without regularly replacing its armour materials are essential for a fusion reactor to be commercially viable. Meeting such requirements using present day technologies are very challenging which makes investigating alternative divertor solutions a necessity.

The use of liquid plasma facing components (PFCs) can potentially alleviate many of the heat exhaust issues in the divertor. A liquid wall is self-healing as material displacement due to off-normal plasma impact is reversible. Lifetime issues related to erosion are less problematic because a liquid can replenish itself which prevents damage accumulation, leading to a potentially longer lifetime. Additional heat transport by convective movement of the liquid, evaporative cooling [152] and a reduction of neutron issues [163] are other potentially beneficial properties of liquid PFCs. Finally and most importantly, when operating in the vapour shielding regime where a cloud of evaporated neutrals exists in front of the plasma-exposed surface [71, 153], any accidental exhaust power excursion leads to increased evaporation which may mitigate the impact on the divertor armour by self-protection. Despite these advantages, liquid metals are still at a low technology readiness level and require further development.

The effect of additional heat dissipation channels was recently demonstrated by the observation of a self-regulated heat flux mitigation phenomenon due to the presence of a Sn vapour cloud [164]. The upstream plasma heat flux was found to be almost completely decoupled from the average target surface temperature while the plasma temperature decreased to values close to 0.5 eV in front of the target surface. Although equilibrium timescale effects of the vapour presence were made clear in this study, the dynamical evolution and mechanism of the shielding phenomenon were not described.

Such questions have now been addressed and outcomes are reported here. The response of liquid Sn targets exposed to H or He plasmas in the power flux range of q_{ref}=0.5-22 MW m^{-2} have been investigated. Conditions were chosen such that the Sn vapour pressure was of similar magnitude as the plasma pressure [164]. Solid Mo targets without vapour cloud formation were consequently exposed to equivalent plasma conditions, thus serving as a reference case.

The key result is that, during steady-state vapour shielding, the width and extent from the surface of the Sn vapour cloud oscillates in time in correlation with the target surface

temperature and Sn emission intensity. A periodically varying shielding effectiveness resulting in a dynamic equilibrium between plasma and liquid surface is concluded. The obtained findings shed light on the dynamical aspects of steady-state vapour shielding by liquid metals at divertor-relevant plasma conditions. The outcomes of these investigations are pointing into a direction where the divertor-strike points are equipped with liquid metal technology (Sn, Li) while operated in a regime where the vapour pressure is of similar magnitude as the plasma pressure. If realized, steady-state operation of a liquid fusion reactor divertor is likely to be feasible.

2.2   Results

2.2.1   Surface temperature oscillations

Our previous work [164] reported on the striking difference between the thermal response of liquid Sn versus solid Mo when exposed to equal plasma heat fluxes: the surface temperature at the end of the plasma discharge in the case of Sn was found to remain approximately constant while that of Mo continuously rose in accordance with increasing q_{ref}. Another difference in the thermal response by these materials is evidenced by looking at the surface temperature over the course of the plasma discharge. Clear oscillations in surface temperature at an amplitude up to $200\,\text{K}$ and period of roughly $100\,\text{ms}$ are regularly observed at both the edge and centre of the Sn target, while the temperature response of the Mo target remains approximately constant once thermal equilibrium is reached. An example of this oscillatory behaviour is given in figure 2.46 which shows the temperature evolution in both the centre and at the edge of the target during He discharges at q_{ref}=22.0 and $12.2\,\text{MW}\,\text{m}^{-2}$.

The magnetic field strength is plotted versus time in figure 2.46a. This dominantly sets q_{ref} which is thus seen to be approximately constant over the discharge duration. The edge temperature is seen to gradually increase followed by a rapid drop over the course of a single oscillation period while the temperature changes in the centre are much smaller during this period but are seen to rise rapidly at the end of each cycle. The grey box in panel a shows the period which is analysed in detail in figures 2.47 and 2.48. Figure 2.46b shows oscillations in the surface temperature which are less regularly spaced but of much larger amplitude and temporal extent. This particular discharge therefore proved to be very suitable for analysis using diagnostics that have a time response which is usually too slow to observe fast fluctuating signals, such as target potential and spectroscopic measurements.
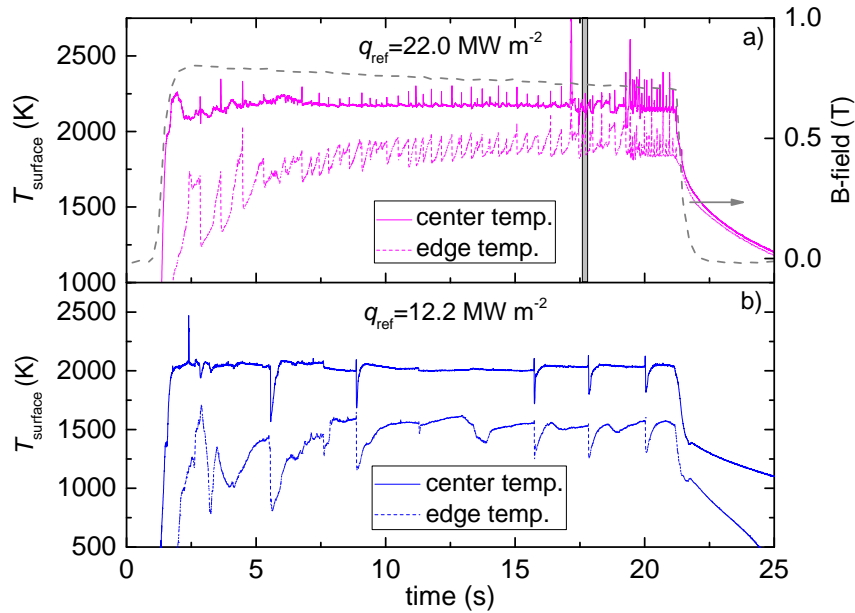
Fig. 2.46 Evolution of the liquid Sn surface temperature. *The temperature at the target centre and edge while exposed to a 22*MWm^{-2} *(a) and 12.2*MWm^{-2} *(b) He plasma as recorded by a fast IR camera. Fast temperature oscillations around a constant base value are regularly observed during discharges. The magnetic field strength over time is shown in a by the right axis and is identical for both q$_{ref}$. The grey box indicates a temporal range which is analysed in detail in figures 2.47 and 2.48. The discharge at 12.2* MWm^{-2} *shows slowly evolving temperature changes at larger time intervals.*

2.2.2 Emission from neutral Sn

Recording the intensity of a distinct neutral Sn transition (I_{Sn0}) at 452.5 nm ($5s^2 5p 6s$ to $5s^2 5p^2$) using the tangentially positioned fast camera allowed for investigating the vapour dynamics with high temporal resolution. A sequence of characteristic frames within a single oscillation cycle during a discharge at 22 MWm^{-2} are shown in figure 2.47. Frames in figure 2.47*a-c* qualitatively show the growth of the emissive region and magnitude of emission which is the phase of continuous evaporation of Sn. Panel 2.47*d* shows the quenching of the plasma due to the high Sn impurity presence and is discussed later.

The neutral Sn emission is proportional to the product of the Sn atomic density n_{Sn0}, the electron density n_e and the electron excitation rate coefficient $C_{exc}(T_e)$:

$$I_{Sn0} \propto n_{Sn0} n_e C_{exc}(T_e). \tag{14}$$

Excitation from Sn0 to this particular excited state Sn0* ($5s^2 5p 6s$) is much larger than the combined recombination rates from Sn^{+1} to Sn0* at temperatures 0.5-0.8 eV [164], even
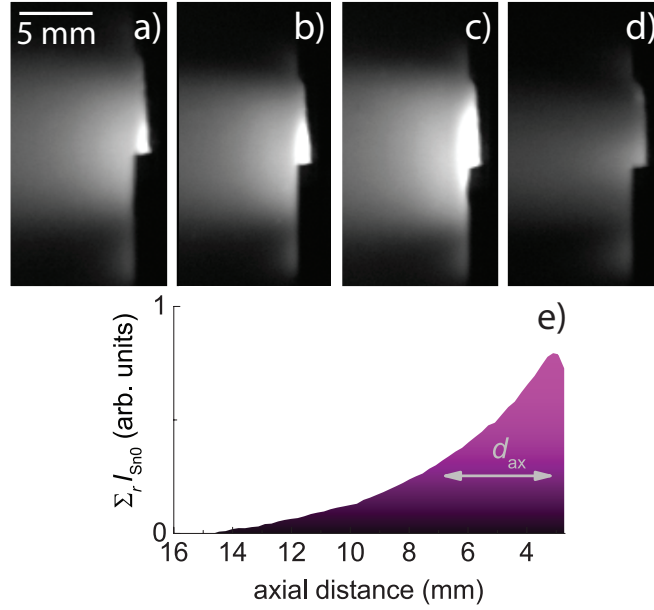
Fig. 2.47 Oscillatory emission intensity from neutral Sn. *A sequence of characteristic images during a single vapour shielding cycle as obtained from neutral Sn emission. The timestamps of the images a-d are 17.6, 17.64, 17.71 and 17.75 s after initiating a discharge at 22* MW m^{-2}*. The decay of Sn0 emission versus distance from the target (t=17.54 s) is shown in e.*

when taking into account that a large fraction of Sn is ionized [101]. This makes I_{Sn0} in equation 14 suitable for qualitative investigation of the Sn0 density.

Figure 2.47*e* shows $\sum_r I_{Sn0}$ (integrated over the beam radius) as a function of axial distance from the target. Given its exponential-like distribution, the ratio of the local intensity $\sum_r I_{Sn0}(x)$ and the maximum intensity $\sum_r I_{Sn0}(0)$ can be expressed by

$$\frac{\sum_r I_{Sn0}(x)}{\sum_r I_{Sn0}(0)} = e^{-x/d_{ax}}, \tag{15}$$

with the typical axial penetration length of the evaporated Sn neutrals given by $x = d_{ax}$. This treatment was repeated similarly for the intensity parallel to the target surface, giving the typical width of the Sn vapour cloud (assuming axial symmetry).

Figure 2.48*a-b* shows both the surface temperature at the edge and centre of the target respectively while the neutral Sn emission characteristics during this period are shown in panels *c-e*. The intensity at 452.5 nm was line-integrated and summed over all pixels in the non-saturated part of the image and is denoted as $\sum I_{Sn0}$. A comparison of figures 2.48*a-b* and 2.48*c* shows that the surface temperature oscillates in correlation with $\sum I_{Sn0}$. Results of time-resolved d_{ax} and the vapour cloud width (radial *e*-fold length) are shown in figures 2.48*d* and 2.48*e* respectively.
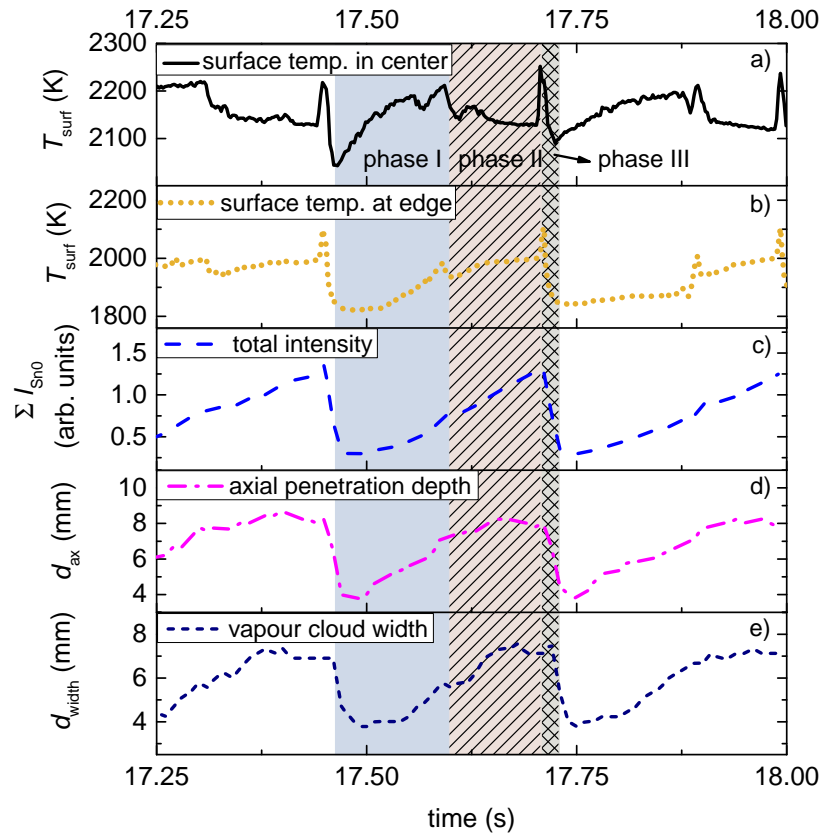
Fig. 2.48 Vapour shielding dynamics. *The surface temperature at the target centre (a) and edge (b) and Sn emission (c-e) during 17.2-18s after initiating a 22.0 MW m^{-2} He discharge. Three characteristic phases within a typical oscillation period are indicated by the Roman numerals I-III. Panel c shows the total line-integrated intensity at 425.5nm and panels d-e show respectively the penetration into the upstream plasma and the radial extent of the vapour cloud.*

Three phases during each oscillation period can be identified when examining the information in figure 2.48. Phase I is defined as the phase where the surface temperature increases in accordance with increasing $\sum I_{Sn0}$ (roughly half the oscillation duration). Secondly, at half the cycle period, the phase where the central surface temperature starts to decline while d_{ax} still slowly increases is called phase II. Interestingly, $\sum I_{Sn0}$ keeps progressively rising throughout this phase together with the edge surface temperature which naturally results in a flattened radial surface temperature distribution at the end of phase II relative to phase I. Finally, phase III indicates a sharp increase in surface temperature followed by a sudden drop which characterizes the end of the cycle. This rapid temperature excursion does not show up in parallel in the emission profile and will be discussed later.

Both d_{ax} and d_{width} are seen to oscillate in time with the same periodicity as the surface temperature. Interestingly, when the cloud extends ~7mm into the plasma (~100ms into

phase I) the surface temperature of the centre starts to decrease (entering phase II). The Sn vapour cloud extends further upstream in the remainder of the cycle and its width increases as indicated by the increasing e-folding lengths. The increase in d_{width} is in agreement with the continuously rising edge surface temperature. Since $d_{ax} \propto 1/\sigma n_e$, where σ represents the collision cross section which is proportional to T_e, a decrease of T_e and/or n_e is implied in this region. We thus reason that the static plasma pressure, $p = 2n_e k T_e$ (assuming $T_e = T_i$), periodically decreases as a result of interactions with the Sn cloud. This conclusion is in accordance with increased recombination as previously reported [164]. It is further concluded that the point at which the target temperature starts to decrease is set by the Sn vapour density depending on q_{ref}, which is the period where effective shielding occurs (phase II).

2.2.3   Plasma sheath potential

The floating potential V_{fl} of the Sn and Mo targets during the plasma discharges is measured at a time resolution of 250 ms. V_{fl} is the sum of the plasma potential V_p, the sheath potential V_{sh}, and pre-sheath V_{ps} potential relative to the ground: $V_{fl} = V_p + V_{sh} + V_{ps}$. As the upstream plasma conditions and source behaviour are found not to change when switching between Sn and Mo targets, V_p is assumed to remain equal as well. Therefore, since $V_{sh} \approx 2.5 k_B T_e/e$ relative to V_p [21], measuring the floating potential provides an indirect method of investigating T_e.

Figure 2.49a shows a comparison of the floating target potential during exposures of Mo and Sn targets averaged during the phase of constant magnetic field (3-21 s after initiating the discharge). A less negative target potential by a factor >2 is consequently observed for He exposures on liquid Sn and the effect seems to increase at larger q_{ref}. The effect is small but also observable for the lower heat flux discharges using H. The relative increase in sheath potential when comparing the Sn and Mo exposures (V_p remains the same) at fixed q_{ref} directly correlates to reduced T_e in the case of Sn as obtained from Boltzmann plots made during the same discharges [164].

Due to temporal constraints associated with these measurements, only the relatively slow oscillations that occurred during the 12.2 MW m^{-2} discharge could be well studied. Figure 2.49b shows both the surface temperature and time-resolved floating potential of this discharge for comparison. As can be seen, $V_{fl} \approx -10$ V during the non-oscillatory phases 4-21 s after the start of the discharge. V_{fl} decreases however maximally to values ranging -20 to -15 V during the last phase of the vapour shielding cycle where the surface temperature strongly decreases. The latter values are close to the floating potentials as measured during Mo exposures presented in figure 2.49*a*.
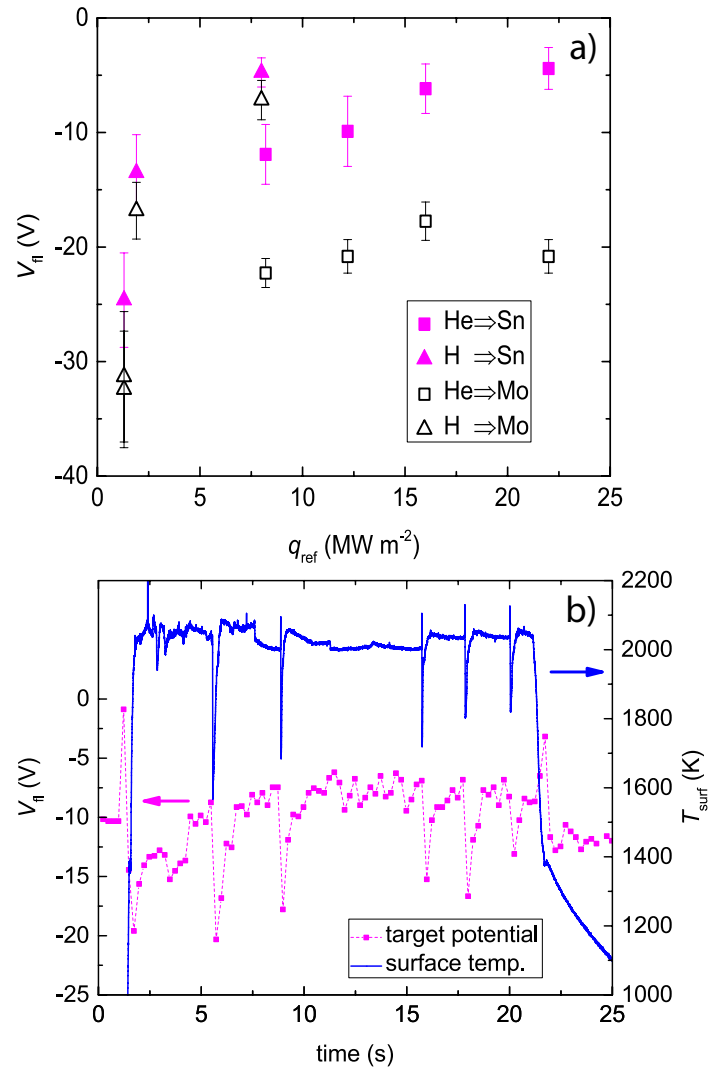
Fig. 2.49 Changes in target potential during Sn vapour shielding. *The average target floating potential in discharges on Mo and Sn (a) and temporal changes of the target floating potential measured during a 12.2* MW m^{-2} *He discharge on liquid Sn in comparison to the Sn surface temperature evolution (b). V_{fl} in (a) is obtained from averaging the target floating potential over the range of constant magnetic field. The error bars represent the s.d. of these datasets.*

Given that the target floating potential correlates with T_e, it is concluded that T_e reduces during phase II while temporarily increasing during the period marked by the end of phase III and the start of phase I. Cooling of the plasma by neutral-ion elastic collisions and subsequent ion-electron elastic collisions [161] is previously interpreted as the mechanism [164]. This statement is in agreement with the behaviour of the floating potential as reported above: the increase in vapour emission (figure 2.48*c*) means increased neutral Sn density causing increased neutral-ion friction via elastic collisions. The plasma cools by

ion-electron cooling which is reflected in a less negative target potential. Once the vapour cloud is lost, T_e increases causing a more negative (Mo-like) target potential. Hence, also T_e is found to oscillate during the vapour shielding cycle.

2.2.4   Continuum radiation

Emission spectra in the range of 360-580 nm in the near-surface region have been recorded. The continuum emission, clearly observable between the characteristic line emission features, emerges due to a combination of Bremsstrahlung and recombination radiation. It can be expressed as a simplified proportionality in the following way:

$$\epsilon_{\text{cont}} \propto \sum_i \frac{n_i n_e}{\sqrt{T_e}} = \frac{n_e}{\sqrt{T_e}}(n_{\text{He}^+} + n_{\text{Sn}^+}) = \frac{n_e^2}{\sqrt{T_e}} \quad [\text{Wm}^{-3}\text{sr}^{-1}\text{nm}^{-1}], \tag{16}$$

where the sum indicates a summation over all ionic species present in the plasma. More complicated factors of T_e that predominantly affect the shape of the continuum emission distribution rather than its absolute levels are neglected in the proportionality expressed in (16). We used the assumption that both the He and Sn species are only maximally singly ionized which cancels the dependency on the effective charge via Z_i^2 which appears in the full expression of ϵ_{cont} [165].

The spectral radiance during exposures of liquid Sn are measured and polynomial fits to the data are presented in figure 2.50a. When changing q_{ref} from 8.2 to 16.0 MWm^{-2}, n_e changes from 4.1×10^{20} to 6.1×10^{20} m^{-3} (see table 5). Since T_e is found to be highly similar at ~0.6 eV for these discharges [164], the increase in density should lead to an increase in the continuum emission by a factor $(6.1/4.1)^2 = 2.2$ which is confirmed by the data shown in figure 2.50a.

It follows from (16) that analysing the changes in continuum emission during a vapour shielding cycle provides insight in the evolution of the plasma parameters during the oscillation phase. Figures 2.50b and 2.50c show the spectral radiance and polynomial fits to the data of He discharges at 22.2 and 12.2 MWm^{-2} respectively. Spectra at the start of phase I, where the surface temperature starts to increase but is still at a minimum, are now being compared to the spectra where vapour shielding most effectively occurs, namely halfway phase II where the central surface temperature is relatively constant or decreasing.

It is found that n_e changes by a factor $\sqrt{1.7} = 1.3$ and $\sqrt{18.6} = 4.3$ during the vapour shielding cycle for q_{ref}=22.2 and 12.2 MWm^{-2} respectively. Recall that the emission from neutral Sn is found to steadily increase over the course of the vapour shielding cycle as shown in figure 2.48b. Also, despite the decrease of surface temperature in the centre
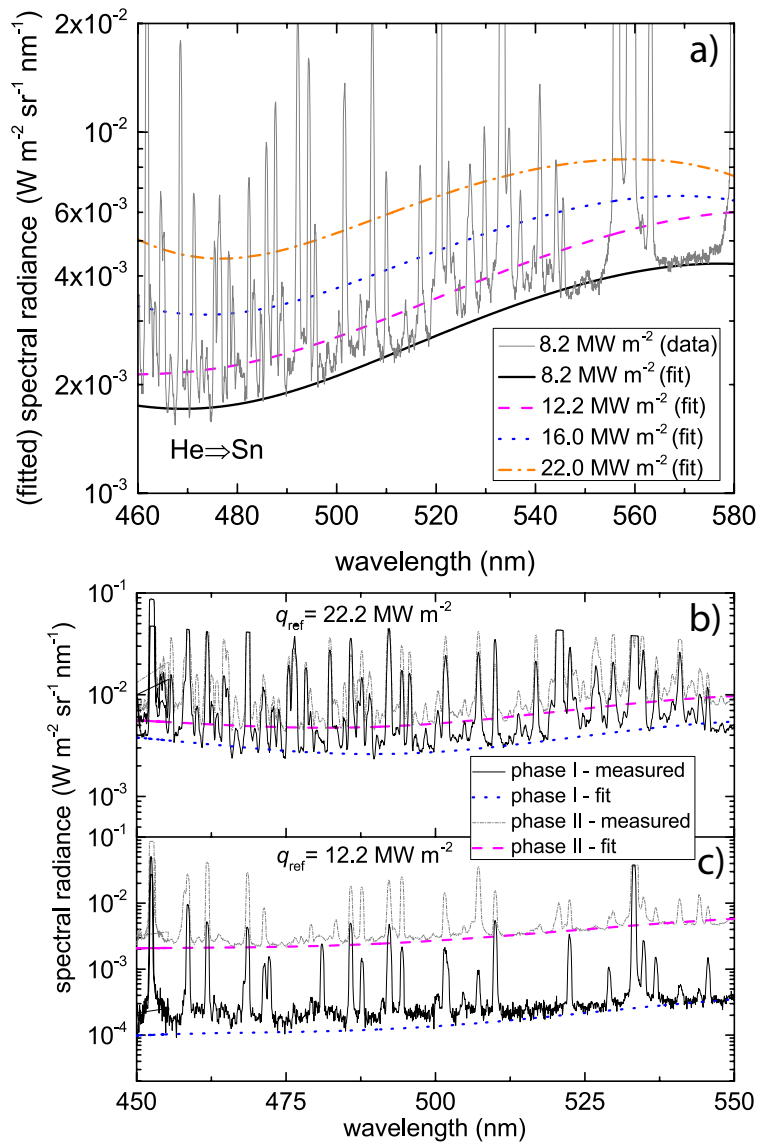
Fig. 2.50 Oscillations in Sn/He plasma continuum emission. *Polynomial fits representing the continuum emission acquired during measurements of the spectral radiance during He plasma exposures of Sn (a). Experimental data of the discharge at 8.2 MW m^{-2} is shown for comparison. The spectral radiance of the near-surface plasma with a large fraction of Sn for discharges at q_{ref}=22.2 MW m^{-2} (b) and q_{ref}=12.2 MW m^{-2} (c). The continuum emission (fits to the experimental data) of the near-surface plasma at the start of phase I and during phase II are shown by the dotted blue lines and dashed red lines respectively.*

during phase II, the edge temperature still rises (figure 2.48), implying a continuously increasing flux of Sn atoms released from the target. It is mentioned in section 2.2.2 that the increase in mean free path of Sn atoms during the vapour shielding cycle as shown in figure 2.48c implied a reduction n_e and/or T_e in the centre of the plasma beam. However,

from the increase of ϵ_{cont} which is proportional to $n_e{}^2$, an increase in electron density during the vapour shielding cycle is concluded. By realizing that the collision cross section of neutral Sn is highly sensitive on T_e while weakly dependent on n_e, it is thus concluded that mean free path is increased due to reduction of T_e despite increasing n_e. Hence, the observed increase in continuum radiation over the course of the vapour shielding cycle is explained by increasing n_e by a factor up to ~4 during this period. Since T_e is reduced by roughly the same factor when moving from a liquid to a solid target at equal upstream plasma conditions [164], pressure ($\propto n_e T_e$) along the plasma beam is conserved as expected.

2.2.5   Liquid metal transport

A thin layer of Sn is formed on the target surface during plasma exposure while the CPS secures the bulk liquid. This free liquid surface may give rise to convective flow which influences the heat distribution along the target surface. Azimuthally directed liquid flow was observed during phases I and II of the vapour shielding cycle while phase III displayed a radial flow directed from edge to centre. A succession of IR images at 5 different times during one vapour shielding cycle, illustrating the different phases, are shown in figure 2.51. The IR images are linked to the temperature trace by the given numbers.

The speed of the liquid motion was quantified by monitoring the movement of emissive surface impurities in a succession of IR images similar to those shown in figure 2.51 and assuming that their speed equals that of pure Sn. Results of the average rotation speeds (v_{rot}) and radial velocity (v_{radial}) are shown in figure 2.52a and 2.52b respectively. An increase in v_{rot} proportional to q_{ref} in case of rotation speed during phase II is observed. The rotational velocity as function of the phase within the oscillation cycle could only be analysed for discharges >10 MW m^{-2} since distinguishable impurities were found absent below this q_{ref}. Although small, v_{rot} is seen to decrease in time when comparing phase I to phase II during discharges at 12.2 and 16.0 MW m^{-2}. No changes in the liquid flow velocity were seen at highest q_{ref} when comparing between these phases. The rotation speed during phase III could only be measured for discharges at >16 MW m^{-2}. When comparing phase III to the start of the cycle in the discharge at 22.2 MW m^{-2}, a decrease in v_{rot} by 25 % is observed. This effect is however not clear at 16.0 MW m^{-2}. Furthermore, a radial component to the flow velocity, shown in figure 2.52b, is absent during phase I and phase II but rises however to approximately 2.1 m s^{-1} during phase III. The origins and magnitude of competing flow mechanisms as observed are discussed hereafter.
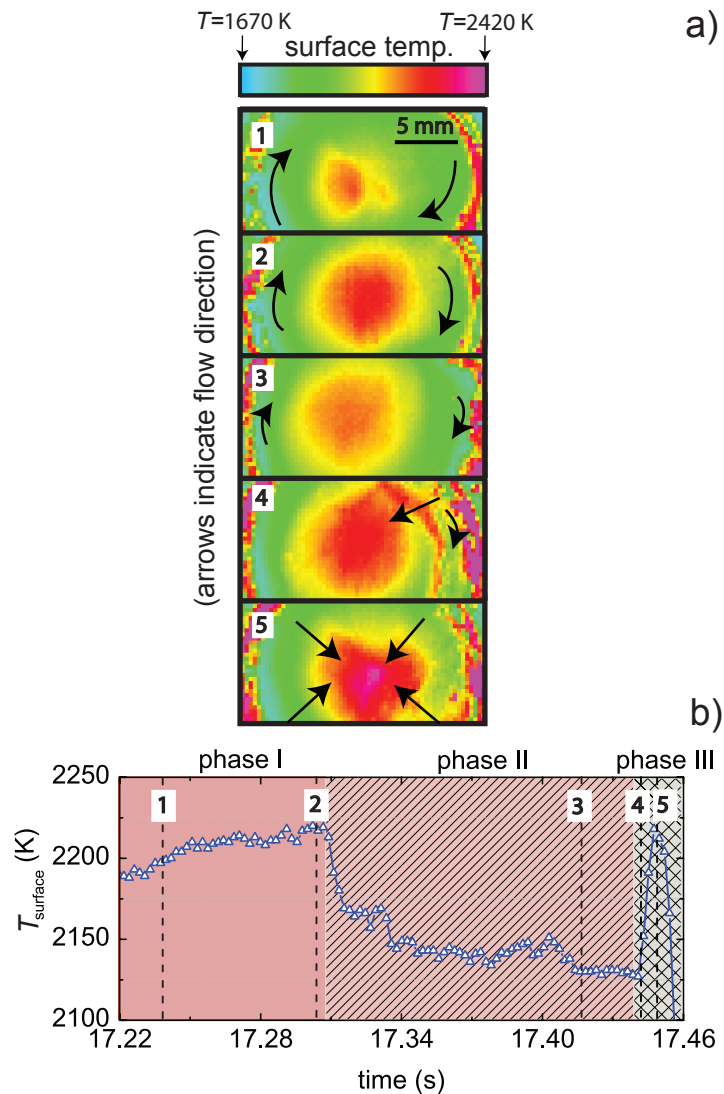
Fig. 2.51 Flow dynamics of surface Sn during shielding cycle. *A succession of IR images of the target surface during one vapour shielding cycle (a) and the temperature evolution during this cycle (b). Time frames corresponding to the images are indicated by vertical dashed lines and labels. The arrows indicate the direction of the dominant surface flow while the sizes of the arrows qualitatively indicate changes in rotation speed.*

2.2.6   Azimuthal flow

Liquid flow in a magnetic field (**B**) may arise as a result of Lorentz forces due to the presence of electric currents in the liquid. Since the flow was observed to rotate while **B** is directed into the plane of the target, a radial current must be present in the target. Both thermoelectric currents and externally injected current from the plasma column are potential candidates for this.
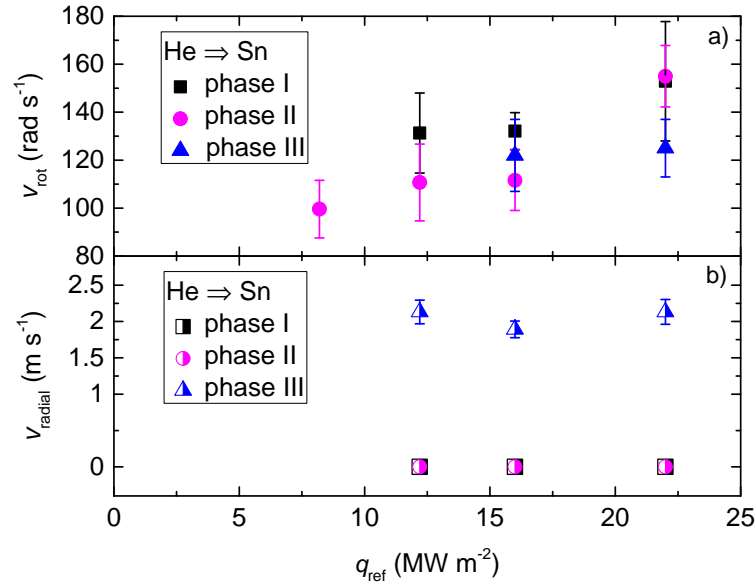
Fig. 2.52 Liquid surface flow velocity. *The velocity of rotating Sn at the edge of the target as function of q_{ref} for different stages during the oscillation cycle (a). The rotational flow during phase II is seen to increase with q_{ref}. A small decrease in rotation speed occurs during a single shielding cycle at heat fluxes of 12.2 and 16 $\mathrm{MW\,m^{-2}}$. A radial component to the flow velocity, only observed during phase III, is shown in b. The data points represent the average of approximately 10 independent measurements at equal phases within different vapour shielding cycles. The error bars represent the s.d. of these datasets.*

Radial currents are naturally occurring in the plasma column of Pilot-PSI as a result of its source potential configuration [89, 166]. It is clear from this work that there exists a net current carried by electrons in the centre of a floating target while the edge receives a net ion current. Such radial currents give rise to $\mathbf{J} \times \mathbf{B}$ driven rotation of the liquid [167].

Since a radial temperature profile exists along the metallic interface comprised of the W mesh and liquid Sn, also a radial current (from centre to edge) in opposite direction of the thermal gradient arises as a result of so-called thermoelectric magneto-hydrodynamic (TEMHD) effect [168]. Following [169], the thermoelectric current density J_{TEMHD} can be expressed as:

$$J_{\text{TEMHD}} = \frac{\sigma P \nabla T}{C+1}, \tag{17}$$

where P ($=P_{\text{W}} - P_{\text{Sn}}$) represents the thermoelectric power of the solid-liquid pair and ∇T the thermal gradient along their interface. C denotes a non-dimensional thermal impedance ratio between liquid and solid and is calculated as $C = \sigma_{\text{Sn}} h / \sigma_{\text{W}} t_{\text{w}}$ where σ_{Sn} and σ_{W} represent the electric conductivity of Sn and W respectively, h the liquid layer thickness and t_{w} the thickness of the W mesh. Given the directions of the aforementioned currents, the residual current density in the target J can be expressed as $J = J_{\text{p}} - J_{\text{TEMHD}}$

with J_p the current density injected by the plasma. The rotation speed (v_{rot}) as measured can now be used to calculate the incident current density from the plasma [169]:

$$J_p = v_{rot}\sigma B \left[1 - \frac{1}{\cosh(Ha)} \right]^{-1} + J_{TEMHD} \tag{18}$$

with $\sigma = \sigma_{Sn}$ and Ha the dimensionless Hartmann number describing the ratio of electromagnetic forces to viscous forces in a liquid. The Hartmann number is defined as $Ha = Bh\sqrt{\sigma/\mu}$ with μ the dynamic viscosity of the liquid.

Equations 17 and 18 are now evaluated for the case of the 22.0 MW m^{-2} discharge in He with $v_{rot} = 140 \pm 14$ rad s^{-1}. This yields a tangential velocity component of 1.4 ± 0.14 m s^{-1} at $r = 10$ mm, close to the target edge. A linearly decreasing surface temperature from edge to centre is assumed for simplicity. All parameters are evaluated at a temperature which equals the average between the edge and centre as can be found in figure 2.48: $T_{av} = (2050 + 1850)/2 = 1950$ K and $\nabla T = (2150 - 1850)/0.01 = 2 \times 10^4$ K/m (r=10 mm) with a 10 % error. Expressions for the temperature dependent thermoelectric powers of Sn and W up to 548 K are given in [170]. P_{Sn} above the Sn melting point is close to zero while P_W linearly rises at much higher values. We therefore estimate the relative thermoelectric power of Sn-W by assuming the value for W at 1950 K which is 59.7 μV K^{-1}. Given the large extrapolation, an error of 30 % is assigned to the thermoelectric power. Values to the remaining variables in equations 17 and 18 and the expression for C are assigned as follows: $B = 0.8 \pm 0.08$ T, $\sigma_{Sn} = 1.17 \pm 0.12 \times 10^6$ $\Omega^{-1}m^{-1}$, $\sigma_W = 2.1 \pm 0.21 \times 10^6$ $\Omega^{-1}m^{-1}$, $h = 5 \pm 2.5 \times 10^{-4}$ m, $t_w = 5 \pm 0.1 \times 10^{-5}$ m, $\mu = 6.95 \pm 0.7 \times 10^{-4}$ Pa s, and, from this, $Ha = 16.6 \pm 5.2$. The temperature dependent electrical conductivity of W is calculated from the temperature dependent thermal conductivity [171] using the Wiedemann-Franz law. The error in liquid layer thickness is assumed to be 25 %.

Substituting these numbers yield $J_{TEMHD} = 20.7 \pm 9.7$ A cm^{-2} and $J_p = 158 \pm 105.9$ A cm^{-2}. We thus conclude that the dominant radial current is induced by the plasma rather then by thermoelectric effects. This is in agreement with the observed azimuthal flow in clockwise direction. The weaker thermoelectric current flows in the opposite direction and would have caused counter-clockwise rotation if it were dominant.

2.2.7 Radial flow

We secondly explore the radial surface transport. Since large temperature gradients exist across the liquid surface, surface tension driven flows as described by the Marangoni effect may be present. The spatial temperature gradient is largest in the radial direction which induces a radially outward surface tension driven flow. The treatment as provided

in [172] can be applied, giving the surface flow velocity as function of the tangential heat flux gradient with a normal incidence **B** as:

$$u_{\text{rad}} = \frac{d\gamma}{dT} \frac{h^2}{\mu k_{\text{Sn}}} \frac{\partial q}{\partial r} \frac{\sinh(Ha)}{Ha \cdot \cosh(Ha)} \tag{19}$$

where $d\gamma/dT$ is -0.14 mN m^{-1} K^{-1}, obtained from differentiating Eötvös law [64]. The liquid thermal conductivity is obtained by extrapolating a dataset valid up to 1473 K [66], providing $k_{\text{Sn}} = 6.7 \pm 0.7$ W m^{-2} K^{-1}. A linearly decreasing heat flux over the target radius is assumed, estimated to be $\partial q/\partial r \approx 5 \pm 1/0.01 = 500 \pm 100$ MW m^{-2} m^{-1}. All parameters are again evaluated at T_{av}=1950 K resulting in $u_{\text{rad}} = 0.23 \pm 0.17$ m s^{-1}. Note that no radial flow in phases I and II could be observed (figure 2.52). It is however to be mentioned that the much faster azimuthal flow may have impeded the observation of outward radial movement.

The ratio of convective to conductive heat transfer upon receiving a heat flux normal to the surface can be estimated as [172]:

$$\xi = h^2 u_{\text{rad}} \frac{\rho C_{\text{s}}}{k_{\text{Sn}}} \tag{20}$$

with ρ the Sn density and C_{s} the heat capacity equal to 6099 kg m^{-3} and 141.1 J kg^{-1} K^{-1} respectively [64]. Inserting furthermore the thickness of the liquid surface layer, its radial velocity (u_{rad}) and length equal to the target radius one finds $\xi = 0.74$.

Since this ratio is close to 1, both convective and conductive heat transport are important. The fraction of heat transported by convection is thus not found to be dominant owing to its shallow depth and low flow velocity. It is furthermore hypothesized that the decrease of v_{rot} over the course of an oscillation period is caused by a reduction of plasma flux (mostly electrons) in the beam centre due to vapour shielding while the edge of the target continuous to receive heat flux (mostly ions). This is in agreement with the observation that the edge surface temperature rises during a cycle while the central temperature remains approximately constant. As a result of the effective shielding in the target centre, the sheath potential becomes less negative here (see figure 2.49) while the edge sheath remains unaffected. The collapse of rotation and strong radial flow overall indicate that the plasma flux reaching the surface is strongly reduced during phase III, resulting in cool-down of the target prior to a new cycle. Given that the plasma pressure is temporarily decreased as a result of detachment, we explain the inward movement in phase III by surface tension forces minimizing the surface area after it is distorted by the

pressure gradient imposed by the plasma. An inwardly spiralling flow in phase III results from this, despite the target centre being still hotter than the edge.

2.3 Discussion

The ionization- and recombination rate coefficients for H and He are shown as function of T_e for $n_e = 10^{20}\,\mathrm{m}^{-3}$ in figure 2.53. The data is extracted from ADAS [97] while rates for Molecular Assisted Recombination (MAR) processes are obtained from [162]. Only a weak dependency on n_e is found for these numbers.
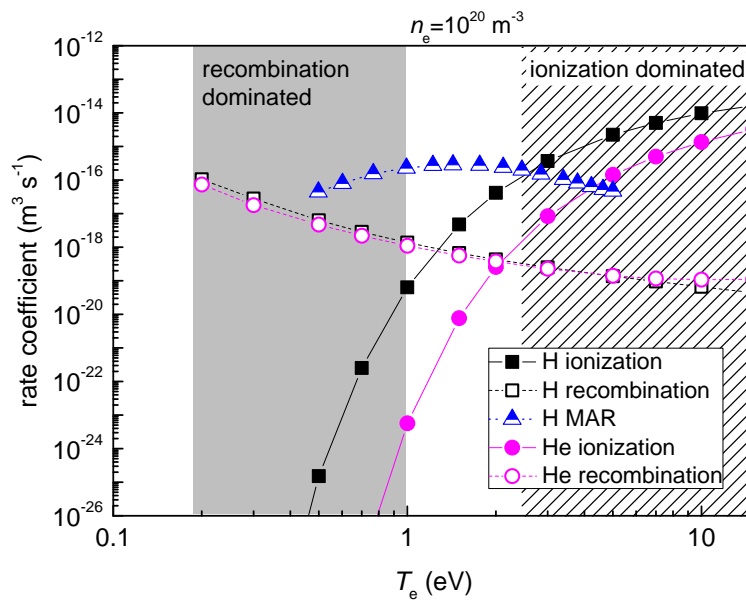
Fig. 2.53 Ionization and recombination rate coefficients of H and He. *The coefficients, valid at n_e=$10^{20}\,\mathrm{m}^{-3}$, are extracted from the ADAS database [97]. Molecular Assisted Rate (MAR) coefficients were obtained from [162]. The shaded region on the right highlights T_e values of a H and He plasma where ionization is the dominant process. The grey box on the left indicates a recombination dominated temperature regime.*

With help of these rate coefficients, we seek to explain the oscillatory vapour shielding by the following model. The evaporation of Sn during phases I and II of the shielding cycle progresses until a critical Sn density (depending on q_{ref}) in the near-surface plasma is reached (figure 2.48). The plasma ions lose their energy by interaction with the neutral cloud followed by ion-electron cooling [161]. T_e reduces to values lower than 0.5-0.8 eV [164], where strong recombination of the plasma occurs (figure 2.53), starting from the target centre where the neutral fraction is highest and stretching gradually to the edges during phase II. This recombination process affects the plasma in a positive feedback loop: recombination produces neutrals that further cool the plasma causing additional

recombination. The result is a temporary detachment-like state of the plasma [173] where q_{ref} is significantly reduced, combined with a small floating target potential relative to the plasma potential (low T_e), and increased n_e as described in section 2.2.4. The rotation speed of the liquid film at the target surface is dominated by $\mathbf{J} \times \mathbf{B}$ induced forces in phases I and II which decreases over the course of the shielding cycle as q_{ref} reduces. At the same time, the reduction of static plasma pressure ($P_p = 2n_e kT_e$ [21]), is highest in the target centre relative to the target edge. Hence, with reduced azimuthal inertia of the liquid in phase III, the surface tension difference between centre and edge drives the liquid from the edge inwards (section 2.2.7). When q_{ref} at the end of phase II is reduced due to plasma detachment, the surface starts to cool and the evaporation flux of Sn (an exponential function of temperature), quickly decreases. The vapour cloud almost completely disappears in phase III and the plasma thus reaches the target surface without strong interaction with the vapour (plasma is attached), hence the floating potential reaches values similar to that of a solid target. At this point, the plasma starts heating the surface again which results in the common conduction-type heating curve as observed at the start of phase I. Consequently, a new vapour shielding cycle is initiated and the process repeats itself.

The oscillatory nature of the vapour shielding effect is thus understood to be a result of periodical plasma detachment induced by the high neutral Sn density in the near-surface plasma, constituting a mutually interacting system between q_{ref} and Sn evaporation. The oscillation frequency is observed to be roughly 10 Hz (figure 2.46) and likely to be driven by the characteristic thermal equilibration timescale which is slow compared to the rapid detachment process. The timescale of the latter can be approximated by the ion-electron collision time: $\tau_{ie} = \tau_{ei} = \tau_e m_{He}/2m_e \simeq 0.2\,\mu s$ at T_e=0.8 eV and n_e=10^{20} [164]. A conservative estimate of the characteristic time for the vapour cloud to disappear in phase III can be estimated as $\tau_v = d_{ax}/\sqrt{(2k_B T_{surf})/m} \approx 16\,\mu s$ when taking the thermal speed equal to the surface temperature at 1950 K. Therefore, on short timescales, while the plasma undergoes rapid cooling due to the runaway detachment process, the surface temperature rapidly decreases as conduction to the coolant q_{cond} is approximately uniform and still high. This can be expressed by $T_{surf}(t) = (T_0 - T_{cool})e^{(-t/\tau_c)}$, yielding $\tau_c \simeq 250\,\mu s$ (figure 2.48). The subsequent heating phase occurs however over a longer period due to the slower equilibration time for conduction, particularly at the plasma edge where the heating rate is relatively low so that $q_{cond} \approx q_{ref}$. The mismatch in the characteristic timescales (μs versus ms) between thermal material processes and atomic physics taking place in the plasma is understood to be the ultimate cause of the oscillatory behaviour.

The rapid increase in surface temperature observed in phase III (spike) is discussed now. Firstly, no transient increase in Sn0 emission is observed. Secondly, from inverting

the 1D heat diffusion equation, an additional heat flux of $4\,\mathrm{MW\,m^{-2}}$ would be necessary on top of the existing q_{ref} to replicate the typical surface temperature increase as observed in figure 2.48. Given that such a transient additional heat flux is highly unlikely and such rapid heating/cooling unphysical, we regard the interpretation of a rapid temperature change erroneous. It is therefore likely to be a change in emissivity which gives a false reading to the IR camera, possibly as a result of surface waves due to relaxation of the surface tension forces following the detachment phase (section 2.2.7).

The scheme which we describe is applicable for a tokamak divertor region, where, if the neutral pressure (created by evaporation from a liquid metal and/or conventional detachment) is large enough, ion energies up to tens of eV are likely to be reduced. Furthermore, $\mathbf{J} \times \mathbf{B}$ driven flow would be directed in the radial direction of the machine. Since the magnitude and directionality of plasma-induced currents in a divertor could be highly different (and time-dependent) from the radial plasma-induced currents as observed in this study, the magnitude of TEMHD effects may become more important in such a geometry. The rotational flow as described in this paper is likely to be absent in a tokamak divertor due to the different orientation of $\mathbf{B}$. Despite the differences in liquid metal flows between a tokamak and linear device, the oscillations are ultimately found to be induced by a detachment-like phenomenon of the plasma and differences in timescales between thermal equilibria of the liquid metal and the atomic physics taking place. The liquid flow and its time-varying nature affects the replenishment rate of the liquid surface and are therefore ultimately linked to liquid divertor design. A key parameter may be found in the effective heat conductivity between the liquid surface and cooled solid substrate, as this affects the cooling-rate of the surface during the phase of efficient vapour shielding (phase II) and hereby the extent of the variation in surface temperature/evaporation during a cycle. Hence, it is implied from these arguments that the oscillatory vapour shielding phenomenon as described here is generic and not specific to the linear plasma geometry as used in the experiments.

Oscillations may be an indispensable mechanism for the heat flux dissipation by the liquid surface to be self-regulated. It is hypothesized that matching the vapour pressure to the plasma pressure [164] is a key requirement to reach this regime. For the case of Sn, temperatures $>1800\,\mathrm{K}$ are required which can be reached during Edge-Localized-Modes and disruptions in tokamaks. Steady-state operation might be possible using adequate substrate materials and strong baffling of the divertor to prevent excessive ingress of Sn to the main chamber, along the lines of a vapour box concept as developed for Li [76, 45]. However, the same regime could be reached for temperatures around $1000\,\mathrm{K}$ when using Li for which, by being low-Z, a much larger impurity fraction can be tolerated in the plasma,

particularly under high-flux conditions where a high local redeposition is expected. The results as shown here using Sn may therefore be regarded as a proxy for Li experiments which are technologically more challenging due to the protected atmosphere required. Experimental investigations of steady-state Li vapour shielding are currently carried out and are expected to be reported soon.

Concluding, the Sn vapour/plasma system is found to oscillate around a stability point between plasma heat flux and surface temperature/evaporation, indicating the presence of a dynamical equilibrium set by the characteristic timescale of thermal processes in the liquid metal. The oscillations emerge from periodic changes between an attached plasma phase with strong evaporation of neutral Sn and a phase characterized by a detachment-like plasma culminating in a loss of the vapour cloud due to reduced evaporation. The oscillatory vapour shielding in response to a steady-state divertor plasma would also hold for a tokamak environment, given the nature of the processes and should therefore be considered in future liquid metal divertor designs. Regardless of the complicated oscillation mechanism, the results over the explored parameter range indicate oscillatory vapour shielding can have a significant reductive effect on the plasma power load received by the PFC [164].

2.4   Methods

2.4.1   Linear plasma generator Pilot-PSI

The experiments were performed in the linear plasma device Pilot-PSI, designed to study plasma-wall-interactions in ITER-like divertor regimes [87] and is schematically shown in figure 2.54a. Although part of the results from this experimental campaign has been published before [164], a description of the experimental setup is repeated here for completeness. Plasma in Pilot-PSI is produced by a cascaded arc source [88] operating at a DC current ranging 130-210 A. Both H and He gas were flown into the source at 2.5 slm. By switching on an axial magnetic field up to 1.2 T, the plasma is confined into a beam hitting the target resulting in a typical particle flux of $5x10^{24}\,\mathrm{m^{-2}\,s^{-1}}$. The electron temperature was 0.4-3.2 eV at densities $1\text{-}5x10^{20}\,\mathrm{m^{-3}}$ in the centre of the plasma column. These values were obtained from Thomson Scattering (TS) [154] which measures the plasma parameters at a position of 11 mm in front of a solid Mo target.

2.4.2   Diagnostics

The emission of Sn neutrals in the vapour cloud was recorded by a fast visible camera (Phantom V12) equipped with a 452.5 nm Sn0 filter positioned tangentially to the target
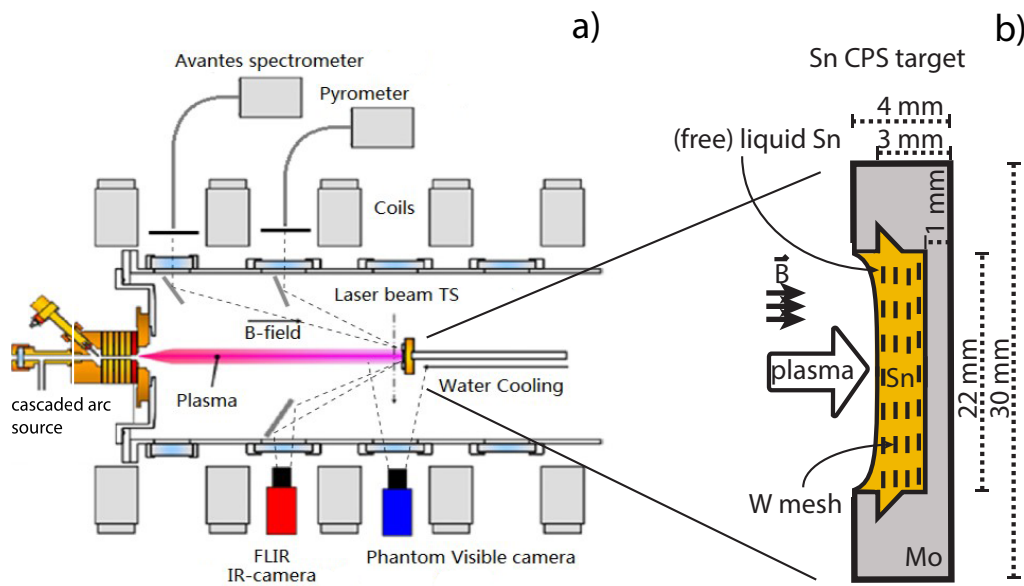
Fig. 2.54 Schematic drawing of Pilot-PSI and liquid sample design. *The linear plasma generator Pilot-PSI and the applied diagnostics are shown in a. Plasma is produced by a cascaded arc source. The expanding plasma is confined into a beam hitting the target by magnetic fields. A schematic drawing of the Sn CPS sample is shown in b.*

surface. Recordings of the neutral cloud dynamics were made at 10 kHz temporal resolution. Spectroscopic information of the emitting cloud was obtained using an absolutely calibrated two-channel spectrometer (Avantes ULS2048), measuring photon intensities in the range of 360-580 nm. The system was aligned at a ~15 degree angle from the target normal and focused at the target centre with a spot size of ~1 mm. The resulting spectral intensities in $W\,m^{-3}\,sr^{-1}\,nm^{-1}$ are multiplied by the path length in the plasma of 0.02 m to yield the line-averaged spectral radiance in $W\,m^{-2}\,sr^{-1}\,nm^{-1}$. Time frames during a phase of (relatively) constant surface temperature were selected. H and He discharges below 8 $MW\,m^{-2}$ are omitted as the continuum emission was found to be indistinguishable from the instrument noise. Finally, the surface temperature of the target was measured both using an infrared camera (FLIR SC7500MB) operated at 4.5 kHz and a multi-wavelength spectropyrometer (FAR associates FMPI). The latter provides an emissivity independent temperature measurement localized with a 1 mm diameter spot at the target centre which is used to determine the emissivity of liquid Sn used by the IR camera.

2.4.3 Liquid Sn sample technology

Splashing and ejection of liquid Sn into the plasma was limited by employing the so-called Capillary-Porous-System (CPS) in our sample manufacturing process [94]. This system for

liquid metal containment has been tested on a number of tokamaks [55, 74] and employs capillary action to resist gravity. The targets used in our experiments consist of a 3 mm deep Mo cup of 22 mm in diameter holding the liquid Sn which is immersed in a stack of W meshes with a pore size of 0.2 mm. A schematic drawing of the sample, including the direction of the plasma and the magnetic field in our setup is shown in figure 2.54*b*.

2.4.4   Exposure conditions

Strong evaporation was required to investigate the effect of the near-surface neutral Sn cloud on the power handling capabilities of the liquid target. A 4 mm thick Mo ring was placed behind the cup in order to reduce the heat conduction path between the target and the cooling structure due to the created interfaces. As such, a relative modest plasma power was found sufficient to yield a vapour cloud of similar vapour pressure as the plasma pressure [164].

The particle- (Γ_{part}) and heat flux (q) at the TS position were calculated from the radially resolved plasma density (n_{e}) and electron temperature (T_{e}) obtained from TS measurements during plasma exposure of the solid Mo target. The following equations have been applied [21]:

$$\Gamma_{\text{part}} = \frac{1}{2} n_{\text{e}} \sqrt{k(T_{\text{e}} + \gamma T_{\text{i}})/m_{\text{i}}} \tag{21}$$

$$q = \gamma_{\text{sh}} k_{\text{B}} T_{\text{e}} \Gamma_{\text{part}}. \tag{22}$$

$T_{\text{i}} \approx T_{\text{e}}$ is assumed where $\gamma = 5/3$ (adiabatic flow with isotropic pressure). The ion mass (H or He) is represented by m_{i}. The total sheath heat transmission coefficient (γ_{sh}) in equation 22 is set equal to 7 again assuming $T_{\text{e}} \approx T_{\text{i}}$ [21]. The particle- and heat flux profiles are typically Gaussian in Pilot-PSI. Consequently, a Gauss fit (FWHM 10.4 mm) is applied to the raw data and its peak value as given in table 5 is used for analysis. The fractional errors of n_{e} and T_{e} are <6 % and <7 % respectively for radial values ranging from -7 to 7 mm w.r.t. the centre of the plasma beam. Propagation of errors results in a fractional error of q_{ref} below 7 %. Given that q_{ref} results from a fit, this error is an upper limit.

The upstream plasma heat flux (q) should be highly similar for both the solid and liquid target case as the penetration of Sn neutrals up to the TS position is negligible (see figure 2.46) and the current and voltage traces of the source are found to be independent of the target material. The TS measurements made on solid references therefore represent the upstream electron temperature and density in both the liquid and solid case, hence, $q = q_{\text{ref}}$. Sn and Mo targets were also identically mounted ensuring equal conduction cooling properties.

gas	$\mathbf{B}$ (T)	T_e (eV)	n_e ($\times 10^{20}\,\mathrm{m^{-3}}$)	q_{ref} ($\mathrm{MW\,m^{-2}}$)
He	0.4	1.6	3.2	2.5
	0.8	2.4, 2.5, 2.7, 3.1	4.1, 5.5, 6.1, 7.0	8.2, 12.2, 16.0, 22.0
H	0.4	0.4	1.4	0.47
	0.8	1.2, 0.9, 0.9	0.6, 1.3, 1.5	1.3, 1.9, 8.0

Table 3 Experimental conditions during exposures of Mo and Sn targets. *The heat flux is expressed as the peak values from Gaussian fitted profiles of TS data. The gas flow was held constant at 2.5*slm *while the plasma current was varied between 130 and 210*A.

2.4.5 Data availability

All data that support the findings of this study are available from the corresponding author upon reasonable request.

2.4.6 Acknowledgements

2.4.7 Author contributions

The experiment was designed and executed by G.G. van Eden and T.W. Morgan while the overall strategy of the project is led by M.C.M. van de Sanden. The design and handling of the liquid Sn samples and the analysis involving atomic Sn rate coefficients was carried out by K. Kvon. All further analysis was done by G.G. van Eden with guidance of T.W. Morgan. The article was written by G.G. van Eden with contributions of all co-authors."

2.4.8 Competing interests

The authors declare that there are no competing financial interests.

3   Design and characterization of a prototype divertor viewing Infrared Video Bolometer for NSTX-U

G.G. van Eden, M.L. Reinke, B.J. Peterson, T.K. Gray, L.F. Delgado-Aparicio, M.A. Jaworski, J. Lore, K. Mukai, R. Sano, S.N. Pandya, and T.W. Morgan

Abstract - The InfraRed Video Bolometer (IRVB) is a powerful tool to measure radiated power in magnetically confined plasmas due to its ability to obtain 2D images of plasma emission using a technique that is compatible with the fusion nuclear environment. A prototype IRVB has been developed and installed on NSTX-U to view the lower divertor. The IRVB is a pinhole camera which images radiation from the plasma onto a 2.5 µm thick, $9 \times 7 \, cm^2$ Pt foil and monitors the resulting spatio-temporal temperature evolution using an IR camera. The power flux incident on the foil is calculated by solving the 2D+time heat diffusion equation, using the foil's calibrated thermal properties. An optimized, high frame rate IRVB, is quantitatively compared to results from a resistive bolometer on the bench using a modulated 405 nm laser beam with variable power density and square wave modulation from 0.2 Hz to 250 Hz. The design of the NSTX-U system and benchtop characterization are presented where signal-to-noise ratios are assessed using three different IR cameras: FLIR A655sc, FLIR A6751sc and SBF-161. The sensitivity of the IRVB equipped with the SBF-161 camera is found to be high enough the measure radiation features in the NSTX-U lower divertor as estimated using SOLPS modeling. The optimized IRVB has a frame rate up to 50 Hz, high enough to distinguish radiation during edge-localized-modes (ELMs) from that between ELMs.

3.1   Introduction

Measurements of the radiated power in the boundary of magnetically confined plasmas are critical for studying the physics of detachment and confirming the overall power balance. The InfraRed Video Bolometer (IRVB) diagnostic, tested extensively on the LHD and JT-60U devices, has been demonstrated to be a useful alternative or complement to conventional resistive bolometers [174, 116]. NSTX-U [111] is presently not equipped with absolute radiated power measurements and is exploring multiple techniques to

accomplish a variety of core and boundary physics missions, motivating demonstrations of an IRVB. A prototype IRVB, designed to provide a 1D poloidal view of the lower NSTX-U divertor has been extensively investigated on the benchtop and is currently being deployed for testing during the 2016 experimental campaign.

The IRVB concept relies on heating of a thin metal foil by absorbing radiation from the plasma where temperature changes measured by an IR camera are used to solve the 2D heat equation yielding the radiative power flux impinging on the foil [115]. While data interpretation and calibration of the IRVB is more complicated than that of resistive bolometers, the technique is attractive due to the avoidance of electrical pickup and the cost reduction possible due to the IRVB's increased bolometer channels per area. There is particular motivation in boundary plasma studies where the 2D radiation distribution near the x-point region of the tokamak would benefit from increased spatial resolution and when non-axisymmetric fields are used to create 3D radiation structures.

The IRVB hardware design, signal-to-noise ratio (SNR) and temporal response of the system are discussed hereafter. The performance of three different IR cameras with unique spatial and temporal specifications are quantitatively compared, demonstrating the SNR and temporal response of the IRVB at expected NSTX-U signals. The overall detection limits of the NSTX-U IRVB are finally compared to those of conventional resistive bolometers. A primary objective of the prototype is to explore the temporal resolution limits of the IRVB in order to confidently distinguish radiation during edge localized modes (ELMs) from that between ELMs. Scoping the camera performances is expected to aid future IRVB optimization and upgrades.

3.2 IRVB design for NSTX-U

3.2.1 Hardware

The IRVB is installed on the Bay-J upper port of NSTX-U, angled 75 degrees w.r.t. the horizontal axis. A poloidal view of the entire lower divertor and part of the centre stack is obtained using this position, as shown in Fig. 3.55. While the diagnostic is capable of imaging 2D radiation patterns, the field of view (FOV) is restricted to a single poloidal fan due to the in-vessel passive plate structures of NSTX-U. The basic hardware design is shown in Fig. 3.55a-b and consists of a 8" nipple section attached to a 6" nipple where the Pt foil detector flange is mounted between these parts. While nearly all previous IRVB designs utilized re-entrant layouts, this design was made to be attached directly to a gate valve, allowing installation after the main vacuum chamber is pumped down. The Cu plates holding the Pt foil in place are mounted in the centre of a 8" to 6" zero-

length adapter piece while an offset provides pressure relief between the chambers. The 2.5 μm thick Pt foil [175] of dimensions $9 \times 7 \, mm^2$ is calibrated on the bench to yield the spatially resolved thermal conductivity, diffusivity and emissivity [176]. An aperture flange is mounted on the front end, built directly into a double-sided flange which mates to the gate valve, while a 3" clear aperture Del Mar Photonics ZnSe window is mounted on the back end of the diagnostic. The aperture has dimensions $7.5 \times 2.75 \, mm^2$. The whole interior as well as both sides of the foil are blackened using Aerodag-G graphite spray, reducing stray-light reflections. The camera is located 43.8 cm from the foil and is set by the distance required to fully image the rectangular foil by the camera when using a 25 mm lens. Liquid nitrogen cooling requires the camera to be mounted horizontally and a gimbal mounted mirror is necessary to project the foil image onto the camera. The IRVB is pumped through the aperture down to the mTorr range followed by pumping through the foil chamber to reach UHV. A Santa Barbara Focal Plane SBF-161 IR camera is being used for the prototype IRVB. This camera is sensitive to 2-12 μm radiation (8-12μm using a Janos Tech. Varia 25 mm lens), has 128x128 pixels and can collect full frame images at 1.6 kHz. No magnetic shielding is required and the camera itself is non-magnetic.
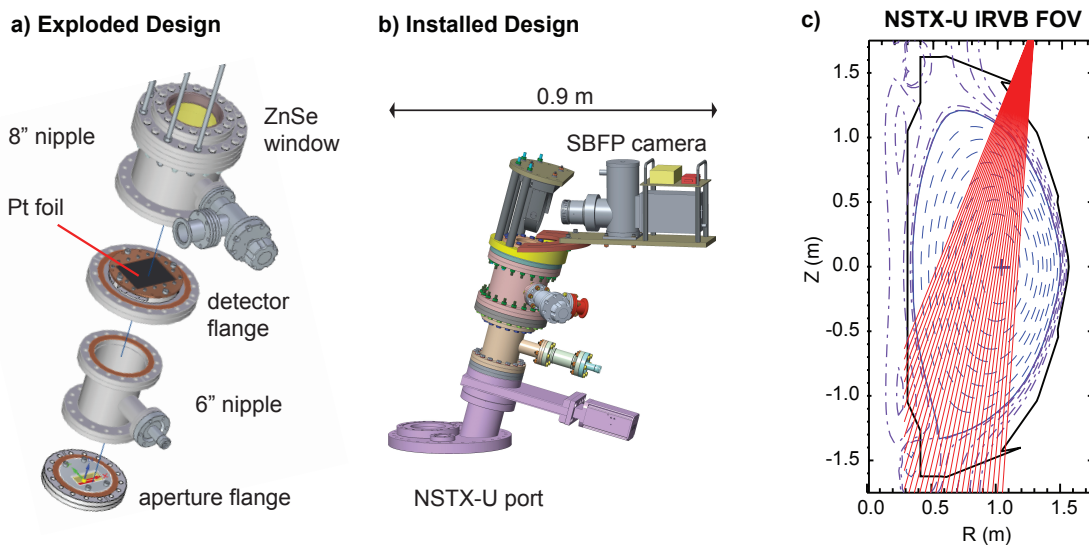
Fig. 3.55 Design and Field-Of-View of the IRVB. *Exploded design of the new prototype IRVB for NSTX-U (a). Installed design, including camera plate coupler and SBF-161 camera, connected to the gate valve (b). The FOV of the IRVB installed on the NSTX-U Bay-J upper port (c). The lines of sight for each IRVB super-pixel are shown relative to the NSTX-U flux surfaces.*

3.2.2 Expected power levels in NSTX-U

Camera pixels are averaged as to obtain a 1D array consisting of 30 bolometer super-pixels (channels) of $7.5 \times 2.11 \, \text{mm}^2$. SOLPS [177] modeling of a NSTX-U density scan (n_e= 0.2-1.0$\times 10^{20} \, \text{m}^{-3}$) with 10 MW of input power was used to scope estimated signal levels. Within this scan, simulations predict movement of narrow radiation features in the NSTX-U divertor and development of a MARFE-like radiation structure along the inner wall. Integration of the predicted emissivities along the IRVB sight lines, accounting for finite viewing cone geometry, yields IRVB signal levels ranging 0.2-190 W m^{-2}, as shown in Fig. 3.56, and above the estimated noise equivalent power density <2 W m^{-2}. These simulations do not include contributions from core radiation which outside of on-axis impurity accumulation is expected to be present but at a much lower level based on results from resistive bolometer diagnostics with similar viewing geometries.
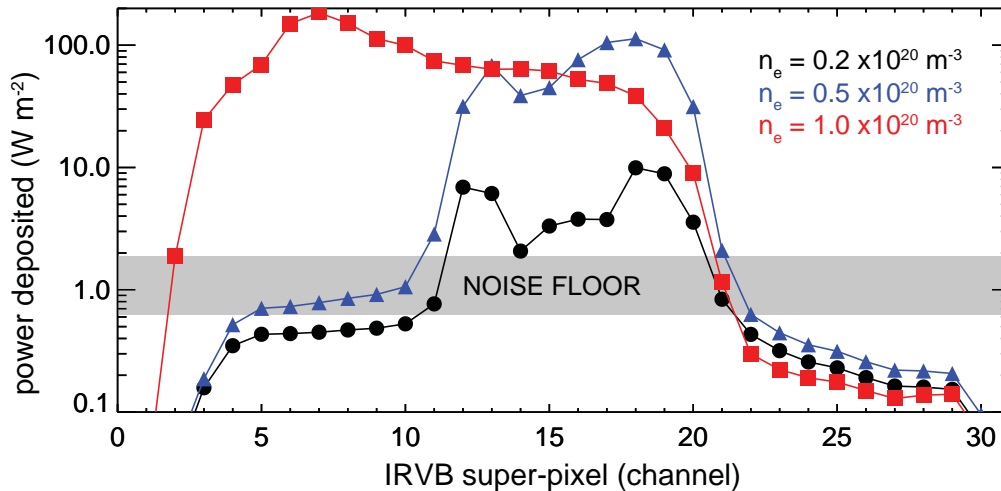
Fig. 3.56 Expected radiation levels in NSTX-U *Radiated power densities impinging on the IRVB super-pixels from SOLPS modeling of a 10 MW input power NSTX-U discharge.*

3.2.3 Benchtop testing of frequency and power response

The response of the IRVB to the range of power densities estimated from SOLPS were investigated by exposing the foil to a ~5 mW laser (Global Laser BlueLyte), emitting at 405 nm capable of modulation up to 750 kHz using an external function generator. A vacuum window mounted to the aperture plate in place of the gate valve sealed the diagnostic and fore-line pumping allowed the pressure in the IRVB chamber to reach <1 mTorr, low enough to neglect the effect of the foil cooling via conduction with air.

The diverging laser overfilled the IRVB aperture, leaving a rectangular irradiation pattern on the foil of power densities ranging 0.2-95 W m^{-2}, measured using a Thorlabs

PDA36A. A systematic laser frequency and power scan were performed while the IR signal levels were measured by three different IR cameras with unique sensor technologies: FLIR A655sc (microbolometer), FLIR A6751sc (InSb detector) and SBF-161 (MCT sensor). The laser frequency was varied 0.2-150 Hz (square pulse) at a power density of $95.5\,\mathrm{W\,m^{-2}}$ during the FLIR A655sc test and $40.9\,\mathrm{W\,m^{-2}}$ during FLIR A6751sc and SBF-161 tests.

The IRVB SNR can be increased by both averaging over frames (reducing temporal resolution) and pixels (reducing spatial resolution) [178]. In order to effectively compare different cameras on their expected performance in an IRVB, frames were averaged as to obtain ~200 frames per second (fps) regardless of the camera frame rate while neighbouring camera pixels were averaged yielding bolometer super-pixels of ~1/8 of the laser spot area. The camera specifications and subsequent bolometer performance after spatial and temporal averaging can be found in table 4. The number of IR pixels dedicated to image the foil relative to the total number of pixels was slightly different among the cameras, due to different lens characteristics and distance to the foil. The A6751sc and SBF-161 had a similar fraction of foil pixels to camera pixels while this fraction was 47 % lower for the A655sc camera. In case of similar foil to detector fraction as the SBF-161 setup, 47 % more pixels would have been attributed to image the laser spot, hereby increasing the A655sc performance by $\sqrt{(1.47 \times 10 \times 10)}/\sqrt{(10 \times 10)} = 1.21$ (1.02 for A6751sc).

Table 4 *Characteristics of cameras tested for IRVB.*

camera	frame rate (fps)	pixel number	bolo. frame rate (fps)	bolo. super-pixels
SBF-161	1610	128x128	200	4x4
A655sc	200	640x120	200	10x10
A6751sc	450	640x128	225	11x11

The raw IR signal increase measured by the IRVB super-pixel during heating of the foil by the laser has been divided by the standard deviation of the signal without laser pulse, calculated over 50 frames to yield the SNR. Figure 3.57*a* shows the results as function of laser power density while the IRVB was equipped with different cameras. The foil was heated by the laser during 1 s. The A655sc camera shows a poor performance below $10\,\mathrm{W\,m^{-2}}$ (even when considering a factor 1.21 increase in sensitivity) whereas the SBF-161 is superior over the A6751sc in the measured range of $1.5\text{-}31.4\,\mathrm{W\,m^{-2}}$. The SNR of both the A6751sc and SBF-161 cameras during benchtop testing are higher than that of resistive bolometers as deployed at Alcator C-Mod [120]. The resistive bolometer sensitivity as measured on the benchtop, absent of the inherent electromagnetic interference in the tokamak test cell, is however roughly 4 times higher than that of the best IRVB performance.
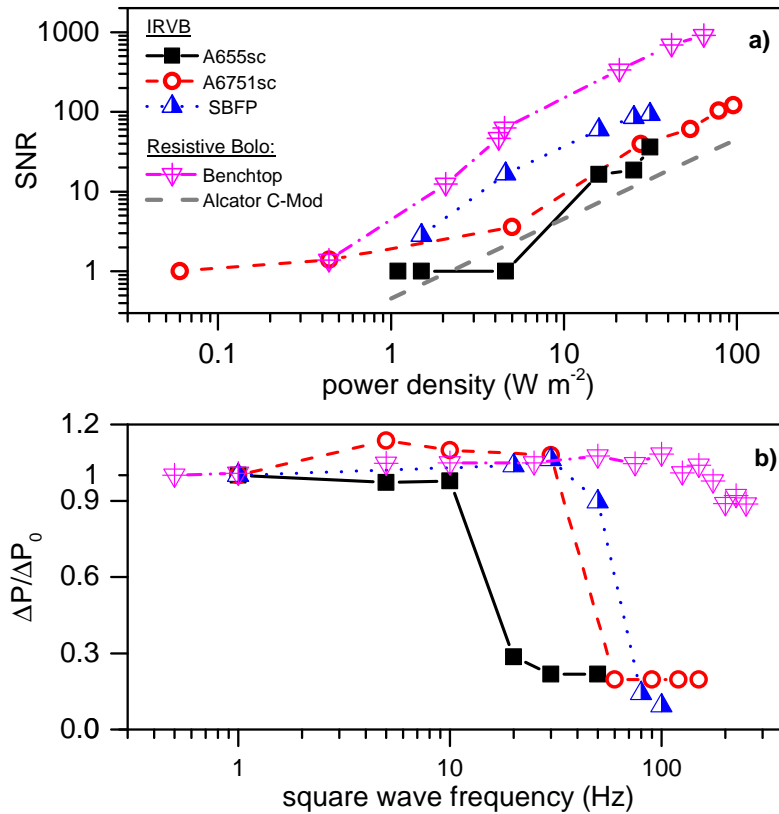
Fig. 3.57 Signal-To-Noise Ratio and time response of IRVB. SNR of the IR signals received by different cameras as function of incident power density from the laser (a). Fig. *b* shows the square wave signal increase (ΔP) normalized to the slowest pulse rate (ΔP$_0$) versus laser frequency.

The temporal shape of the radiated power absorbed by a single super-pixel can be approximated (neglecting spatial diffusion) by the proportionality: $P_{\mathrm{rad}} \propto P = S + \tau \partial S / \partial t$, where *S* represents the raw IR count level while τ is the time constant. Similarly, for the resistive bolometer analysis, the measured bridge voltage is used for *S*. ΔP represents the difference between *P* during and prior to laser exposure. The laser pulse frequency was varied while ΔP of a single, 200 fps, super-pixel was measured. As the laser power is held constant, ΔP should be independent of frequency provided the IRVB can temporally resolve the signals. The results are shown in Fig. 3.57*b* where ΔP is normalized to the signal increase at slowest pulse rate (ΔP$_0$) and compared between camera setups as well as that of the resistive bolometer. The ultimate time response of the resistive bolometer, digitized using standard IPT-Albrecht analyzer modules with a 1 kHz low-pass filter, is not determined in the measured range. For the IRVB, varying signals up to 50 Hz can be reconstructed when equipped with the SBF-161 and A6751sc cameras. This is measurably

lower than that of the resistive bolometer during lab testing but expected to be sufficient to discern between ELM and inter-ELM phases in the type-I regime.

3.3   Conclusion

The development of a prototype IRVB for NSTX-U is completed and recently installed. Benchtop laser testing of the device has shown that the SNR is high enough to detect divertor radiation features as predicted by SOLPS modeling. Radiative features up to 50 Hz can be resolved using the SBF-161 camera while the SNR is competitive to resistive bolometers in a tokamak environment. Finally, benchtop laser testing has provided benchmark data of the noise levels and temporal response of the system equipped with three different IR cameras to be used for future IRVB designs.

3.4   Acknowledgements

4 Plasma radiation studies in Magnum-PSI using resistive bolometry

G.G. van Eden, M.L. Reinke, S. Brons, G. van der Bijl, B. Krijger, R. Lavrijsen, S.P. Huber, R. Perillo, M.C.M. van de Sanden, T.W. Morgan
Submitted to Nuclear Fusion

Abstract - Both the physics of divertor detachment and vapour shielding are characterized by a relatively large amount of radiation produced in the divertor. The linear plasma generator Magnum-PSI is well-suited to study such processes due to its ITER-divertor relevant plasma conditions, simplified geometry and diagnostic accessibility. The need the quantify the plasma radiated power close to the target surface motivated the development of a 4-channel resistive bolometer for Magnum-PSI, and marks the first deployment of such a diagnostic on a linear device. An axially resolved measurement of plasma emission at arbitrary distances from the target surface is now possible. The radial position of the detector can be varied, hereby viewing the full diameter of the plasma column or down to a central region. The overall system design is discussed alongside a comparison of the spectral absorbance of carbon-coated versus non-coated Au/Al bolometer sensors. Despite low electron temperatures of the plasma (1-5 eV), the observed power densities were found to be 10-37 times the sensor noise floor of $\sim 0.1\,\mathrm{W\,m^{-2}}$. A synthetic diagnostic based on collisional radiative model calculations from ADAS could well match observed values from H and Ne plasmas while the measured values for Ar and He were more difficult to reproduce. The obtained findings allow for approximate power balance calculations in Magnum-PSI indicating that maximally $\sim 27\,\%$ of the total power is lost by radiation in the case of Ar. The results demonstrate the feasibility of resistive bolometry in low temperature high density plasma regions and on long timescales ($>450\,\mathrm{s}$) which is of relevance to ITER. Due to long-term temperature drifts which were observed, a planned upgrade involves the installation of a shutter and FPGA-based electronics for increased accuracy.

4.1 Introduction

The power entering the scrape-off-layer (SOL) in future fusion reactors such as DEMO is expected to be several times larger than the predicted levels for ITER [25]. Ensuring

the integrity and successful long-term heat handling performance of the tungsten (W) ITER divertor over time is challenging, making a solution for DEMO even more difficult to attain. In DEMO, reducing the exhaust power to acceptable divertor heat loads is foreseen through strong radiative dissipation in SOL and divertor [147]. Any potential loss of control over this scheme is however still likely to result in divertor heat fluxes exceeding limits which can be safely tolerated, hereby potentially damaging components [145].

Operation in semi- or full-detached divertor plasma scenarios are envisioned to mitigate this issue [31]. Here seeding impurities will be introduced which will radiate predominantly in the plasma edge and SOL to reduce the parallel heat flux prior to arrival at the divertor surface [107]. From the material side, liquid metals are considered for DEMO as a plasma facing material in the divertor [142].

Such materials may further aid in increasing the damage tolerance in response to high heat loads since the material can be self-replenishing [47] and self-protecting once the vapour shielding regime is entered where evaporated impurities act as a partial barrier between the plasma and the liquid surface [164, 179]. In both plasma detachment and vapour shielding, the incoming plasma energy is partially converted into radiation and neutral particles which are spread over a wider area, hence reducing the local target heat flux.

Quantifying the amount of power dissipated via radiation in the divertor SOL is identified as a key parameter in both detachment and vapour shielding studies but it is unclear how this extrapolates to reactor designs. Particularly steady-state radiated power loss produced close to the target surface, as is the case during vapour shielding, has not been studied in detail up to now.

The Magnum-PSI linear plasma generator [82, 85] offers the capability of replicating ITER divertor target conditions while allowing for ease of diagnostic access, controllable conditions and simplicity of the plasma beam geometry compared to full-scale tokamak tests. While also the neutral pressure during operation can be varied in the expected ITER range (1-10 Pa) [180], the parallel heat transport, $q_{\parallel}$, cannot be fully replicated which impacts the feasibility of investigating the complete physics of detachment. Despite this, linear plasma generators offer a useful platform in validating radiation modelling for low-temperature, high-density plasmas with a variable background pressure, to address important questions related to detachment physics [124].

Current experimental campaigns in Magnum-PSI are aimed at understanding the physics occurring during the change from sheath-limited to detached plasma regimes, similar to previous studies in Pilot-PSI [181]. Also, extensive campaigns investigating the power handling capabilities of liquid Sn and Li plasma facing components (PFCs) and the

physics of liquid metal vapour shielding have been performed in both machines [164, 179]. However, no means of a direct measurement of the radiated power loss from the plasma had been available up to now.

The need to quantify radiated power loss at arbitrary distances from the target surface motivated the development of a bolometry system [127] for Magnum-PSI. Despite a lower time resolution and overall sensitivity, a resistive bolometer system was chosen due to its approximately flat response over the plasma photon energy range and superior long-term sensitivity stability as compared to e.g. AXUV diodes [126]. Since the Magnum-PSI plasma volume is much smaller (FWHM≈20 mm) than e.g. (divertor) tokamak plasmas and the electron temperature (T_e) is typically only a few eV, the line-integrated emissivity was expected to be low, potentially even below the typical resistive bolometer noise-equivalent-power density of ~0.1 W m^{-2}. However, initial modelling of a synthetic diagnostic and a collisional radiative model using the ADAS package [97] simulating the Magnum-PSI plasma yielded a signal-to-noise ratio (SNR) >5, providing confidence in the feasibility of resolving the radiated power from the plasma above the instrument noise.

A 4-channel resistive metal foil bolometer system viewing the plasma beam perpendicularly, close to the target region, has hence been designed and installed. Two channels have been provided with a thin layer of deposited carbon to increase absorption in the visual wavelength range [132], with two left uncoated for comparison purposes. The hardware design and spectral response of the Magnum-PSI bolometry system are described. Measurements of steady-state radiated power loss close to the target surface in Magnum-PSI are reported for the first time, showing challenges associated with long-pulse measurements. Successful bolometry operation is further demonstrated during divertor-like detachment studies, impurity seeding experiments and volumetric plasma emission tests. The SNR during operation in H, He, Ne and Ar at a range of plasma conditions and the fraction of radiation in the overall power balance are presented.

4.2 Methods

4.2.1 Magnum-PSI

The Magnum-PSI linear plasma device utilizes a wall-stabilized cascaded arc source [182] to produce a low temperature (1-5 eV), high-density (~10^{20} m^{-3}) plasma. A superconducting magnet produces a variable magnetic field strength up to 2.5 T, to confine the plasma into a beam (FWHM ≈20 mm) allowing for steady-state exposures of target materials in ITER-relevant conditions [183]. The background pressure near the target can be reduced to < 1 Pa by means of a differential pumping scheme along three chambers from source

to target [184], and the near-surface plasma is considered to be in the strongly-coupled regime [85]. Both the positions of the plasma source and that of the target can be adjusted along a wide range along the centre axis of the machine (z).

Radial profiles of T_e and n_e were measured at a position of 1250 mm from the source (close to the target region) using a Thomson Scattering (TS) system [154] located at z=0. The particle flux received by the target was calculated from T_e and n_e assuming γ_{sh}=7 and $T_i \approx T_e$ as well as adiabatic flow with isotropic pressure yielding $\gamma = 5/3$ [185]. The radial particle- and heat flux profiles in Magnum-PSI can be well approximated by Gaussian functions which allow for analytical 2D areal integration yielding the total power in the beam. The targets used during the plasma emissivity and detachment experiments were 1 mm thick W disks of 30 mm in diameter.

4.2.2 Resistive bolometer

The Magnum-PSI bolometer is a 4-channel resistive metal foil detector from IPT Albrecht. Each sensor of dimensions 1.3x3.8 mm^2 is a 5 μm thick gold (Au) foil covered with a 150 nm thick aluminium (Al) heat conducting layer. Two out of four sensors are additionally provided with a 150 nm thick C layer to enhance absorption at longer wavelengths. The spectral absorption of this multi-layered sensor is shown in Fig. 4.58. Further details can be found in A.3.
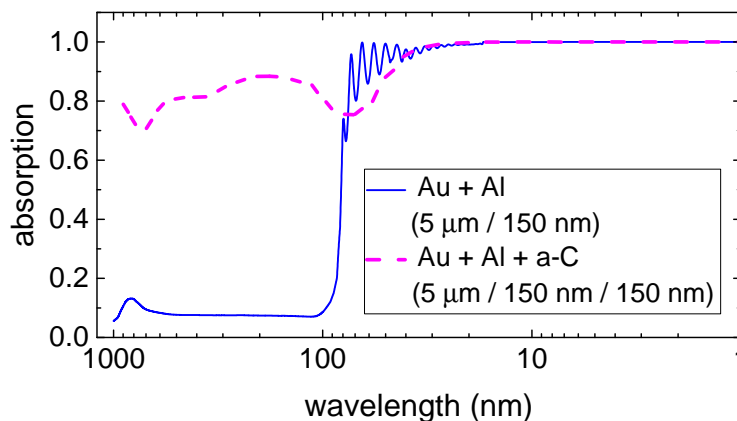
Fig. 4.58 Spectral absorption of bolometer sensors. The (uncoated) Au+Al and (coated) Au+Al+a-C bolometer sensors are compared for the range of 1-1000 nm. Details are provided in A.3.

The temperature of the sensor rises due to impinging radiation and neutral particles which results in an electrical resistance change in two opposite legs of a Wheatstone bridge circuit, at a theoretical detection limit of 1 μW cm^{-2}. The two remaining resistors in the circuit are shielded from radiation in order to correct for temperature drifts of the detector

head as a whole. Each sensor is excited by a $U_{pp} = 20\,\text{V}$, $20\,\text{kHz}$ sine voltage provided by an individual amplifier unit. Any imbalance arising between the heat absorbing and shielded resistors is obtained from the output signal using AC synchronous detection [127]. The resulting bridge voltage is consequently amplified between 10 and 5000x and demodulated and filtered by the amplifier unit. The DC output voltage from the amplifier, U_b is send to a digitizer (12-Bit MC USB-200) and finally stored in a PC. The parameter ΔU_b is defined to be the voltage difference during plasma radiation exposure with respect to the level before (hence a DC imbalance). The power absorbed by each sensor (P_s) is then obtained from ΔU_b using the following equation [134], taking into account the sensor sensitivity S (V/W) and time constant τ (s):

$$P_s = \frac{1}{S}\Big(\Delta U_b + \tau \frac{d\Delta U_b}{dt}\Big). \tag{23}$$

The calibration of S and τ are done using existing methods [186] and is discussed in A.2. Equation 23 is a simplification of the full relation which includes the cable resistance and capacitance [135]. The cable length used in this study is $10\,\text{m}$ which results in a cable resistance equal to $1.1\,\%$ of the bolometer input impedance, leading to an error in the radiated power of similar magnitude.

The power incident on the bolometer detector (P_s) can be related the line-integrated brightness of the plasma ($\int \varepsilon \, dl$) within the bolometer viewing cone using the geometrical constrains set by the aperture size (A_{ap}), sensor size (A_s) and distance from sensor to aperture ($l_{s,ap}$)

$$P_s = \frac{1}{4\pi} \frac{\cos^2(\theta)\, A_s\, A_{ap}}{l_{s,ap}{}^2} \int \varepsilon \, dl \tag{24}$$

where θ indicates the misalignment of the surface normal of the aperture and sensor surfaces to the line of sight. The latter angle varies maximally $6.1°$ which reduces the effective sensor surface by $1.1\,\%$ and is neglected during analysis.

4.2.3 Field of view

Projections of the bolometer FOV in the axial and radial direction of the plasma beam in Magnum-PSI are shown in Fig. $4.59a$ and $4.59b$ respectively.

The extent of the observable volume in the radial direction of the beam (ΔR) as function of the adjustable distance between sensors and aperture, $l_{s,ap} = 72.8 - 172.8\,\text{mm}$, can be expressed as

$$\Delta R = 2h_d\Big(\frac{l_{p,d}}{l_{s,ap}} + \frac{1}{2}\Big) \tag{25}$$
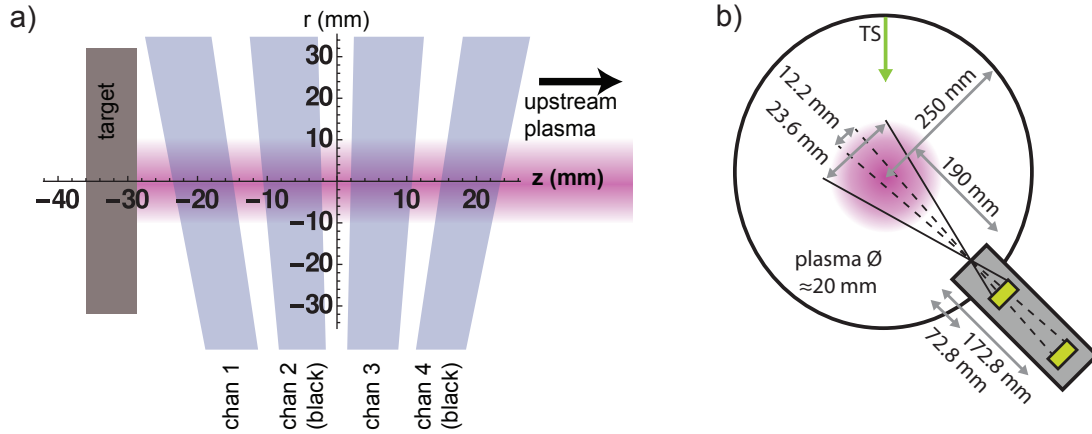
Fig. 4.59 Bolometer field-of-view. Axial extent of the plasma beam when $l_{ap,d}$=72.8 mm (*a*). The radial extend of the viewing cone in the case of shortest distance between sensor and aperture is 23.6 mm (solid lines) and 12.2 mm at the farthest position (dashed lines) (*b*). The axial position of the target can be freely adjusted along *z*.

with h_d=3.8 mm the sensor height and $l_{p,d}$=190 mm the distance between the plasma beam centre and the aperture. When the detector is moved closest to the aperture, ΔR is 23.6 mm which is similar or slightly larger than the typical FWHM of the plasma beam, depending on operational settings. Its radial viewing width decreases to 12.2 mm if the bolometer is positioned farthest away from the aperture which allows for better radial resolution at the expense of signal level due to the increased solid angle.

The coordinate *z*=0 corresponds to the TS measurement position [154] where the total observable *z*-range by the bolometer is approximately 50 mm (Fig. 4.59*a*). It is known that the plasma parameters in Magnum-PSI may change along *z* when comparing source to target conditions, as is reported [187] from studies in Pilot-PSI, the predecessor of Magnum-PSI. Especially variation in T_e may lead to significant changes in the plasma emission ε. However, given that *z*-range spanned by the bolometer is much smaller than the typical distance from the FOV to the plasma source (Δz=1250 mm) we make the assumption that T_e and n_e are independent of *z* around the bolometer viewing position which makes the interpretation of the signals by different sensors simpler.

This assumption is no longer tenable when the target surface is brought in close vicinity of the FOV. In such cases, large variations in plasma emissivity along *z* may be induced due to recycled neutrals and the formation of a pre-sheath. The pre-sheath length in the sheath-limited strongly coupled regime can be approximated by the ion-neutral charge exchange mean free path, which is typically ~10 mm for H and ~1 mm for Ar in

standard Magnum-PSI conditions with a floating target [188, 189]. Similar radiation levels for each of the 4 sensors are thus to be expected if the target is located at $z \lesssim$ -35 mm.

4.3 Results and discussion

4.3.1 Time-evolution of plasma emission

The line-integrated emissivity obtained by channels 2 and 3 during a 225 s plasma exposure of a W sample are shown in Fig. 4.60. This parameter is evaluated using Eq. 24 and calculating P_s as in Eq. 23 from the increase of the bolometer bridge voltage due to impinging plasma radiation (ΔU_b). A linear drift correction has been applied to ΔU_b by assuming the phase of Ar emission (t=25-110 s) to be constant in time, which is confirmed by current and voltage measurements of the plasma source. Furthermore, an offset correction has been applied by defining ΔU_b=0 at t=0. The digitizer operated at 100 samples per second and no data smoothing is used.
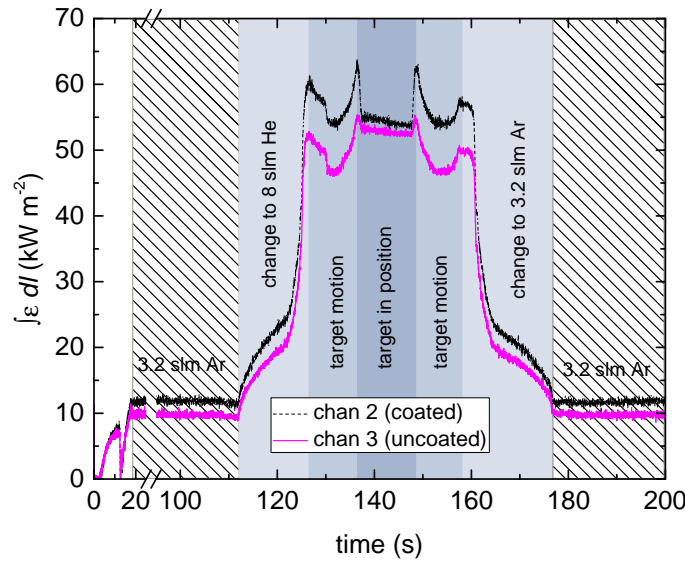
Fig. 4.60 Time evolution of the line-integrated emissivity from the plasma. The radiated power, measured by channels 2 and 3, is strongly affected by the gas species (Ar and He), plasma conditions and presence of the target near the bolometer FOV. The difference in absorbance between channel 2 (coated) and channel 3 (uncoated) can be clearly seen.

Several phases during the plasma discharge, distinguished by different settings of the plasma source and position of the target, can be identified when examining the emission evolution in Fig. 4.60. The magnetic field strength is held constant at 1 T. Firstly, the plasma source is ignited at t=0 by feeding 3.2 slm (standard litre per minute, equal to 4.5×10^{20} particles s^{-1}) Ar gas and establishing a source current of 105.5 A. The target is far away

from the bolometer FOV at this stage. Secondly, at t=110 s, the Ar gas flow is reduced while He is gradually injected in the source up to 12 slm and the source voltage adjusted to reach I_s =126 A. The radiated power clearly increases in this phase. Thirdly, the target is moved just in front of the bolometer FOV (z=-28.5 mm) at t=130-149 s, affecting the local emission properties due to particle recycling and subsequent cooling and recombination of the plasma near the target. A z-dependency on the plasma emission is clearly visible from the strong reduction in the signal of channel 2 while channel 3 increases. After retraction of the target at t ~150 mm, the gas flow is gradually switched back to Ar reaching 3.2 slm at t=175 s.

From the steady-state emission phase in Ar (t=25-110 s) with the target far away from the FOV, the difference in absorbance between channels 2 and 3 is clearly seen. The blackened channel 2 shows a higher absorbance of roughly 22 %. Interestingly, the difference between channels 2 and 3 reduces to ~15 % during the phase of pure He emission, likely due to a change of the dominant line emission towards smaller wavelengths than the optical range. The latter increased absorbance factor is similar to values of 13-15 % obtained in the divertor region of TCV [132].

Figure 4.61a shows another time evolution of plasma emission throughout a Ar/H discharge including a period of N_2 seeding. The sample rate of the bolometer digitizer was only 10 Hz and no smoothing has been applied. Nitrogen is injected near the target chamber wall via a remote controlled pressure valve. The N_2 pressure distribution close to the plasma can be considered uniform since the distance from plasma to injection valve is much larger than the plasma beam diameter. The raw bolometer output voltage has again been corrected for linear drifts and an offset voltage has been applied by taking ΔU_b=0 at the phase before igniting the plasmas source (at t=0-2 s). The z-position of the target with respect to the bolometer FOV and the pressure in the target chamber are shown in panels 4.61b and c respectively while panel d shows the gas flow in the source. It is clear that changing from Ar to H is accompanied by strongly rising plasma emission.

As inferred from 4.61c, the gas pressure in the target chamber temporarily increases as a result of opening the N_2 seeding valve, followed by a similar reduction in pressure when the valve is closed. The period of N_2 addition is highlighted in Fig. 4.61 by the grey box and vertical dotted lines. The overall pressure equilibrates at 1 Pa for the remaining time and is found to be independent of the gas species used. We therefore conclude that the strong increase in bolometer signal is due to the radiated power flux rather than carried by neutrals from the plasma. The effect of the target position on plasma emission is small but measurable, as indicated by the slight increase at t=175-220 s (dashed vertical lines).
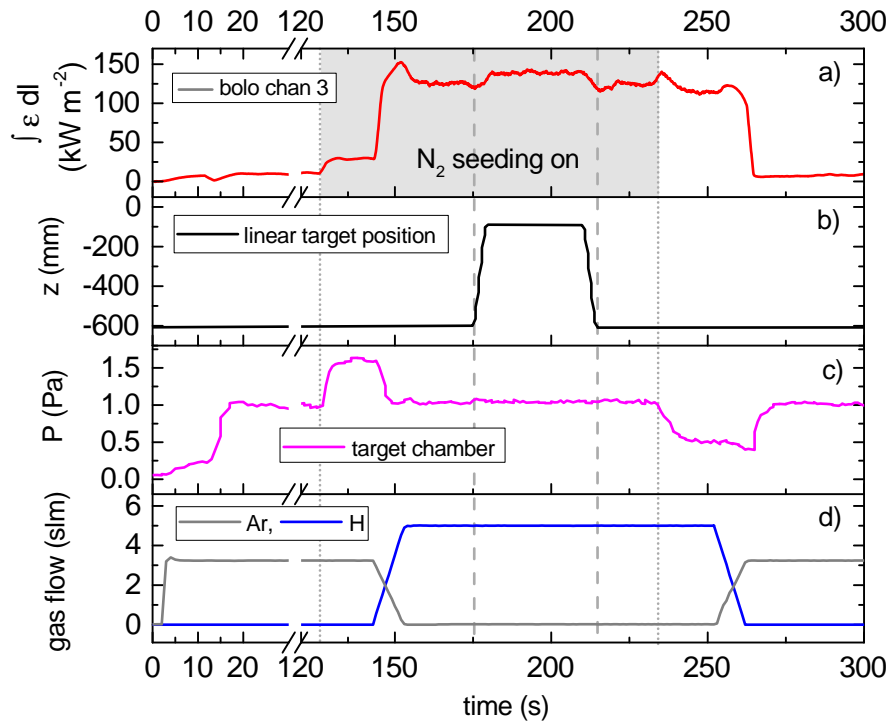
Fig. 4.61 Plasma radiated power with N$_2$ seeding. Time-dependent line-integrated emissivity from a Ar/H plasma with N$_2$ injection (*a*), distance between target and the bolometer FOV (*b*), pressure in the target chamber (*c*) and gas flow in the source (*d*). N$_2$ is seeded at location *z*=0 for a duration as illustrated by the grey box in panel *a* and indicated by the dotted lines. The phase where the target is moved close to the bolometer FOV is highlighted by the dashed vertical lines.

The N$_2$ seeding valve is opened at *t*=125 s when an Ar plasma is present, resulting in tripling the radiated power loss. Enhanced radiation by N$_2$ species and/or the potential increase of n_e are expected to account for this, as T_e is likely to drop due to the gas puff which should result in lower emission from both Ar and N$_2$. The change to H in the plasma source, initiated at *t* ~135 s, results in a 5-fold increase of the line-integrated emission compared to the previous level of Ar+N$_2$. Enhanced radiation due to presence of Molecular Assisted Recombination (MAR) processes occurring at the plasma beam edge [190, 162] is the dominant process responsible for this, potentially intensified by H$_2$-N$_2$ mixing. A study of the origin of radiation from this mixture and the overall H$_2$-N$_2$ chemistry in the Magnum-PSI plasma is described elsewhere [191].

4.3.2 Detachment studies

Figure 4.62*a* shows the time evolution of steady-state plasma operation in H while the background pressure in the target chamber is varied. The target position with respect to the centre of the bolometer FOV as a function of time is shown in panel 4.62*b*. The

background gas pressure in the target chamber is increased up to levels of 4 and 2 Pa by injecting H_2 gas at the wall at a position of z=0. The overall background pressure without additional H_2 injection is 0.34 Pa. As a result of increasing background pressure, the plasma transitions from sheath-limited conditions to a detached regime characterized by reduced plasma pressure in the near-surface region as measured by TS. The target heat flux reduces as evidenced from calorimetry and a reduction in visible light emission in front of the target.
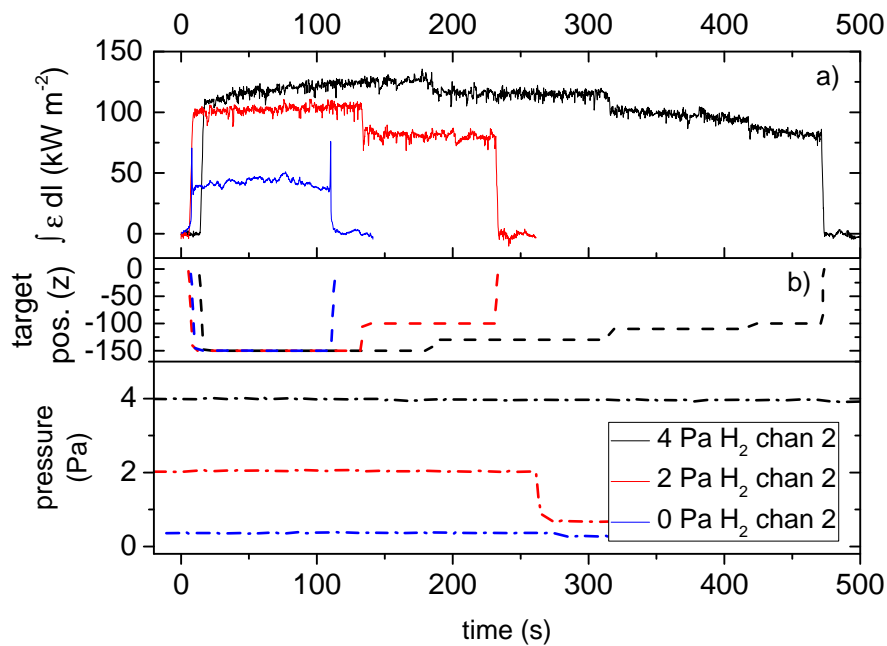
Fig. 4.62 Time evolution of line-integrated emissivity at increased background pressures. Time evolution of line-integrated emissivity during plasma operation in H at increased background pressures (*a*) and position of the target as function of time (*b*). The background pressure in the target chamber is shown in panel (*c*). Radiated power loss from the plasma increases with increasing H_2 background pressure. The position of the target affects the emissive region and therefore the bolometer measurement. Given that the background pressure remains constant during the bolometer measurement, the drift in the signal (notably at 4 Pa) is not attributed to a change in the neutral particle flux hitting the sensor surface.

The target was located at z=70 mm each time operational settings were adjusted. This position fully blocks the bolometer detector from receiving radiation while neutrals can still diffuse towards the sensors (Fig. 4.59). A zero procedure which equilibrates the Wheatstone bridge resulting in ΔU_b=0 is then applied before moving the target to z= -150 mm in order to compensate for gas pressure variations which may result from the change in plasma conditions. Caution is normally required when interpreting bolometer signals due to possible effects of high-energetic charge exchange (CX) neutrals hitting

the sensors [129]. This issue is however expected to be much reduced in Magnum-PSI where the energies of such neutrals are small ($T_n \leq T_i \approx T_e \approx 5\,\text{eV}$). Active pumping of the Magnum-PSI target chamber [86] which is connected to the bolometer housing by additional air vents next to the aperture (see A.1), further mitigates parasitic heating of the sensors due to neutral impact.

The electron densities in the cases of 4, 2 and 0.34 Pa, are 1.5, 1.1 and $1.0\text{x}10^{20}\,\text{m}^{-3}$ respectively while T_e is 0.5, 1 and 2.1 eV. Increasing the background pressure to 2 Pa by H_2 gas puffing causes the emission to increase by a factor 2.2 as compared to the reference case without adding gas. This is attributed to both increased line emission from excited neutrals and enhanced recombination radiation since T_e decreases from 2.1 to 1 eV which means that the plasma changes from an ionization dominated to a recombination dominated regime at the mentioned typical density. Doubling the background pressure again to 4 Pa only increases the radiated power by a factor 1.2 with respect to the level at 2 Pa background pressure. The modest increase in radiation resulting from the latter step is explained by increased neutral line emission as the plasma already resides in a recombination dominated state as opposed to the change from 0.34 Pa to 2 Pa.

The stepwise reduction in emissivity over the course of time for the cases of 4 and 2 Pa are due to the changing target position. In detached conditions, T_e near the target is strongly reduced as opposed to attached conditions. In line with visible camera observations, the region of maximum brightness moves away from the target surface while this is highest just in front of the target surface during sheath-limited conditions. For this reason, moving the target closer to the bolometer FOV results in reduced line-integrated emissivity as observed in Fig. 4.62.

Although the bolometer functioning is designed to be immune to thermal excursions of the detector head, slowly drifting signals at presumably constant plasma irradiation were observed as can be clearly seen in the H plasma exposure at a duration of $t >450\,\text{s}$ in Fig. 4.62. The bolometer detector in its current design is thermally isolated and did not have a shutter installed. The temperature of the detector housing thus slowly increases due to a non-uniform areal power flux centered on the active sensor array by radiation through the aperture. Due to differences in path length between the passive and active sensor arrays with respect to the region of power input (centered on the active array), it is hypothesized that a slight imbalance between the active and passive legs in the Wheatstone bridge arises which causes a drift and/or offset in the signal.

This issue is not present during most bolometer applications on current tokamaks where the pulse duration is in the order of seconds or less and front-end heating of the detector housing by radiation is negligible. Resistive bolometry operation in future fusion

devices operating at long pulse lengths may however encounter this effect. Also, the calibration constants may slightly change as a result of thermal drifts which is not taken into account so far. Improving the thermal stability of the detector and rebalancing each channel on a regular time base by blocking the impinging light via a shutter can help mitigate the drift issue. Periodic remote calibration may improve accuracy during long time-scale exposures. The aforementioned issues can be solved by utilizing novel FPGA-based bolometer electronics [140] in combination with the installation of a shutter system, both foreseen to be implemented in the near future.

4.3.3 Volumetric plasma emission and comparison to synthetic diagnostic

Radiated power loss from H, He, Ne and Ar plasmas in Magnum-PSI was experimentally investigated for T_e and n_e ranging 1-6 eV and 0.3-25$\times 10^{20}$ m^{-3} respectively in the centre of the plasma beam. Measurements were carried out during steady-state plasma conditions while the target was positioned at z= -70 mm, allowing for an almost constant axial emission profile around the bolometer FOV. Prior to the measurement, the target fully obstructed the bolometer FOV while neutrals from the plasma could diffuse towards the sensor in order to set U_b=0, thus cancelling the influence of neutrals on the bolometer signal.

A 0D time-independent collisional radiative model (CRM) provided by ADAS [97] was applied in parallel to calculate the radially resolved plasma emissivity $\varepsilon(r)$ (in W m^{-3}) in the Magnum-PSI plasma beam. Radial profiles of n_e and T_e measured at z=0 by TS simultaneous to the bolometer measurement were fitted by Gaussian functions serving as inputs to this model. ADAS photon emissivity coefficients (PEC values in W cm^3) were calculated for a range of suitable n_e and T_e values using the ADAS405 routine which simultaneously solves the time-independent atomic state population distribution at specified conditions taking ADAS ADF11 data as input [97]. The PEC values were subsequently interpolated by both the radial values of T_e and n_e in the plasma beam. The obtained radial PEC value is then multiplied by $n_e(r)$ and the density of radiating atoms $n_a(r)$ (sum of neutrals and ions) obtained from the (local) atomic population distribution provided by the CRM, yielding $\varepsilon(r) = PEC(r)n_e(r)n_a(r)$.

A number of synthetic sight lines from bolometer detector to the plasma is then considered, of which the angle with respect to the centre line is varied between 0 and 2.95°, set by ray tracing for the case of $l_{s,ap}$ =72.8 mm. The power density collected by each unique synthetic viewing cord Q_i is consequently found by summing the product of the path length dl (distance between radial coordinates) and the local emissivity $\varepsilon(r)$ over the entire length of the viewing cord traversing the plasma: $Q_i = \sum_i \varepsilon(r)dl$.

In this way, the integral $\int \epsilon \, dl$ which appears in Eq. 24 can be approximated for each synthetic line of sight. Power incident on the detector for each viewing cord easily follows by inserting the hardware dimensions in this equation while unity spectral absorption of the radiation by the sensor is assumed for simplicity. Averaging over the total number of viewing chords finally yields the total power incident on the detector (P_s). This procedure is repeated for all gas species and plasma conditions where a simultaneous measurement of bolometry and TS was performed.

The comparison of power incident on the bolometer detector (in mW) is compared to the results from the synthetic diagnostic based on the same plasma parameters in Fig. 4.63. The dashed line indicates a 1:1 agreement. Considering the practical noise equivalent power density of $0.1\,\mathrm{W\,m^{-2}}$, a SNR of 10 (He) to 37 (Ar) is obtained. The match between
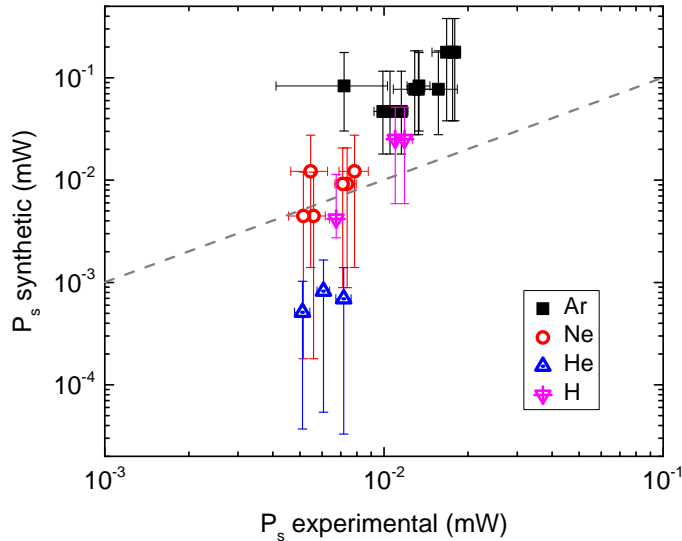
Fig. 4.63 Comparison between average power received by the bolometer detector and a synthetic diagnostic. Expected radiation levels are calculated with a CRM from the ADAS package [97] while taking T_e and n_e measured by TS as inputs.

the synthetic diagnostic and the measurements are found to be in agreement within error for H and Ne species while the bolometer measurement for He is overall 10 times higher than predicted by modelling. In contrast, the measurement of the power incident on the sensor during Ar plasma exposure is a factor 10 lower than predicted. A wide range of emission levels at our conditions is expected based on atomic physics considerations where differences by an order of magnitude in the cooling functions of He, Ne and Ar species at similar values of T_e are present [192]. This behaviour is however not reflected in the measured values of power incident on the detector.

In order to explain this apparent discrepancy, it should be realized that non-coronal radiation, plasma opacity effects, charge exchange recombination and plasma transport phenomena affecting radiation are not taken into account in the model described above. Detector reflectivity effects, particularly relevant for non-coated sensors at longer wavelengths (see Fig. 4.58), are also not taken into account. Hence, given the rudimentary nature of the model, the deviation between measured and predicted values for the case of He and Ar are believed to be within limits to conclude that resistive bolometry in Magnum-PSI is found effective in assessing total radiated power loss from the plasma.

4.3.4   Power balance

The previously determined values of P_{s} and thus $\int \varepsilon \, dl$ via Eq. 24 yields the possibility of assessing the total power balance in Magnum-PSI. When neglecting power loss through particle diffusion out of the magnetized beam, the power balance can simply be expressed as $P_{in} = P_{rad} + P_{tar}$, where P_{in} and P_{rad} represent the input power and radiative losses respectively and P_{tar} the power transferred to the target.

By utilizing symmetry arguments, P_{tar} is obtained by performing a 2D areal integration of the Gauss-fitted radial heat flux distribution $q(r)$, calculated from $n_{e}(r)$ and $T_{e}(r)$ [185]. The term P_{rad} can be found from the line-integrated plasma emissivity measured by the bolometer, assuming homogeneous emission over the length (z_{tot}) of the plasma beam:

$$P_{rad} = \frac{1}{4} \pi \, d_{p} \, z_{tot} \int \varepsilon \, dl \qquad (26)$$

where d_{p} represents the diameter of the plasma beam.

Figure 4.64 shows P_{rad} as function of $P_{tot} = P_{rad} + P_{tar}$ for the gas species Ar, Ne, He and H. The plasma beam length in this case was 1250 mm while d_{p}=FWHM, obtained from the radial n_{e} distribution. The radiated power loss is seen to increase with rising total beam power and is a fixed fraction of the input power for a specific atomic species. Also, the radiative loss at similar input power, is larger for Ar than Ne which is in agreement with increased expected emissivity of the former based on theory.

The applicability of the bolometer for power balance purposes is demonstrated. However, the absolute magnitude of the radiated power fraction obtained in this fashion is likely to be an overestimation of the real fraction for the following reasons. Firstly, the fraction of P_{rad}/P_{tot} decreases when particle diffusion exiting the plasma beam is taken into account in the power balance (which increases P_{tot}). Secondly, the plasma beam width becomes larger with increased z due to radial diffusion of the plasma particles. Given that the bolometer measures at a downstream position, the local $\int \varepsilon \, dl$ is larger than
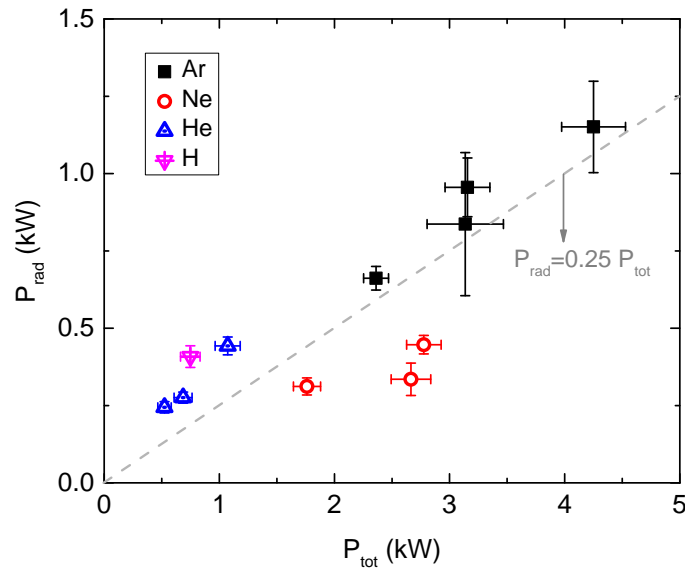
Fig. 4.64 Radiated power measured by the bolometer as function of total power in the plasma beam. Only power loss through radiation and transfer to the target is considered in this simplified model.

at an upstream position which, together with increased beam width, over-predicts P_{rad} in Eq. 4.64. These factors are counter-balanced by the fact that the plasma parameters, especially T_e, are larger upstream which again increases the upstream radiative contribution. Future studies should compare bolometric measurements of the total radiated power to the difference between total power in the beam between source and target position. This requires TS measurements at target and source position at equal plasma conditions with bolometric analysis which is in principle possible in Magnum-PSI.

4.4 Conclusion and outlook

A 4-channel resistive bolometer, capable of measuring total radiated power loss from the plasma, has been successfully deployed on Magnum-PSI, which marks the first demonstration of this sort of diagnostic on a linear plasma device. The detector is equipped with two carbon-coated sensors out of a total of four viewing the plasma perpendicularly, hereby providing an axially resolved measurement around the Thomson Scattering position. The observed region can be varied from a diameter of 12.2 to 23.6 mm by linearly adjusting the detector position, giving the capability to observe the entire beam diameter. Time-traces of steady-state plasma radiation over the course of >450 s are obtained, hereby encountering voltage drift effects attributed to thermal excursions of the detector which may be expected similarly during application of resistive bolometers in future reactors

operating at long timescales. Measurements of the power lost via radiation from H, He, Ne and Ar plasmas using standard settings in Magnum-PSI yielded sensor power densities of 10-37 times the practical noise-equivalent power density of ~0.1 W m^{-2}. Increasing the background pressure by H$_2$ and N$_2$ seeding greatly increased the radiated power density to maximally ~125 kW m^{-2}. A comparison of measured radiated power levels to those obtained from a synthetic diagnostics based on ADAS CRM calculations, yielded good agreement for H and Ne species whereas the prediction for Ar emission was too high and for He too low by a factor 10. The obtained emissivity values were used to make a rough estimation of the power balance in Magnum-PSI, resulting in maximally 27 % lost power through radiation by Ar assuming only power loss through radiation and energy transfer to the target.

The Magnum-PSI bolometry system is demonstrated to be a valuable diagnostic in studies of power balance and divertor detachment studies. Given that the system is capable of providing axial resolved scans of the radiated power profile in front of a target, new plasma-surface interaction science can be performed, for instance in assessing the total radiated power fraction during vapour shielding of divertor targets.

A near-term upgrade of the system involves the installation of a shutter located just in front of the detector, blocking radiation but allowing for gas transfer which eases the bridge rebalancing procedure and increases measurement accuracy. In addition, a frequently performed remote calibration of the sensitivity and time constant in changing plasma conditions, hereby correcting for parasitic effects due to neutrals, can be performed using new FPGA-based electronics.

4.5   Acknowledgements

A   Appendices

A.1   Hardware design of bolometer housing on Magnum-PSI

An exploded CAD drawing of the bolometer housing designed for Magnum-PSI is shown in Fig. A.2. The entire structure is mounted on the S3-225 port which is positioned at an

equal axial distance from the plasma source as the TS system such that the measurement region of the bolometer incorporates the TS measurement position. Inside the tube,
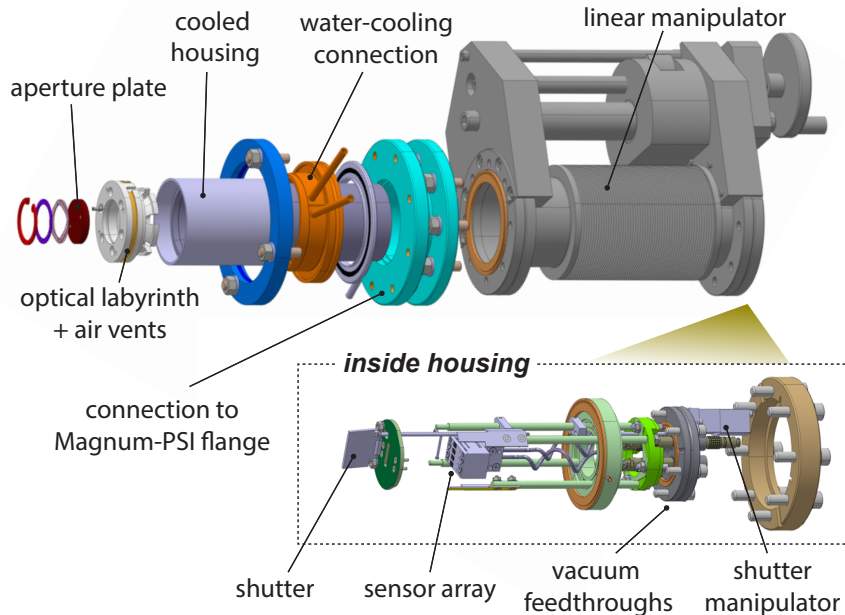
Fig. A.2 Exploded view of Magnum-PSI bolometer. The 4-channel resistive bolometer detector is mounted on a linear manipulator arm in a water-cooled tube attached the Magnum-PSI target chamber. The distance between aperture and the plasma beam centre is 190 mm while the distance between aperture and sensor can be varied between 72.8 and 127.8 mm. Internal reflections in the bolometer housing are minimized by blackened and textured surfaces surrounding the detector.

the bolometer sensor array is attached to four arms only fixed to the rear flange which also contains the electrical feedthroughs for the sensor cables (drawn separately in the bottom of Fig. A.2). The rear flange on its turn is attached to a 100 mm linear translation manipulator, hereby providing the possibility of adjusting the distance between sensor and aperture ($l_{\text{s,ap}}$) from 72.8 mm to 172.8 mm. Bringing the aperture (A_{ap}=1.3x3.8 mm^2, equal to size of a sensor) closer to the plasma region increases the solid angle and thus the signal level, at the expense of spatial resolution (see Fig. 4.59b). For the same reason, the aperture plate is mounted on a tube which intrudes into the Magnum-PSI target chamber by 60 mm, yielding a fixed distance of 190 mm between the centre of the plasma column and the aperture. The water-cooled tube between aperture and detector is entirely blackened (using hot chemical blackening) and textured in order to minimize internal reflections. As well as the aperture opening, additional air vents provided with an optical labyrinth structure allows the pressure inside the bolometer housing to be readily equilibrated with the pressure in the target chamber. The shutter and shutter manipulator drawn in Fig. A.2 are part of a planned upgrade.

A.2 Calibration of the bolometer sensor

The sensitivity S is obtained from presenting an Ohmic heating pulse of known power to the bolometer while measuring the voltage increase ΔU_b [186]. The time constant is obtained from fitting an exponential decay function to $\Delta U_b(t)$ after transiently heating the bolometer sensor with a pulsed laser (0.7 mW, 532 nm). The calibration constants for each sensor at both atmospheric pressure and at 10^{-3} Pa are shown in table 5. The

chan	blackened	air		vacuum	
		S (V/W)	τ (ms)	S (V/W)	τ (ms)
1	no	10.0±0.16	80.5±1	16.1±0.1	148.5±1.2
2	yes	10.7±0.2	86.8±2.4	16.1±0.1	150.1±2.4
3	no	10.5±0.1	86.8±1.8	15.9±0.1	149.8±5.9
4	yes	10.8±0.2	84.8±0.4	15.7±0.2	147.5±0.8

Table 5 Bench-top calibration values of the different bolometer channels at atmospheric pressure and 10^{-3} Pa.

time resolution of the diagnostic is ~100 Hz as determined in a similar setup [193] but ultimately depends on the incident power density. Transient response is not addressed and only results obtained in steady-state plasma conditions relative to the bolometer time resolution are discussed here.

A.3 Sensor absorbance

The standard IPT bolometer sensors are 5 μm thick Au foils provided with a 150 nm Al heat conducting layer. This type of sensor exhibits approximately unity spectral absorbance for wavelengths <100 nm [194] where most of the plasma radiated power is emitted, especially in a tokamak environment. A significant fraction of plasma emission in Magnum-PSI is however expected to occur in the visible wavelength range, given that $T_e \approx$ 1-5 eV [82]. The increase in reflectivity of the Au+Al sensor at longer wavelengths can lead to an underestimation of the radiated power in particularly divertor-like plasma conditions [132]. Hence, In order to enhance absorption by the foils at the lower end of the photon energy spectrum, bolometer sensors 2 and 4 have been coated by a thin layer (maximally 150 nm) of carbon (99.99 % purity) via DC magnetron sputter deposition at room temperature.

This thickness must be regarded as an upper limit valid in the centre of the foil since the thickness around the edges is expected to be lower due to partial shielding by the mask during deposition. The bolometer detector and blackened sensors are shown in Fig. A.3.
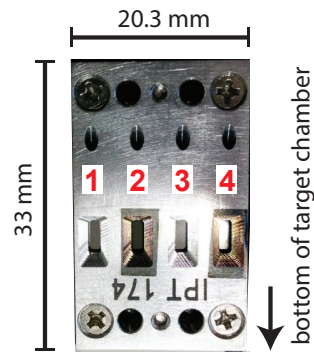
Fig. A.3 The bolometer detector head. Channel numbers as indicated. A 150 nm thick layer of carbon is applied to channels 2 and 4. The bottom of the detector is oriented towards the bottom of the Magnum-PSI target chamber.

No difference in the calibration constants S and τ due to addition of the coating has been found as can be inferred from table 5.

The theoretical spectral absorption of both the Au+Al sensors (channel 1 and 3) and Au+Al with amorphous carbon (channels 2 and 4) are shown in Fig. 4.58 in section 4.2.2 for the range of 0.1-1000 nm. Data is obtained from a simulation of specular reflection for two simulated layered samples, with perfect interfaces, i.e. without layer intermixing or surface roughness [195]. Vacuum is assumed above the first layer and below the last. The angle of incidence of the incident unpolarized beam was 1.5 degrees with respect to the surface normal, which is similar to the bolometer lines of sight. Optical constants for larger wavelengths were partly used from experimental measurements [196] while these at shorter wavelengths were derived from experimental atomic scatter factors [197] with densities of 2.2, 3.26, 19.32 g cm^{-3} for the a-C, Al and Au layers respectively.

The increase in absorption for the wavelength range 100-1000 nm due to addition of a C coating is evident from Fig. 4.58. Although the radiated power loss from the plasma in divertor conditions is predominantly carried by photons with shorter wavelengths [132], the addition of the C coating is deemed necessary for accurately determining total radiated power loss in such an environment.

References

[1] N. Adger *et al.*, "Climate Change 2007: Impacts , Adaptation and Vulnerability," *Intergovernmental Panel on Climate Change*, 2007.

[2] S. Fetzek and J. Mazo, "Climate , Scarcity and Conflict," *Survival - Global Politics and Strategy*.

[3] UNFCCC, "Paris Agreement," *Conf. of the Parties on its twenty-first Sess.*, 2015.

[4] United Nations Department of Economic and Social Affairs, "World Population Prospects," tech. rep., 2017.

[5] Shell, "Signals & Signpoints," tech. rep., 2011.

[6] European Commission, "Energy Roadmap 2050," tech. rep., 2015.

[7] F. Wagner, "Surplus from and storage of electricity generated by intermittent sources," *Eur. Phys. J. Plus*, vol. 131, no. 12, pp. 1–21, 2016.

[8] R. Conn *et al.*, "Economic, safety and environmental prospects of fusion reactors," *Nucl. Fusion*, vol. 30, no. 9, pp. 1919–1934, 1990.

[9] European Commission, *Strategic Energy Technology Plan.* 2017.

[10] F. Romanelli, "Fusion Electricity: A roadmap to the realisation of fusion energy," tech. rep., 2012.

[11] ITER, "ITER technical basis," *ITER EFDA Doc. Ser. 24*, 2002.

[12] X. Mi, "Fast Reactor Technology Development in China Status and Prospects," *Eng. Sci.*, vol. 5, no. 4, pp. 76–83, 2007.

[13] Y. Wan *et al.*, "Overview of the present progress and activities on the CFETR," *Nucl. Fusion*, vol. 57, no. 10, 2017.

[14] J. Wesson, *Tokamaks.* Oxford: Clarendon Press, 3rd ed., 2004.

[15] J. Ongena, R. Koch, R. Wolf, and H. Zohm, "Magnetic-confinement fusion," *Nat. Phys.*, vol. 12, pp. 398–410, 2016.

[16] S. C. Cowley, "The quest for fusion power," *Nat. Phys.*, vol. 12, no. 5, pp. 384–386, 2016.

[17] F. Perkins, "Heating tokamaks via the ion-cyclotron and ion-ion hybrid resonances," *Nucl. Fusion*, vol. 17, p. 6, 1977.

[18] V. Tribaldos, J. Jiménez, J. Guasp, and B. van Milligen, "Electron cyclotron heating and current drive in the TJ-II stellarator Electron cyclotron heating and current drive in the TJ-II stellarator," *Plasma Phys. Control. Fusion*, vol. 40, p. 2113, 1998.

[19] E. Speth, "Neutral beam heating of fusion plasmas," *Reports Prog. Phys.*, vol. 52, no. 1, pp. 57–121, 1989.

[20] A. Fasoli, S. Brunner, W. Cooper, J. Graves, P. Ricci, O. Sauter, and L. Villard, "Computational challenges in magnetic-confinement fusion physics," vol. 12, no. May, 2016.

[21] P. Stangeby, *The Plasma Boundary of Magnetic Fusion Devices.* IOP Publishing Ltd., 2000.

[22] T. Barrett *et al.*, "Progress in the engineering design and assessment of the European DEMO first wall and divertor plasma facing components," *Fusion Eng. Des.*, vol. 109-111, pp. 917–924, 2015.

[23] A. W. Kleyn, N. J. Lopes Cardozo, and U. Samm, "Plasma–surface interaction in the context of ITER," *Phys. Chem. Chem. Phys.*, vol. 8, no. 15, pp. 1761–1774, 2006.

[24] S. Carpentier-Chouchana *et al.*, "Status of the ITER full-tungsten divertor shaping and heat load distribution analysis," *Phys. Scr.*, vol. T159, 2014.

[25] D. Maisonnier *et al.*, "Power plant conceptual studies in Europe," *Nucl. Fusion*, vol. 47, no. 11, pp. 1524–1532, 2007.

[26] T. Eich *et al.*, "Scaling of the tokamak near the scrape-off layer H-mode power width and implications for ITER," *Nucl. Fusion*, vol. 53, no. 9, p. 093031, 2013.

[27] R. Goldston, "Heuristic drift-based model of the power scrape-off width in low-gas-puff H-mode tokamaks," *Nucl. Fusion*, vol. 52, no. 1, p. 013009, 2011.

[28] C. S. Chang *et al.*, "Gyrokinetic projection of the divertor heat-flux width from present tokamaks to ITER," pp. 1–20, 2013.

[29] R. Wenninger *et al.*, "The physics and technology basis entering European system code studies for DEMO," *Nucl. Fusion*, vol. 57, no. 1, p. 016011, 2017.

[30] H. Reimerdes *et al.*, "Assessment of the DEMO compatibility of alternative plasma exhaust solutions," pp. 1–55, 2016.

[31] S. I. Krasheninnikov, A. Kukushkin, W. Lee, A. Phsenov, R. Smirnov, A. Smolyakov, A. Stepanenko, and Y. Zhang, "Edge and divertor plasma: detachment, stability, and plasma-wall interactions," *Nucl. Fusion*, vol. 57, p. 102010, 2017.

[32] D. J. Ward, "The physics of DEMO," *Plasma Phys. Control. Fusion*, vol. 52, no. 12, pp. 0–12, 2010.

[33] P. Valanju, M. Kotschenreuther, S. Mahajan, and J. Canik, "Super-X divertors and high power density fusion devices," *Phys. Plasmas*, vol. 16, no. 5, 2009.

[34] D. Ryutov, R. Cohen, T. Rognlien, and M. Umansky, "A snowflake divertor: A possible solution to the power exhaust problem for tokamaks," *Plasma Phys. Control. Fusion*, vol. 54, no. 12, 2012.

[35] F. L. Tabarés, "Present status of liquid metal research for a fusion reactor," *Plasma Phys. Control. Fusion*, vol. 58, no. 1, p. 014014, 2016.

[36] R. Neu, "Experience with high-Z plasma-facing materials and extrapolation to future devices," *IEEE Trans. Plasma Sci.*, vol. 38, no. 3 PART 1, pp. 453–460, 2010.

[37] M. Kaufmann and R. Neu, "Tungsten as first wall material in fusion devices," *Fusion Eng. Des.*, vol. 82, no. 5-14, pp. 521–527, 2007.

[38] M. Rieth *et al.*, "Recent progress in research on tungsten materials for nuclear fusion applications in Europe," *J. Nucl. Mater.*, vol. 432, no. 1-3, pp. 482–500, 2013.

[39] M. Baldwin and R. Doerner, "Formation of helium induced nanostructure 'fuzz' on various tungsten grades," *J. Nucl. Mater.*, vol. 404, pp. 165–173, sep 2010.

[40] M. Balden, S. Lindig, A. Manhard, and J. You, "D_2 gas-filled blisters on deuterium-bombarded tungsten," *J. Nucl. Mater.*, vol. 414, no. 1, pp. 69–72, 2011.

[41] G. G. van Eden, T. W. Morgan, H. J. van der Meiden, J. Matejicek, T. Chraska, M. Wirtz, and G. De Temmerman, "Effect of high-flux h plasma exposure on tungsten surface damage during transient heat loads," *Nucl. Fusion*, vol. 54, p. 123010, 2014.

[42] M. R. Gilbert, S. Zheng, R. Kemp, L. W. Packer, S. Dudarev, and J. Sublet, "Comparative Assessment of Material Performance in DEMO Fusion Reactors," *Fusion Sci. Technol.*, vol. 66, no. 1, pp. 9–17, 2014.

[43] L. Singheiser, T. Hirai, J. Linke, G. Pintsuk, and M. Rödig, "Transactions of The Indian Institute of Metals Plasma-facing materials for thermo-nuclear fusion devices," vol. 62, no. 2, pp. 123–128, 2009.

[44] J. P. Sharpe, D. A. Petti, and H. W. Bartels, "A review of dust in fusion devices: Implications for safety and operational performance," *Fusion Eng. Des.*, vol. 63-64, pp. 153–163, 2002.

[45] R. J. Goldston, A. Hakim, G. W. Hammett, M. A. Jaworski, and J. Schwartz, "Recent advances towards a lithium vapor box divertor," *Nucl. Mater. Energy*, vol. 12, pp. 1118–1121, 2017.

[46] V. Kvon, E. Zoethout, P. Rindt, W. Arnold Bik, J. W. Genuit, S. Camp, J. Wang, and T. W. Morgan, "High re-deposition ratio of metals under high-flux plasma sputtering in Magnum-PSI," *Submitted to Nucl. Fusion*, 2018.

[47] M. Abdou and The APEX team, "On the exploration of innovative concepts for fusion chamber technology," *Fusion Eng. Des.*, vol. 54, no. 2, pp. 181–247, 2001.

[48] R. Kaita *et al.*, "Extremely low recycling and high power density handling in CDX-U lithium experiments," *J. Nucl. Mater.*, vol. 363-365, pp. 1231–1235, 2007.

[49] D. P. Boyle, R. Maingi, P. B. Snyder, J. Manickam, T. H. Osborne, R. E. Bell, and B. P. LeBlanc, "The relationships between edge localized modes suppression, pedestal profiles and lithium wall coatings in NSTX," *Plasma Phys. Control. Fusion*, vol. 53, no. 10, p. 105011, 2011.

[50] M. G. Bell *et al.*, "Plasma response to lithium-coated plasma-facing components in the National Spherical Torus Experiment," *Plasma Phys. Control. Fusion*, vol. 51, no. 12, p. 124054, 2009.

[51] M. Ono *et al.*, "Recent progress in the NSTX/NSTX-U lithium programme and prospects for reactor-relevant liquid-lithium based divertor development," *Nucl. Fusion*, vol. 53, no. 11, p. 113030, 2013.

[52] D. A. Gates *et al.*, "Overview of results from the National Spherical Torus Experiment (NSTX)," *Nucl. Fusion*, vol. 49, no. 10, p. 104016, 2009.

[53] S. I. Krasheninnikov, L. E. Zakharov, and G. V. Pereverzev, "On lithium walls and the performance of magnetic fusion devices," *Phys. Plasmas*, vol. 10, no. 5 II, pp. 1678–1682, 2003.

[54] L. E. Zakharov, W. Blanchard, R. Kaita, H. Kugel, R. Majeski, and J. Timberlake, "Low recycling regime in ITER and the LiWall concept for its divertor," *J. Nucl. Mater.*, vol. 363-365, no. 1-3, pp. 453–457, 2007.

[55] S. V. Mirnov, E. S. Azizov, V. A. Evtikhin, V. B. Lazarev, I. E. Lyublinski, A. V. Vertkov, and D. Y. Prokhorov, "Experiments with lithium limiter on T-11M tokamak and applications of the lithium capillary-pore system in future fusion reactor devices," *Plasma Phys. Control. Fusion.*, vol. 48, no. 6, pp. 821–837, 2006.

[56] W. Chen, Q. W. Yang, and W. Li, "Simulation of radiation losses using non-coronal model on HL-2A," *Chinese Phys.*, vol. 15, no. 12, pp. 50–52, 2006.

[57] F. Tabarés, E. Oyarzabal, A. Martin-Rojo, D. Tafalla, A. de Castro, and A. Soleto, "Reactor plasma facing component designs based on liquid metal concepts supported in porous systems," *Nucl. Fusion*, vol. 57, no. 1, p. 016029, 2017.

[58] R. Nygren and F. Tabarés, "Liquid surfaces for fusion plasma facing components—A critical review. Part I: Physics and PSI," *Nucl. Mater. Energy*, vol. 9, pp. 6–21, 2016.

[59] V. A. Evtikhin, A. V. Vertkov, I. E. Lyublinski, B. I. Khripunov, V. B. Petrov, and S. V. Mirnov, "Research of lithium capillary-pore systems for fusion reactor plasma facing components," *J. Nucl. Mater.*, vol. 307-311, pp. 1664–1669, 2002.

[60] T. W. Morgan, P. Rindt, G. G. Van Eden, V. Kvon, M. A. Jaworksi, and N. J. Lopes Cardozo, "Liquid metals as a divertor plasma facing material explored using the Pilot-PSI and Magnum- PSI linear devices," *Plasma Phys. Control. Fusion*, vol. 60, p. 014025, 2018.

[61] J. W. Coenen, G. De Temmerman, G. Federici, V. Philipps, G. Sergienko, G. Strohmayer, A. Terra, B. Unterberg, T. Wegener, and D. C. M. Van den Bekerom, "Liquid metals as alternative solution for the power exhaust of future fusion devices: status and perspective," *Phys. Scr.*, vol. T159, p. 014037, 2014.

[62] M. Baldwin, R. Doerner, S. Luckhardt, R. Seraydarian, D. Whyte, and R. Conn, "Plasma interaction with liquid lithium: Measurements of retention and erosion," *Fusion Eng. Des.*, vol. 61-62, pp. 231–236, nov 2002.

[63] H. Moriyama, S. Tanaka, D. K. Sze, J. Reimann, and A. Terlain, "Tritium recovery from liquid metals," *Fusion Eng. Des.*, vol. 28, pp. 226–239, 1995.

[64] T. Iida and R. I. L. Guthrie, "The physical properties of liquid metals," *Mater. Sci. Eng. A*, vol. 114, pp. 215–216, 1989.

[65] M. V. Peralta-Martinez and W. A. Wakeham, "Thermal conductivity of liquid tin and indium," *Int. J. Thermophys.*, vol. 22, no. 2, pp. 395–403, 2001.

[66] E. Yamasue, M. Susa, H. Fukuyama, and K. Nagata, "Deviation from Wiedemann–Franz Law for the Thermal Conductivity of Liquid Tin and Lead at Elevated Temperature," *Int. J. of Thermophysics*, vol. 24, no. 3, pp. 713–730, 2003.

[67] E. A. Brandes and G. B. e. Brook, *Smithells Metals Reference Book*. 7nd ed., 1992.

[68] R. Ohse, *Handbook of thermodynamic and transport properties of alkali metals*. Oxford: Blackwell Scientific, 1985.

[69] V. Riccardo, "Disruptions and disruption mitigation," *Plasma Phys. Control. fusion*, vol. 45, no. 12A, pp. A269–A284, 2003.

[70] A. Sestero, "Protection of walls from hard disruptions in large tokamaks," *Nucl. Fusion*, vol. 17, no. 1, pp. 115–123, 1977.

[71] J. Gilligan, D. Hahn, and R. Mohanti, "Vapor Shielding of Surfaces Subjected To High Heat Fluxes During a Plasma Disruption," *J. Nucl. Mater.*, vol. 162–164, pp. 957–963, 1989.

[72] J. Gilligan, M. Bourham, O. Hankins, W. Eddy, J. Hurley, and D. Black, "Vapor shield protection of plasma facing components under incident high heat flux," *J. Nucl. Mater.*, vol. 196-198, pp. 596–601, 1992.

[73] S. Borthakur, N. Talukdar, N. K. Neog, and T. K. Borthakur, "Design of a coaxial plasma accelerator for fusion relevant material studies," *Fusion Eng. Des.*, vol. 122, pp. 131–139, 2017.

[74] S. Mirnov, "Plasma-wall interactions and plasma behaviour in fusion devices with liquid lithium plasma facing components," *J. Nucl. Mater.*, vol. 390-391, pp. 876–885, 2009.

[75] J. J. Zielinski, H. J. Van Der Meiden, T. W. Morgan, M. H. 't Hoen, D. C. Schram, and G. De Temmerman, "Self-shielding of a plasma-exposed surface during extreme transient heat loads," *Appl. Phys. Lett.*, vol. 104, no. 12, pp. 1–5, 2014.

[76] R. J. Goldston, R. Myers, and J. Schwartz, "The lithium vapor box divertor," *Phys. Scr.*, vol. T167, p. 014017, 2016.

[77] A. Vertkov, I. Lyublinski, M. Zharkov, G. Mazzitelli, M. Apicella, and M. Iafrati, "Liquid tin limiter for FTU tokamak," *Fusion Eng. Des.*, vol. 117, pp. 130–134, 2017.

[78] A. A. Tuccillo *et al.*, "Overview of the FTU results," *Nucl. Fusion*, vol. 49, no. 10, p. 104013, 2009.

[79] G. Mazzitelli *et al.*, "Review of FTU results with the liquid lithium limiter," *Fusion Eng. Des.*, vol. 85, no. 6, pp. 896–901, 2010.

[80] M. Poradziński, I. Ivanova-Stanik, G. Pełka, and R. Zagórski, "Integrated core-SOL-divertor modelling for DEMO with tin divertor," *Fusion Eng. Des.*, vol. 124, pp. 248–251, 2017.

[81] B. de Groot *et al.*, "Extreme hydrogen plasma fluxes at Pilot-PSI enter the ITER divertor regime," *Fusion Eng. Des.*, vol. 82, no. 15-24, pp. 1861–1865, 2007.

[82] H. J. N. van Eck, A. W. Kleyn, A. Lof, H. J. Van Der Meiden, G. J. Van Rooij, J. Scholten, and P. A. Zeijlmans van Emmichoven, "Divertor conditions relevant for fusion reactors achieved with linear plasma generator," *Appl. Phys. Lett.*, vol. 101, no. 22, 2012.

[83] J. Rapp *et al.*, "Construction of the plasma-wall experiment Magnum-PSI," *Fusion Eng. Des.*, vol. 85, no. 7-9, pp. 1455–1459, 2010.

[84] C. B. Alcock, V. P. Itkin, and M. K. Horrigan, "Vapour Pressure Equations for the Metallic Elements: 298–2500K," *Can. Metall. Q.*, vol. 23, no. 3, pp. 309–313, 1984.

[85] G. De Temmerman, M. A. Van Den Berg, J. Scholten, A. Lof, H. J. Van Der Meiden, H. J. N. Van Eck, T. W. Morgan, T. M. De Kruijf, P. A. Zeijlmans Van Emmichoven, and J. J. Zielinski, "High heat flux capabilities of the Magnum-PSI linear plasma device," *Fusion Eng. Des.*, vol. 88, no. 6-8, pp. 483–487, 2013.

[86] H. J. N. van Eck, T. A. R. Hansen, A. W. Kleyn, H. J. van der Meiden, D. C. Schram, and P. A. Zeijlmans van Emmichoven, "A differentially pumped argon plasma in the linear plasma generator Magnum-PSI: gas flow and dynamics of the ionized fraction," *Plasma Sources Sci. Technol.*, vol. 20, p. 045016, 2011.

[87] G. J. Van Rooij *et al.*, "Extreme hydrogen plasma densities achieved in a linear plasma generator," *Appl. Phys. Lett.*, vol. 90, no. 12, pp. 1–4, 2007.

[88] W. A. J. Vijvers, C. A. J. Van Gils, W. J. Goedheer, H. J. van der Meiden, D. C. Schram, V. P. Veremiyenko, J. Westerhout, N. J. Lopes Cardozo, and G. J. van Rooij, "Optimization of the output and efficiency of a high power cascaded arc hydrogen plasma source," *Phys. Plasmas*, vol. 15, no. 9, 2008.

[89] A. E. Shumack, H. J. de Blank, J. Westerhout, and G. J. van Rooij, "Two-dimensional electric current effects on a magnetized plasma in contact with a surface," *Plasma Phys. Control. Fusion*, vol. 54, no. 12, p. 125006, 2012.

[90] H. J. van der Meiden *et al.*, "Advanced Thomson scattering system for high-flux linear plasma generator," *Rev. Sci. Instrum.*, vol. 83, no. 12, 2012.

[91] M. A. Van Den Berg, K. Bystrov, R. Pasquet, J. J. Zielinski, and G. De Temmerman, "Thermographic determination of the sheath heat transmission coefficient in a high density plasma," *J. Nucl. Mater.*, vol. 438, no. SUPPL, pp. 1–16, 2013.

[92] A. Shumack *et al.*, "Rotation of a strongly magnetized hydrogen plasma column determined from an asymmetric balmer-β spectral line with two radiating distributions," *Phys. Rev. E.*, vol. 78, p. 046405, 2008.

[93] V. Kvon, E. Oyarzabal, E. Zoethout, A. B. Martin-rojo, T. W. Morgan, and F. L. Tabarés, "Secondary electron emission of tin and tin-lithium under low energy helium plasma exposure," *Nucl. Mater. Energy*, vol. 13, pp. 21–27, 2017.

[94] V. A. Evtikhin, I. E. Lyublinski, A. V. Vertkov, V. G. Belan, I. K. Konkashbaev, and L. B. Nikandrov, "Calculation and experimental investigation of fusion reactor divertor plate and first wall protection by capillary-pore systems with lithium," *J. Nucl. Mater.*, vol. 271-272, pp. 396–400, 1999.

[95] L. T. Benos and N. A. Pelekasis, "Flow Arrangement and Heat Transfer Capabilities of a Plasma Facing Component in the Form of a CPS," *8th GRACM International Congress on Computational Mechanics*, 2015.

[96] V. Kvon, R. Al, K. Bystrov, F. J. J. Peeters, M. C. M. van de Sanden, and T. W. Morgan, "Tin re-deposition and erosion measured by cavity-ring-down-spectroscopy under a high flux plasma beam," *Nucl. Fusion*, vol. 57, p. 086040, 2017.

[97] H. P. Summers, "The ADAS User Manual," *version 2.6.*

[98] H. R. Griem, *Principles of Plasma Spectroscopy.* Cambridge: Cambridge University Press, 1st ed. ed., 1997.

[99] J. R. Harrison, S. W. Lisgo, K. J. Gibson, P. Tamain, J. Dowling, and The Mast Team, "Characterisation of detached plasmas on the MAST tokamak," *J. Nucl. Mater.*, vol. 415, no. 1 SUPPL, 2011.

[100] H. K. Chung, M. H. Chen, W. L. Morgan, Y. Ralchenko, and R. W. Lee, "FLYCHK: Generalized population kinetics and spectral model for rapid spectroscopic analysis for all elements," *High Energy Density Phys.*, vol. 1, no. 1, pp. 3–12, 2005.

[101] I. H. Hutchinson, *Principles of Plasma Diagnostics.* Cambridge University Press, 2nd ed., 2002.

[102] N. Mott and H. Massey, *The Theory of Atomic Collisions.* Oxford: Oxford University Press, 1965.

[103] R. Teachout and R. Pack, "The static dipole polarizability of all the neutral atoms in their ground states," *At. Data*, vol. 3, pp. 195–214, 1971.

[104] D. Nishijima, U. Wenzel, K. Ohsumi, N. Ohno, Y. Uesugi, and S. Takamura, "Characteristics of detached plasmas associated with electron-ion and molecular assisted recombinations in NAGDIS-II," *Plasma Phys. Control. Fusion*, vol. 44, no. 5, pp. 597–610, 2002.

[105] P. Rindt, N. J. Lopes Cardozo, J. A. van Dommelen, R. Kaita, and M. A. Jaworski, "Conceptual design of a pre-loaded liquid lithium divertor target for NSTX-U," *Fusion Eng. Des.*, vol. 112, pp. 204–212, 2016.

[106] V. G. Baryakhtar, L. E. Mikhailova, A. G. Ilyinskii, A. V. Romanova, and T. M. Khristenko, "The Thermal Expansion Mechanism of Liquid Metals," *Zh. Eksp. Teor. Fiz.*, vol. 95, no. 4, pp. 1404–1411, 1989.

[107] A. Kallenbach *et al.*, "Impurity seeding for tokamak power exhaust: from present devices via ITER to DEMO," *Plasma Phys. Control. Fusion*, vol. 55, no. 12, p. 124041, 2013.

[108] Kallenbach, A and others, "H-mode discharges with feedback controlled radiative boundary in the ASDEX Upgrade tokamak," *Nucl. Fusion*, vol. 35, no. 1231, 1995.

[109] A. Kallenbach, M. Bernert, T. Eich, J. C. Fuchs, L. Giannone, A. Herrmann, J. Schweinzer, and W. Treutterer, "Optimized tokamak power exhaust with double radiative feedback in ASDEX Upgrade," *Nucl. Fusion*, vol. 52, no. 12, 2012.

[110] M. Ono *et al.*, "Exploration of spherical torus physics in the NSTX device," *Nucl. Fusion*, vol. 40, no. 3, pp. 557–561, 2000.

[111] M. Ono *et al.*, "Progress toward commissioning and plasma operation in NSTX-U," *Nucl. Fusion*, vol. 55, no. 7, p. 073007, 2015.

[112] H. Kugel *et al.*, "NSTX plasma operation with a Liquid Lithium Divertor," *Fusion Eng. Des.*, vol. 87, no. 10, pp. 1724–1731, 2012.

[113] H. W. Kugel *et al.*, "Physics design requirements for the National Spherical Torus Experiment liquid lithium divertor," *Fusion Eng. Des.*, vol. 84, no. 7-11, pp. 1125–1129, 2009.

[114] T. Gray, J. Canik, R. Maingi, A. McLean, J.-W. Ahn, M. Jaworkski, R. Kaita, M. Ono, and S. Paul, "The effects of increasing lithium deposition on the power exhaust channel in NSTX," *Nucl. Fusion*, vol. 54, no. 2, p. 023001, 2014.

[115] B. J. Peterson *et al.*, "Bolometer diagnostics for one- and two-dimensional measurements of radiated power on the Large Helical Device," *Plasma Phys. Control. Fusion*, vol. 45, no. 7, pp. 1167–1182, 2003.

[116] B. J. Peterson, H. Parchamy, N. Ashikawa, H. Kawashima, S. Konoshima, A. Y. Kostryukov, I. V. Miroshnikov, D. Seo, and T. Omori, "Development of imaging bolometers for magnetic fusion reactors," *Rev. Sci. Instrum.*, vol. 79, no. 10, p. 10E301, 2008.

[117] G. A. Wurden, B. J. Peterson, and S. Sudo, "Design of an imaging bolometer system for the large helical device," *Rev. Sci. Instrum.*, vol. 68, no. 1, pp. 1–4, 1997.

[118] B. J. Peterson, "Infrared imaging video bolometer," *Rev. Sci. Instrum.*, vol. 71, no. 10, p. 3696, 2000.

[119] B. J. Peterson, R. Sano, M. L. Reinke, J. M. Canik, L. F. Delgado-Aparicio, J. D. Lore, K. Mukai, T. K. Gray, G. G. van Eden, and M. A. Jaworski, "Preliminary design of a tangentially viewing imaging bolometer for NSTX-U," *Rev. Sci. Instrum.*, vol. 87, no. 11, p. 11D410, 2016.

[120] M. L. Reinke and I. H. Hutchinson, "Two dimensional radiated power diagnostics on Alcator C-Mod," *Rev. Sci. Instrum.*, vol. 79, no. 10, p. 261, 2008.

[121] M. Reinke *to be submitted to Rev. Sci. Instrum.*, 2018.

[122] I. H. Hutchinson, "Alcator C-Mod Program," *J. Fusion Energy*, vol. 10, no. 4, pp. 7–9, 1991.

[123] A. W. Leonard, "Review of divertor diagnostics," *Rev. Sci. Instrum.*, vol. 483, 1995.

[124] N. Ohno, "Plasma detachment in linear devices," *Plasma Phys. Control. Fusion*, vol. 59, no. 034007, pp. 1–9, 2017.

[125] J. Rapp *et al.*, "The Development of the Material Plasma Exposure Experiment," *IEEE Trans. Plasma Sci.*, vol. 44, no. 12, pp. 3456–3464, 2016.

[126] M. Bernert, T. Eich, A. Burckhart, J. C. Fuchs, L. Giannone, A. Kallenbach, R. M. Mc-Dermott, and B. Sieglin, "Application of AXUV diode detectors at ASDEX Upgrade," *Rev. Sci. Instrum.*, vol. 85, no. 3, 2014.

[127] K. F. Mast, J. C. Vallet, C. Andelfinger, P. Betzler, H. Kraus, and G. Schramm, "A low noise highly integrated bolometer array for absolute measurement of VUV and soft x radiation," *Rev. Sci. Instrum.*, vol. 62, no. 3, pp. 744–750, 1991.

[128] H. Meister, T. Eich, N. Endstrasser, L. Giannone, M. Kannamüller, A. Kling, J. Koll, T. Trautmann, P. Detemple, and S. Schmitt, "Optimization of a bolometer detector for ITER based on Pt absorber on SiN membrane," *Rev. Sci. Instrum.*, vol. 81, no. 10, pp. 1–4, 2010.

[129] H. Verbeek, J. Stober, and D. P. Coster, "Interaction of charge exchange neutrals with the main chamber walls of plasma machines," *Nucl. Fusion*, vol. 38, p. 1789, 1998.

[130] H. Meister, M. Willmeroth, D. Zhang, A. Gottwald, M. Krumrey, and F. Scholze, "Broad-band efficiency calibration of ITER bolometer prototypes using Pt absorbers on SiN membranes," *Rev. Sci. Instrum.*, vol. 84, no. 12, p. 123501, 2013.

[131] B. L. Henke, E. M. Gullikson, and J. C. Davis, "X-ray interactions: Photoabsorption, scattering, transmission, and reflection at E = 50-30.000 eV, Z = 1-92," *At. Data Nucl. Data Tables*, vol. 54, no. 2, pp. 181–342, 1993.

[132] U. A. Sheikh, B. P. Duval, B. Labit, and F. Nespoli, "A novel carbon coating technique for foil bolometers," *Rev. Sci. Instrum.*, vol. 87, no. 11, p. 11D431, 2016.

[133] H. J. N. van Eck *et al.*, "Operational characteristics of the high flux plasma generator Magnum-PSI," *Fusion Eng. Des.*, vol. 89, no. 9-10, 2014.

[134] A. Murari, K. F. Mast, L. D'Ambra, P. T. Lang, L. Marrelli, P. Martin, and A. Romagnolo, "Multichord calibrated bolometer array for the RFX experiment," *Rev. Sci. Instrum.*, vol. 66, no. 1, pp. 665–667, 1995.

[135] L. Giannone, K. Mast, and M. Schubert, "Derivation of bolometer equations relevant to operation in fusion experiments," *Rev. Sci. Instrum.*, vol. 73, no. 9, p. 3205, 2002.

[136] H. P. Summers, W. J. Dickson, M. G. O'Mullane, N. R. Badnell, A. D. Whiteford, D. H. Brooks, J. Lang, S. D. Loch, and D. C. Griffin, "Ionization state, excited populations and emission of impurities in dynamic finite density plasmas: I. The generalized collisional-radiative model for light elements," *Plasma Phys. Control. Fusion*, vol. 48, no. 2, pp. 263–293, 2006.

[137] IPT Albrecht GmbH *http://www.ipt-albrecht.de/*.

[138] J. Lovell, "Development of Smart , Compact Fusion Diagnostics using Field-Programmable Gate Arrays," *PhD thesis*, 2017.

[139] D-tAcq solutions Ltd. *http://www.d-tacq.com/*.

[140] J. Lovell, G. Naylor, A. Field, P. Drewelow, and R. Sharples, "An FPGA-based bolometer for the MAST-U Super-X divertor," *Rev. Sci. Instrum.*, vol. 87, no. 11, p. 11E721, 2016.

[141] G. Federici *et al.*, "Overview of the design approach and prioritization of R&D activities towards an EU DEMO," *Fusion Eng. Des.*, vol. 109-111, pp. 1464–1474, 2016.

[142] T. W. Morgan, P. Rindt, G. G. van Eden, V. Kvon, M. A. Jaworski, and N. J. Lopes Cardozo, "Liquid metals as a divertor plasma facing material explored using the Pilot-PSI and Magnum- PSI linear devices," *Plasma Phys. Control. Fusion*, vol. 60, no. 1, p. 014025, 2018.

[143] R. Doerner, M. Baldwin, S. Krasheninnikov, and D. Whyte, "Behavior of high temperature liquid surfaces in contact with plasma," *J. Nucl. Mater.*, vol. 313-316, pp. 383–387, 2003.

[144] A. Petrova, V. Kaufman, and L. Vdovina, "The selection of materials resistant to molten tin at high temperatures," *Met .Sci. Heat. Treat.*, vol. 11, p. 819, 1969.

[145] R. A. Pitts *et al.*, "A full tungsten divertor for ITER: Physics issues and design status," *J. Nucl. Mater.*, vol. 438, pp. 1–9, 2013.

[146] B. Riccardi, P. Gavila, R. Giniatulin, V. Kuznetsov, R. Rulev, N. Klimov, D. Kovalenko, V. Barsuk, V. Koidan, and S. Korshunov, "Effect of stationary high heat flux and transient ELMs-like heat loads on the divertor PFCs," *Fusion Eng. Des.*, vol. 88, no. 9-10, pp. 1673–1676, 2013.

[147] H. Zohm, "Assessment of DEMO challenges in technology and physics," in *Fusion Eng. Des.*, vol. 88, pp. 428–433, 2013.

[148] C. Costin, V. Anita, G. Popa, J. Scholten, and G. De Temmerman, "Tailoring the charged particle fluxes across the target surface of Magnum-PSI," *Plasma Sources Sci. Technol.*, vol. 25, no. 2, p. 25023, 2016.

[149] T. W. Morgan, A. Vertkov, K. Bystrov, I. Lyublinski, J. W. Genuit, and G. Mazzitelli, "Power handling of a liquid-metal based CPS structure under high steady-state heat and particle fluxes," *Nucl. Mater. Energy*, vol. 12, pp. 210–215, 2017.

[150] A. Leonard, A. Herrmann, K. Itami, J. Lingertat, A. Loarte, T. Osborne, W. Suttrop, the ITER Divertor Modeling and Database Expert Group, and the ITER Divertor Physics Expert Group, "The impact of ELMs on the ITER divertor," *J. Nucl. Mater.*, vol. 266-269, pp. 109–117, 1999.

[151] A. B. Murphy, "The effects of metal vapour in arc welding," *J. Phys. D. Appl. Phys.*, vol. 43, no. 43, p. 434001, 2010.

[152] Y. Nagayama, "Liquid lithium divertor system for fusion reactor," *Fusion Eng. Des.*, vol. 84, no. 7-11, pp. 1380–1383, 2009.

[153] T. Sizyuk and A. Hassanein, "Scaling mechanisms of vapour/plasma shielding from laser-produced plasmas to magnetic fusion regimes," *Nucl. Fusion*, vol. 54, no. 2, p. 023004, 2014.

[154] H. J. van der Meiden *et al.*, "High sensitivity imaging Thomson scattering for low temperature plasma.," *Rev. Sci. Instrum.*, vol. 79, no. 1, p. 013505, 2008.

[155] ANSYS, Inc., "ANSYS Academic Research Mechanical, Release 16, Help System, Coupled Field Analysis Guide," 2015.

[156] I. Langmuir, "The Condensation and Evaporation of Gas Molecules," *Proc. Natl. Acad. Sci.*, vol. 3, no. 3, pp. 141–147, 1917.

[157] T. W. Morgan, D. C. M. van den Bekerom, and G. De Temmerman, "Interaction of a tin-based capillary porous structure with ITER/DEMO relevant plasma conditions," *J. Nucl. Mater.*, vol. 463, pp. 1256–1259, 2015.

[158] H. Shen, V.K., Siderius, D.W., Krekelberg, W.P., and Hatch, ed., *NIST Standard Reference Simulation Website, NIST Standard Reference Database Number 173.* Gaithersburg MD: National Institute of Standards and Technology.

[159] D. Nishijima, U. Wenzel, K. Ohsumi, N. Ohno, Y. Uesugi, and S. Takamura, "Characteristics of detached plasmas associated with electron-ion and molecular assisted recombinations in NAGDIS-II," *Plasma Phys. Control. Fusion*, vol. 44, no. 5, pp. 597–610, 2002.

[160] D. U. B. Aussems, D. Nishijima, C. Brandt, R. P. Doerner, and N. J. L. Cardozo, "Spectroscopic characterization and imaging of laser- and unipolar arc-induced plasmas," *J. Appl. Phys.*, vol. 116, no. 6, 2014.

[161] N. Ohno *et al.*, "Static and dynamic behaviour of plasma detachment in the divertor simulator experiment NAGDIS-II," *Nucl. Fusion*, vol. 41, no. 8, pp. 1055–1065, 2001.

[162] A. Y. Pigarov, "Collisional Radiative Kinetics of Molecular Assisted Recombination in Edge Plasmas," *Phys. Scr.*, vol. T96, no. 1, p. 16, 2002.

[163] R. F. Mattas *et al.*, "ALPS – advanced limiter-divertor plasma-facing systems," *Fusion Eng. Des.*, vol. 49, no. 50, pp. 127–134, 2000.

[164] G. G. Van Eden, T. W. Morgan, D. U. B. Aussems, M. A. Van Den Berg, K. Bystrov, and M. C. M. Van De Sanden, "Self-Regulated Plasma Heat Flux Mitigation Due to Liquid Sn Vapor Shielding," *Phys. Rev. Lett.*, vol. 116, no. 13, pp. 1–5, 2016.

[165] J. M. Muñoz Burgos, K. Tritz, D. Stutman, R. E. Bell, B. P. Leblanc, and S. A. Sabbagh, "Applications of advanced kinetic collisional radiative modeling and Bremsstrahlung emission to quantitative impurity analysis on the National Spherical Torus Experiment," *Phys. Plasmas*, vol. 22, no. 12, 2015.

[166] C. Costin, V. Anita, G. Popa, J. Scholten, and G. De Temmerman, "Tailoring the charged particle fluxes across the target surface of Magnum-PSI," *Plasma Sources Sci. Technol.*, vol. 25, no. 2, p. 025023, 2016.

[167] G. De Temmerman, J. Daniels, K. Bystrov, M. A. van den Berg, and J. J. Zielinski, "Melt-layer motion and droplet ejection under divertor-relevant plasma conditions," *Nucl. Fusion*, vol. 53, no. 2, p. 023008, 2013.

[168] M. A. Jaworski, T. K. Gray, M. Antonelli, J. J. Kim, C. Y. Lau, M. B. Lee, M. J. Neumann, W. Xu, and D. N. Ruzic, "Thermoelectric magnetohydrodynamic stirring of liquid metals," *Phys. Rev. Lett.*, vol. 104, no. 9, pp. 1–4, 2010.

[169] M. A. Jaworski, S. P. Gerhardt, N. B. Morley, T. Abrams, R. Kaita, J. Kallman, H. Kugel, R. Majeski, and D. N. Ruzic, "Macroscopic motion of liquid metal plasma facing components in a diverted plasma," *J. Nucl. Mater.*, vol. 415, no. 1 SUPPL, pp. S985–S988, 2011.

[170] P. Fiflis, L. Kirsch, D. Andruczyk, D. Curreli, and D. N. Ruzic, "Seebeck coefficient measurements on Li, Sn, Ta, Mo, and W," *J. Nucl. Mater.*, vol. 438, no. 1-3, pp. 224–227, 2013.

[171] F. Incropera and D. Dewitt, *Fundamentals of Heat and Mass Transfer.* Wiley, 2nd ed., 1985.

[172] M. A. Jaworski, N. Morley, and D. Ruzic, "Thermocapillary and thermoelectric effects in liquid lithium plasma facing components," *J. Nucl. Mater.*, vol. 390-391, pp. 1055–1058, 2009.

[173] S. I. Krasheninnikov, A. S. Kukushkin, and A. A. Pshenov, "Divertor plasma detachment," *Phys. Plasmas*, vol. 23, no. 5, 2016.

[174] B. J. Peterson *et al.*, "Bolometric imaging of detached plasmas in LHD," *J. Nucl. Mater.*, vol. 415, no. 1 SUPPL, pp. S1147–S1150, 2011.

[175] B. J. Peterson, E. A. Drapiko, D. Seo, and N. Ashikawa, "Comparison of Au and Pt Foils for an Imaging Bolometer," *Plasma Fusion Res.*, vol. 5, pp. 035–035, 2010.

[176] R. Sano, B. J. Peterson, E. A. Drapiko, D. Seo, Y. Yamauchi, and T. Hino, "Foil calibration for IR imaging bolometer by laser irradiation," *Plasma Fusion Res.*, vol. 7, pp. 3–6, 2012.

[177] D. Coster, X. Bonnin, B. Braams, D. Reiter, and R. Schneider, "Simulation of the Edge Plasma in Tokamaks," *Phys. Scr.*, vol. T108, pp. 7–13, 2004.

[178] S. N. Pandya, B. J. Peterson, M. Kobayashi, S. P. Pandya, K. Mukai, and R. Sano, "A reconsideration of the noise equivalent power and the data analysis procedure for the infrared imaging video bolometers," *Rev. Sci. Instrum.*, vol. 85, no. 12, 2014.

[179] G. G. van Eden, V. Kvon, M. C. M. van de Sanden, and T. W. Morgan, "Oscillatory vapour shielding of liquid metal walls in nuclear fusion devices," *Nat. Commun.*, vol. 8, no. 1, p. 192, 2017.

[180] A. Kukushkin, H. Pacher, A. Loarte, V. Komarov, V. Kotov, M. Merola, G. Pacher, and D. Reiter, "Analysis of performance of the optimized divertor in iter," *Nucl. Fusion*, vol. 49, p. 075008, 2009.

[181] Y. Hayashi, K. Ješko, H. J. van der Meiden, J. W. M. Vernimmen, T. W. Morgan, N. Ohno, S. Kajita, M. Yoshikawa, and S. Masuzaki, "Plasma detachment study of high density helium plasmas in the Pilot-PSI device," *Nucl. Fusion*, vol. 56, p. 126006, 2016.

[182] W. A. J. Vijvers, D. C. Schram, A. E. Shumack, N. J. Lopes Cardozo, J. Rapp, and G. J. van Rooij, "Experimental and theoretical determination of the efficiency of a sub-atmospheric flowing high power cascaded arc hydrogen plasma source," *Plasma. Sources. Sci. Tech.*, vol. 19, p. 065016, 2010.

[183] H. J. N. van Eck, H. H. J. ten Kate, A. V. Dudarev, T. Mulder, and A. Hervé, "A 2.5-T, 1.25-m Free Bore Superconducting Magnet for the Magnum-PSI Linear Plasma Generator," *IEEE Transactions on Applied Superconductivity*, vol. 28, 2018.

[184] J. Scholten *et al.*, "Operational status of the Magnum-PSI linear plasma device," *Fusion Eng. Des.*, vol. 88, no. 9-10, pp. 1785–1788, 2013.

[185] P. Stangeby, *The Plasma Boundary of Magnetic Fusion Devices.* Taylor & Francis, 2000.

[186] A. Murari, M. Cecconello, L. Marrelli, and K. Mast, "Analysis of the calibration methods and error propagation for the sensitivity S and the cooling time constant τ_c of the gold metal foil bolometers," *Rev. Sci. Instrum.*, vol. 75, no. 8, pp. 2692–2699, 2004.

[187] W. A. J. Vijvers *et al.*, "Transport of high fluxes of hydrogen plasma in a linear plasma generator," *Proc. 28th Int. Conf. Phenom. Ioniz. Gases (Prague, Czech Republic)*, pp. 1793–1796, 2007.

[188] R. Janev, D. Reiter, and U. Samm, *Collision processes in low-temperature hydrogen plasmas.* academia.edu, 2003.

[189] D. Rapp and W. Francis, "Charge exchange between gaseous ions and atoms," *J. of Chem. Phys.*, vol. 37, p. 2631, 1962.

[190] N. Ohno, N. Ezumi, S. Takamura, S. I. Krasheninnikov, and A. Y. Pigarov, "Experimental evidence of molecular activated recombination in detached recombining plasmas," *Phys. Rev. Lett.*, vol. 81, pp. 818–821, 1998.

[191] R. Perillo, R. Chandra, G. Akkermans, W. Vijvers, W. Graef, I. Classen, J. van Dijk, and M. de Baar., "Studying the influence of nitrogen in a detached-like hydrogen plasma by means of numerical simulations," *submitted to Plasma. Phys. Contr. Fus.*, 2018.

[192] A. A. Mavrin, "Radiative Cooling Rates for Low-Z Impurities in Non-coronal Equilibrium State," *J. Fusion Energy*, vol. 36, no. 4, pp. 1–12, 2017.

[193] G. G. van Eden *et al.*, "Design and characterization of a prototype divertor viewing infrared video bolometer for NSTX-U," *Rev. Sci. Instrum.*, vol. 87, no. 11, p. 11D402, 2016.

[194] A. Huber *et al.*, "Upgraded bolometer system on jet for improved radiation measurements," *Fus. Eng. Des.*, vol. 82, pp. 1327–1334, 2007.

[195] S. P. Huber, R. W. E. van de Kruijs, A. E. Yakshin, E. Zoethout, K. Boller, and F. Bijkerk, "Subwavelength single layer absorption resonance antireflection coatings," *Optics Express*, vol. 22, p. 490, 2014.

[196] E. Palik, *Handbook of Optical Constants of Solids.* Academic Press, Inc., 1985.

[197] Atomic Scattering Factor Files *http://henke.lbl.gov/optical_constants/asf.html.*

Summary

Vapour shielding of liquid metal walls in nuclear fusion devices

Nuclear fusion power is desirable in a future energy system due to its high energy density, zero CO_2 emission, and abundance of fuel without the intermittency limitation common to renewables. The problem of heat exhaust in future magnetically-confined fusion devices, especially at the scale required for economic exploitation, poses an unprecedented engineering challenge however and is currently viewed as the largest hurdle in its development path. Solid metal divertor materials such as tungsten are prone to damage accumulation when exposed to plasmas at the expected peak heat flux of ~20 MWm^{-2} in DEMO which may reduce their heat handling efficiency and may increase the risk of erosion which can trigger hazardous plasma disruptions. Liquid metals are proposed as a solution to ameliorate this issue since the liquid may act as a sacrificial layer which can be self-healed. The complex plasma-surface interaction physics can hence be decoupled from structural constraints of the divertor materials, hereby likely increasing the operational temperature window of plasma facing components and allowing for better tolerance to otherwise damaging events. In addition, improved power handling may be possible by virtue of additional power dissipation channels available for liquid metals, for instance during vapour shielding where a cloud of neutrals in front of the liquid surface spreads the incoming power via momentum loss and radiation, leading to a reduced power flux to the target surfaces.

Although frequently proposed as a promising mechanism, the possibility and effectiveness of vapour shielding by liquid metals, particularly during stationary conditions, were unclear at the outset of this work. This doctoral dissertation therefore examines the physics of vapour shielding and its potential application as a power exhaust mechanism for nuclear fusion devices, contributing to a solution for protecting fusion reactor walls.

It was expected that vapour shielding would be efficient in conditions where the vapour pressure is balanced by the plasma pressure. This hypothesis was experimentally con-

firmed by exposing liquid tin and liquid lithium to helium and hydrogen plasmas to divertor-relevant heat fluxes (maximally $22\,\mathrm{MW\,m^{-2}}$ for the case of tin) in the linear plasma generators Pilot-PSI and Magnum-PSI. These devices are especially designed to create a high density ($\sim 10^{20}\,\mathrm{m^{-3}}$), low temperature (1-5 eV) plasma typical for the divertor of ITER and beyond. Additionally due to their good diagnostic coverage and high level of plasma control, vapour shielding in such conditions during continuous operation could hence be studied in detail for the first time, resulting in several new observations, particularly for the case of liquid tin.

Firstly, the formation of a tin vapour cloud is observed to be self-regulating in mitigating the plasma heat flux, as is shown by the surface temperature which is found to become 'locked' with respect to the upstream heat flux. Up to one third of the calorimetric energy yield (the conduction pathway) is volumetrically converted into radiation and mass loss carrying energy away from the near-surface region. Secondly, the electron temperature in the vapour cloud is found decreased to 0.5-0.8 eV, which is ~5 times lower than the electron temperature in front of a solid reference material and found to be independent of the upstream heat flux.

Cooling of the plasma is found to occur in several stages. One electron energy loss channel proceeds via ionization and excitation of the evaporated liquid metal ions and neutrals. A second one is also for plasma ions to lose their energy via momentum exchange collisions with the cold evaporative neutrals, the rate of which becomes extremely high when a high neutral density ($\sim 10^{22}\,\mathrm{m^{-3}}$) in the near-surface plasma is reached due to strong evaporation. Through Coulomb collisions with the cooled plasma ions the electrons are also cooled. Eventually low enough electron temperatures are reached such that plasma recombination becomes important and pressure loss and surface heat flux reduction is increased further. We define this regime as 'impurity-induced detachment', similar to conventional divertor detachment and conclude that it is a promising operational regime for a liquid metal divertor without the need for extrinsic gas puffing.

Another important finding is that continuous vapour shielding is found to be oscillatory by nature, concluded from coupled oscillations in photon emission from the vapour cloud and surface temperature. The effect is explained by the presence of mutually interacting systems operating at widely different timescales: thermal diffusion of the plasma facing material ($\sim 10^{-4}$ s) versus plasma physics phenomena ($\sim 10^{-7}$ s). The mechanism is experimentally confirmed for both tin and lithium and is believed to be possible in a divertor geometry as well. A tin surface temperature >1850 K while relying on >99 % surface re-deposition appears to be compatible with core plasma operation, which are suitable conditions to enable heat flux mitigation through vapour shielding in a divertor.

This temperature is likely exceeding material limitations but is still promising in protecting divertor materials during transient excursions of the plasma exhaust over the course of seconds. Due to the combination of a low atom number and high vapour pressure, lithium is a natural candidate liquid metal where continuous vapour shielding is deemed effective, similar to tin but at a lower divertor wall temperature.

The investigation of the overall power balance during vapour shielding raises the question of what fraction of power is lost by radiation, in order to disentangle the combined loss contribution of neutral particles and radiation. This question motivated the development of two diagnostic systems to measure the total radiated power loss from a plasma: an InfraRed Video Bolometer (IRVB) designed for the National Spherical Torus Experiment Upgrade in Princeton, USA, and a resistive bolometer designed for Magnum-PSI at DIFFER, The Netherlands. The IRVB is attractive for tokamak applications due to increased number of channels at reduced cost, 2D plasma radiation mapping and absence of electromagnetic disturbances commonly encountered with a resistive system. However, the signal-to-noise ratio of the IRVB is found worse by a factor ~10 compared to a resistive bolometer. Given the low expected radiation levels in Magnum-PSI, the latter design was chosen for this machine.

The resistive bolometer has been successfully added to the diagnostic suite of Magnum-PSI. First measurements of the plasma radiated power were above the noise equivalent power density of $0.1\,\mathrm{W\,m^{-2}}$ by a factor 10-37 during standard plasma operation, confirming calculations based on a synthetic diagnostic using a collisional radiative model provided by the ADAS database. The linearly adjustable 4-channel detector enables axially resolved measurements of plasma radiation loss at arbitrary distances from the target, hereby providing means to study emission profiles during vapour shielding and e.g. plasma detachment experiments. Approximate power balance calculations revealed maximally 27 % total power loss through radiation from argon in Magnum-PSI. Also, the possibility of performing long time-scale (>100 s) measurements in Magnum-PSI provides a test bed for ITER bolometry where diagnostics with similar durations are required.

Although quantifying the radiative power dissipation pathway during vapour shielding could not be performed within the scope of this thesis project, Magnum-PSI is now prepared to address this question using the (upgraded) bolometry setup. The results described in this thesis are believed to have advanced the understanding of high heat flux power handling of liquid metals, especially that of liquid tin during continuous vapour shielding. Increased understanding of the liquid metal wall solution for nuclear fusion devices is imperative to make a meaningful comparison to solid wall materials, thereby progressing further towards the ultimate goal of realizing fusion power on earth.

Samenvatting

Damp afscherming van vloeibare metalen wanden in kernfusiereactoren

Voor het energiesysteem van de toekomst is kernfusie een aantrekkelijke optie. Kernfusie heeft een hoge energiedichtheid, stoot geen CO_2 uit, de brandstof is rijkelijk aanwezig en de techniek wordt niet beperkt door de wisselvalligheid die andere hernieuwbare energiebronnen kenmerkt. In toekomstige fusiereactoren volgens het principe van magnetische opsluiting, met name op de schaal die nodig is voor economische inzetbaarheid, is het probleem van de warmteafvoer echter een ongeëvenaarde technische uitdaging. Dit probleem wordt momenteel gezien als het grootste obstakel op het ontwikkelingspad van kernfusie. Vaste metalen voor de uitlaatwand (divertor) zoals wolfraam raken beschadigd tijdens blootstelling aan plasma's met de verwachte maximum hitteflux van $20\,\mathrm{MW\,m^{-2}}$ in DEMO. Daardoor kunnen ze minder efficiënt warmte afvoeren en kan het risico van erosie toenemen, wat kan leiden tot een plasmadisruptie. Vloeibare metalen zijn voorgesteld als een oplossing om dit probleem te beperken omdat de vloeistof zichzelf kan repareren na blootstelling aan het plasma. De complexe natuurkunde van de plasma-wand interactie kan op deze manier ontkoppeld worden van de mechanische eisen die aan het materiaal van de divertor worden gesteld. Daarbij valt te verwachten dat componenten die worden blootgesteld aan het plasma een groter operationeel temperatuurbereik krijgen, en een grotere tolerantie tegen schadelijke gebeurtenissen zullen hebben. Verder zal het materiaal beter in staat zijn om het binnenkomende vermogen te verwerken omdat er voor vloeibare metalen extra manieren bestaan om hitte af te voeren. Zo is er het verschijnsel van damp afscherming, waarbij een wolk van neutrale deeltjes vlakbij het vloeistofoppervlak de inkomende energie verspreidt door middel van impulsverlies en straling, waardoor het onderliggende oppervlak een lagere vermogensbelasting te verwerken krijgt.

Hoewel damp afscherming herhaaldelijk is voorgesteld als een veelbelovend mechanisme, was de haalbaarheid en effectiviteit van damp afscherming door vloeibare metalen, met name tijdens stationaire condities, nog onduidelijk bij aanvang van dit werk. Dit

proefschrift onderzoekt daarom de natuurkunde achter damp afscherming en de mogelijke toepasbaarheid hiervan als een methode om in kernfusiereactoren hitte af te voeren en zo de wanden van een fusiereactor te beschermen.

De verwachting was dat damp afscherming efficiënt zou zijn in condities waar de verdampingsdruk in evenwicht is met de plasmadruk. Deze hypothese was experimenteel bevestigd in de lineaire plasmageneratoren Pilot-PSI en Magnum-PSI, door vloeibaar tin en vloeibaar lithium bloot te stellen aan helium- en waterstofplasma's met een divertor-relevante plasma hitteflux (maximaal $22\,\mathrm{MW\,m^{-2}}$ in het geval van tin). Deze machines zijn speciaal ontworpen om een plasma op te wekken van hoge dichtheid ($\sim 10^{20}\,\mathrm{m^{-3}}$) en lage temperatuur (1-5 eV), typisch voor de divertor van ITER en zijn opvolgers. Dankzij de goede diagnostische dekking en goede controle over het plasma kon damp afscherming voor de eerste keer in detail worden onderzocht in deze condities en in steady-state condities. In het bijzonder voor het geval van vloeibaar tin zijn verschillende nieuwe observaties gedaan.

Ten eerste is gevonden dat de vorming van een dampwolk tin zelfregulerend is in het verminderen van de hitteflux van het plasma, wat blijkt uit de oppervlaktetemperatuur die stabiel blijft ten opzichte van de stroomopwaartse hitteflux. Tot wel één derde van de calorimetrische energieopbrengst (het geleidingskanaal) is ruimtelijk omgezet in straling en massaverlies waarbij energie wordt weggedragen vanuit het volume vlakbij het oppervlak. Ten tweede is gevonden dat de elektronentemperatuur in de dampwolk afneemt tot 0.5-0.8 eV, wat ~5 keer lager is dan de elektronentemperatuur in de nabijheid van een vast referentiemateriaal, onafhankelijk van de stroomopwaartste hitteflux.

Koeling van het plasma vindt plaats in verschillende stappen. Eén energieverlieskanaal wordt gevormd door ionisatie en excitatie van verdampte metaalionen en -neutralen. Een tweede kanaal geldt ook voor plasma-ionen die hun energie verliezen door impulsuitwisseling met koude, verdampte neutrale deeltjes, waarvan de trefkans extreem hoog wordt door de hoge dichtheid (dankzij sterke verdamping) van neutralen ($\sim 10^{22}\,\mathrm{m^{-3}}$) in het plasma nabij het oppervlak. De elektronen koelen af door Coulomb-botsingen met afgekoelde plasma-ionen. Uiteindelijk wordt een dermate lage elektronentemperatuur bereikt dat plasma recombinatie belangrijk wordt en de plasmadruk en de oppervlaktetemperatuur verder afnemen. Het regime wat zodanig betreden wordt, definiëren we als 'onzuiverheid-geïnduceerde onthechting', vergelijkbaar met conventionele divertor plasma-onthechting, en we concluderen dat dit een veelbelovend operationeel regime is voor een divertor van vloeibaar metaal, zonder dat het nodig is om extrinsiek gas toe te voegen.

Een belangrijke vondst daarnaast is dat continue damp afscherming fundamenteel oscillatoir van aard is, wat we concluderen op basis van oscillaties in het uitgezonden licht van de dampwolk gekoppeld aan de oppervlaktemperatuur. We verklaren dit effect door de aanwezigheid van wederzijds interacterende systemen die zich gedragen op zeer verschillende tijdschalen: thermische diffusie van het plasma-blootgestelde materiaal ($\sim 10^{-4}$ s) versus fenomenen van plasmafysische aard ($\sim 10^{-7}$ s). Het mechanisme is experimenteel aangetoond voor zowel tin als lithium en we voorspellen dat dit ook mogelijk moet zijn in een divertorgeometrie. Een tin oppervlaktetemperatuur >1850K met >99 % redepositie op het oppervlak lijkt compatibel met plasmascenario's in de kern, wat passende condities zijn om hittefluxbeperking door damp afscherming te bewerkstelligen. Deze temperatuur gaat waarschijnlijk voorbij aan materiaallimieten maar toch is het proces veelbelovend ter bescherming tijdens intense, kortdurende excursies van de plasma-afvoer op de tijdschaal van seconden. Dankzij de combinatie van een laag atoomnummer en hoge dampdruk is lithium de natuurlijke kandidaat voor een vloeibaar metaal waar continue damp afscherming effectief geacht wordt, vergelijkbaar met tin maar bij een lagere temperatuur van de divertorwand.

Het onderzoek naar de algehele vermogensbalans tijdens damp afscherming roept de vraag op welk deel van het vermogen verloren gaat in de vorm van straling, met name om de gecombineerde verliesterm van neutrale deeltjes en straling te ontkoppelen. Deze vraag vormde de motivatie voor de ontwikkeling van twee diagnostische systemen om het totale stralingsverlies van een plasma te meten: een InfraRood Video Bolometer (IRVB) voor de *National Spherical Torus Experiment Upgrade* in Princeton in de Verenigde Staten, en een resistieve bolometer voor Magnum-PSI bij DIFFER in Nederland. Een IRVB systeem is aantrekkelijk voor toepassing in tokamaks vanwege de grote hoeveelheid aan meetkanalen en gereduceerde kosten, de mogelijkheid tot het in kaart brengen van 2D plasma profielen en de afwezigheid van elektromagnetische verstoringen die normaliter een resistief systeem plagen. Daarentegen is de signaal-ruis-verhouding van de IRVB ~10 keer slechter dan die van een resistieve bolometer. Omdat het verwachte stralingsniveau in Magnum-PSI laag geschat werd, is dit laatste soort ontwerp gekozen voor deze machine.

De resistieve bolometer is succesvol toegevoegd aan de diagnostische uitrusting van Magnum-PSI. De eerste metingen aan het stralingsvermogen van het plasma bleken hoger dan de ruisvermogensdichtheid van $0.1\,\mathrm{W\,m^{-2}}$ met een factor 10-37 gedurende standaard plasma operatie. Dit bevestigt berekeningen van een synthetische diagnostiek gebaseerd op een botsings-stralingsmodel uit de ADAS database. De lineair regelbare 4-kanaals detector maakt axiaal-opgeloste metingen van plasmastralingsverlies op willekeurige afstanden van de trefplaat mogelijk, waarmee de mogelijkheid ontstaat om emissieprofie-

len gedurende damp afscherming en bijvoorbeeld plasma-onthechtingsexperimenten te verkrijgen. Initiële schattingen van de vermogensbalans hebben uitgewezen dat maximaal 27 % van het totale vermogensverlies plaatsvindt via straling in het geval van een standaard argon scenario in Magnum-PSI. Daarnaast schept de mogelijkheid tot het verrichten van metingen op lange tijdschalen (>100 s) in Magnum-PSI een testomgeving voor bolometrie in ITER, waar dit soort diagnostieken op vergelijkbare tijdschalen nodig zullen zijn. Hoewel binnen dit promotieonderzoek het stralingsverlieskanaal tijdens damp afscherming niet is vervuld, is Magnum-PSI nu geheel voorbereid om deze vraag te adresseren met behulp van de (verbeterde) bolometrie-opstelling. De resultaten die in dit proefschrift beschreven staan hebben bijgedragen aan het begrip van hoge hitteflux vermogensverwerking van vloeibare metalen, in het speciaal dat van vloeibaar tin tijdens continue damp afscherming. De toegenomen kennis over de oplossing van vloeibare metaalwanden voor kernfusiereactoren is noodzakelijk voor gedegen vergelijking met vaste materialen, waarmee een belangrijke stap gezet wordt naar het ultieme doel: het realiseren van fusie-energie op aarde.

List of Publications

Academic publications related to this thesis work:

- **Plasma radiation studies in Magnum-PSI using resistive bolometry.**
  G.G. van Eden, M.L. Reinke, S. Brons, G. van der Bijl, B. Krijger, R. Lavrijsen, S.P. Huber, R. Perillo, M.C.M. van de Sanden and T.W. Morgan.
  Submitted to Nuclear Fusion.

- **Liquid metals as a divertor plasma facing material explored using the Pilot-PSI and Magnum-PSI linear devices.**
  T.W. Morgan, P. Rindt, **G.G. van Eden**, V. Kvon, M.A. Jaworski and N.J. Lopes Cardozo.
  Plasma Phys. Contr. Fus., 60 (2018) 014025

- **Oscillatory vapour shielding of liquid metal walls in nuclear fusion devices.**
  G.G. van Eden, V. Kvon, M.C.M. van de Sanden and T.W. Morgan.
  Nature Comms. 8 (2017) 192

- **Self-regulated plasma heat flux mitigation due to liquid Sn vapor shielding.**
  G.G. van Eden, T.W. Morgan, D.U.B. Aussems, M.A. van den Berg, K. Bystrov and M.C.M. van de Sanden.
  Phys. Rev. Lett. 116 (2016) 13

- **Preliminary design of a tangentially viewing imaging bolometer for NSTX-U.**
  B.J. Peterson, R. Sano, M.L. Reinke, J.M. Canik, L.F. Delgado-Aparicio, J.D. Lore, K. Mukai, T.K. Gray, **G.G. van Eden** and M.A. Jaworski.
  Rev. Sci. Instrum. 87 (2016) 11

- **Development of plasma bolometers using fiber-optic temperature sensors.**
  M.L. Reinke, M. Han, G. Liu, **G.G. van Eden**, R. Evenblij, M. Haverdings and B.C. Stratton.
  Rev. Sci. Instrum. 87 (2016) 11

- **Design and characterization of a prototype divertor viewing infrared video bolometer for NSTX-U.**
  G.G. van Eden, M.L. Reinke, B.J. Peterson, T.K. Gray, L.F. Delgado-Aparicio, M.A. Jaworski, J.D. Lore, K. Mukai, R. Sano, S. Pandya and T.W. Morgan.
  Rev. Sc. Instrum. 87 (2016) 11

Other academic publications:

- **Operational characteristics of the superconducting high flux plasma generator Magnum-PSI.**
  M.J. van de Pol, S. Alonso van der Westen, D.U.B. Aussems, M.A. van den Berg, S. Brons, H.J.N. van Eck, **G.G. van Eden**, H.J.W. Genuit, H.J. van der Meiden, T.W. Morgan, J. Scholten, J.W.M. Vernimmen, E.G.P. Vos and M.R. de Baar. *In preparation for publication in Fus. Eng. Des.*

- **Performance of the lithium metal infused trenches in the magnum PSI linear plasma simulator.**
  P. Fiflis, T.W. Morgan, S. Brons, **G.G. van Eden**, M. van den berg, W. Xu, D. Curreli and D.N. Ruzic.
  Nucl. Fus. 55 (2015) 11

- **Characterizing the recovery of a solid surface after tungsten nano-tendril formation.**
  G. Wright, **G.G. van Eden**, L.A. Kesler, G. De Temmerman, D.G. Whyte and K.B. Woller.
  J. Nucl. Mat. 463 (2015) 294-298

- **Effect of high-flux H/He plasma exposure on tungsten damage due to transient heat loads.**
  G. De Temmerman, T.W. Morgan, **G.G. van Eden**, T. de Kruif, M. Wirtz, J. Matejicek, T. Chraska, R.A. Pitts and G.M. Wright.
  J. Nucl. Mat. 463 (2015) 198-201

- **The effect of high-flux H plasma exposure with simultaneous transient heat loads on tungsten surface damage and power handling.**
  G.G. van Eden, T.W. Morgen, H.J. van der Meiden, J. Matejicek, T. Chraska, M. Wirtz and G. De Temmerman.
  Nucl. Fusion 54 (2014) 123010

- **Operational characteristics of the high flux plasma generator Magnum-PSI.**
  H.J.N. van Eck, T. Abrams, M.A. van den Berg, S. Brons, **G.G. van Eden**, M.A. Jaworski, R. Kaita, H.J. van der Meiden, T.W. Morgan, M.J. van de Pol, J. Scholten, P.H.M. Smeets, G. De Temmerman, P.C. de Vries and P.A. Zeijlmans van Emmichoven.
  Fus. Eng. Des. 89 2150-2154 (2014)

- **ELM-induced melting: assessment of shallow melt layer damage and power handling capability of tungsten in a linear plasma device.**
  T.W. Morgan, **G.G. van Eden**, T.M. de Kruif, M.A. van den Berg, J. Matejicek, T. Chraska and G. De Temmerman.
  Phys. Scr. T159 014022 (2014)

- **Thermal response of nanostructured tungsten.**
  S. Kajita, G. De Temmerman, T.W. Morgan, **G.G. van Eden**, T. de Kruif and N. Ohno.
  Nucl. Fus. 54 033005 (2014)

Popular science:

- G.G. van Eden ***"Vloeibare fusiereactorwanden in de media"*** - Nederlands Tijdschrift voor Natuurkunde. 83 (2017) 10

- G.G. van Eden ***"De kunst der pianistiek, begrepen door fysici?"*** - Nederlands Tijdschrift voor Natuurkunde. 83 (2017) 7

- G.G. van Eden ***"Metaaldamp beschermt uitlaat fusiereactor tegen plasmabombardement"*** - Nederlands Tijdschrift voor Natuurkunde. 82 (2016) 10

- G.G. van Eden ***"Van gedachte-experiment naar realiteit"*** - defusie.net. (2013)

Dutch media attention to thesis work:

- *"Doorbraak: wand fusiereactor kan worden beschermd met dun laagje vloeibaar metaal"* - de Volkskrant, 05-08-2017

- *"Nederlandse uitvinding brengt kernfusie dichterbij"* - NOS.nl, 07-08-2017

- *"Fusiereactor krijgt 'vloeibare' wand"* - NRC Handelsblad, 09-08-2017

- *Wetenschappers ontwikkelen bescherming voor reactorwand bij kernfusie* - Tweakers.net, 07-08-2017

- *"Vloeibaar metaal beschermt wand fusiereactor"* - De Ingenieur, 07-08-2017

- *Reactorwand van vloeibaar metaal* - Technisch Weekblad, 08-08-2017

- *"Kernfusie dichterbij dankzij Eindhovense wetenschappers"* - Eindhovens Dagblad, 09-08-2017

- *"Een doucheputje van vloeibaar tin"* - De Ingenieur, 10-07-2017

- *"Een zon op aarde"* -ScienceGuide.nl, 08-04-2016

- *"Vloeibaar metaal bij kernfusie"* - Eindhovens Dablad, 05-04-2016

Award:

- NEVAC artikelprijs 2017 (Nederlandse Vacuümvereniging)
  G.G. van Eden ***"Stralingsenergie meten in een fusiereactor".***

Acknowledgements

"Whoever has come so far that he no longer errs is also no longer working" - Max Planck

Zo. Eén avond voordat dit proefschrift gedrukt wordt mag ik eens te raden gaan aan wie ik dit toch allemaal te danken heb! Afhankelijk van of ik met jou in het Engels of Nederlands sprak zal ik je in die taal toespreken. Ik zal natuurlijk mensen vergeten, bij voorbaat excuses als ik je gemist heb, je zal het zelf weten en ik kom er vast weer op zodra dit uit de printer is gerold.

Tom, I'm most indebted to you. I'm grateful for all your support and guidance that I have received. I have thought of ways to be creative in writing when I was asking yet another time for you to comment on my text in the "16th paragraph of the 2nd section of the 8th version of the appendix of a paper", but failed in this and you kept diligently replying. You have thought me a lot about PSI physics and were always available, even at the start of the project four years ago when things were sometimes improvisational due to the absence of a group leader. I'm proud to be one of your first graduate students. I hope there are many to follow and that you will fix that divertor issue after all.

Op de tweede plaats richt ik mijn dank naar mijn promotoren. Richard, hoewel we elkaar niet zo vaak spraken was jij er op kritieke momenten. Ik ben je dankbaar voor de altijd efficiënte en nuttige adviezen. Ik kan me ons telefoongesprek herinneren toen ik in Princeton zat, waarin je voorstelde mijn eerste paper op te splitsen. Zonder die ingreep en je vertrouwen in mij, waren m'n publicaties in PRL en Nature Communications er niet geweest! Ik wil je ook bedanken (of moet ik FOM/NWO zeggen?) voor het mogelijk maken van m'n fantastische tijd bij het Princeton Plasma Physics Lab en voor het meedenken over m'n verdere loopbaan. Niek, wij spraken elkaar pas aan het einde van de rit, toen ik nog een 'masterclass' kernfusie en haar inzetbaarheid van je kreeg. Niet alvorens we eerst piano hadden gespeeld natuurlijk. Dank voor het delen van je kennis en je inzet!

Switching back to English to say thanks to my American colleagues and friends which I gathered during my Princeton year. First of all: thank you Mike J, for making my visit

possible in the first place. I have found it inspirational to work with you and I promise to never bike around the PPPL campus without a helmet anymore. Matt, I have spent most of the time in the lab with you which was really fun and inspirational. It has made me realize how much there is too learn... The post-it "come to my office when your pants are on", which I found in my office after my yoga practice, is still with me as a reminder to one of such meetings. Chapters 3 and 4 certainly wouldn't have been there without you, thanks for that. Byron, although short, I have valued our time together in the cramped basement lab, pondering about IRVBs. It is you who thought me the phrase which is stated on top of this page, an important lesson in helping me to put things in perspective.

Damien, beste paranimf, jij verdient natuurlijk je eigen paragraaf, al kan ik een boek over je schrijven. Ik denk dat ik rustig kan zeggen dat we sinds het begin van onze PhD's vrienden zijn. Het begon natuurlijk met die Lorentz Workshop in Leiden in 2014 om het daarna te bezegelen met een trip door Japan na een conferentie. Het verkennen van wolkenkrabberdaken, illegaal reizen onder een deken in de Shinkansen en kamperen in een auto in het wild met gestolen badjassen. En dit was nog maar het begin... Met de Gregxit hadden we beide een wat lastige start, jij meer dan ik. Onze grappen en eerlijke, soms diepe maar meestal weerzinwekkend oppervlakkige gesprekken geven me nog binnenpret voor de komende 12 jaar. Ik ben dankbaar om een maat zoals jij in m'n kantoor gehad te hebben om mee te kunnen reflecteren in onze eigen taal (letterlijk). De rit was een stuk zwaarder geweest zonder jou al bijrijder. Ik hoop dat we elkaar volgen in de achteruitkijkspiegel.

Battyboy, geachte Sebastiaan, jij bent er sinds het begin bij geweest. Samen zaten we in de universiteitsbankjes op de Minnaert faculteit in Utrecht en je hebt op afstand dit boekje zien ontstaan. Vanzelfsprekend ben jij, als enige echte vriend van de natuurkunde-faculteit, mijn paranimf. De enige die het vocabulaire 'handstand, 'Pentium', 'Descartes', en 'cyclops' vloeiend verstaat en ook nog 'Shos' en 'Rach' op waarde kan schatten. We stonden samen eenzaam te midden van een vreemd ecosysteem waar we soms de ballen van begrepen. Ik zal de gevolgen van "wat sta je nou te zwalken" nooit vergeten. Het is je humor en intelligentie die me de nodige positieve vibes gaven, zolang ik niet herinnerd wordt aan je drumtics en je onuitputtelijke reservoir aan citaten uit televisieshows uit 1982. Hoogtepunt was natuurlijk onze epische roadtrip door Amerika op muziek van Shostakovich en fietsen door het besneeuwde Yellowstone park met overstekende bizons. Oja, voordat ik het vergeet, nog bedankt voor die kwantum 2 adviezen, ik had het anders niet gehaald! Monorail.

Dan zijn er natuurlijk vele toffe DIFFER collega's die me in het groot of in het klein hebben bijgestaan. Dirk, jou ken ik daar al het langste, leuk om vanuit een kasteelkelder

samen te zijn opgeklommen naar de tweede verdieping van een BREEAM-gecertificeerd gebouw. Dankjewel Gieljan voor je bereidheid altijd m'n stukken van feedback te voorzien en prachtige media-releases voor elkaar te boxen. Yaoge, I realize that our conversations have been shallow, but it's in between the lines that I know you are a great guy. Renato, thanks for having helped me to mboat my way, I wish you luck to do the same. Ah, there is many of you, the DIFFER ecosystem is special. Thank you Teofil, Karol, Bram W, Mohammed, Vladimir, Srinath, Fiona, Anna, Tesfaye, Dozi, Floran(tine), Mozhkan, Gijs, Bob K (ik zal op soldeercursus gaan!), Yu, Wei, Han, Wim A-B, Jan-Willem en Henny. Jordy, Santi, John, Marc, Serge, Richard A en Ronald, dankjewel voor alle technische hulp en Pilot/Magnum operations! Frank, Wim M, Henk en Hans, dank voor al die gerende kilometers en spierpijn.

One of my best memories is obviously the 2017 planet DIFFER cabaret. Thank you George, Kieran, Tom B, Qin, Martijn and the support from Sander, Bram B, Bob, Alex, Bobby and Adelbert. I can't think of a better way to bring an ode to the life at our institute than through making this documentary. I have truly loved being part of this endeavour.

My time in Princeton has been amazing and I'm grateful to have gathered a circle of great friends who have helped me to quickly feel at home. Jorge, you are one of the most talented and remarkable persons I have ever met. Thanks for your patience in teaching me about atomic physics modelling and the purpose of life. I believe you will make it as an astronaut. Soha, Evan and Mike, thanks for being my buddy's both in and outside of the lab. Mochi, I'm grateful for you being my fishing, climbing, hookah, hiking, basketball, conversational and above all, party mate. Thank you too: Jesse, Freddy, Elaine, Brandon and Sarah for being part of wonderful Princeton. Erez, I mean Hans Kamminga, what a wonderful coincidence we met at the baseball field. Come back for sailing, quick dates on the island of Texel and other shrewd ploys.

Hans en Julia, jullie als familie boden me nog een plekje 'thuis' in het geweld van New York City. Mijn dank is groot voor de talloze keren logeren in Brooklyn. Meike und Bernd, danke für alles. Zusammenleben in den Vereinigten Staaten war toll.

Jan Gerrit, beste oom, ik bedank je voor je indirecte hulp door jullie prachtige huis in de Spaanse Pyreneeën open te stellen als 'schrijversretraite' voor PhD studenten. Het grootste deel van dit boekje is op jouw dakterras geschreven. Deze plek gaf me de moed hieraan te beginnen, alleen afgeleid door schaapsbellen en het zoemen van roofvogels in de wind. De aanwezigheid van Pepa, met al haar wijsheid en levensinspiratie, was daar overal nog voelbaar en haar wijze woorden die ik tijdens m'n leven ontving kwamen terug. Dankjewel voor jouw (en jullie) grootse gastvrijheid, nu nogmaals door je galerie open te stellen voor een feestje.

Natuurlijk is m'n geestelijke ondersteuning thuis in Utrecht en omstreken niet te vergeten. Jullie waren er altijd als ik afleiding nodig had (en soms ook toen ik het niet nodig had...). Thanks Jop, Rein (die ontbrekende pijl!), Mich, Toon, Maria, Pim, David, Sicco, Alex, Bou en Ilse. Gert, jij hebt me geleerd thuis ook eens pauze te nemen! Gerhard and Andre, thanks for the friendship for life, laughs, (f)ery good conversations, and, recently, help on my book cover. You guys are the best.

Ondanks de vele uren die in dit werk zijn gaan zitten is de uitwerking van muziek op mij alleen maar verdiept. Dank jullie wel voor de bekrachtiging hiervan: Misha en Andiamo maatjes Dionne en Marieke. Arjen, zonder jou had ik mijn passies misschien wel niet weten te verbinden tot op dit punt.

Lieve pa en ma, broertje en zusje, Carola, Ahmed, het is bijna gek jullie expliciet te bedanken, zo vanzelfsprekend voelt jullie steun. Toch had ik überhaupt nooit kunnen beginnen zonder jullie liefde en een warme maaltijd op z'n tijd. Anja, Olaf en Mirjam, dank ook voor de altijd warme ontvangst bij jullie.

Tot slot, hoe kan het ook anders, mijn lieve Esther. De hoeveelheid onvoorwaardelijke psychologische support die jij hebt gegeven in dit proces is niet te bevatten. Nog belangrijker, jij hielp me de dingen los te laten en soms te mogen ontspannen. Je beschikt over kernkrachten die ik nog níet doorgrond...

Curriculum Vitae

Stein van Eden was born on 19-09-1986 in Bilthoven, The Netherlands. After finishing his *Atheneum* degree in 2004 at the Montessori Lyceum Herman Jordan in Zeist, The Netherlands, he studied Civil Engineering at Delft University of Technology during one year (*propedeuse* degree), followed by a Bachelor of Science in Physics and Astronomy combined with a minor track in Music Sciences at Utrecht University. He graduated in 2008 on a thesis project carried out in the field of subatomic physics: modelling energy loss from a quark-gluon plasma. A few months later, Stein won the second prize and audience award during the international student piano competition held in Utrecht. In the same period, he commenced a Bachelor of Arts in classical music performance (piano) at the Conservatory of Utrecht, jointly with a Master of Science in Nanomaterials: Science and Applications at Utrecht University. Stein completed his music studies in 2012 after having received further coaching at the *Hochschule für Musik und Tanz* in Cologne, Germany, during five months. In 2013 he graduated within the Plasma Material Interactions group of DIFFER in Nieuwegein, The Netherlands, on the topic of tungsten surface damage evolution exposed to simultaneous plasma and laser pulses. He started his PhD project at the same research institute in February 2014 focussed on the physics of vapour shielding of liquid metals in a fusion reactor divertor environment, of which the results are presented in this dissertation. As part of this thesis work, Stein was a visiting scholar at the Princeton Plasma Physics Laboratory in the U.S.A. during one year, where he was involved in the development of a new plasma radiation instrument for the National Spherical Torus Experiment Upgrade. Stein returned to DIFFER located in Eindhoven in April 2016 (after DIFFER's relocation). He is still an avid pianist and performs in concerts with his Andiamo chamber music trio and participates in music masterclasses.